Time-Lapse Seismic Monitoring of Waterflooding in Turbidite Reservoirs

Nader Kooli

A thesis submitted for the Degree of Doctor of Philosophy
Institute of Petroleum Engineering
Heriot-Watt University, Edinburgh, Scotland

April, 2010

Abstract

An integrated, multi-disciplinary approach was developed to examine waterflooding processes in deepwater stacked turbidite reservoirs. Fluid flow in porous rocks was reviewed both at the pore and the reservoir section scales. The importance of a favourable mobility ratio for a stable oil/water displacement was highlighted. This information guided our choices for fluids characteristics to use in our fluid flow simulation models. A geological review of deepwater turbidite reservoirs provided a sound understanding of their geological characteristics, with a special emphasis on their impact on fluid flow within the reservoir. The vertical permeability distribution across the reservoir was identified as having a crucial impact on waterflooding efficiency in turbidite reservoirs. Permeability distribution within a channel element of a stacked turbidite reservoir follows three characteristic trends: homogeneous distribution, fining upward distribution, and coarsening upward distribution.

A series of idealised reservoir models, representative of a single flow unit within a turbidite reservoir, was built. The idealised models represented the three different permeability distributions commonly found in turbidites and another model was added to simulate bottom drive waterflooding. Two scenarios were run on the models: water injection with pressure support and water injection where the pressure dropped by a maximum of 1500 psi. The change in V_p was around 4 to 5% regardless of the reservoir geology or the pressure variations. Pressure change has a global dimming effect on the P-wave velocity. It happens very briefly after the start of the simulation and spreads across the whole reservoir. Change in V_p due to pressure decline was around -0.5% and could not be detected on the synthetic seismic. The waterfront is easily interpreted both on 4D cross-section and 4D attribute maps.

A realistic turbidite geological model based on the Ainsa II outcrop was built. The model was populated with rock characteristics of a turbidite reservoir on the West of Africa. The model was then up-scaled and fluid flow simulation was performed. Permeability values and NTG distribution played a major role in the advance of the waterfront inside the reservoir and controlled its shape and location. Petrophysical modelling showed that P-waves velocity would increase by up to 7% due to the substitution of oil by water and suggested that it can be extremely sensitive to water saturation changes. Even the smallest changes (less than 10%) would have a noticeable effect on Vp values, which is of crucial importance when time-lapse seismic is to be used in a quantitative way. Synthetic seismic was created using three different frequencies (35 Hz, 62 Hz, and 125 Hz). On 3D seismic sections, different channels within the reservoir were resolved separately on the high resolution seismic. Tuning phenomenon is observed for the three modelled frequencies due to the presence of very thin beds (1-2 meter thick). The interpretation of the OOWC or the MOWC on those sections is challenging because the reflections at the fluids front are obscured by reflections from geological interfaces. The complex geology of the reservoir resulted in 3 different RMS seismic amplitude maps showing an increasing degree of heterogeneity as the seismic dominant frequency increased. Interpretation of MOWC on time-lapse seismic cross-sections and maps is challenging and the inclusion of different attributes in the interpretation workflow might be necessary in order to assess the complexity of the waterflooding signature.

Time-lapse seismic monitoring of waterflooding processes in deepwater turbidite reservoirs requires sound a-priori knowledge of the geology of the reservoir. On the other hand, an accurate interpretation of the time-lapse seismic signature of Waterflooding can improve our understanding of the reservoir characteristics. Therefore, the task should be performed by multi-disciplinary teams, where geologists, reservoir engineers, and geophysicists work closely together.

To Najla Bouden-Romdhane

« *Humanum fuit errare, diabolicum est per animositatem in errore manere* »

St. Augustine 354 – 430

Acknowledgements

I would like to thank my supervisor Prof. Colin MacBeth for his continuous support and guidance throughout the course of my PhD studies. I am very grateful to Dr. Asghar Shams for providing his support and advice whenever needed. I would like to thank Dr. Andy Gardiner for the insightful geological discussions and advises. Dr. Gillian Pickup help with the up-scaling workflow is much appreciated. Dr. Eric MacKay inputs and recommendations for the fluid flow simulations were invaluable.

I would like to thank Prof. Yanghua Wang and Dr. Eric MacKay for the time and effort invested in reading and examining this thesis.

I am very grateful to all the members and alumni of the ETLP group for the interesting discussions. Special thanks to Said Al-Busaidi, Faisal Al-Kindi, Mariano Floricich, Hansel Gonsalez, Neil Hodgson, Mehdi Paidayesh, Amran Benguigui, Weisheng He, and Hamed Amini for their help and support.

Last but not least, I would like to thank my family and friends for their encouragement and for always being there for me.

ACADEMIC REGISTRY
Research Thesis Submission

Name:	Nader Kooli		
School/PGI:	Institute of Petroleum Engineering		
Version: *(i.e. First, Resubmission, Final)*	Final	Degree Sought (Award **and** Subject area)	Doctor of Philosophy

Declaration

In accordance with the appropriate regulations I hereby submit my thesis and I declare that:

1) the thesis embodies the results of my own work and has been composed by myself
2) where appropriate, I have made acknowledgement of the work of others and have made reference to work carried out in collaboration with other persons
3) the thesis is the correct version of the thesis for submission and is the same version as any electronic versions submitted*.
4) my thesis for the award referred to, deposited in the Heriot-Watt University Library, should be made available for loan or photocopying and be available via the Institutional Repository, subject to such conditions as the Librarian may require
5) I understand that as a student of the University I am required to abide by the Regulations of the University and to conform to its discipline.

* *Please note that it is the responsibility of the candidate to ensure that the correct version of the thesis is submitted.*

Signature of Candidate:		Date:	15/08/2010

Submission

Submitted By *(name in capitals):*	
Signature of Individual Submitting:	
Date Submitted:	

For Completion in Academic Registry

Received in the Academic Registry by *(name in capitals):*			
Method of Submission *(Handed in to Academic Registry; posted through internal/external mail):*			
*E-thesis Submitted (**mandatory for final theses from January 2009)***			
Signature:		Date:	

Contents

List of Figures

List of Tables

List of Symbols

A	Initial amplitude of the seismic wavelet
$C\mathrm{P}$	Coefficient related to the change in pressure of the reservoir
$C\mathrm{S}$	Coefficient related to the change in saturation of the reservoir
$c\mathrm{f}$	Fluid compressibility
$E\kappa$	Characteristic pressure function
$E\mu$	Characteristic pressure function
IP	P-wave impedance
IS	S-wave impedance
$P\kappa$	Characteristic pressure constant
$P\mu$	Characteristic pressure constant
$P\varphi$	Characteristic pressure constant
R	Reflectivity
R	Gas constant
$R\mathrm{s}$	Solution gas ratio
$R\mathrm{pp}$	P-wave reflectivity
$R\mathrm{s}$	S-wave reflectivity
S	Saturation
$S\mathrm{a}$	Salinity
SG	Specific gravity
S_{oi}	Initial oil saturation
S_{of}	Final oil saturation
$S\mathrm{g}$	Saturation of gas
$S\mathrm{o}$	Saturation of oil
$S\mathrm{w}$	Saturation of water
$S\kappa$	Stress sensitivity factor
$S\mu$	Stress sensitivity factor
T	Time
T	Temperature
V	Volume

V	Wavelet velocity
V_p	Compressional wave velocity
V_s	Shear wave velocity
Z	Depth
Z	Gas compressibility
Δ	Difference
ΔP	Change in the pressure field between the two survey dates
ΔP_max	Maximum pressure change in the reservoir
ΔA	4D seismic amplitude
ΔS	Average saturation change
$\Delta\mathrm{IP}$	P-wave impedance change
$\Delta\mathrm{IS}$	S-wave impedance change
$\Delta V\mathrm{p}$	Compressional wave velocity change
$\Delta V\mathrm{s}$	Shear wave velocity change

Greek letters

α	Attenuation coefficient
α	P-wave velocity
β	S-wave velocity
φ	Porosity
φ_eff	Effective porosity (net-to-gross multiplied by sand porosity)
$\gamma\mathrm{o}$	Ratio of heat capacity at constant pressure to that at constant volume
κ	Bulk modulus
κ_∞	Bulk modulus asymptote at high pressure
κ_w	Water bulk modulus
κ_d	Bulk modulus of dry-frame
κ_fl	Fluid bulk modulus
κ_g	Gas bulk modulus
$\kappa*$	Bulk modulus of the porous rock frame, (drained of any pore-filling fluid)
κ_o	Mineral or grain bulk modulus

κo	Oil bulk modulus
κb	Brine bulk modulus
κf	Bulk modulus asymptote at high pressure
κ_{sat}	Bulk modulus of saturated rock
K	Horizontal permeability
K_{rel}	Oil relative permeability evaluated at initial saturation conditions
Λ	Wavelength
μ	Viscosity
μ	Shear modulus
μ	Fluid viscosity
μ_{∞}	Shear modulus asymptote at high pressure
μ_d	Shear modulus of dry-frame
μ_f	Fluid shear modulus
μ_g	Gas shear modulus
μ_o	Oil shear modulus
μ_{sat}	Shear modulus of saturated rock
ρ	Density
ρ_b	Brine density
ρ_w	Water density
ρ_d	Density of dry-frame
ρ_f	Fluid mixture density
ρ_g	Gas density
ρ_m	Mineral or grain density
ρ_o	Oil density
ρ_{sat}	Density of saturated rock
ω	Wavelet frequency

Abbreviations

4D	Multiple 3D surveys at different times; the fourth dimension is time
API	American Petroleum Institute

AVO	Amplitude versus offset
NTG	Net –to-gross
OWC	Oil - water contact
OOWC	Original oil - water contact
RMS	Root - mean - square
SNR	Signal to noise ratio
HCSTP	homogeneous model with constant pressure
HDECP	homogeneous model with declining pressure
BD	homogeneous model under basal drive
FUP	Heterogeneous model with lower permeability at the top
CUP	Heterogeneous model with higher permeability at the top

Chapter 1

Introduction

This chapter presents the main challenges of the thesis and the research methodology adopted to address those challenges. The thesis outline is also highlighted.

1.1 Preamble

With the constant increase in oil demand, oil companies started exploring new area looking for more reserves, and soon, oil once was discovered in the North Sea, Gulf of Mexico, Africa and Greenland. Once these discoveries had been made, it became clear that major new oil discoveries would be found less frequently. Most of the sedimentary basins have been explored and the potentially oil-bearing reservoirs identified.

As the demand on oil is growing exponentially, oil activity has increasingly been shifting to integrated reservoir management technologies to better recover bypassed oil, monitor injection programmes, optimize development well placement, and ultimately increase recovery from existing assets. In fact, in the past few years, several major oil companies have already reported that more than half of their geoscientists work already on production-related rather than exploration-related projects (Lumley, 2004).

The average oil recovery for most reservoirs is less than 40%, so it is understandable that the slight increase of this recovery factor will lead to an important economic reward, especially in giant oil fields. Injecting fluids into the reservoir to displace oil and maintain the pressure has become a common practice and, due to its abundance and availability, water injection was the first increased oil recovery technique to be applied to oil reservoirs.

Exploration, drilling and production technology have advanced significantly, especially after the introduction of rotary drilling, seismic, and computers. Exploration, which used to consist of identifying oil sweeps and drilling nearby changed into a high-tech industry. The advance of computing technology allows more information to be extracted from increasingly larger data volumes (Rauch, 2001). The development of 3D seismic technology; an earth imaging technique that yields relatively detailed 3D images of the subsurface, and the constant increase in seismic resolution established the seismic methods as the principal form for oil exploration. 4D seismic, the difference between two 3D seismic surveys shot over the same reservoir in two different calendar times, became a popular reservoir management tool and narrowed the gap between the two worlds of geophysics and reservoir engineering. In fact, changes in fluid saturations, pressure and temperature due to production in a reservoir, result in changes in seismic velocities and density which result in changes in impedance that, under appropriate conditions, can be detected in seismic differences.

The successful application of time-lapse techniques can provide valuable information about the dynamic reservoir properties in the intra-well regions. Time-lapse seismic can be used to identify bypassed oil and undrained compartments, and also to target infill drilling wells, thus adding more reserves to production and extending the field’s economic life.

1.2 Main challenges of the thesis and research methodology

To accurately estimate the efficiency of a Waterflooding process, reservoir internal structure, reservoir rock properties and fluid properties need to be accurately estimated.

Reservoir structure plays an important part in controlling the displacement of oil by water inside the reservoir. Permeability and NTG variations across the reservoir and the presence of flow barriers will determine the drainage patterns and whether any bypassed oil is left behind at the end of Waterflooding. Rock properties such as permeability, porosity, and relative permeability determine how freely can both fluids, oil and water, flow within the reservoir rocks pores hence influencing both flow directions, speed and also displacement efficiency. Fluid properties, such as density and viscosity, have a determining influence on the speed of flow within the rock pores and the movable oil volumes, therefore influencing the efficiency of Waterflooding processes.

Successfully applying time-lapse seismic techniques in the monitoring of Waterflooding processes depends on several factors involving both the state of the reservoir itself (geology, fluids, pressure, etc) and the geophysical parameters of the seismic acquisition (data quality, repeatability, seismic resolution, etc).

Time-lapse seismic signatures of Waterflooding can be complex in some reservoir settings. In addition to the fact that time-lapse signature of Waterflooding is the result of several changes that occur simultaneously within the reservoir (pressure, fluids saturation, temperature, porosity, etc), structurally complex reservoirs, such as deep water turbidite reservoirs, would add more complexities to the 4D signal. To correctly understand and interpret those signatures, an a priori knowledge of the reservoir geological variations and fluids content is needed.

The aim of this thesis is to provide a global understanding of time-lapse seismic monitoring of Waterflooding processes in vertically stacked deep water turbidite reservoirs. The study, even though carried out from a geophysical perspective, comprises a review of fluid flow in reservoir rocks, the effect of the reservoir geology on the efficiency of Waterflooding processes and the several parameters affecting the numerical simulation of such processes.

A multi-disciplinary approach was adopted in this thesis in order to understand Waterflooding processes and the resulting time-lapse signatures. We worked on synthetic reservoir models as it allowed us to have a complete confidence in our knowledge of the reservoir geology, structure and fluids allowing for an accurate interpretation of the complex signatures of Waterflooding process in turbidite reservoirs. Fluid flow simulations were performed on a series of synthetic reservoirs with a varying degree of geological complexities. A petro-elastic model was defined to transform the flow simulation output, i.e. pressure and saturation values at every grid cell and at different time steps, into seismic properties.

We started with a simple reservoir model, representative of a flow unit within a channel in a turbidite reservoir and exhibiting three different vertical distribution of permeability values commonly found in turbidite reservoirs: fining up-ward, coarsening up-ward and homogeneous. Several Waterflooding scenarios were simulated and the resulting 4D signatures interpreted. Then an outcrop based fine scale geological model of a stacked turbidite reservoir was used as the foundation to build a realistic simulation model for a complex turbidite reservoir. A Waterflooding process was simulated and simulation output was used to create synthetic seismic at different calendar times in order to simulate 4D seismic signatures of Waterflooding in that particular geological setting. Figure 1.1 summarizes the workflow of the adopted methodology.

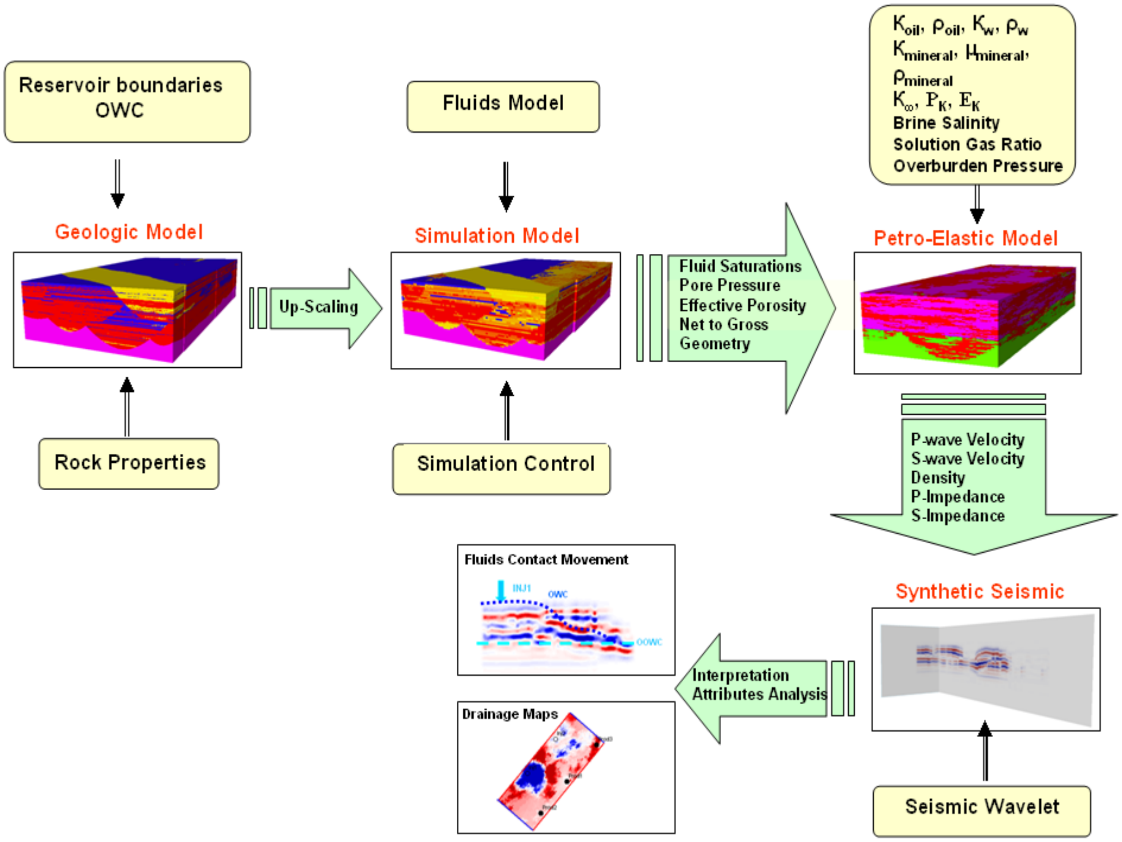

Figure 1.1: Workflow applied for the various studies. The geological model which incorporates the spatial positions of the major boundaries of the formations, including the effects of faulting, folding, and erosion (unconformities), reservoir facies, reservoir quality, and fluids type and distribution is up-scaled to perform fluid flow simulation. Outputs from the simulator are then used in the petrophysical modelling to compute the seismic properties of the reservoir rocks. Last, time-lapse seismic attributes are created and interpreted.

This approach is first applied to idealised reservoir models, representative of a single flow unit within a turbidite reservoir and exhibiting three different vertical distribution of permeability values commonly found in turbidite reservoirs: fining up-ward, coarsening up-ward and homogeneous. Then, a realistic, fine-scale outcrop based turbidite model is built and the workflow applied.

1.3 Thesis outline

The remainder of this thesis is divided into six chapters:

Chapter 2 describes the parameters affecting the efficiency of Waterflooding processes. The time-lapse seismic signatures of Waterflooding are studied with a focus on the challenges faced for a correct interpretation of such signatures. A literature review on the use of time-lapse seismic as a reservoir management tool is presented. Several examples where time-lapse seismic was successfully used in the evaluation of Waterflooding processes are discussed.

Chapter 3 examines the different parameters affecting the efficiency of Waterflooding. The influence of the reservoir internal geology and reservoir fluids properties are highlighted. A series of idealised reservoir models of thick and clean sandstone are built. The different models present varying degree of geological variations and are representative of one flow unit within a channel in a turbidite reservoir. Several Waterflooding scenarios are run; the results of the petrophysical modelling and the 4D signature associated with every scenario are studied.

Chapter 4 gives a geological description of deepwater turbidite reservoirs and their different elements. The seismic characteristics of these different elements are listed through example from the literature. The challenges for an optimal deep water turbidite reservoir management are discussed. The AINSAII outcrop model used in our flow simulation studies is introduced; the results of the flow simulation are discussed.

Chapter 5 presents the petrophysical modelling study performed on the AINSAII simulation model output. Synthetic seismic created using three different frequencies is studied and time lapse seismic interpretation was carried on for the three frequencies highlighting resolution issues and their influence on an accurate interpretation of Waterflooding signatures in a geologically complex setting.

Chapter 6 presents the time lapse seismic attributes analysis performed on a high resolution seismic created from the simulation outputs of Waterflooding in the synthetic turbidite reservoir. Both time shifts attribute and 4D amplitude RMS attributes are studied. The combined response from these two attributes is used to better assess the efficiency of the Waterflooding process by identifying swept areas and fluids contact more accurately.

Chapter 7 presents a summary and conclusions for this work. Suggestions for future research are also included.

Chapter 2

Estimation of Waterflooding efficiency: the added value of 4D seismic

This chapter describes the parameters affecting the efficiency of Waterflooding processes. The time-lapse seismic signatures of Waterflooding are studied with a focus on the challenges faced for a correct interpretation of such signatures. A literature review on the use of time-lapse seismic as a reservoir management tool is presented. Several examples where time-lapse seismic was successfully used in the evaluation of Waterflooding processes are discussed.

2.1 Parameters affecting the efficiency of Waterflooding

Waterflooding efficiency in macroscopic reservoir sections is controlled by three major factors:

- a- Mobility ratio
- b- Reservoir heterogeneities
- c- Gravity

These three factors combine together to govern the water movement aerially and across the reservoir.

2.1.1 Mobility ratio

Mobility, k/μ, is defined as permeability of a porous material to a given phase divided by the viscosity of that phase. Mobility ratio, M, is defined as mobility of the displacing phase divided by the mobility of the displaced phase. In the case of Waterflooding,

$$M= \frac{K'_{rw} / \mu_w}{K'_{ro} / \mu_o}\ ; \qquad (2.1)$$

where K'_{ro} is the relative permeability for oil, K'_{rw} is the relative permeability for water, μ_o is the viscosity of oil and μ_w is the viscosity of water. The incorporation of the maximum end-point relative permeabilities means that, by direct application of Darcy's law, the mobility ratio represents the ratio of the maximum velocity of the displacing phase (water) by the maximum velocity of the displaced phase (oil). A piston-like displacement occurs when the injected water moves slower than the displaced oil, i.e. the mobility ratio is lower than 1. Given that the displacement is immiscible and the oil viscosity is low, a sharp front will separate the water from the oil, and the water will keep pushing the oil in a piston-like manner. The displacement in this case is stable and highly efficient such that all the moveable oil is recovered by the injection of an equivalent volume of water. On the other hand, if M > 1, on account of high oil viscosity, the water can move faster than the oil and since it is the water that is pushing the oil, it channels through the oil in an unstable fashion known as fingering. The Waterflooding is inefficient in this case as water breaks through prematurely and it might require the circulation of several pore volumes of water to recover the movable oil volume (Figure 2.1). It is worth noting however that most of the oil fields selected for development by Waterflooding have low oil viscosity, generally associated with a favourable mobility ratio (M <1) (Dake, 2001). The effects of the mobility ratio of the efficiency of water-oil displacement are visible only on the microscopic, one dimensional scale. In the case of Waterflooding of a reservoir, one must also consider the heterogeneity and gravity effects on the overall flooding efficiency.

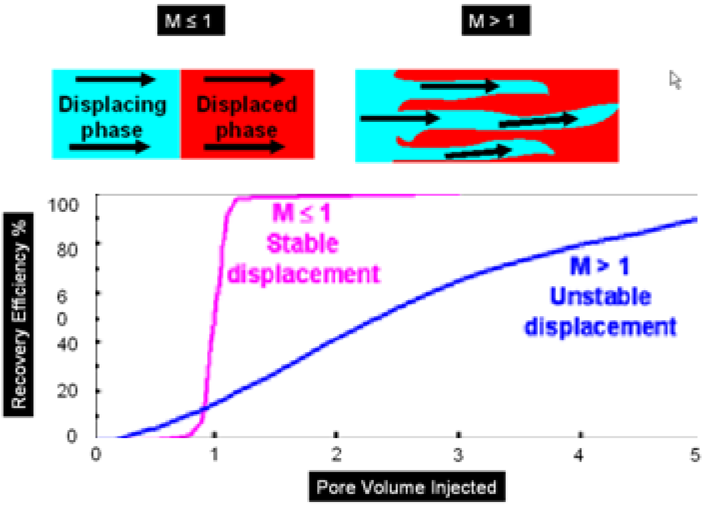

Figure 2.1: Effects of mobility ratio on water-oil displacement.

2.1.2 Reservoir heterogeneities and gravity:

In reservoir sections, scale, gravity and heterogeneity are closely interrelated and they have a combined influence on the Waterflooding efficiency. The gravity effect is always combined with the heterogeneity effects to produce a stable or a non-stable water-oil displacement. The mobility ratio influence is swamped but it can indicate the ease with which water can be injected into a reservoir.

In assessing the heterogeneity of the reservoir, the most significant parameter to consider is the permeability and in particular its degree of variation across the reservoir section (Willhite, 1986). This is due to the fact that permeability can vary by several orders of magnitude within a matter of a few feet which makes its influence overshadow the influences of other parameters like porosity and water saturation. In the case of coarsening upward of the permeability across the reservoir section, a piston-like displacement may occur provided the cross-flow of fluids under the influence of gravity is not prohibited (vertical equilibrium conditions). In this situation, the heterogeneity of the reservoir (mainly controlled by the vertical permeability distribution) and the gravity complement each other and can produce a piston-like displacement even for an unfavourable mobility ratio. In fact, as the water enters the structure, it moves faster in the higher permeability top layers according to Darcy’s law. But as the water progresses away from the well, the viscous driving forces from the injection pumping decrease and at some point diminish so that gravity will govern. The water then slumps to the base and the overall effect is the development of a sharp front and perfect piston-like displacement across the reservoir section.

If the higher permeability is in the bottom of the reservoir (coarsening downward), the gravity effect will be intensified and an unfavourable displacement will happen leading to the necessity to circulate huge amount of water in order to move the oil in place, even with a mobility ratio less than unity (Figure 2.2).

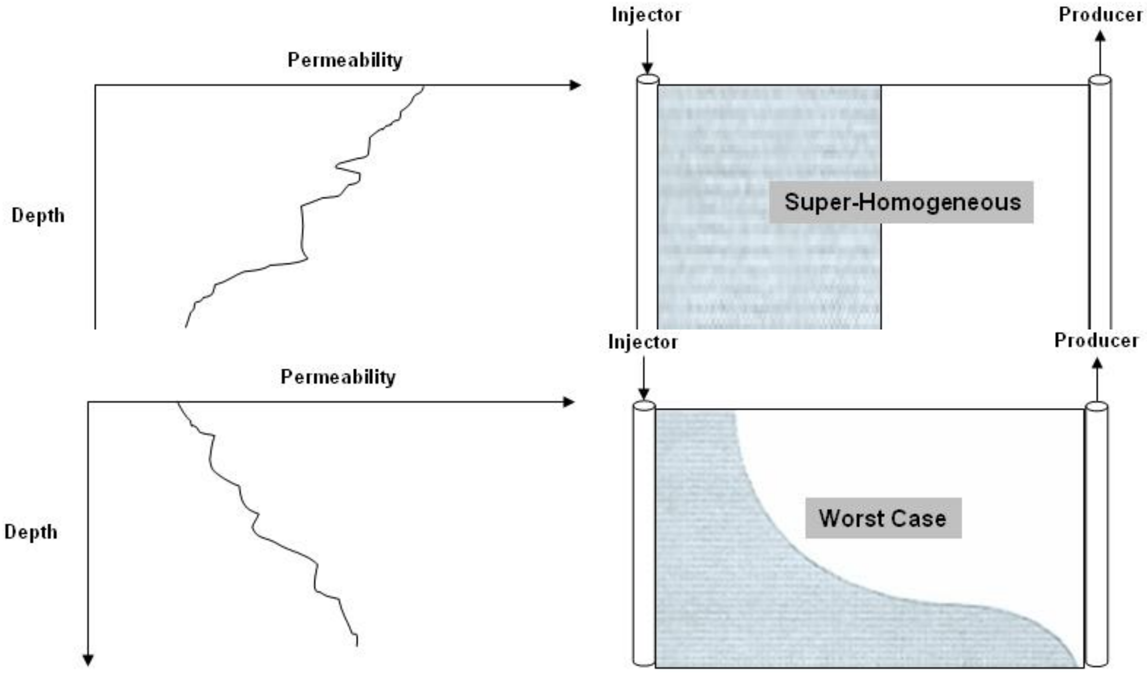

Figure 2.2: Effect of permeability distribution of Waterflooding efficiency.

2.2 Time-lapse seismic signature of Waterflooding

2.2.1 Theoretical background

Our study focused on two phases (oil and water) systems, where water is injected into the reservoir to displace the oil towards the producers. In this case the waterfront is the oil-water contact so both terms are used interchangeably across the whole chapter. In the case where a natural aquifer is present in the reservoir, the oil/water contact will be called original oil/water contact (OOWC) for clarity purposes. The identification of OWC movement from 4D seismic was one of the earliest practical applications of this technique. Even at the qualitative stage, it brought valuable information revealing unswept areas, or flow barriers that cannot be determined without dynamic seismic information. The successful identification of contact movement that can be obtained from the simple subtraction of base and monitor surveys depend among other factors on the signal to noise ratio or tuning that is why other seismic attributes are often used to emphasize the contact variation that eventually cannot be observed using simple amplitude subtraction. Inverted acoustic impedance maps and cross-sections are powerful tools for the identification of fluids contact and are widely used as the preferred 4D seismic attribute to extract the OWC movement (Khahar et al., 2006). Complex attributes were proven useful in the identification of such contacts and their movement across the reservoir (Schinelli, 2006).

The identification of OWC movement from time-lapse seismic is not only constrained by the seismic acquisition parameters (S/N ratio, source wavelet, etc.) but also by the inherent reservoir geology such as rock petrophysical and elastic parameters, heterogeneities, etc. The fluids characteristics, mainly the acoustic contrast between the displacing (water) and displaced (oil) fluids, will also determine whether any fluids substitution is seismically detectable. This means that not every reservoir undergoing Waterflooding as a secondary recovery technique is a suitable candidate for time-lapse seismic Waterflooding. Investigating the feasibility of such monitoring is beyond the scope of this thesis (Wang et al., 1991). Our work will focus on turbidite reservoirs where several successes were reported (MacBeth et al., 2005).

Interpretation of the 4D signature of Waterflooding gives information about swept/unswept areas in the reservoir and the location of the OWC at the time of the seismic acquisition of the monitor survey. However in order for this interpretation to be meaningful, the complex nature of this signature has to be understood. In fact, during Waterflooding, several dynamic reservoir properties are changing simultaneously. Laboratory investigations and theoretical analysis have shown that the velocities and density of rocks are affected by changes in the temperature, composition, density and pressure of pore fluids (Wang and Nur, 1986; Wang et al., 1990; Batzle and Wang, 1992). The fluid substitution that occurs during the production of hydrocarbon reservoirs changes the compressibility of the pore fluids, thus changing the velocity of the overall rock. In Waterflooding, the injected water decreases the overall compressibility of the rock, raising the velocity. Many investigations in the laboratory have shown that pore pressure changes affect the seismic velocity (Wyllie et al., 1958; Han et al., 1986; Freund, 1992). During production, fluid injection will increase pore pressure, decreasing the effective stress and lowering velocities. Hydrocarbon extraction can cause a decline in pore pressure, which results in increasing velocity until the bubble point is reached, after which gas comes out of solution, decreasing the seismic velocity.

Consider a reservoir in which only two phases, oil and water, are present; and where the oil is assumed to be undersaturated and hence the reservoir pressure is above bubble point. Generally, the seismic attribute A, computed at the top reservoir, base or some intra-reservoir horizon, is dependent on the reservoir thickness (τ), lithology (L), porosity (Φ), reservoir pressure (P) and oil saturation (S_o) (MacBeth et al., 2004)

$$A=A(x, y, \tau, L, \Phi, P, S_o) \tag{2.2}$$

where A represents a mapped function of x and y defined on the interval of interest. In the specific case of a non-compacting reservoir and assuming that the geomechanical effects in the overburden are insignificant, production induces reservoir pressure and saturation changes, but only very small changes in τ or Φ. Thus, the repeat survey response $A_r(x, y)$ can be written in terms of the baseline survey response $A_b(x, y)$, and the time-lapse changes by use of a first-order Taylor expansion assuming P and S_o change slowly

$$A_r\left(x,y,\tau,L,\phi,P,S_o\right)\approx A_b\left(x,y,\tau,L,\phi,P,S_o\right)+\frac{\partial A}{\partial S}\Delta S_o+\frac{\partial A}{\partial P}\Delta P \tag{2.3}$$

where ΔS_o and ΔP are changes in oil saturation and reservoir pressure. The partial derivatives on the right hand side of the equation are dependent on the nature of the interface, the rock stress sensitivities, fluid saturation laws, wave interference and tuning within the internal reservoir architecture, and the initial reservoir state. Equation 2.3 forms the basis for the linear approximation of the time-lapse signature ΔA given by the difference of the repeat and baseline surveys (Equation 2.4)

$$\Delta A(x,y)\approx C_S\Delta S_o(x,y)+C_P\Delta P(x,y) \tag{2.4}$$

where C_S and C_P are constants to be determined, and ΔS_o and ΔP are average oil saturation and fluid pressure. Initially, the coefficients C_S and C_P are considered to be invariant across the reservoir. This imposes the condition of a weak facies and porosity variation across the reservoir, and invariant cap-rock properties. In addition, the velocities changes in the cap rock due to stress changes are considerable insignificant. This could not be the case in some reservoirs or areas of the reservoir with considerable change in stress in the overburden.

The above equation holds, provided that changes in pressure and saturation are not unreasonably large. Figure 2.3 gives some idea of the validity of the assumptions upon which it is based. In several oil reservoirs, the pressure fluctuation is held at a small percentage of the initial pressure, as it is generally not in the best economic interests to do otherwise. Typically, a reservoir may deplete by up to 5 to 10 MPa (725 to 1450 psi), while during injection (with the exception of the immediate vicinity of the well) the pressure might fluctuate by no more than 10 MPa (1450 psi). The change of pressure also depends on proximity to the bubble point, and good management practice tends to ensure pressure maintenance a few MPa above the bubble point. The linear approximation of amplitude versus pressure will hold with a small overall percentage error for pressure changes of 5 to 10 MPa. Typically, in an oil-water system, for example, oil saturation will change from $1-S_{wc}$ (approximately 60-85%) to S_{or} (approximately 15-25%). Calculations, however, have shown that even under these situations the linearity assumption appears adequate as a working rule (Figure 2.3).

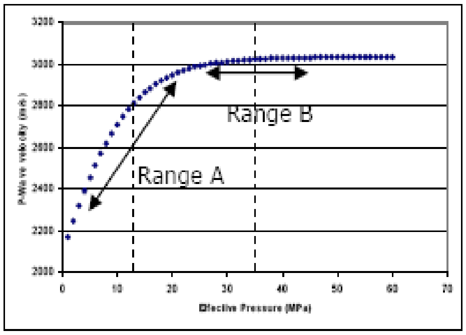

Range A: Pi=12MPa

Range B: Pi=35MPa

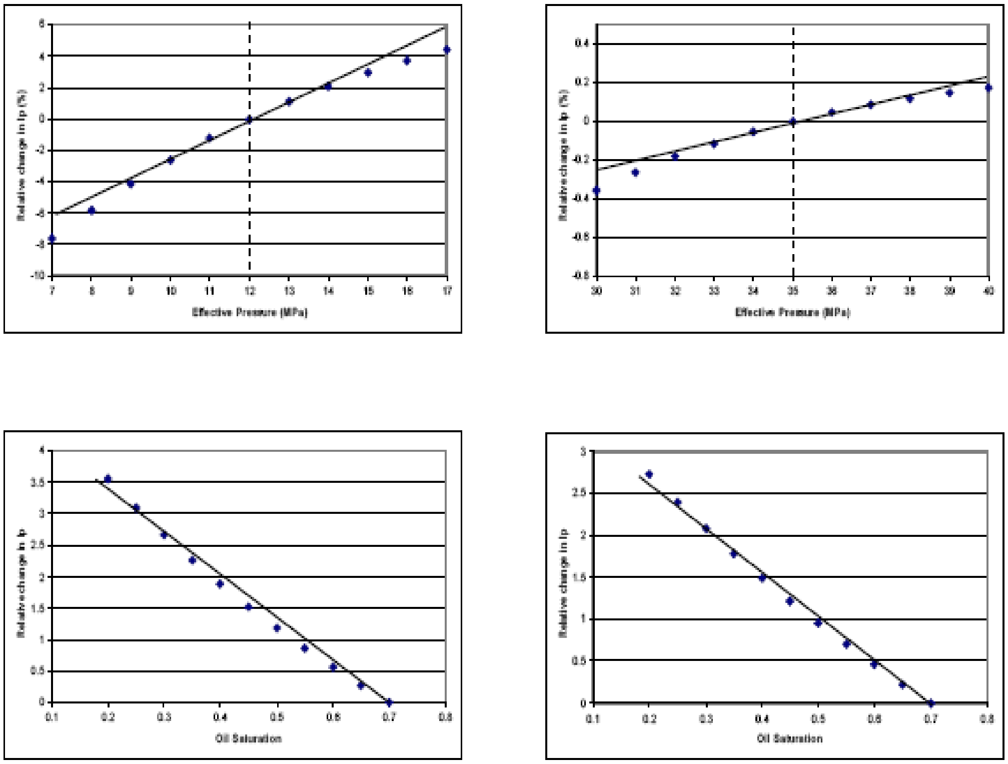

Figure 2.3: Test of linearity relationship between the seismic response (impedance in this case) and pressure and saturation changes. Results are from rock and fluid physics modelling based on laboratory measurements of pressure sensitivity for the Palaeocene turbidite reservoirs of the West of Shetlands (MacBeth, 2004a). Points plot the response to pressure variations of 5 MPa either side of an initial pressure, where initial pressure is chosen to be either in a non-linear (Range A, with initial pressure 12 MPa, on the left-hand side) or a linear region (Range B, with an initial pressure of 35 MPa, on the right-hand side) of the pressure sensitivity curve shown in the upper plot. Saturation variations simulate a change from oil-filled rock to water-flushed rock. (after Floricich, 2006).

2.2.2 Overlapping of Pressure and saturation change effects

Fluid saturation and pore pressure changes will to alter the seismic response of the rock. These changes could have opposite effects on the seismic velocities. In water injection, the substitution of oil by water increases the P-wave velocity, but a pore pressure increase reduces the P-wave velocity (Figure 2.4). The magnitude of these changes is controlled by the physical properties of the rock frame and the fluids. Figure 2.5 illustrates the effect of pore pressure and fluid saturation changes on acoustic impedance (AI), which is a function of density and P-wave velocity and therefore has a combined response to pressure and saturation change.

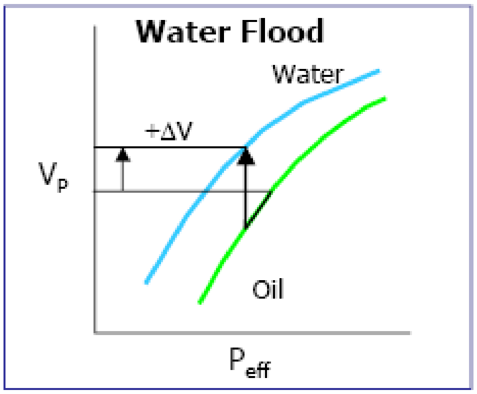

Figure 2.4: Effect of water injection on the P-wave velocity (after Waggoner, 2000)

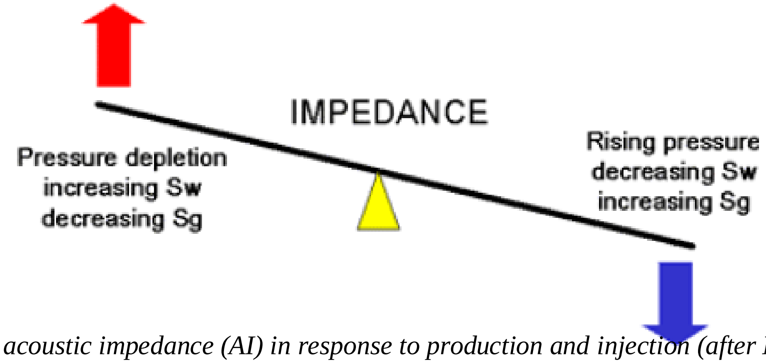

2.5: Change of acoustic impedance (AI) in response to production and injection (after Marsh, 2004)

Figure 2.6 illustrates how challenging it could be to pick up the saturation front from 4D seismic as pressure and saturation changes effects mix together resulting in a smoothing of the front as these two effects tend to cancel each other.

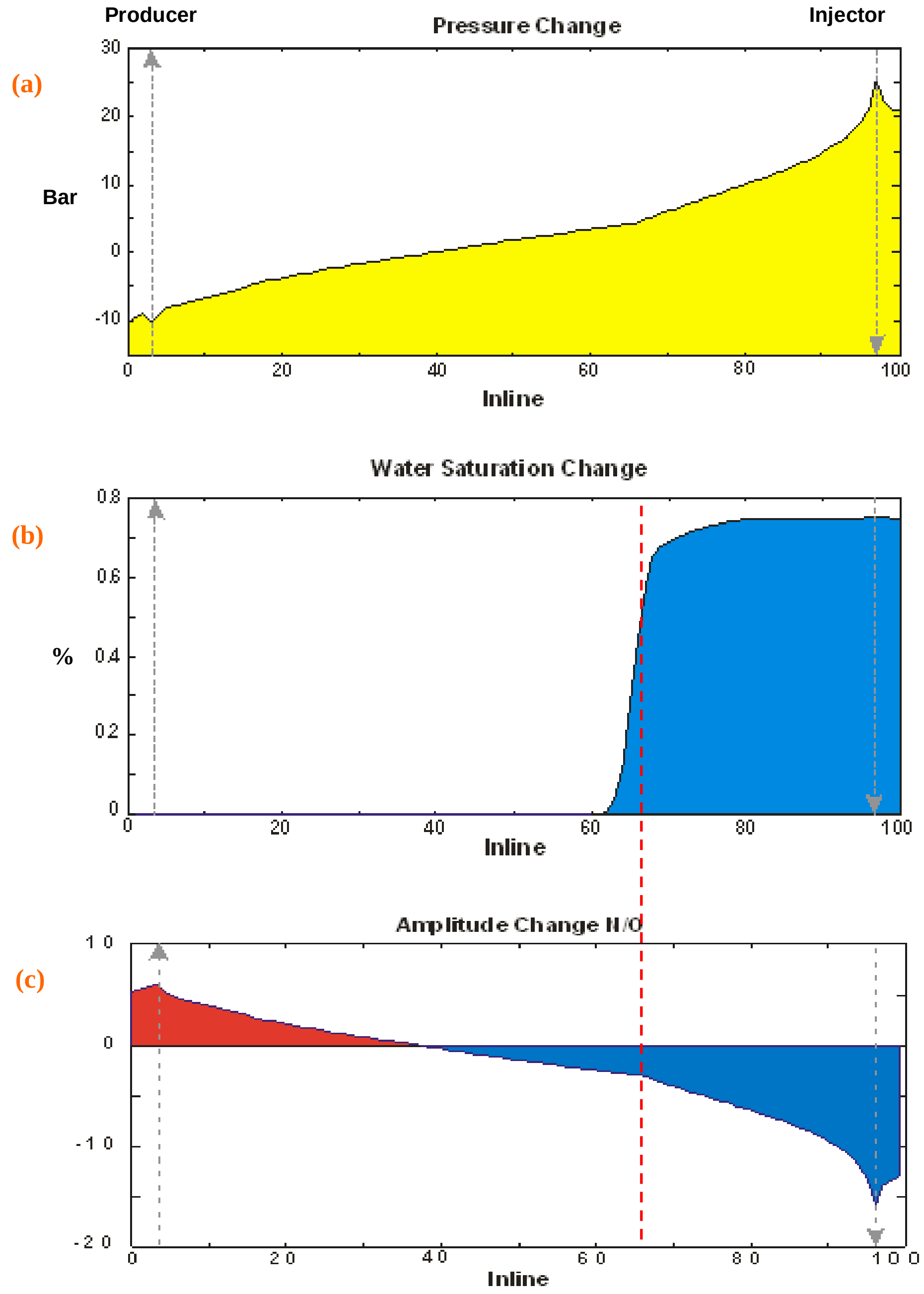

Figure 2.6: Example of overlapping pressure and saturation signals. (a) Pressure change ; (b) Saturation change; (c) Near off-set amplitude change computed using equation 2.3 and weighting coefficient derived from a North Sea reservoir.

2.3 Time-lapse seismic as a reservoir management tool

3D seismic provides structural information about the reservoir. It helps identify the reservoir limits, dip and azimuth of different layers, layers thickness, faults location and extent. The seismic measurement is based on the fact that the various earth layers exhibit different elastic properties; density, shear modulus, and bulk modulus. These differences create reflection interfaces which are imaged when they are hit by an incident seismic wave. While 3D seismic gives information about the static properties of a reservoir, repeated 3D seismic, or Time Lapse (4D) seismic yields information regarding changes in the reservoir state, which is characterised by saturation, effective pressure and temperature. Hydrocarbon production induces a change in one or more aspects of the reservoir state in turn affecting the elastic properties of the rock. The objective of time-lapse seismic is to image the effects of fluid flow in a producing reservoir by relating changes in amplitude, velocity, impedance or VP /VS ratio to corresponding changes in fluid pressure and/or saturation that can in turn be related to reservoir production mechanisms such as solution gas drive or Waterflooding, and the corresponding field-production data (e.g. production and/or injection rates and volumes, pressures in and around wells, composition of produced fluids). Time-lapse seismic images give information on fluid movements, position of barriers and compartments, sealing/communicating faults and general connectivity; which could improve the production strategy and extend a field’s economic life.

4D seismic is used as a reservoir tool at three different levels. The first level consists of using 4D amplitude/attributes maps and cross sections to qualitatively account for known production related changes near wells (Figure 2.7). Observations are checked with well and production information to gain confidence in the meaning of the different anomalies. In addition, the volumetric continuity of anomalies is checked as a way of potentially excluding difference noise. At the end of such an investigation and validation phase, the 4D results can be interpreted as production changes within the reservoir.

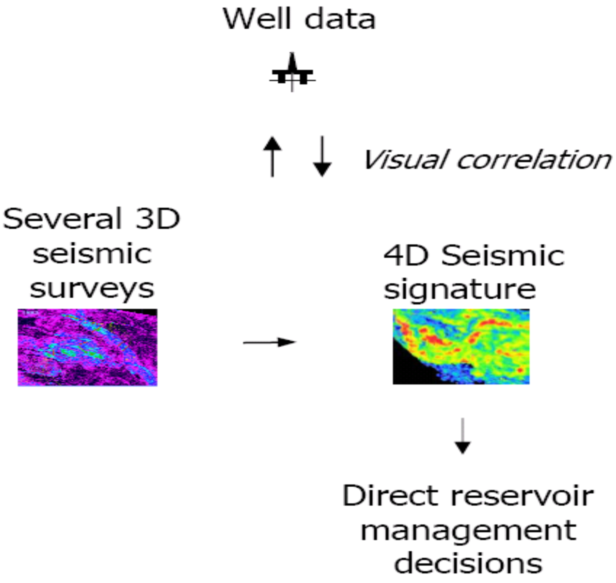

Figure 2.7: Conventional Time-Lapse seismic interpretation, (after Floricich, 2006)

Marsh et al. (2003) identified unswept areas for an infill producer drilling location in the Arbroath field in the North Sea. This simple evaluation involved identifying the original oil–water contact (OWC) on seismic data and screening 4D difference sections to identify those areas where the contact appeared to have moved. A seismic attribute map was then calculated which showed up these areas which were cross-matched to water-cut development in the existing wells (Figure 2.8).

The map indicated that the proposed infill location south of the platform did not seem to have suffered visible water migration. The size and shape of this unswept area supported that postulated by the original reservoir simulation modeling. The producer was drilled in mid-2001 and came on at a good oil rate and negligible water-cut.

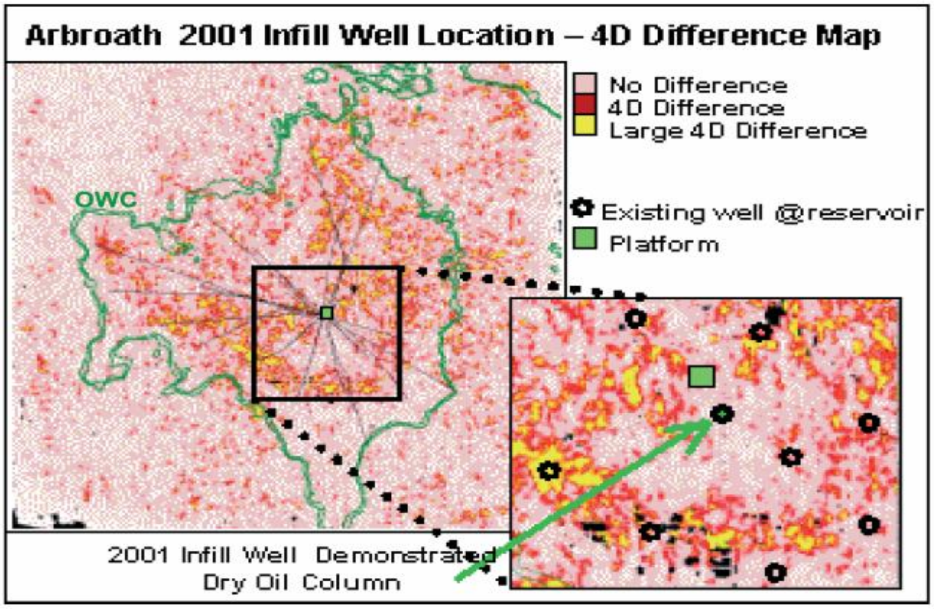

Figure 2.8: Unswept area identified as the drilling location for the new producer, (after Marsh et al., 2003)

The qualitative interpretation of 4D signals did not stop around the wells. Mapping of oil/water contact movement represents one of the most common uses of 4D seismic at the qualitative stage. 4D seismic cross-sections were used to identify the extend of the aquifer flood and locate infill drill location (Staples et al., 2006) (Figure 2.9). Landro et al. (Landro et al., 1999) identified OWC movement from 4D amplitude cross-sections; the visual interpretation also provided valuable information about potentially un-swept areas (Figure 2.10). Marsh et al. (2003) used time-lapse impedance differences to identify the oil/water contact movement (Figure 2.11).

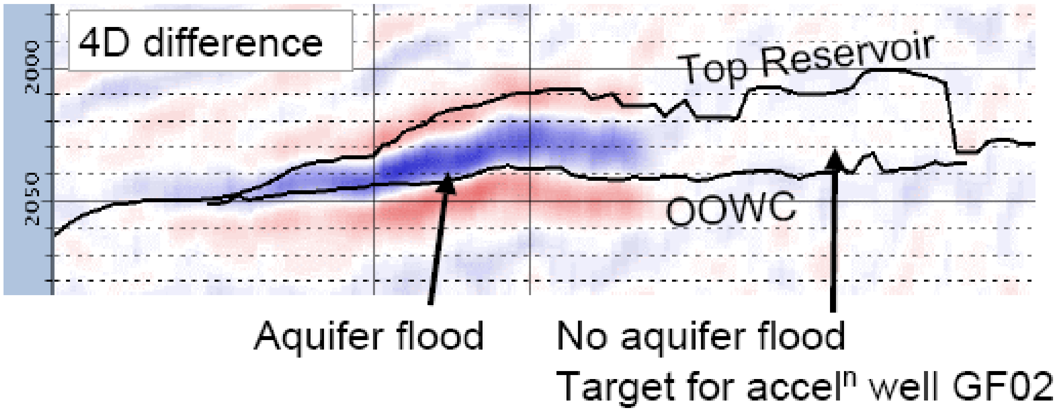

Figure 2.9: Direct evidence of an acceleration infill target (unswept area) at Gannet field, (after Staples, 2006).

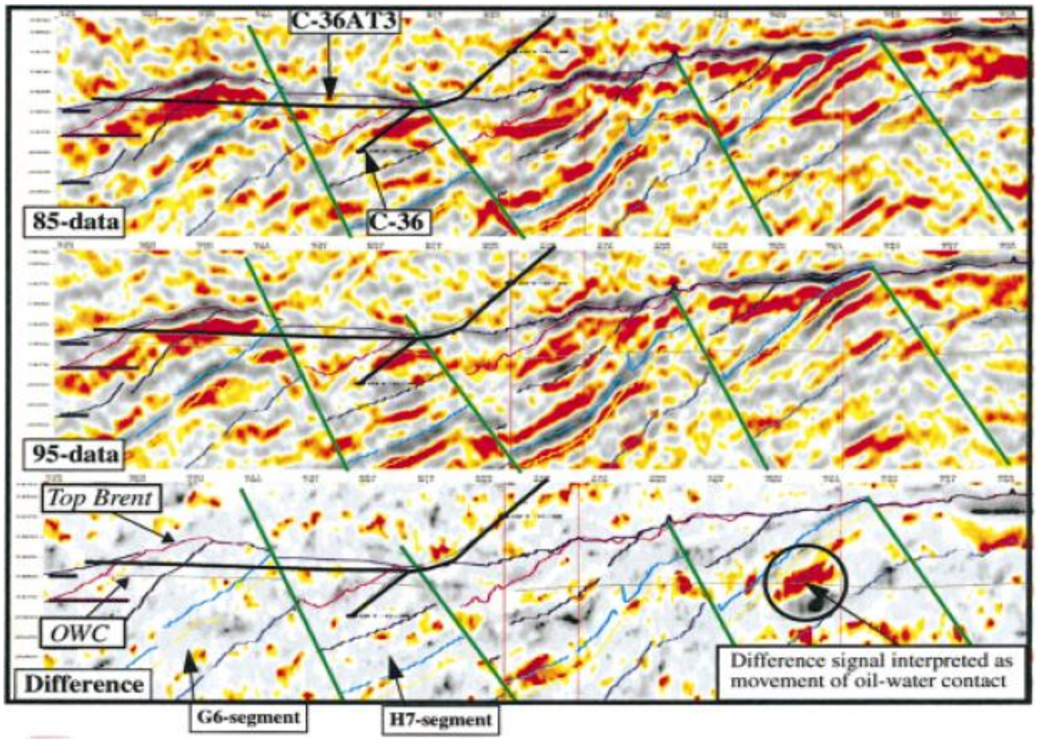

Figure 2.10: a) Base survey; b) Monitor survey; c) 4D difference showing oil/water contact movement (black circle, right) and unswept areas (H7 and G6 segments), (after Landro et al., 1999)

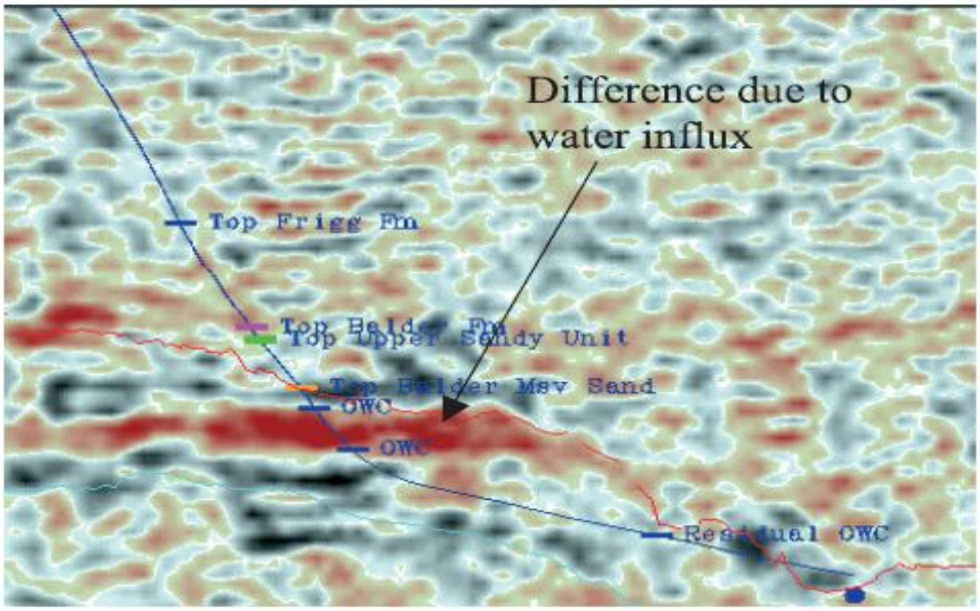

Figure 2.11: Difference in impedance along a well section in the Harding Field showing water swept area, (after Marsh et al., 2003). The water movement is associated with an increase in acoustic impedance.

Successful application of time-lapse seismic monitoring of Waterflooding was first reported in clastic reservoirs. But this success was soon extended to more complex reservoir settings. Beyerley et al. (2006) used a combination of 4D time shifts and amplitude change at the top of the reservoir to identify water swept areas and optimise well placement in the Ekofisk field (Figure 2.12). The Ekofisk field is a chalk reservoir located in the Norwegian sector of the North Sea, characterised by a high porosity (exceeding 40% in some areas) and production induced compaction hence presenting a complex 4D signature. Strong 4D signal around the oil producers was interpreted as the response to the pressure depletion (Figure 2.13).

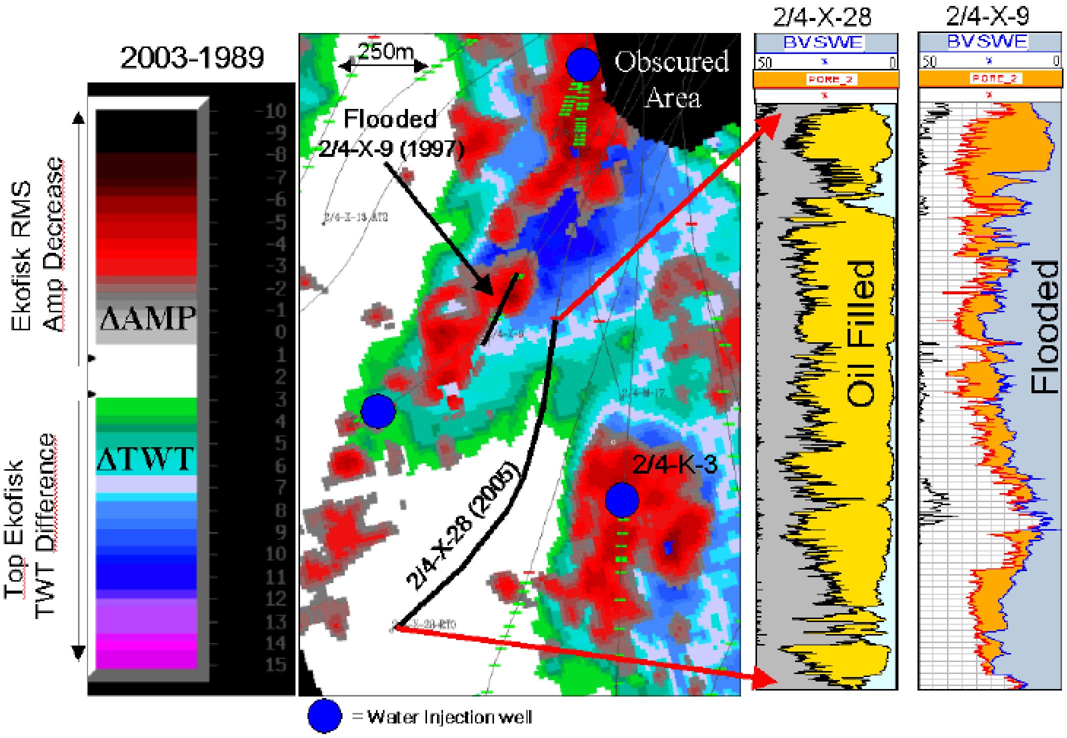

Figure 2.12: Combined 4D travel time and amplitude difference map indicating water injection fronts and the flooded area around the 2/4-X-9 well (red area). The wedge shaped region showing no 4D signal was interpreted as an unswept area. This area was the target for the 2/4-X-28 well which encountered unswept reservoir through the entire well, (after Beyerley et al., 2006)

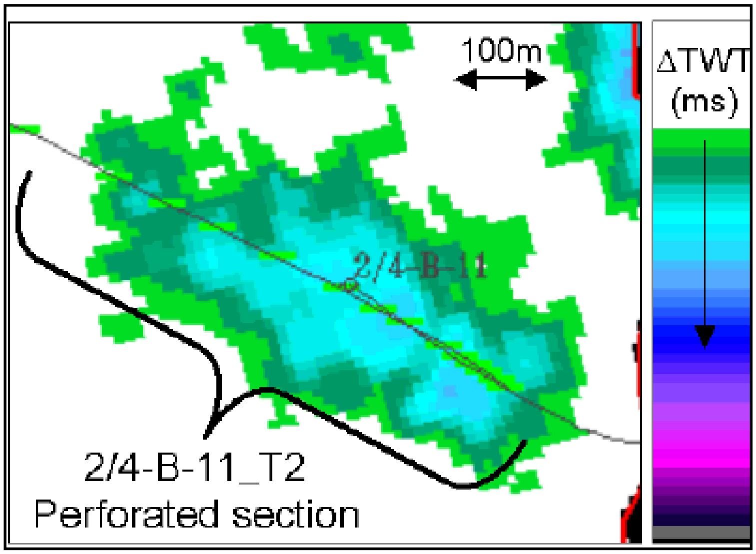

Figure 2.13: 4D Top Ekofisk travel time difference from an oil producer. The 4D map indicates a strong depletion response along the completed portion of the well, (after Beyerley et al., 2006)

4D anomalies can be visually compared to the simulation results. As an example, the correlation between the observed 4D anomalies and the simulated water saturation differences in the Ekofisk field confirm that the observed 4D signal is genuinely related to the waterfront movement and the simulation model is correctly simulating the fluids flow paths (Figure 2.14).

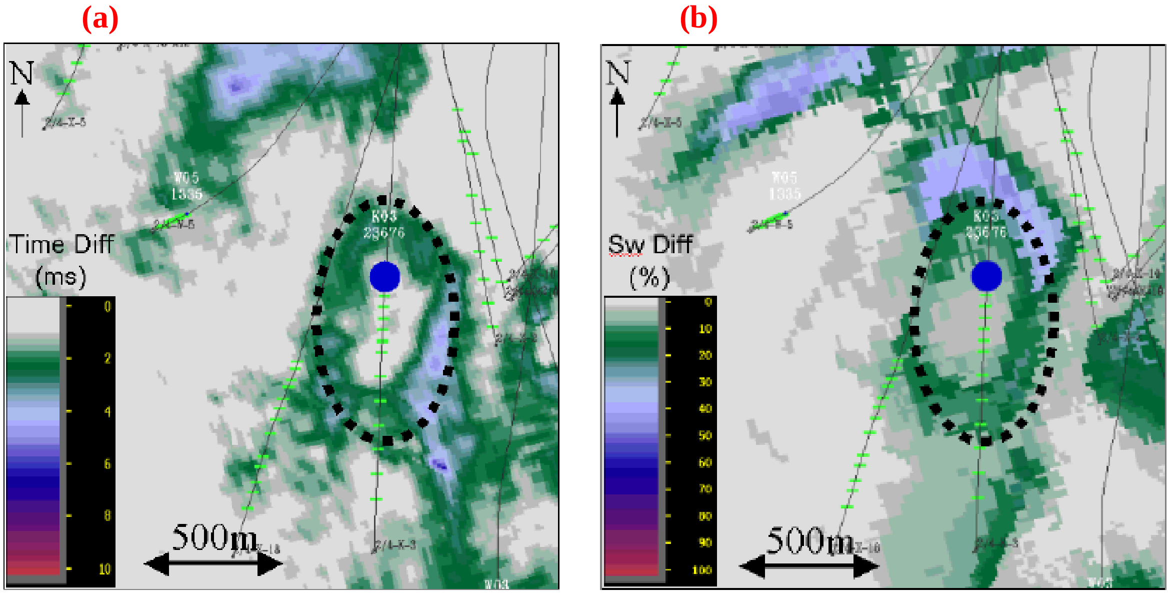

Figure 2.14: (a): Top Ekofisk 4D time difference map showing halo indicating where the water front has moved away from the injector (blue dot) from 1999 to 2003; (b): 2003-1999 water saturation difference extracted from the lower Ekofisk layer of the reservoir simulation, (after Beyerley et al., 2006)

Landro et al. (1999) generated two types of drainage maps in the structurally complex Gullfaks field. Drainage maps based on the reservoir engineers' interpretation of production and reservoir data, as well as drainage maps based on 4D seismic data. The maps are produced by drawing the respective interpretations on to structural depth maps. Input data for the seismic interpretations have been the horizon maps and attribute maps at the OOWC. The Rannoch Formation drainage maps are shown in Figure 2.15. The two maps are quite similar but the 4D observations show a less smooth and continuous waterfront.

The most significant indications of Waterflooding are observed by an OWC movement. The 4D difference anomalies in the I4 segment (top right of the map (b)) show water moving from the injector C10 and reaching the producer C33, which was not shown in the reservoir engineers interpretation, this was confirmed by the water cut rise in the well C33. Landro propose to integrate the two Waterflooding interpretations by a multidisciplinary team in order to generate an improved reservoir model.

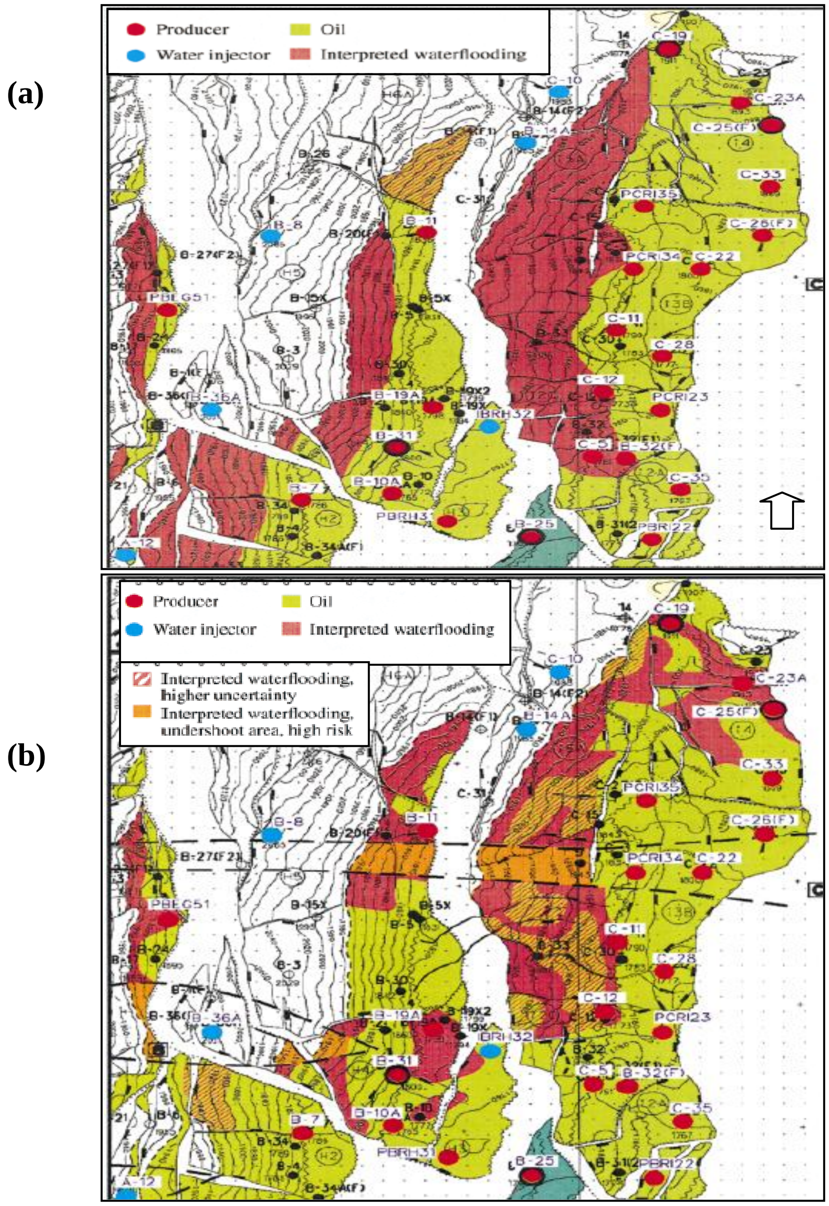

Figure 2.15: Rannoch Formation: (a) 1995 drainage interpreted by reservoir engineers; (b) drainage based on time-lapse seismic data, (after Landro et al., 1999)

It is common in reservoir simulation that equiprobable model realizations are generated. Several of these models can be history matched to production data with the same level of accuracy. Comparing interpreted time-lapse changes against predictions from multiple models can lead to the exclusion of some of the models that do not match the 4D anomalies and help choose the best model for reservoir management (Figure 2.16).

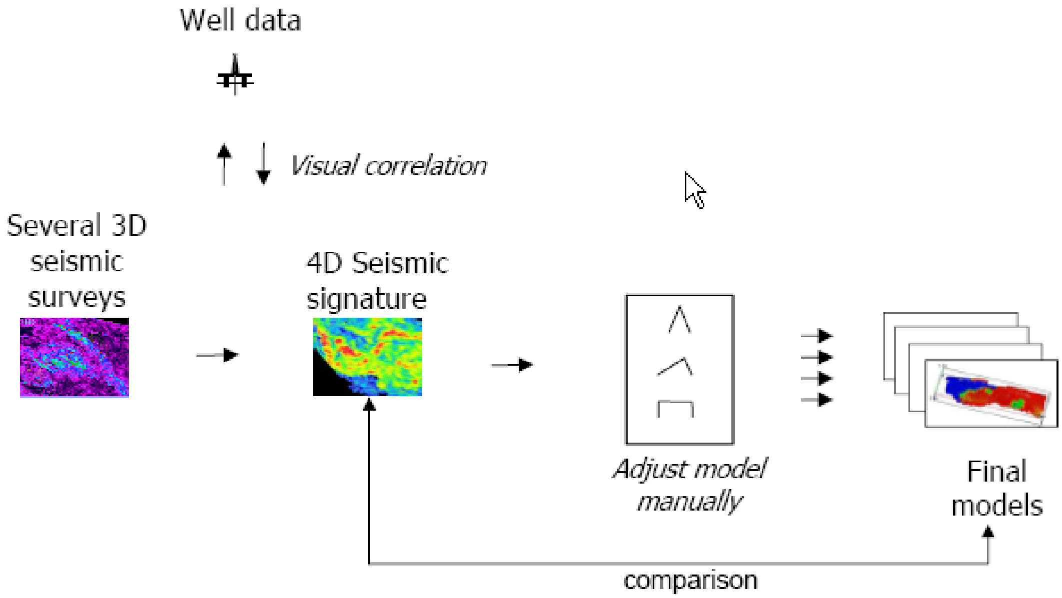

Figure 2.16: Simulation model selection constrained by 4D seismic, (after Floricich, 2006)

Koster et al. (2000) showed an example for the Draugen Field, in the North Sea. In the Draugen field, water injectors at the north and south end of a low-relief anticline structure push oil toward the central producers. The lack of wells between the producers and the injectors resulted in a considerable uncertainty in reservoir properties, and several reservoir simulation models were built using different communication paths between the aquifer and the reservoir. All versions of the reservoir model had assumed that water movement would occur along both flanks of the field (Figure 2.17). These models can all be matched to the production data. However, these models have significantly different forecast production profiles for the field. Therefore, knowledge of the true communication path would allow optimization of the production strategy. The communication path also has a significant impact on the location of the waterfront within the reservoir. Figure 2.17d shows a map of the difference in amplitudes at a picked event. This clearly shows where water has replaced oil, giving a snapshot of the waterflood situation away from the wells, and therefore resolving many uncertainties. The measured 4D shows the injected water moving along the western flank, with no displacement on the eastern flank. Also, a northern fault is clearly shown to be sealing during the production time. The reservoir model that was closest to the 4D result was selected for reservoir management purposes.

Forward rock physics modelling is used to create synthetic seismic from the simulation results. The comparison of the real 4D signal with the synthetic one can help ascertain the robustness of the simulation model and assist in the interpretation of the real time-lapse seismic signal. Staples et al. (2006) used forward modelling in the Gannet C field to improve history matching, with a manual history matching cycle including updates to the static model (Figure 2.18). This technique is also used to reduce the non-uniqueness of reservoir flow simulation results. In fact, reservoir simulation can yield multiple equiprobable realisations which honour the historical production data. Lumley et al. (1998) showed an example where forward rock physics modelling helped choose the best model that matched both production data and 4D seismic data (Figure 2.19).

Other examples summarizing semi-quantitative integration of time-lapse seismic and production data can be found in Al-Najjar et al. (1999); Waggoner (2001); Staples et al. (2002) and Marsh et al. (2003). A review of these articles shows that the comparison of the 4D signature with the predicted output from a simulation model has been successful at locating dynamic barriers, varying fault transmissibility (seal or no seal), altering aquifer connectivity, identifying injected water slumping and running on top of shales (gas running under shales; identification of thief zones), and STOIIP adjustment. This process is, however, non-unique and not strictly quantitative.

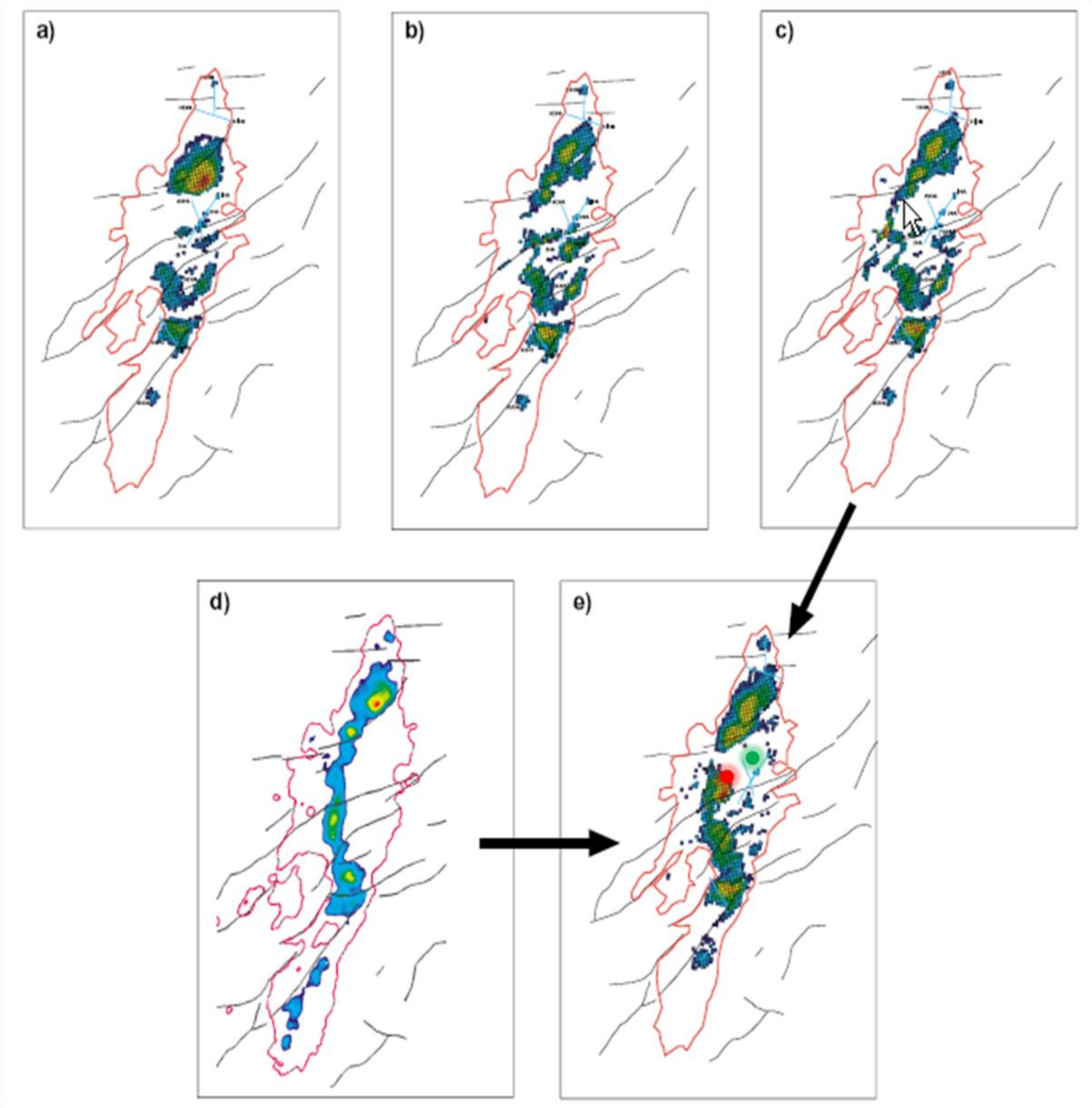

Figure 2.17: Map over the Draugen Field of the change in equivalent hydrocarbon column as calculated by the reservoir simulator. Colour scale runs 0-5 m. Faults (black) and the extent of the OOWC (red) are indicated. (a) Communication in the north. The large water influx expected in the north is not confirmed by 4D seismic, so this model is ruled out. (b) Communication through faults. Water encroachment immediately south of the platform is not seen by 4D seismic, so this model is also ruled out. (c) Communication in the west. This model best matches the 4D seismic results so it was used as a starting point for seismic matching. (d) Actual observation from 4D seismic. (e) Final model matched to seismic and production history. The red dot represents the originally planned location of the new well, the green dot the revised location. (after Koster et al., 2000).

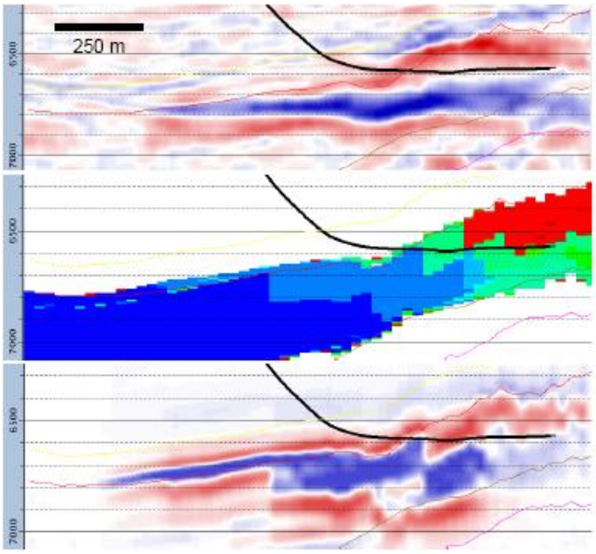

Figure 2.18: A comparison of 98-93 difference seismic (upper panel), simulation saturations from 98 (middle panel), and the corresponding simulator difference synthetic 98-93 in the Gannet C field. (after Staples et al., 2006)

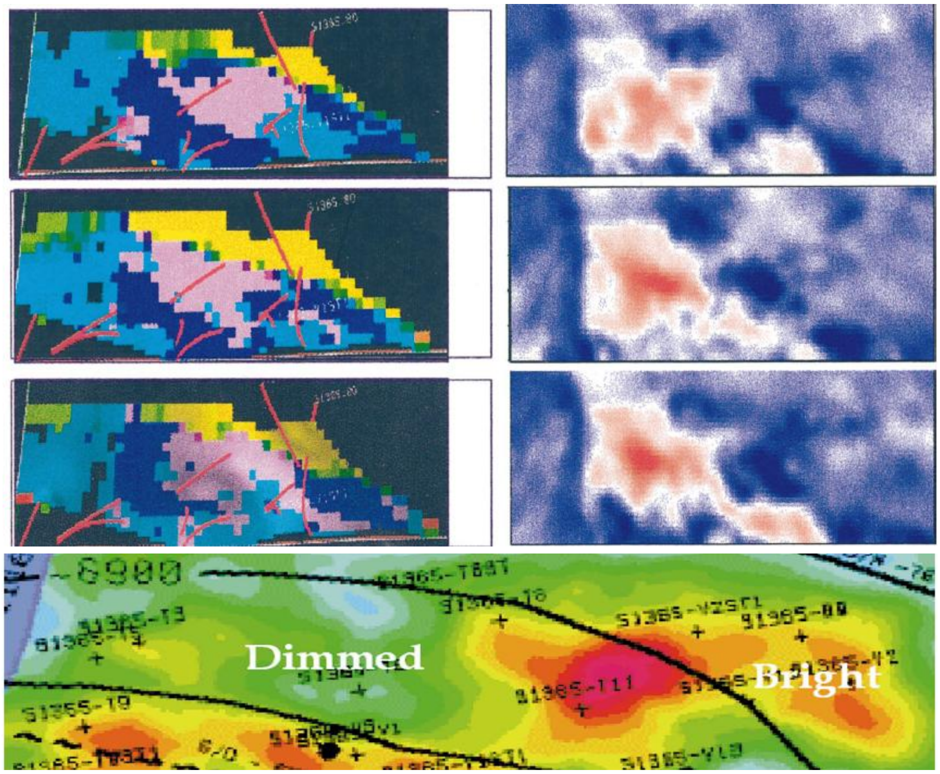

Figure 2.19: Oil saturations (left panels) and resulting synthetic seismic maps (right panels) from three equiprobable model realizations from a Gulf of Mexico field. The lowermost model gives the best simultaneous match of both the production data and the bright amplitude area in the field seismic data (lower panel) (after Lumley et al., 1998).

Creating synthetic 4D seismic and comparing it to the real measured 4D seismic can result in the improvement of the reservoir simulation model. This process can be included into a history matching workflow to add more constraints into the objective function that the algorithm is minimizing, this process is known as seismic history matching (SHM). The classical history matching workflow compares the measured and simulated production data at wells, but seismic history matching add one more step by comparing the simulated and measured 4D seismic (Figure 2.20). The methodology consists of the parameterization and optimization of a group of reservoir properties (i.e. fault transmissibility, porosity distribution, relative permeability curves) considered as unknowns. An objective function is estimated, which basically measures the difference between the measured and synthetic 4D data and also the difference in the predicted and actual production data. Both the production and 4D quantified differences can then be combined into a single objective function for use in an optimization algorithm.

Due to the nature of 4D seismic signature, i.e. being a mixture of pressure changes and fluids changes effects, plus geomechanical effects in some reservoirs, it is generally difficult to use time-lapse amplitude attributes or any other seismic attributes to directly match the pressure and saturation evolution in the simulation model. Separating pressure and saturation effects is one of the most important research topics in the quantification of 4D seismic. Several techniques have been proposed and some successful case studies have been reported in the literature. Saturation and pressure information derived from 4D seismic can be included in the seismic history matching workflow (Figure 2.21) and lead to a better understanding of the reservoir dynamics and help in reservoir management.

It can be seen through the literature examples listed above that the application of time-lapse seismic techniques in the monitoring of Waterflooding processes was performed on different reservoir types and to achieve different purposes. Indeed, time-lapse seismic is used to identify oil-water contact movements, to assess water encroachment at production wells, to produce drainage maps and identify unswept areas and by-passed oil zones.

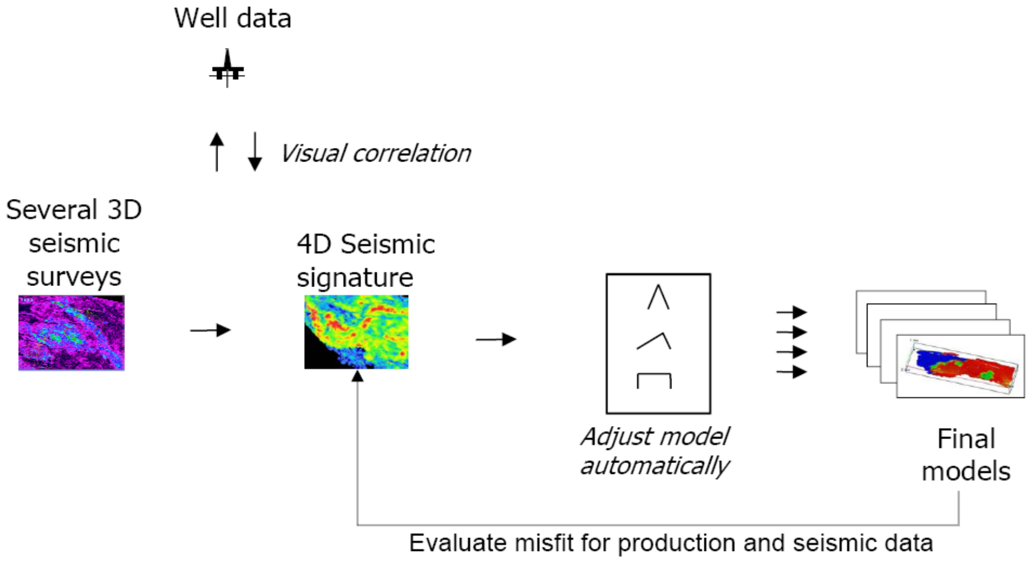

Figure 2.20: Workflow for automatic seismic history matching. The best simulation model is selected by minimizing the difference in measured and simulated production data and time-lapse seismic (after Floricich, 2006).

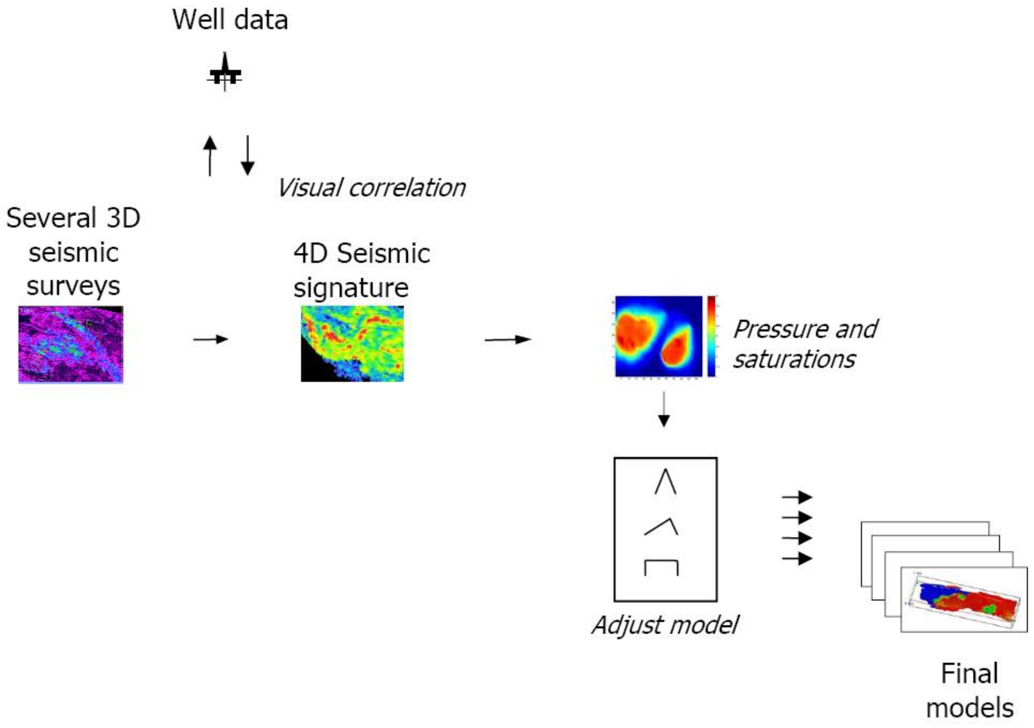

Figure 2.21: Towards a quantitative 4D seismic interpretation: pressure and saturation are estimated from time-lapse seismic and compared with simulation models (after Floricich, 2006).

Information derived from time-lapse seismic data interpretation can therefore be used at different stages of the reservoir management process. It can carry direct information about the reservoir state at a specific production time, i.e. fluids contacts, unswept zones, pressure variations. But it also, if correctly interpreted, gives valuable information about the reservoir inherent geological complexities and variations.

Waterflooding monitoring using the time-lapse seismic techniques can therefore be seen on various levels: from the qualitative assessment of fluids contacts locations and flooded zones identification, to semi-qualitative drainage maps to be calibrated with production data and compared to reservoir simulation outputs, to quantitative maps of separate estimations of pressure and saturation changes within the reservoir. This in turn provides information about reservoir compartmentalization and connectivity and the sealing nature of internal faults and fractures.

Changes in the reservoir conditions inevitably result in changes in the rock’s seismic properties. Whether these changes are detectable using 3D and 4D seismic imaging depends on several factors (oil gravity, substituting-fluids/substituted-fluid acoustic contrast, reservoir geology, seismic acquisition parameters, etc). Detectability is the ability to detect changes in the seismic response due to alterations in pressure and saturation during production. An appropriate rock physics model is critical to assessing detectability (Behrens et al., 2002).

Time-lapse seismic studies are tied to the particular production scenario in a given reservoir, whether being a primary or a secondary production mechanism. Gassmann (Gassmann, 1951) equations, whose applicability in porous media is limited to homogeneous isotropic rocks under isobaric conditions, are frequently used to link the seismic response to changes in reservoir properties. A typical form for Gassmann equation is the following:

$$K_{sat} = K_{dry} + \frac{\left(1 - \frac{K_{dry}}{K_0}\right)^2}{\frac{\phi}{K_{fluid}} + \frac{(1-\phi)}{K_0} + \frac{k_{dry}}{K_0^{\ 2}}}$$

$$\mu_{sat} = \mu_{dry}$$

where K_{sat} is the saturated-rock modulus, K_{dry} the frame (dry) bulk modulus, while K_0 and K_{fluid} correspond to the grain and fluid bulk moduli, respectively, and Φ is porosity.

Although the equations are not explicit functions of thermodynamic conditions in a reservoir, pressure and temperature effects can be accounted for through empirical equations. Batzle and Wang (1992) expresses effects of pressure and temperature of the fluid phase, while an elastic piezosensitivity relationship can be used for the dry-rock bulk modulus (MacBeth, 2004). This latter relationship relates the rock elastic moduli with differential pressure (confining minus pore pressure).

In conventional time-lapse studies, synthetic monitors are used to estimate likely changes in the seismic response. These estimates are employed to help with the decision-making process of production strategies. Studies start with an initial estimate of physical parameters that control the seismic response, upon which updating of the reservoir conditions follow. Parameters for the application of Gassmann equation generally come from well and core data, plus empirical equations. The values of Vp and Vs are, in general, estimated from full-wave sonic logs. Saturated rock moduli can be obtained from estimated Vp and Vs values, while reservoir density, in turn, can be calculated from sonic logs and core measurements. From all these parameters, the frame (dry) bulk modulus (Kd) can be computed, but knowledge of fluid properties (saturation, fluid bulk modulus and density at reservoir conditions), porosity and grain bulk modulus are necessary. Some of these parameters can be estimated from well or core data, while others can be found in tables. As for the fluid phases, since in a real reservoir there are several fluid components occupying the pore space, it is then necessary to estimate effective fluid density and bulk modulus.

On the other hand, changes in the seismic response are linked to changes in both the solid and fluid phases. Therefore, it is important to understand how changes in fluid and solid properties contribute to those changes in the seismic response, for the different stress and production scenarios. Our analysis, however, will disregard geomechanical effects such as subsidence or compaction that can be relevant in certain scenarios of production, but considers the type of reservoir geology and reservoir dynamics.

2.4 Conclusion

Waterflooding had a tangible impact on oil recovery efficiency by substantially increasing production from an oil field and delaying abandonment. This success caused a surge of interest in understanding fluids displacement in porous media and oil/ water movement within the reservoir rocks. The early techniques to assess Waterflooding process efficiency were mainly analytical, and generally carried out by engineers. The advances on computing capabilities, the emergence of new geophysical methods; like reflection seismic and well logging, and the pressing need to integrate the engineering domain with the geophysical domain to optimise reservoir management allowed geoscientists to tackle the issue of Waterflooding through reservoir simulation, petrophysical modelling and 4D seismic interpretation. Time-lapse seismic proved to be a powerful tool in the monitoring of Waterflooding. It allowed the identification of un-swept areas inside the reservoir and the accurate mapping of fluids contacts giving valuable information as for infill drilling locations and production/injection optimisation.

The displacement of oil by injected water inevitably causes changes in the reservoir dynamic properties such as pore pressure and fluids saturation. The interpretation of the time-lapse seismic signature associated with those changes is not straight forward. Pressure and saturation changes for example can have opposite effects on seismic amplitude yielding a very weak 4D signature where important dynamics changes occurred inside the reservoir. Seismic resolution, 4D seismic repeatability and the quality of the seismic data (i.e. signal to noise ratio) have a major impact on our ability to correctly extract the needed information for a proper reservoir management. Waterflooding a geologically complex reservoir adds more challenges as to correctly identify swept/unswept areas and interpreting fluids contact. The injected water will flow in some preferential highways dictated by the internal geology of the reservoir and any flow barriers or compartmentalisation that may be present.

Chapter 3

Waterflooding in a clean, thick, and idealised sandstone reservoir: preliminary study

A series of idealised reservoir models of thick, clean sandstone are built. The reservoir models present different degrees of geological complexities. Several Waterflooding scenarios are run; the effects of the geology on the efficiency of Waterflooding are studied. The results of the petrophysical modelling and the 4D signatures associated with every Waterflooding scenario and reservoir type are studied.

3.1 Introduction

When starting the development of a new hydrocarbon field, 3D seismic data are shot to help, together with the geological information, delineate the reservoir extent. Appraisal wells are drilled to collect information about the subsurface geology and fluids content through well logs, and core data. These data are collected under static conditions; they do not provide any information about the lateral and vertical pressure communications which are indispensable in the planning of a successful secondary recovery. In an onshore environment, production facilities are generally constructed shortly after discovery of the field; discovery wells are produced at high rates to create a pressure sink at the well location that will radiate both vertically and laterally throughout the reservoir. Well tests such as drill stem tests (DST) and repeat formation tester (RFT) are carried on from the appraisal stage and generally the development plan of the field is established with a good knowledge of the vertical and lateral communication in the reservoir. In an offshore environment, however, it is not until the development stage that such dynamic data can be acquired as no production facilities are present before that stage so engineers cannot produce from wells for a sufficient time to cause a significant pressure drop. The important decisions concerning the design of the platform and the injection and production facilities have to be made before the start of the production stage. With little or no information about reservoir compartmentalisation, planning of secondary recovery schemes are mostly predictive and rely heavily on reservoir simulation. However, simulation models do not necessarily give information about the reservoir performance; they just reflect the consequences of the input assumptions made by engineers. Once the development phase starts, the reservoir is finally viewed under dynamic conditions, and the dynamic data are integrated into the reservoir simulation model in a history matching process.

The objective of the work in this thesis is to develop a better understanding of fluid flow in sandstone reservoirs, with a focus on the impact of the geological complexity of the reservoir and their effect on the resultant 4D seismic signature. The workflow of the study consists of the creation of 3D reservoir models, running fluid flow simulations, and then the associated 4D seismic responses are generated through petro-elastic transformation of the simulation output followed by seismic modelling. The ability of 4D seismic to distinguish between the different waterfronts, resulting from different geological settings, is investigated.

3.2 Reservoir models and flow simulation results

This study is divided into two parts. First, the influence of the reservoir geology and the production mechanism on the sweep efficiency of Waterflooding is investigated. This is done by running several Waterflooding scenarios on a series of idealised, synthetic reservoir models with different degrees of geological complexity. Both edge drive and basal drive Waterflooding are modelled with the edge drive Waterflooding being run with and without pressure support. The control of the reservoir geology and the Waterflooding type over the shape and progression of the waterfront, main indicators of the sweep efficiency of Waterflooding processes, are investigated. The second part consisted of petrophysical and seismic modelling.

In this study, various Waterflooding scenarios are investigated. The reservoirs studied are synthetic models with increasingly complex geology. However, some general assumptions are made for all the cases:

- The reservoir consists of 2 phases (oil and water);
- Waterflooding is applied under condition of a favourable mobility ratio, M= 0.6;
- The reservoir is water wet (Figure 3.1). The connate water saturation, S_{wc}, was set to be 0.15 and the irreducible oil saturation, S_{or}, to 0.1.

The simulation is performed using a commercial black oil simulator (Eclipse100™). The reservoir model comprises 24000 cells (20 x 20 x 60) of 5 x 5 feet horizontally and 2 feet vertically (Figure 3.2). The parameters used for the simulation are listed in Table 3.1.

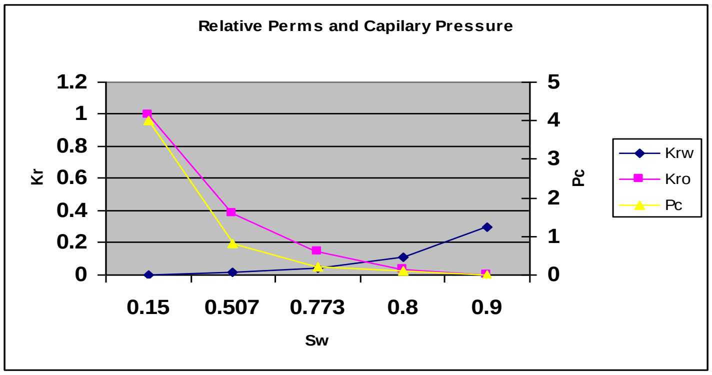

Figure 3.1: Relative permeability curves for water wet reservoir used in all the simulation studies. K_{rw} *: relative permeability for water,* K_{ro}*: relative permeability for oil,* P_c*: oil/water capillary pressure*

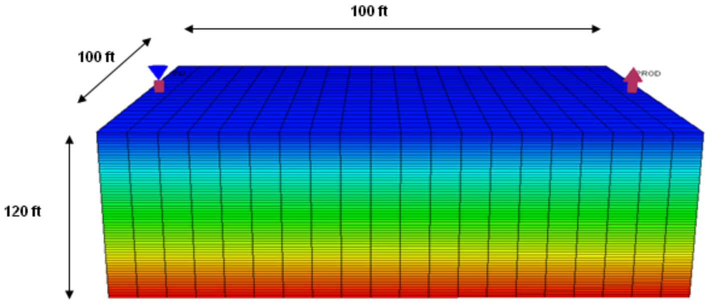

Figure 3.2: Simulation model used in this study. The property shown is depth.

Reservoir top	**7200 ft**
Initial reservoir pressure	**3350 psi**
OOWC	**8000 ft**
PermX	**1000 mD**
PermY	**1000 mD**
PermZ	**100 mD**
NTG	**1**
Porosity	**30%**
Rock compressibility (at 4500 psi)	**2.75e-07 1/psi**
Oil density	**50 lb/ft**
Water density	**63 lb/ft**
Oil viscosity	**0.8 cpoise**
Water viscosity	**0.4 cpoise**

Table 3.1: Rock and fluids parameters used for the simulation study. The parameters were derived from a typical North Sea reservoir.

3.2.1 Homogeneous reservoir

The homogeneous reservoir, which consists of a 120 ft thick block of sand, is subject to three different production scenarios. In the first scenario the reservoir pressure is kept fairly constant while in the second and third cases it dropped by about 1500 psi. The first two models are produced through edge flood, i.e. the water is injected at the edge of the reservoir into the oil leg and it displaces the oil horizontally across the reservoir toward the producers, while in the third case, the water is injected into the aquifer and sweeps the oil vertically in a basal drive fashion.

a. Injection with pressure support

The OOWC was set below the reservoir with the reservoir rocks initially containing oil and connate water. The reservoir pressure was kept constant during production. The reservoir pressure was depleted by only 50 psi (0.34 MPa) for a short period after production started. The pressure was then kept constant at around 3300 psi. The vertical water injector was completed across the whole reservoir section, and water was injected throughout the whole well length. Figure 3.3 shows the water saturation and pressure changes at the time of the second monitor across inline 10, where the producer and injector were placed. The saturation change behind the waterfront is at its maximum with only the irreducible oil saturation left in the pore space. The dispersion front,the area where both oil and water phases are present, stretches over tens of feet.

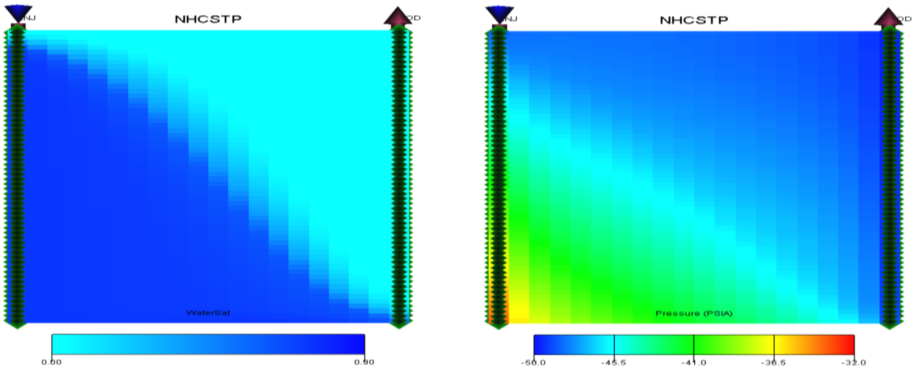

Figure 3.3: ΔS_w (a) and ΔP (b) after 45 days of injection/production.

Since the reservoir permeability was kept constant across its whole thickness, gravity plays the main role in the resulting shape of the waterfront. The efficiency of the displacement is affected by early water breakthrough at the bottom of the reservoir while most of the oil remained unrecovered at the top. The injection of several pore volumes of water may be needed in order to recover the moveable oil volume.

b. Injection without initial pressure support:

The reservoir pressure dropped by 1500 psi on average and then remained constant. The advance of the waterfront from the injection side to the production side of the reservoir is similar to the scenario when the pressure was kept constant. Water slumps down to the bottom of the reservoir, resulting in early water breakthrough; and the injection of a large volume of water is needed to produce all the movable oil. The pressure drop had no noticeable effects on the shape of the waterfront or its progress through time.

c. Bottom drive

To simulate bottom drive Waterflooding, some modifications to the original model described above are made. The original OWC (OOWC) was set at 7280 ft, 80 ft below the top of the reservoir. The part of the reservoir situated below the OOWC is set to act as an aquifer. The injector was completed across the water zone and injected at a constant rate into the aquifer while the producer was completed across the oil leg.

When solving the fluid flow equations, Eclipse™ takes the initial water saturation above the OWC from the first value in the relative permeability table, while the initial water saturation below the OWC is taken from the last value in the same table; therefore this value was set to be one.

To simulate water coning at the producing well, i.e. a cone shaped OWC, the ${}^{K_h}\!/_{K_v}$ has to be increased by an order of 10 to equal one in the vicinity of the wellbore.

Figure 3.4 shows the water saturation and pressure changes profiles across inline 10 of the model.

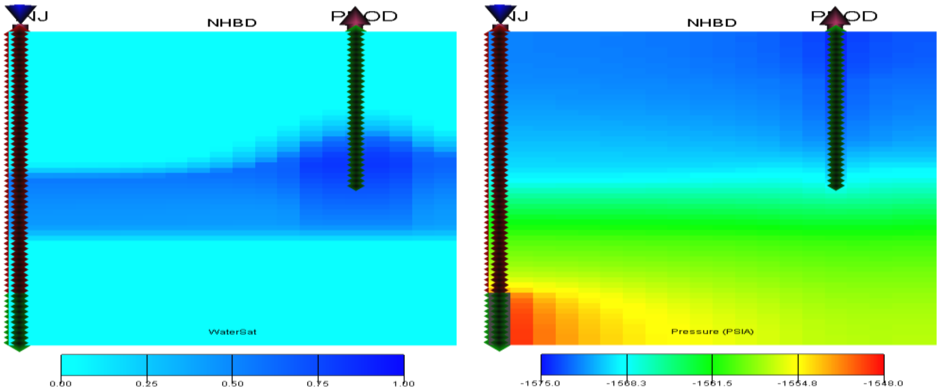

Figure 3.4: ΔS_w (a) and ΔP (b) after 45 days of injection/production.

The pressure change was fairly homogeneous across the whole reservoir, with the highest changes observed around the water injector. The waterfront moves upward and displaces the oil in a stable fashion. Around the production well, water coning is observed.

3.2.2 Heterogeneous reservoir

The heterogeneities investigated in this part of the study are those related to the permeability variation across the reservoir. Two cases are studied: fining up-ward, where the highest values of permeability are at the bottom of the reservoir, and coarsening up-ward, where the highest values are at the top. These two scenarios represent realistic cases associated with two different sedimentation processes. In fact, the nature of permeability distribution in clastic rocks is to a large extent governed by the depositional environment. In a marine environment, cycles of regression (sea receding from land area) and transgression (sea advancing over a land area) give rise to coarsening upward and downward trends in permeability, as illustrated in Figure 3.5. In case (a), point A is originally in deep water and only fine sediment is transported from the land to be deposited at this distance. As the sea recedes, point A is located closer to the shore line resulting in the deposition of a coarser material. The overall result is a coarsening upward in the size of the rock particles and the flow channels between them which is reflected in the permeability. During a period of transgression, Figure 3.5.b, the opposite happens and as the sea level rises finer material is deposited at point A resulting in a coarsening downwards.

Considering the importance of permeability distributions on the vertical sweep efficiency, it was the main geological parameter to be investigated in this study. The rest of the reservoir characteristics are kept constant (the same parameters listed in Table 3.1). The influence of other types of heterogeneity like the presence of intra-reservoir shales, faults and fractures is not considered in this part of the study.

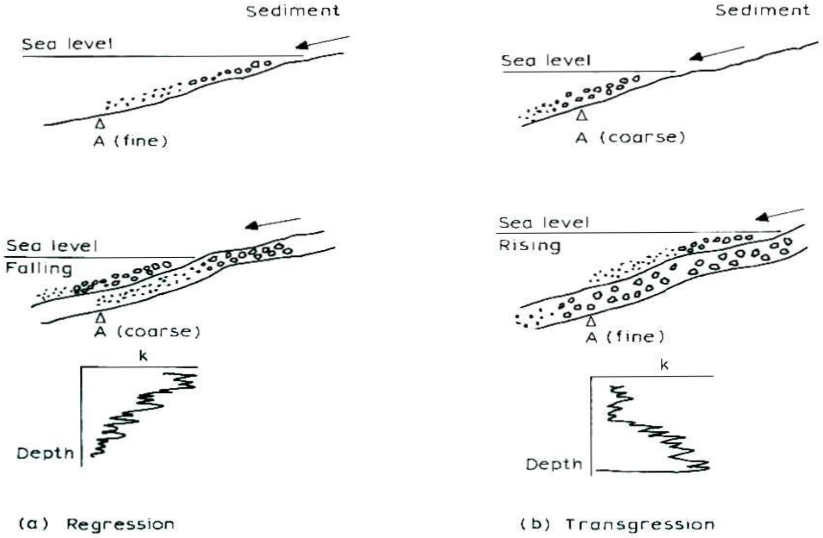

Figure 3.5: The influence of regressive and transgressive cycles on permeability distributions.

a. Fining upward: low permeability at the top of the reservoir

Figure 3.6 illustrates water saturation and pressure changes after 45 days of Waterflooding. The pressure drops in a fairly homogeneous way across the entire reservoir. It should be noticed that due to the fact that the highest permeability values are at the bottom of the reservoir, the majority of the injected water enters at the base of the section at the injection well bore and being heavier it stays there. This leads to premature breakthrough, resulting in a high water cut at relatively short time and the circulation of large volumes of water to recover all the oil trapped at the top of the section.

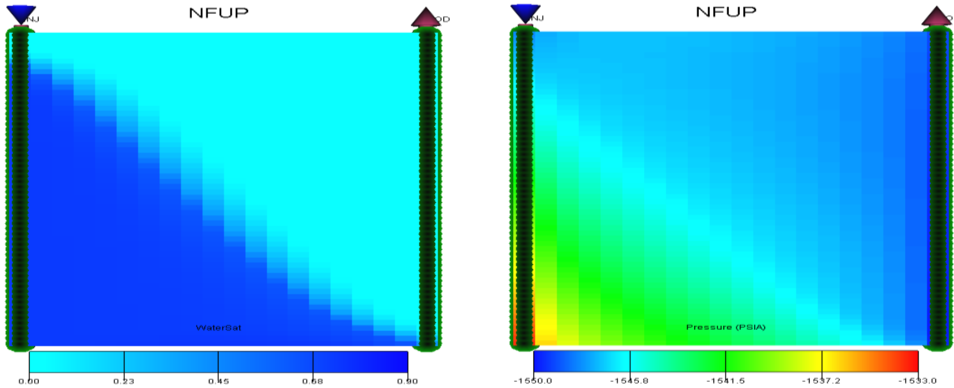

Figure 3.6: ΔS_w (a) and ΔP (b) after 45 days of injection/production.

b. Coarsening up-ward: High permeability at the top of the reservoir

Figure 3.7 illustrates the changes in water saturation across a section comprising the water injector and the producer (the same section as above). At the injection well, the bulk of the water enters the top of the section. However the viscous driving force from the injection decreases logarithmically in the radial direction and before the water has travelled far into the formation it diminishes to the extent that gravity takes over and dominates. The water, which is continually replenished at the top of the formation, then slumps to the base and the overall effect is the development of a sharp front and a piston-like displacement across the macroscopic section. As for the pressure change, it is homogeneous across the entire reservoir

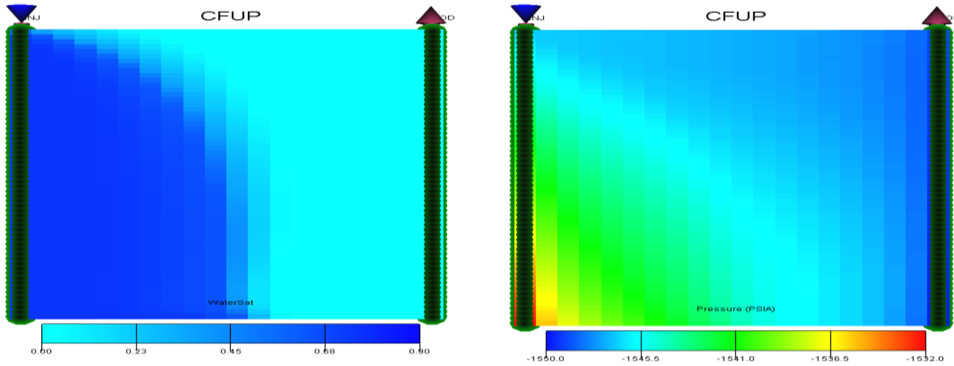

Figure 3.7: ΔS_w (a) and ΔP (b) after 45 days of injection/production.

3.3 Petrophysical modelling

It is necessary for any time-lapse seismic analysis to have an understanding of the changes in P-wave (compressional) velocity, S-wave (shear) velocity, and density as fluid or rock properties change, in order to recognize or predict the effect of changes in seismic amplitudes and travel-times. The petro-elastic modelling links these two domains: the reservoir domain (flow simulation) and the elastic domain (wave propagation) (Falcone et al., 2004). This appendix explains the conventional petro-elastic modelling used to convert the fluid properties (pressures, saturations, fluid densities) and rock properties (porosities, clay content, rock frame bulk moduli) into the saturated elastic moduli, and hence determines P-wave velocities, S-wave velocities and densities.

The static (e.g. porosity, net-to-gross, permeability) and dynamic grid properties (e.g. pressure and saturation output from the simulator) are the inputs to a rock and fluid physics calculation that computes the P- and S-wave velocity and density grids of the same size as the simulation grids for each of the chosen production times. The results of this petro-elastic transformation could be sufficient for feasibility 4D seismic tests, or for part of a more sophisticated full-scale simulator to seismic workflow. For reservoirs without compaction issues due to geomechanical effects, the petro-elastic model consists of three main categories: fluid substitution, fluid-related pressure effects, and the stress-dependency of the rock frame. The properties of the reservoir fluid are determined using the equations of Batzle and Wang (1992) described in Appendix B.

The petro-elastic transformation assumes an isotropic, linear elastic medium. Under these assumptions, the elastic tensor will depend on two constants, the bulk modulus K and the shear modulus μ. P-wave and S-wave velocities (V_p and V_S respectively) can be expressed as a function of these two elastic constants:

$$V_{psat} = \sqrt{\frac{K_{sat} + 4/3\, \mu_{sat}}{\rho_B}} \qquad 3.1$$

$$V_{ssat} = \sqrt{\frac{\mu_{sat}}{\rho_B}} \qquad 3.2$$

where ρ_B is the bulk density of the rock.

3.3.1 Fluid substitution

The most commonly used theoretical approach for fluid substitutions employs the Gassmann theory (Gassmann, 1951; Smith et al., 2003). Adding the temperature and pressure dependent fluid properties and a pressure sensitivity dry-frame modulus, Gassmann's equation can be expressed as follow:

$$K_{sat} = K_{dry} + \frac{\left(1 - \frac{K_{dry}}{K_0}\right)^2}{\frac{\phi}{K_{fluid}} + \frac{(1-\phi)}{K_0} + \frac{k_{dry}}{K_0{}^2}} \qquad 3.3$$

It is important to recognize that the shear modulus in isotropic media and for the assumptions of Gassmann's equations, is insensitive to pore fluid (Biot, 1956; Berryman and Milton, 1991; Berryman, 1999) that is:

$$\mu_{sat} = \mu_{dry} \qquad 3.4$$

where:

K_{sat} is the saturated rock bulk modulus

K_0 is the bulk modulus of the mineral matrix

K_{fluid} is the bulk modulus of the pore fluids

K_{dry} is the bulk modulus of the porous rock frame, drained of any pore-filling fluid or the dry frame bulk modulus

Φ is the porosity of the rock

μ_{sat} is saturated rock shear modulus

μ_{dry} is the dry frame shear modulus

As Gassmann fluid substitution assumes a single fluid phase; the effective fluid bulk modulus must be calculated. If the fluids are mixed uniformly at very fine scales, then the effective bulk modulus of the mixture of fluids (K_{fluid}) can be approximated using harmonic average:

$$K_{fluid} = \left[\sum_i \frac{S_i}{K_i} \right]^{-1} \tag{3.5}$$

where K_i = bulk modulus of the individual fluid and gas phases, and S_i = the saturation of the individual phases.

An additional equation to compute the saturated bulk density of the rock is needed to compute the P-wave and S-wave velocities:

$$\rho_{sat} = \rho_g (1-\phi) + \rho_{fl}\phi \tag{3.6}$$

where ρ_g is the grain density of the rock matrix, ρ_{fl} is the fluid density and Φ is porosity.

ρ_g is set to be equal to 2650 Kg/m^3 which is the density of quartz. ρ_{fl} is calculated using the following equation.

$$\rho_{fluid} = \sum_i S_i \rho_i \tag{3.7}$$

where S_i is the saturation of the individual components and ρ_i is the density of the individual components.

Once the bulk modulus (K_{sat}), shear modulus (μ_{sat}) and rock density (ρ_{sat}) of the saturated rock have been computed, the P- and S- wave velocities are then calculated by:

$$V_{psat} = \sqrt{\frac{K_{sat} + \frac{4}{3}\mu_{sat}}{\rho_B}} \tag{3.8}$$

$$V_{ssat} = \sqrt{\frac{\mu_{sat}}{\rho_B}} \tag{3.9}$$

The acoustic impedance for the P-wave and S-wave is also calculated.

$$Pimp = \rho_B \times V_p \tag{3.10}$$

$$Simp = \rho_B \times V_s \tag{3.11}$$

3.3.2 Stress-dependency of the rock frame

The variation of rock-frame properties with applied effective stress is an important component of the petro-elastic modelling. The stress-dependency of the rock frame generally is based on core-plug laboratory measurements. Ultrasonic velocity measurements are taken at different stress values, and then a curve is fitted between these points. The result is a relationship between variations in velocity as a function of the effective stress. Several semi-empirical pressure dependency equations have been published in the literature. The equation used in our petro-elastic modelling are the ones proposed by MacBeth (2004). These equations predict variations in the elastic moduli rather than velocity.

$$K_{dry}\left(P_{eff}\right)=\frac{\kappa_{\inf}}{1+E_{\kappa}e^{-P_{eff}/P_{\kappa}}} \qquad 3.12$$

$$\mu_{dry}\left(P_{eff}\right)=\frac{\mu_{\inf}}{1+E_{\mu}e^{-P_{eff}/P_{\mu}}} \qquad 3.13$$

The value of the three controlling parameters in each equation will determine how responsive the rock is to applied pressure. MacBeth (2004) compiled a list of different values for these parameters for different reservoir settings. The parameters chosen for our study are those of a moderately stress sensitive sandstone rock from a North Sea reservoir (Table A.1).

$\kappa_{\inf}$	P_{κ}	E_{κ}	$\mu_{\inf}$	P_{μ}	E_{μ}
6.85	5.62	1.12	7.97	5.06	1.08

Table 3.2: Stress-sensitivity parameters (after MacBeth, 2004)

The effective pressure is defined as:

$$P_{eff} = P_{ob} - \alpha \, P_{pore} \qquad 3.14$$

where α is Biot's coefficient, P_{ob} is the overburden pressure and P_{pore} is the pore pressure.

In this study, α is set to be equal to one. The overburden pressure is calculated at the centre of each grid cell using an average overburden pressure gradient of 1 psi/ft.

3.3.3 Mixing of sand and shale

Two options are available for isotropic mixing sands and shales, Backus averaging (for a layered system) and Voigt-Reuss-Hill average (i.e. average of the harmonic and arithmetic means).

Backus Averaging

It is important to note that this option is only valid if the results are used for normal incidence seismic modelling. If non-normal incidence modelling is required, then the fully anisotropic form of Backus averaging is also required. It is anticipated that this will be added to a future release. For the effective isotropic P-wave velocity of a normal incidence wave propagation on a stack of horizontal layers (Backus, 1962):

$$V_{p,ave} = \sqrt{\frac{1}{\rho_{ave}} \left[\sum_{i=1}^{n} \frac{f_i}{\left(\kappa_i + \frac{4}{3}\mu_i \right)} \right]^{-1}} \qquad 3.15$$

And for effective isotropic S-wave velocity:

$$V_{s,ave} = \sqrt{\frac{1}{\rho_{ave}}\left[\sum_{i=1}^{n}\frac{f_i}{\mu_i}\right]^{-1}} \qquad 3.16$$

Where:

$$\rho_{ave} = \sum_{i}^{n} f_i \rho_i \qquad 3.17$$

f_i is the fraction of material i with P-wave velocity $V_{p,i}$, S-wave velocity $V_{s,i}$ and saturated density ρ_i.

In our case we are considering sand/shale mixtures, so that n = 2 and the values of f is either V_{shale} or $1 - V_{shale}$.

VRH Average

The VRH (Voigt-Reuss-Hill) average is the average of the harmonic and arithmetic means. For effective isotropic P-wave velocity:

$$M_{p,\mathrm{Re}uss} = \left[\sum_{i=1}^{n}\frac{f_i}{\left(\kappa_i + \frac{4}{3}\mu_i\right)}\right]^{-1} \qquad 3.18$$

$$M_{p,Voigt} = \left[\sum_{i=1}^{n} f_i\left(\kappa_i + \frac{4}{3}\mu_i\right)\right] \qquad 3.19$$

and

$$M_{p,ave} = \frac{1}{2}\left[M_{p,Voigt} + M_{p,\mathrm{Re}uss}\right] \qquad 3.20$$

finally:

$$V_{p,ave} = \sqrt{\frac{M_{p,ave}}{\rho_{ave}}} \qquad 3.21$$

Similarly for the effective isotropic S-wave velocity:

$$M_{s,\mathrm{Re}uss} = \left[\sum_{i=1}^{n} \frac{f_i}{\mu_i}\right]^{-1} \qquad 3.22$$

$$M_{s,Voigt} = \left[\sum_{i=1}^{n} f_i \mu_i\right] \qquad 3.23$$

and

$$M_{s,ave} = \frac{1}{2}\left[M_{s,Voigt} + M_{s,\mathrm{Re}uss}\right] \qquad 3.24$$

and finally:

$$V_{s,ave} = \sqrt{\frac{M_{s,ave}}{\rho_{ave}}} \qquad 3.21$$

where, in both cases:

$$\rho_{ave} = \sum_{i}^{n} f_i \rho_i \qquad 3.22$$

3.3.4 Fluid properties

The chemical and physical properties of any crude oil vary considerably and depend on the concentration of the type of hydrocarbon. Equations from Batzle and Wang work (1992) are used for the computation of the densities and velocities of oil and brine, hence providing the fluids bulk modulus for the two phases.

Hydrocarbon oils

Oil density is a function of pressure and temperature. To compute the oil density at the reservoir pressure and temperature, we start with computing a reference density, ρ_0 which is the density of oil measured at 15.6 ºC and at atmospheric pressure. ρ_0 is related to the oil API gravity by equation 3.23.

$$\rho_0 = \frac{API + 131.5}{141.5} \qquad 3.23$$

Then the effects of pressure and temperature are taking into account according to equations 3.24 and 3.25 respectively.

$$\rho_P = \rho_0 + (0.00277P - 1.71\times10^{-7}P^3)\times(\rho_0 - 1.15)^2 + 3.49\times10^{-4}P \qquad 3.24$$

$$\rho_{oil} = \frac{\rho_P}{0.972 + 3.81\times10^{-4}(T + 17.78)^{1.175}} \qquad 3.25$$

where P is pressure and T is temperature.

The velocity of oil is a function the oil gravity, pressure and temperature. Equation 3.26 is used to obtain the oil velocity at the reservoir pressure and temperature.

$$V_{oil} = 15450(77.1 + API)^{-1/2} - 3.7T + 4.64P + 0.0115(0.36 API^{1/2} - 1)TP \tag{3.26}$$

where P is pressure, T is temperature and API is the oil gravity.

The bulk modulus of oil is then calculated using equation 3.27

$$K_{oil} = \rho_{oil} \times V_{oil}{}^{2} \tag{3.27}$$

Brine

Batzle and Wang equations are used to compute the bulk modulus of the brine. The density of pure water is first computed using equations 3.28, and then the density of brine is computed using equation 3.29.

$$\begin{aligned}\rho_{water} &= 1 + 1\times10^{-6}(-80T - 3.3T^{2} + 0.00175T^{3} + 489P - 2TP + 0.016T^{2}P - \\ &1.3\times10^{-5}T^{3}P - 0.333P^{2} - 0.002TP^{2})\end{aligned} \tag{3.28}$$

$$\begin{aligned}\rho_{brine} &= \rho_{water} + S\{0.668 + 0.44S + 1\times10^{-6} \\ &\left[300P - 2400PS + T\left(80 + 3T - 3300S - 13P + 47PS\right)\right]\}\end{aligned} \tag{3.29}$$

where T is temperature, P is pressure and S is the brine salinity

The velocity of pure water is computed using equation 3.30.

$$V_{water} = \sum_{i=0}^{4}\sum_{j=0}^{3} w_{ij} T^{i} P^{j} \tag{3.30}$$

where T is temperature, P is pressure and w_{ij} are the constants listed in Table 1.

$w_{00} = 1402.85$	$w_{01} = 1.524$	$w_{02} = 3.437.10^{-3}$	$w_{03} = -1.197.10^{-5}$
$w_{10} = 4.871$	$w_{11} = -0.0111$	$w_{12} = 1.739.10^{-4}$	$w_{13} = -1.628.10^{-6}$
$w_{20} = -0.04783$	$w_{21} = 2.747.10^{-4}$	$w_{22} = -2.135.10^{-6}$	$w_{23} = 1.237.10^{-8}$
$w_{30} = 1.487.10^{-4}$	$w_{31} = -6.503.10^{-7}$	$w_{32} = -1.455.10^{-8}$	$w_{33} = 1.327.10^{-10}$
$w_{40} = -2.197.10^{-7}$	$w_{41} = 7.987.10^{-10}$	$w_{42} = 5.230.10^{-11}$	$w_{43} = -4.614.10^{-13}$

Table 3.3: Coefficients for water velocity computation

The velocity of brine is computed using equation 3.31

$$V_{brine} = V_{water} + S(1170 - 9.6T + 0.055T^2 - 8.5\times10^{-5}T^3 + 2.6P - 0.0029TP - 0.0476P^2) + S^{1.5}(780 - 10P + 0.16P^2) - 820S^2 \qquad 3.31$$

where T is temperature, P is pressure and S is the brine salinity

The bulk modulus of brine is then computed using the following equation:

$$K_{brine} = \rho_{brine} \times V_{brine}{}^2 \qquad 3.32$$

Densities are expressed in [g/cm^3], velocities in [Km/s], pressure in [MPa], temperature in [ºC], salinity in [ppm] and bulk modulus in [GPa].

The reservoir temperature is constant throughout the whole simulation and is set to be equal to 107 ºC. The brine salinity is 100000 ppm.

3.3.5 Homogeneous reservoir: injection with pressure support

The petro-elastic transform gives cubes of P-wave velocities (V_p), S-wave velocities (V_s), and densities (Rho) at each grid cell. P-wave impedance (Pimp) and S-wave impedance (Simp) are then computed. V_p, V_s and Rho grids have the same dimensions as the 3D simulation grid. In this section, we will display the results at a cross-section through the middle of the reservoir, where the water injector and the producer are placed during the simulation (Crossline 10).

The changes in the rock physical properties are the highest in the water-invaded areas. We obtained very low changes in V_p, V_s, Pimp and Simp in the area ahead of the waterfront, where only pressure changes affect the petro-elastic properties.

V_p and V_s respond to Waterflooding in two contrasting ways. V_p decreased by a maximum of -0.073 m/s (-0.0024%) around the oil producer ahead of the waterfront and the maximum increase was 131.529 m/s (4.273%) around the water injector behind the waterfront. V_s decreased by a maximum of -25.0431 m/s (-1.291%) behind the waterfront and the maximum increase is 0.56 m/s (0.0289%) ahead of the waterfront. P-impedance relative changes vary between -0.0047% and 7.0623%, while the changes in S-impedance are between 0.0215% and 1.35% (Figure 3.8).

The pressure being maintained constant, the observed changes can be directly linked to saturation changes. The waterfront forms a transition zone between the water-saturated and oil saturated parts of the reservoir. To ascertain the extent of this transition zone, a row of cells at the mid-depth of the reservoir (layer 30) was extracted from the P-impedance 10th cross-line (Figure 3.9). For saturation changes equal to or greater than 60% (inline 10 and behind) the impedance change is varying between 7% for a ΔS_w of 90% and 5.5% for a ΔS_w of 60%. The impedance values decrease exponentially in the transition zone between inline 10 and 14, falling to almost 0% where no saturation changes occurred. This transition zone, which forms the waterfront of the interface between the displacing fluid, water, and the displaced fluid, oil, extends over 20 feet. In the next section we will examine the seismic detectability of this zone.

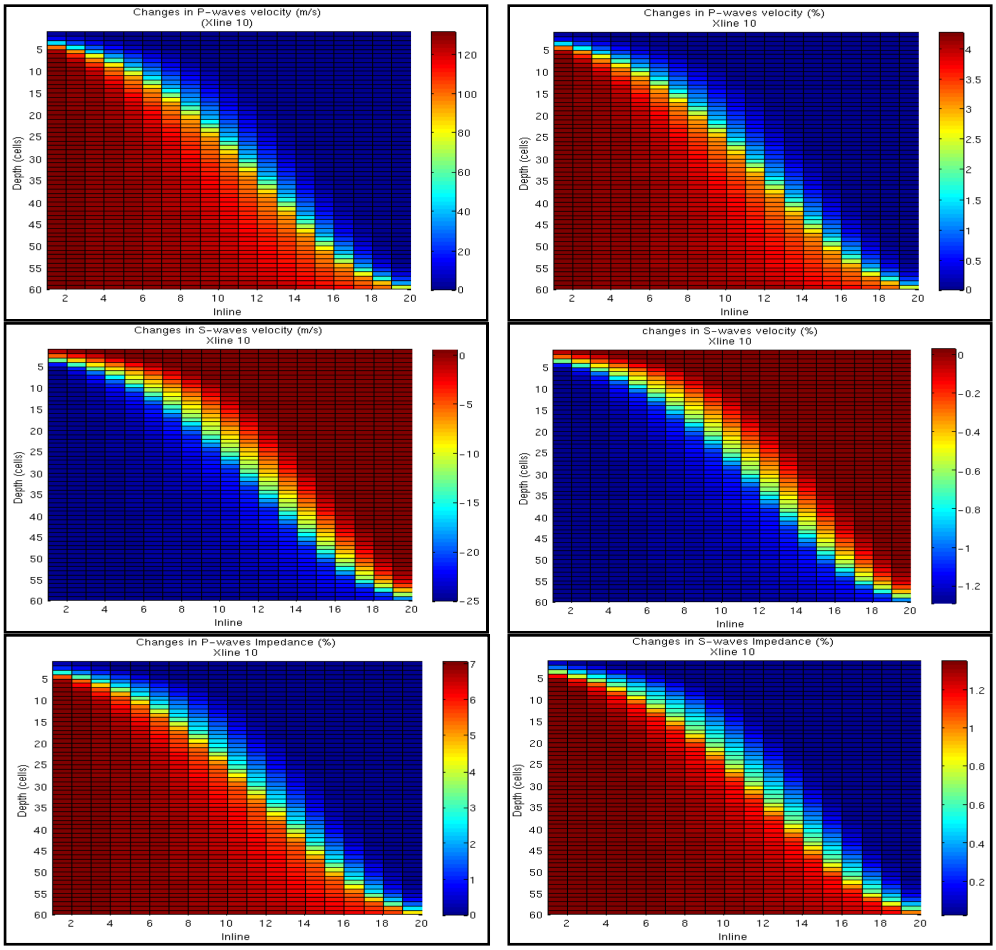

Figure 3.8: Relative changes in S-wave and P-wave impedances and S-wave and P-wave velocities at cross-line 10.

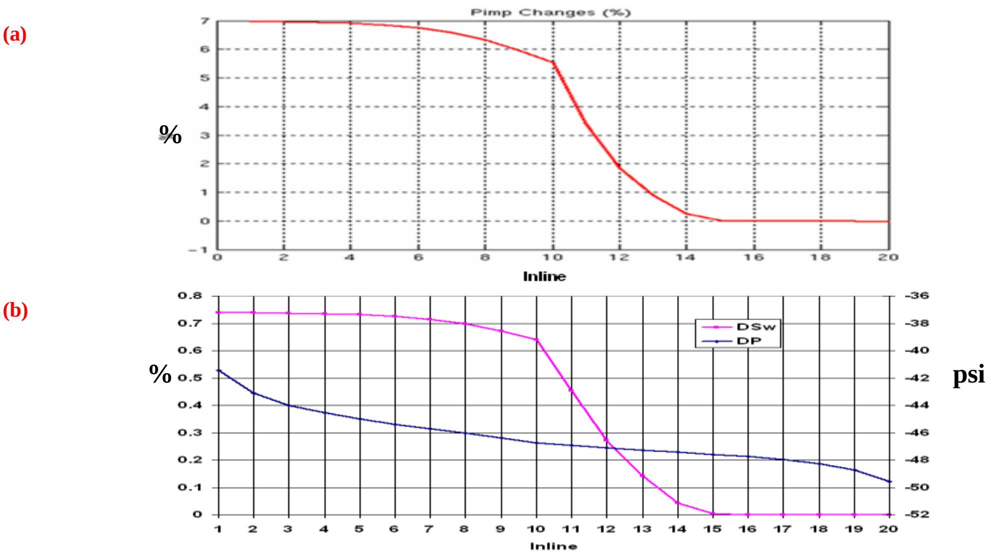

Figure 3.9: (a) P-wave impedance changes across a row of cells. (b) Saturation and Pressure changes across the same row of cells.

3.3.6 Homogeneous reservoir: injection without pressure support

With a pressure drop of around 1500 psi, the effects of pressure changes on the rock properties are expected to be more accentuated. The response of the rock to changes in effective pressure, or the rock stress sensitivity, is accounted for during the petrophysical modelling with the calibrating parameters set to be of a moderate to high stress sensitive rock. The minimum change in V_p is -11.446 m/s (-0.372%) ahead of the waterfront and the maximum is 119.7 m/s (3.888%) at the vicinity of the water injector. V_s decreased by a maximum of -17.781 m/s (-0.917%) ahead of the waterfront and increased by a maximum of 8.511 m/s (0.439%). The minimum P-impedance change is -0.449% while the maximum is 6.583%. The S-impedance changes are from 0.322% to 1.653% (Figure 3.10).

The decrease in pore pressure resulted in a softening of the rock matrix leading to lower P-impedance values. The effects of the pressure decline on P-impedance is bigger than in the case where the pressure drop was controlled and kept to a strict minimum but was still weak and below seismic detectability. These effects are visible ahead of the waterfront. Behind the waterfront, the pressure and saturation effects mix together with the pressure effects tending to cancel-out a part of the saturation effects, giving lower P-impedance changes than in the case where only saturation effects were present during production.

The transition zone between the fully water saturated and non drained parts of the reservoir is investigated by taking a row of cells at mid-depth reservoir in cross-line 10 and examining the evolution of P-impedance as a function of pressure and saturation changes (Figure 3.11).

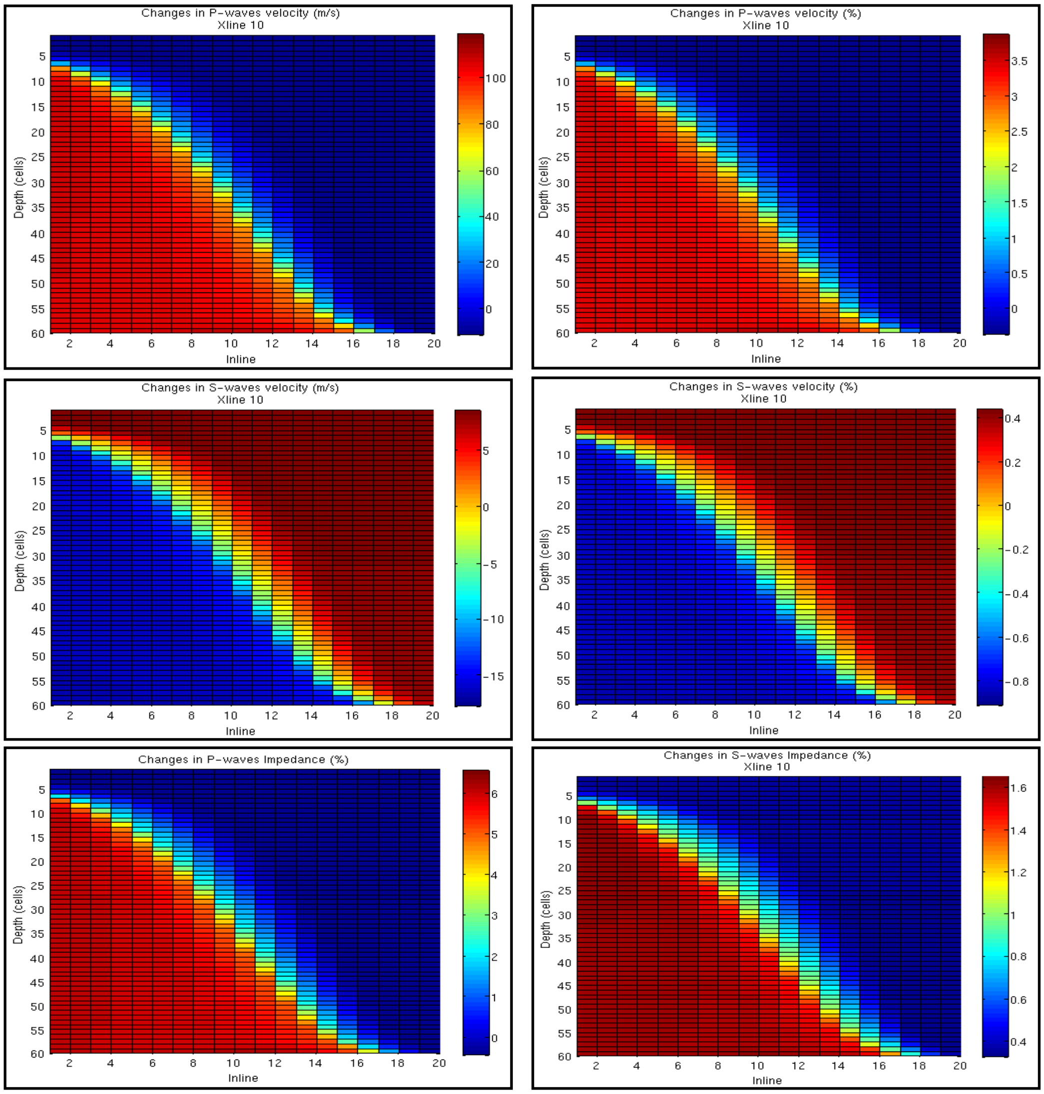

Figure 3.10: Relative changes in S-wave and P-wave impedances at cross-line 10.

Figure 3.11 shows that the maximum change in P-impedance is located between the water injector (inline 1) and inline 6. In this area, P-impedance changes are about 6% and the water saturation changes are higher than 70%. Between inline 6 and inline 8, the water saturation change is 60% and the associated P-impedance change is between 5% and 5.8%. Ahead of the inline 8 and until inline 12, P-impedance changes decrease in an exponential fashion similar to that observed in the previous case where the pressure was kept constant, but instead of reaching a plateau at 0% it stabilises at -0.5%. This slight P-impedance decrease is associated with the pressure drop of 1500 psi caused by the start of the production. This effect is present across the whole reservoir and resulted in lower P-impedance changes than those obtained in the previous case, when the pressure was kept constant, even in fully water invaded areas.

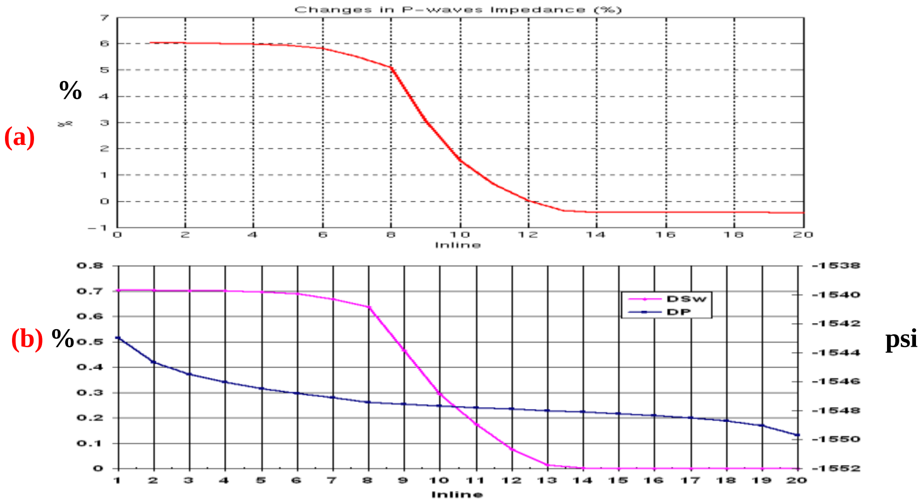

Figure 3.11: (a) P-wave impedance changes across a row of cells. (b) Saturation and pressure changes across the same row of cells.

3.3.7 Homogeneous reservoir: injection without pressure support, basal drive

In this section, the signature of raising OWC is studied. The OWC is cone-shaped around the producer and the biggest water saturation changes occur in this area. The pressure dropped by 1500 psi across the whole reservoir.

The maximum P-wave velocity change is 164 m/s (5.5%) in the vicinity of the producer while it averages 3% in the rest of the drained areas. The minimum change is -0.35%. For the S-wave velocity, the changes varies between -20 m/s (-1%) and 8.5 m/s (0.44%). The P-impedance changes are between 8.4% and -0.44%, the S-impedance changes are between 0.33% and 1.84%. The biggest changes in P-impedance are again around the producing well where the water saturation change is around 80%. Away from the cone-shaped zone, the P-impedance changes average 4% associated with a water saturation change of 45%.

Even though the pressure decline is exactly the same as for the previous example with edge drive, we obtained higher P-impedance changes in the water invaded area for similar water saturation changes.

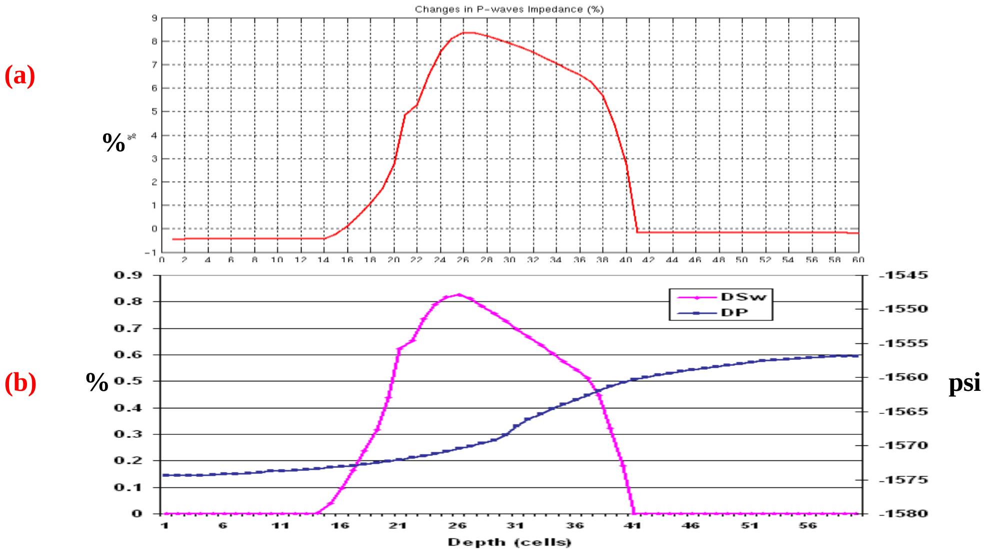

Figure 3.12: (a) P-wave impedance changes across a row of cells at the producer location. (b) Saturation and pressure changes across the same row of cells.

A column of cells was extracted at the producer location and the impedance changes are plotted in Figure 3.12 (a). Figure 3.12 (b) shows the saturation changes across those cells. The acoustic impedance profiles are closely related to the water saturation changes

3.3.8 Heterogeneous reservoir: fining upward

For this study, the average reservoir pressure dropped by 1500 psi. The combined effects of saturation and pressure changes are illustrated. The P-wave velocity changes vary from -11.4 m/s (-0.37%) to 122.2 m/s (3.96%). The S-wave velocity changes are from -18 m/s (-0.92%) to 3.96 m/s (0.44%). The maximum decrease of P-wave impedance is -0.45% around the producer. The maximum increase is 6.7% at the vicinity of the water injector. For the S-wave impedance, the changes vary from 0.32% to 1.66% (Figure 3.13).

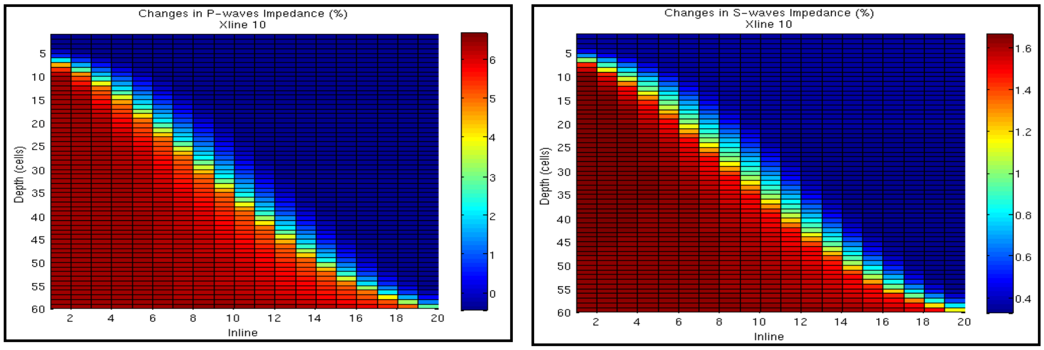

Figure 3.13: Relative changes in P-wave and S-wave impedances at cross-line 10 for fining upward model.

3.3.9 Heterogeneous reservoir: coarsening upward

The changes of P-wave velocity vary from -11.46 m/s (-0.37%) to 125.46 m/s (4.07%). S-wave decreased by a maximum of -18.21 m/s (-0.93%) and increased by a maximum of 8.51 m/s (0.44%). P-wave impedance changes are from -0.45% to 6.82% while those of the S-wave impedance are from 0.32% to 1.71% (Figure 3.14).

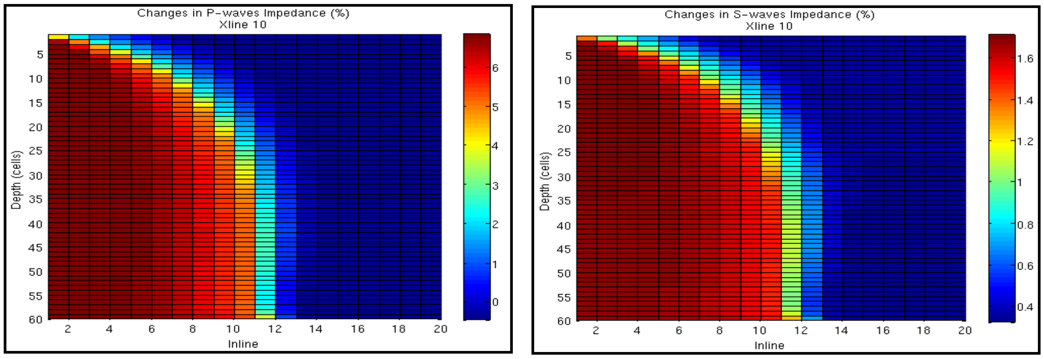

Figure 3.14: Relative changes in P-wave and S-wave impedances at cross-line 10 for coarsening upward model.

3 .4 Synthetic seismic modelling

Synthetic seismic is created for the different cases studied above. The P-wave velocity, S-wave velocity, density, P-wave impedance and S-wave impedance cubes from the two time steps are used to compute the matrix of transmission and reflection coefficients using Aki-Richards (1980) matrix rearrangement of Zoeppritz equation. In order to create realistic reflections at the top and the base of the reservoir, two horizons were added to the model to create the overburden and the underburden. The overburden and the underburden were defined as two homogeneous, uniform half-spaces with properties of shale extracted from North Sea well logs. A 30 Hz Ricker wavelet is then convoluted with the reflectivity matrix to create the synthetic seismic traces.

3.4.1 Homogeneous reservoir with constant pressure:

Figure 3.15 shows a cross-section of the synthetic seismic computed for the homogeneous model with constant pressure (cross-line 10). It shows the first time step corresponding to the base survey. The top and base of the reservoir are also shown and they present opposite polarities. The model is homogeneous and fully saturated with oil; the reflections at the top and the base of the reservoir are the only events present with strong side lobes for the two cases.

Figure 3.16 shows the monitor survey for the same model. The top and the base of the reservoir are also displayed. The strong reflections at the top and the base of the reservoir are similar to those shown in the base survey. Reflections from the waterfront are also present and a tuning effect takes place as the water-swept thickness of the reservoir decreases. The amplitude of the reflections at the oil-water contact is weak compared to the reflections at the top and the base of the reservoir. The base horizon presents a time shift proportional to the height of the water-invaded thickness of the reservoir, with the biggest time shift (2.73 ms) being at the vicinity of the water injector where almost the whole reservoir thickness was drained.

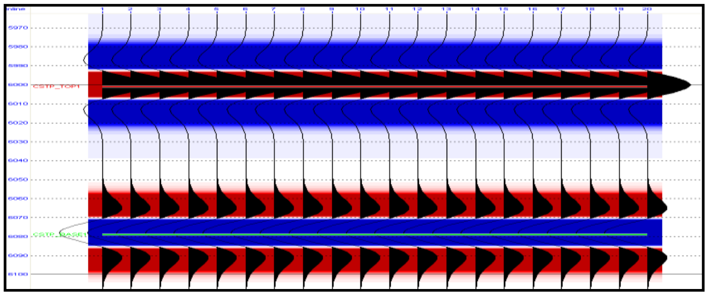

Figure 3.15: Synthetic seismic for the base survey (Homogeneous model with constant pressure)

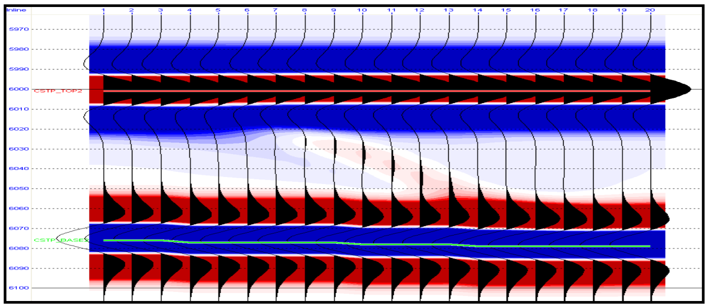

Figure 3.16: Synthetic seismic for the monitor survey (Homogeneous model with constant pressure)

The synthetic time-lapse seismic was computed as the difference between the monitor and the base surveys. Figure 3.17 shows a cross section of the reservoir (cross-line 10). The reflections at the top reservoir cancelled each other out leaving only the 4D signature of the waterfront. At the base reservoir though, the side lobes originally present at the base and the monitor surveys were not completely removed as there was a time shift of the monitor survey as water replaced oil in some parts of the reservoir. The monitor survey needs to be warped in order to remove the effects of the time shift in order to be able to get a proper 4D signal directly associated with the movement of the waterfront.

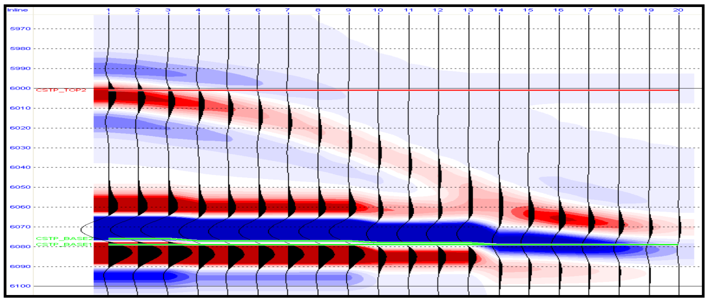

Figure 3.17: Synthetic time-lapse seismic (Monitor-Base, Homogeneous model with constant pressure)

3.4.2 Homogeneous reservoir with declining pressure

Figure 3.18 shows a cross-section (Crossline 10) of the synthetic seismic created for the homogeneous reservoir with a pressure decline of 1500 psi. The reflections at the waterfront are visible as a peak over a trough. As for the case where the pressure was kept constant, the artefacts introduced by the time shift associated to water replacing oil overshadow the 4D signal at the base of the reservoir. The time shift at the base reservoir horizon is also proportional to the height of the swept thickness of the reservoir with a negative time shift in the un-swept area. This seems to be due to the pressure drop. In fact, the replacement of oil by water introduced a positive time shift while the pressure drop caused a negative time shift of approximately 1 ms across the whole reservoir which led to the decrease of the time shift in the swept area where the maximum time shift is 1.73 ms against 2.73 ms in the case where the pressure was kept constant.

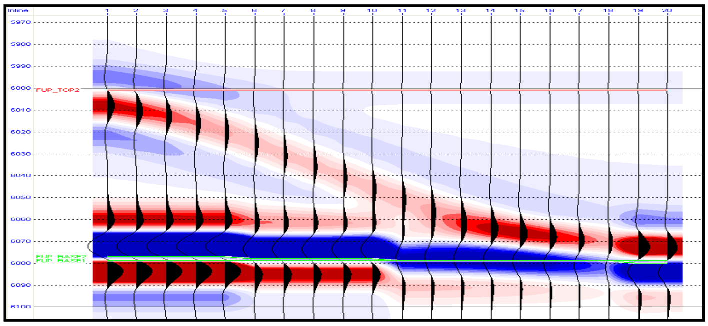

Figure 3.18: Synthetic time-lapse seismic (Monitor-Base, Homogeneous model with declining pressure)

3.4.3 Homogeneous reservoir under basal drive

In this case, the water is displacing the oil vertically across the reservoir. The top and base reservoir horizons are the main events visible in the seismic section with opposite polarities and strong side lobes for both horizons. The original OWC is hard to identify as it is masked by the side lobes from the reflections at the base horizon. The reflections at the oil/water interface on the monitor survey are also easy to identify, making the identification of the new OWC simple.

Cross-section 10 of the computed 4D cube is displayed in Figure 3.19. It shows a strong signature of the OWC movement. The reflections are stronger at the vicinity of the oil producer were the maximum changes in acoustic impedance have been recorded. A constant time shift of -1ms is visible at the base reservoir horizon; this seems to be the result of the pressure decline due to production.

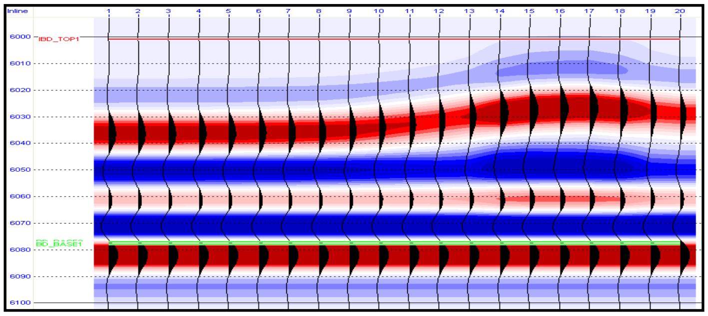

Figure 3.19: Synthetic time-lapse seismic (Monitor-Base, Basal drive)

3.4.4 Heterogeneous reservoir with fining upward permeability distribution

Cross-sections of the monitor survey computed for the heterogeneous model with high permeabilities at the bottom of the reservoir feature the same characteristics as for the homogeneous model, with strong reflections at the top and base reservoir horizons and weaker reflections at the waterfront. Figure 3.20 shows the time-lapse seismic section. As for the homogeneous case, it shows a clearly detectable waterfront movement and a positive time shift at the flooded areas, with a maximum value of 1.35 ms which decreases as the height of the flooded area decreases until it reaches 0 ms toward the edge of the flooded area and stabilizing at -0.42 ms in the un-swept portion of the reservoir.

The structure of the time shift map could be a good indicator of the shape of the waterfront. The time shift between the base and the monitor surveys caused the same artefact observed with the homogeneous model suggesting that a warping processing is necessary in order to proceed with more robust time-lapse interpretation. The tuning effects are also visible in both the monitor and the 4D sections.

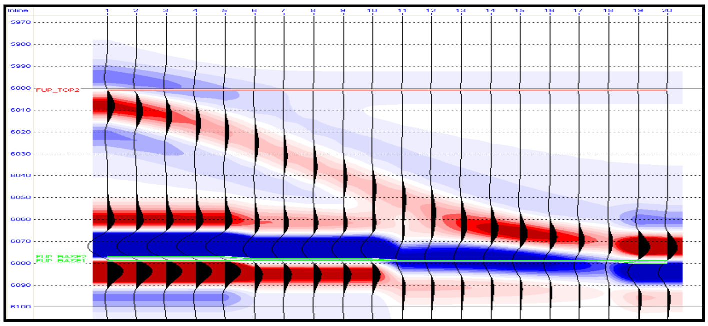

Figure 3.20: Synthetic time-lapse seismic (Monitor-Base, Fining upward permeability)

3.4.5 Heterogeneous reservoir with coarsening upward permeability distribution

In this case, the reservoir model has the higher permeability values at the top. As seen in the simulation results, the resulting waterfront is almost a sharp vertical interface between the swept and the un-swept area of the reservoir. Synthetic seismic created for the monitor survey features strong reflections at the top and base horizons and relatively weak reflections at the waterfront. The waterfront is better resolved in the time-lapse section displayed in Figure 3.21. Figure 3.21 shows the cross-section 10 of the seismic cube, where both the water injector and the producer were placed during simulation. The base horizon is again affected by the time shift induced by water displacing oil. But in this case, the transition zone between the positive time-shift, associated with water flooded areas of the reservoir, and the negative time shift, associated with the un-swept areas, is narrower reflecting the sharpness of the waterfront.

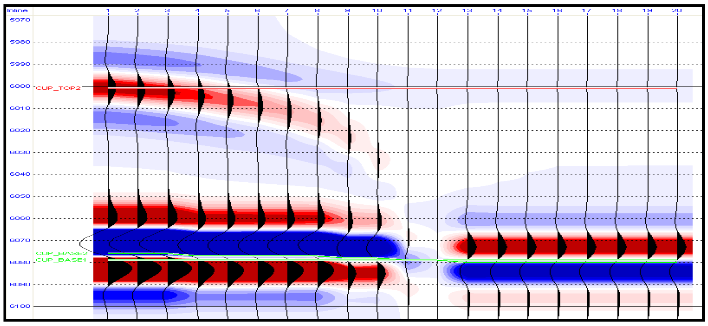

Figure 3.21: Synthetic time-lapse seismic (Monitor-Base, Coarsening upward permeability)

3.5 Comparative study

In this section, a comparative study is carried out to examine the petrophysical modelling results for the different scenarios studied. The effects of those differences on the corresponding time-lapse signature are highlighted.

Table 3.2 shows a summary of the changes in percentage for the different reservoir rock properties after Waterflooding for each scenario.

The maximum changes in P-wave impedance are of similar magnitude for the different Waterflooding scenarios. The petrophysical modelling does not give any indication of the stability of the waterfront.

The pressure change during Waterflooding has an opposite effect on rock properties to that of saturation changes. In the four scenarios run with reservoir pressure declining by up to 1500 psi, we had similar minimum and maximum changes in P-wave impedance values. The minimum P-wave impedance change is around -0.5% regardless of the geology of the reservoir. This minimum change happened ahead of the waterfront, where no saturation changes had yet occurred . When the pressure was kept constant during simulation this change was almost zero (-0.004%).

While saturation changes during Waterflooding increase the P-impedance in case of drainage (oil swept by water), pressure change has a global dimming effect on the P-wave impedances. It happens very briefly after the start of the simulation and spreads across the whole reservoir.

The petroelsatic changes in the reservoir rock properties are the strongest behind the waterfront. The waterfront represents a transition area spread over a couple of feet where the magnitude of the changes decreases gradually.

Changes (%)	**V_p min**	**V_p max**	**Vs min**	**Vs max**	**Pimp min**	**Pimp max**	**Simp min**	**Simp max**
HCSTP	**-0.002**	**4.247**	**-1.291**	**0.028**	**-0.004**	**7.062**	**0.021**	**1.350**
HDECP	**-0.372**	**3.888**	**-0.917**	**0.439**	**-0.449**	**6.583**	**0.322**	**1.653**
FUP	**-0.370**	**3.960**	**-0.920**	**0.440**	**-0.450**	**6.700**	**0.320**	**1.660**
CUP	**-0.370**	**4.070**	**-0.930**	**0.440**	**-0.450**	**6.820**	**0.320**	**1.710**
BD	**-0.350**	**5.500**	**-1**	**0.440**	**-0.440**	**8.400**	**0.330**	**1.840**

Table 3.2: Rock properties change (%) after Waterflooding, for the 5 scenarios. HCSTP: homogeneous model with constant pressure; HDECP: homogeneous model with declining pressure; BD: homogeneous model under basal drive; FUP: Heterogeneous model with lower permeability at the top; CUP: Heterogeneous model with higher permeability at the top

The time-lapse signatures for the different simulated scenarios are similar except for the basal drive model and the piston-like displacement when the reservoir permeability is highest at the top. Figure 3.22 shows time-lapse seismic cross sections and RMS amplitude maps computed from Top reservoir horizon to Base reservoir horizon, for the five simulated scenarios. The waterfront can easily be picked on the time-lapse RMS maps. The gradient of RMS amplitude on those maps gives a direct indication on the elongation of the waterfront on the vertical direction. Combined with the information extracted from time shift maps and fluid properties, this can help assess the inherent reservoir geology.

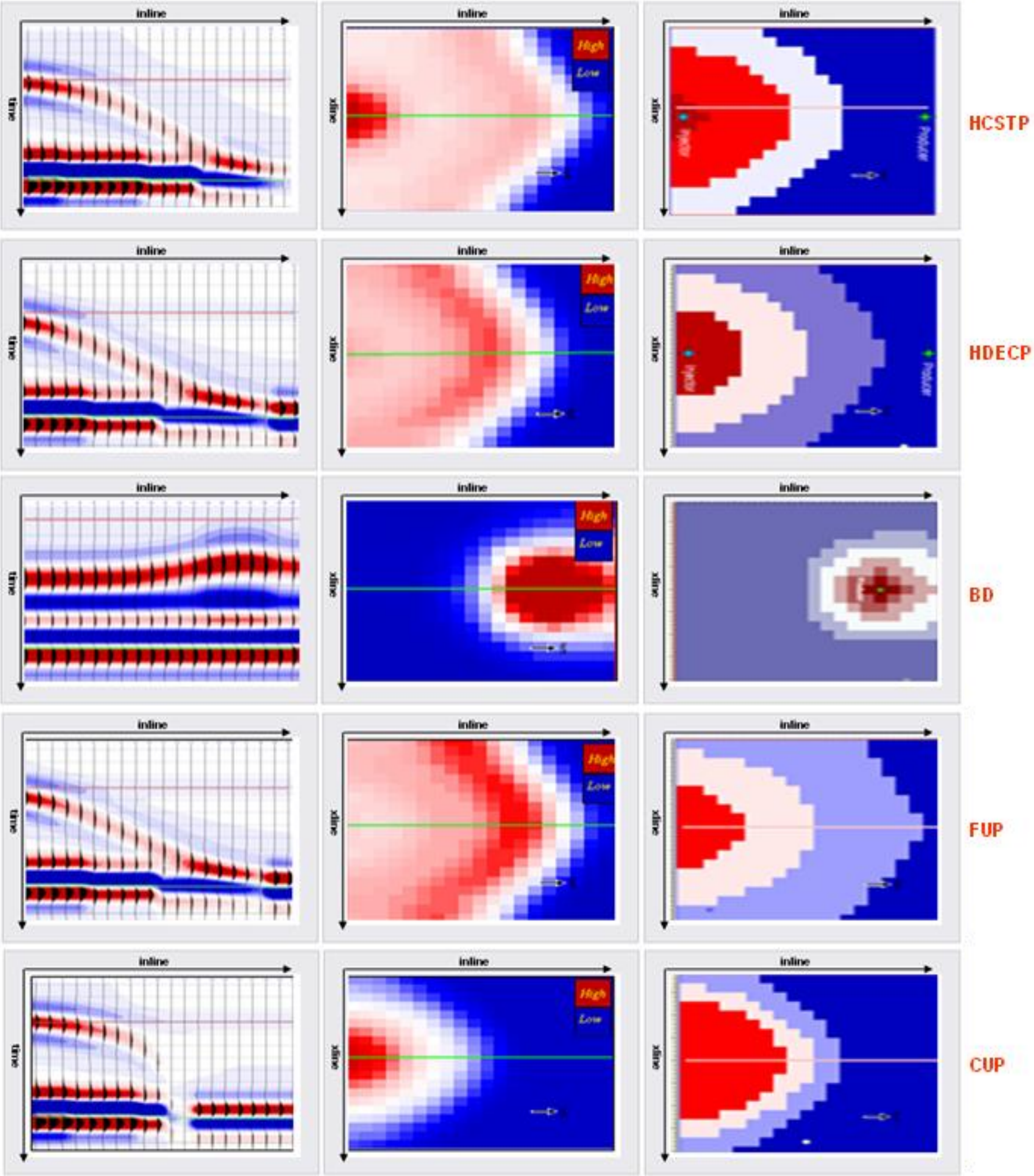

Figure 3.22: Time-lapse cross-sections (left), Time-lapse RMS maps (centre) and time shift (right) for the 5 simulated scenarios. Section view makes little difference between the scenarios where the permeability is constant across the reservoir and where it is increasing with depth. HCSTP: homogeneous model with constant pressure; HDECP: homogeneous model with declining pressure; BD: homogeneous model under basal drive; FUP: Heterogeneous model with lower permeability at the top; CUP: Heterogeneous model with higher permeability at the top

3.6 Conclusion

Waterflooding of a series of thick, idealised reservoir models, consisting of a thick block of sand with varying geological complexity, was simulated. Several scenarios of Waterflooding and their associated petrophysical and time-lapse signatures were studied. Fluid flow simulation showed that the sweep efficiency is mainly controlled by the reservoir geology, i.e. horizontal permeability, NTG, and vertical hydraulic communication between the reservoir layers. Time-lapse seismic analysis showed that inferring OWC on RMS maps is straightforward. The swept and un-swept areas exhibit opposite polarities and the transition zone where both phases (oil and water) coexist is easily interpretable. It is still challenging, though, to infer the vertical water distribution inside the reservoir.

The time-lapse signature of Waterflooding is mainly controlled by fluid saturation changes within the reservoir rocks. Waterflooding a reservoir while maintaining the pore pressure constant produced the same waterfront profile as when the pressure was allowed to drop significantly.

The petrophysical modelling showed that the substitution of oil by water within the reservoir pores produced the same level of change in the petro-elastic properties, regardless of the geology of the reservoir. In fact, changes in V_p, V_s and Rho were comparable for all the Waterflooding cases where the pressure dropped. In the case where pressure was kept constant, V_p, V_s and Rho changes were higher. The pressure decline had a global dimming effect on the time-lapse seismic signature of Waterflooding, due mainly to the absence of any reservoir compartmentalisation.

Seismic attributes analysis showed that in an idealised environment, and in the absence of any 4D seismic noise, the waterfront is visible on both vertical cross-sections and RMS maps. The combination of several seismic attributes may be needed for a more accurate mapping of the fluids contacts especially in cases when Waterflooding heterogeneous reservoirs. This simple reservoir model is meant to be representative of a high net-to-gross flow unit inside a turbidite reservoir. The next step in our study will focus on simulating a realistic turbidite reservoir and investigate the different time-lapse signature in a geologically complex setting.

Chapter 4

Geological overview and challenges for turbidite systems

This chapter gives a geological description of deepwater turbidite reservoirs and their different elements. The seismic characteristics of these different elements are highlighted through example from real reservoirs. The challenges for an optimal deep water turbidite reservoir management are also discussed. The AINSAII geological and simulation models are presented. Waterflooding simulation results are discussed.

4.1 Introduction

With the increased importance of deepwater exploration and development activities worldwide, a huge amount of work has been done to describe and understand turbidite systems. Over the last 50 years, data on composition, texture and structures of sedimentary rocks have grown enormously.The physical processes of sedimentation and their importance in understanding sedimentary structures have been topic of growning interest. This has come about as a response to the emphasis on the need to provide detailed reservoir description of deepwater turbidite reservoirs.

The biggest challenge for hydrocarbon exploration and production is to produce the reservoir with the maximum recovery factor. A reservoir description is a comprehensive three-dimensional picture showing the distribution and continuity of the rocks, pores, and fluids of the reservoir and aquifer system, including flow barriers. For prospect evaluation and play development, it is crucial to obtain this information during the exploration phase. The activity intensifies once a discovery is made. As a reservoir or field goes through the typical life cycle of discovery, appraisal, planning, development and reservoir monitoring, a more complete reservoir description is both necessary and possible.

The principal geophysical, geological, and petro-physical contributions to reservoir description are the external geometry of the reservoir; the internal geometry of the reservoir, including the distribution of fluid-flow barriers and pay types and intervals; the distribution of porosity, permeability, and capillary pressure-saturation properties; the aquifer extent, continuity, permeability and thickness; and the distribution of intra-reservoir shales (Barwis et al., 1990).

In the reservoir description process, it is important to identify all correlative reservoir layers or subzones and the intervening dense, impermeable or low-permeability strata. Generally, these units are correlated between wells using well log data. The correlation is guided by the knowledge of the deposional and diagenetic processes controlling both the reservoir and the non reservoir rock units. Genetic sequence analyses of sand bodies and seismic facies, coupled with knowledge from outcrop studies, can add significantly to interwell correlations. Flow tests and production data along with three-dimensional seismic provide a sound description of continuity-discontinuity of porosity, permeability, capillary properties, vertical and horizontal fluid-flow barriers, and fluids. All zones of unusual permeability contrast are critically important to all recovery processes.

The reservoir description for all displacement recovery processes should include the determination of net pay types, their continuity, and an estimate of the percent of pay that will be floodable based on the well spacing. This determines recovery estimates, the decision to drill infill wells, and the well spacing needed. In this chapter, we will look at the principal geological characteristics of deepwater turbidite reservoirs; their seismic signatures and the added value that time-lapse seismic brought to better understand the architecture of these reservoirs resulting in a better economical development of the hydrocarbon reserves.

4.2 Turbidite reservoirs: a geological overview

Turbidites are defined as sediments initially deposited in deep water, and which may now occur in great water depths (Weimer et al., 1999). Turbidite reservoirs present large stratigraphic variability that affect reservoir performance and development plans (Figure 4.1).

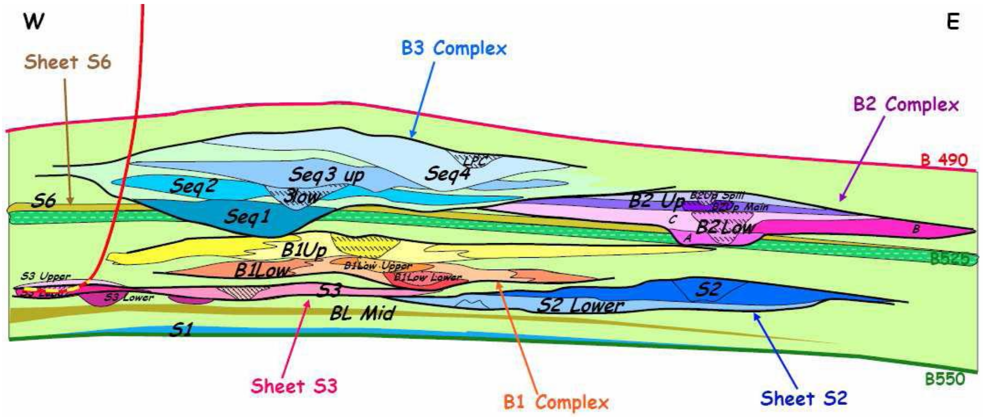

Figure 4.1: Vertical and lateral architectural variability in a channel type turbidite reservoir (Girassol B system), after Delattre et al. 2004

Contrasting styles of architecture (channel-dominated to sheet-dominated), pattern (straight vs. highly sinuous, dendritic vs. lobate), sand percent, bed thickness, and grain size and sorting can be observed in turbidite reservoirs (Figure 4.2). These characteristics can be tied to the sediment delivery system that controls the composition and volume of sediment available to the shelf edge; triggering mechanisms at the shelf edge that control the volume, feed rate, and concentration of the flows, and sea floor gradients that influence the acceleration, steadiness, or deceleration of flows (Figure 4.3). Within any one system, much of the reservoir architecture can be tied back to the sand/mud ratio of flows and to sea floor gradient. A fourth factor influencing final architectural character, particularly on the upper slope, is modification by slumping.

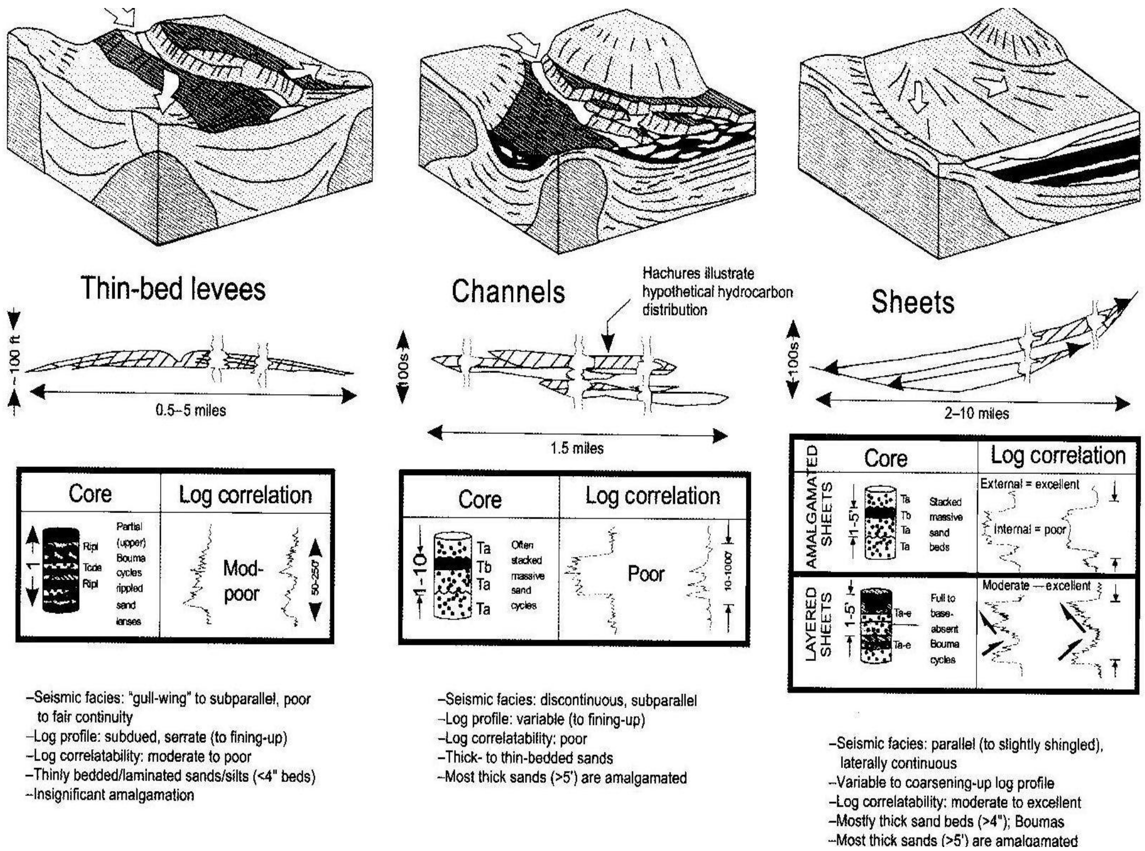

Figure 4. 2: Reservoir classification for deepwater reservoirs, after Chapin et al. (1994)

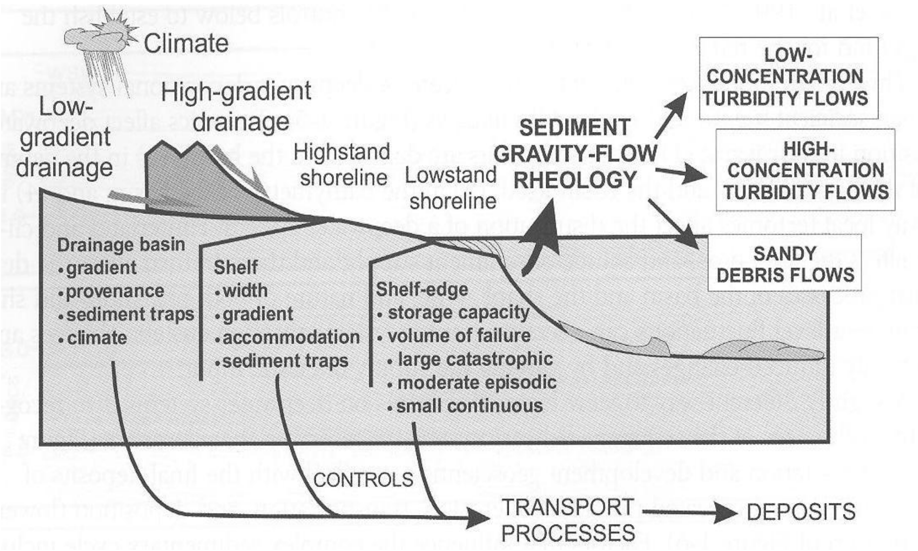

Figure 4.3: Schematic cross section across a margin, illustrating the sediment delivery system's influence on reservoir characteristics, after Garfield et al. (1998)

A number of papers have identified and classified the basic controls and properties of turbidite deposits. Reading and Richards (1994) proposed a classification based on two primary controls: the amount of mud versus sand in gravity flow, and nature of sediment delivery. They propose a fourfold classification for grain size of turbidite systems: gravel-rich, sand-rich, mixed sand/mud, and mud-rich (Figure 4.4). They classified sediments delivery to the slope and basin floor into three groups: single channels delivery, multiple channels delivery, and direct non-channelized slumping from shallower water. The combinations of grain size and delivery systems results in a set of end-member building blocks: wedge, channel, levee, sheets (or amalgamated), and slides (Figure 4.2). Mutti and Normark (1987 and 1991) proposed a similar classification of turbidite elements: channels, overbanks, lobes, channel-lobe transition, and erosional features. Chapin et al. (1994) proposed a similar classification of channel complexes, levees, and sheets.

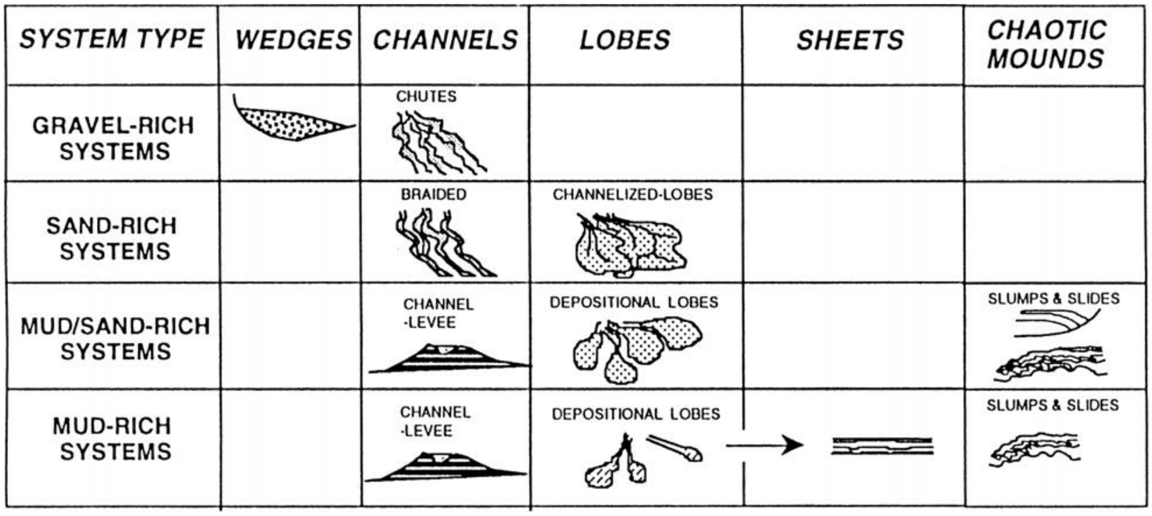

SYSTEM TYPE	WEDGES	CHANNELS	LOBES	SHEETS	CHAOTIC MOUNDS
GRAVEL-RICH SYSTEMS		CHUTES			
SAND-RICH SYSTEMS		BRAIDED	CHANNELIZED-LOBES		
MUD/SAND-RICH SYSTEMS		CHANNEL -LEVEE	DEPOSITIONAL LOBES		SLUMPS & SLIDES
MUD-RICH SYSTEMS		CHANNEL -LEVEE	DEPOSITIONAL LOBES		SLUMPS & SLIDES

Figure 4.4: Principal architectural elements of deepwater clastic systems, after Reading and Richards (1994).

4.3 Challenges in turbidite reservoirs management

In general, the size and geometry of a turbidite reservoir and its internal sand distribution are properties that control ultimate reservoir recovery. Large scale features, like laterally continuous, thick, permeable sands can be determined from seismic attributes, well logs, and well test and production data.

Many problems in turbidite reservoir development; such as early water breakthrough, abrupt reservoir pressure drops, and gas coning; arise from more subtle, subseismic scale properties (Weimer et al., 2000a). Subseismic scale properties, which are beneath the vertical resolution of conventional 3D seismic-reflection data, exert strong control on individual well production rates and ultimate recoveries. Features such as lateral bed continuity, vertical bed connectivity, reservoir quality, and net sand content normally cannot be determined from seismic images, yet these are the features that control fluid flow within the reservoir. Also, small-offset faults and fractures, which are common and critical components of reservoirs, cannot be imaged by conventional seismic. Newer techniques, such as spectral decomposition and PSDM, are improving our ability to detect small-scale stratigraphic and structural compartments; however, there still are the natural physical limits to the resolution of seismic images.

The major architectural elements that form the bulk of turbidite reservoirs are channel-fills, sheets and lobes, and overbank/levees. Although these elements can be recognized on seismic profiles and wireline logs, internal variability exists within each element that can affect reservoir performance. Table 4.1 lists the qualitative attributes of continuity, connectivity, and reservoir quality as they are present within each of these elements.

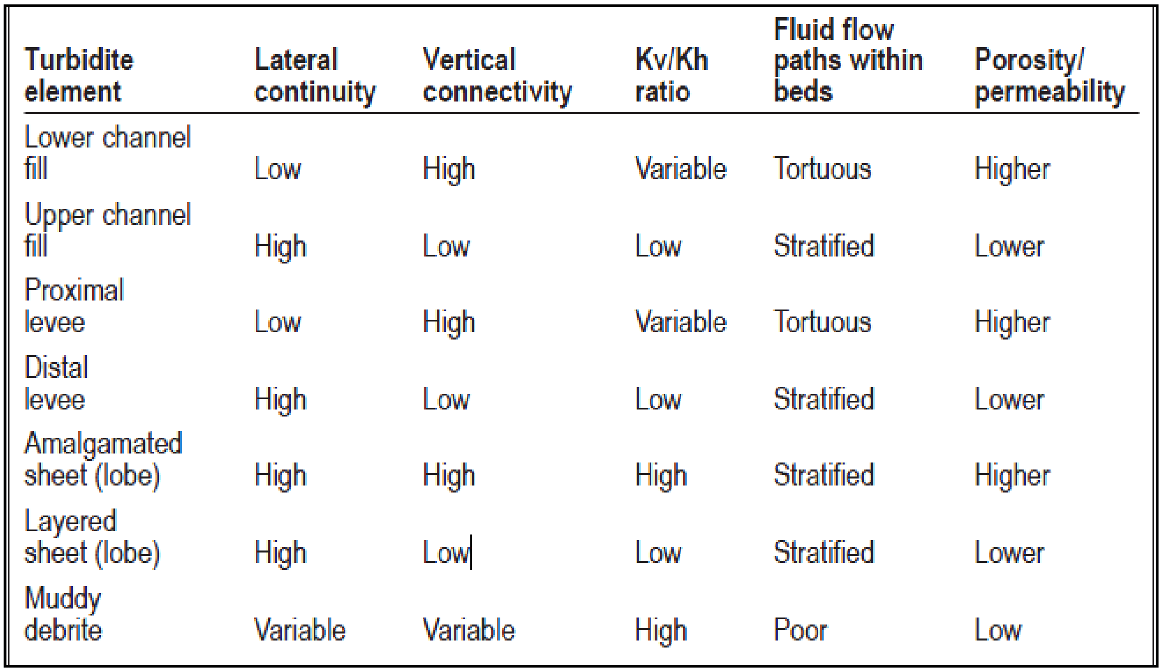

Turbidite element	Lateral continuity	Vertical connectivity	Kv/Kh ratio	Fluid flow paths within beds	Porosity/ permeability
Lower channel fill	Low	High	Variable	Tortuous	Higher
Upper channel fill	High	Low	Low	Stratified	Lower
Proximal levee	Low	High	Variable	Tortuous	Higher
Distal levee	High	Low	Low	Stratified	Lower
Amalgamated sheet (lobe)	High	High	High	Stratified	Higher
Layered sheet (lobe)	High	Low	Low	Stratified	Lower
Muddy debrite	Variable	Variable	High	Poor	Low

Table 4.1: Qualitative continuity, connectivity, and reservoir quality of selected turbidite facies. (after Williams and Slatt, 1998)

The trend in the planning and development of turbidite reservoirs is to drill as few wells as possible, develop these wells with high rates and high ultimate recoveries, and to have little or no intervention planned once production begins (Weimer and Slatt, 1999b). The use of high resolution 3D and 4D seismic, horizontal wells development, reservoir simulation and 4D quantitative reservoir monitoring provided engineers with powerful tools to achieve these goals. As more discoveries are made and developed, understanding of turbidite reservoirs is improving and as a consequence, ultimate recoveries and well production rates.

4.4 The Ainsa II turbidite system

In turbidite reservoirs, key components that must be understood for reservoir characterisation include facies types and probable diagenetic alteration, as well as the vertical stacking patterns associated with high-frequency cycles. At this scale (i.e. meter scale) the fundamental controls over fluid-flow behaviour in the reservoir are commonly exerted. A good understanding of these cycles in the subsurface can be highly challenging as obtaining a sufficient amount of information could prove time and money consuming or simply technically not possible. Philip (1991), states: *"From the viewpoint of natural science, and indeed from any viewpoint concerned with the truth, a disquieting aspect of computer-based modelling is the gap between the model and the real-world events. There is reason to fear that the gap will not grow smaller and that worry about it will ultimately just fade away"*.

It is here that outcrop analogs provide valuable insight into the understanding of the boundaries and internal facies distribution of these high-frequency cycles.

4.4.1 Regional geology

During the early to Mid Eocene the Ainsa Basin developed as a piggyback basin on the propagating frontal thrust belt of the evolving Pyrenees (Fontana et al., 1989; Bentham et al., 1992; Dreyer et al., 1999; Pickering and Corregidor, 2000). The deep-water systems deposited in the Ainsa Basin were confined between two structural highs, which today are expressed as anticlines (Pickering and Corregidor, 2005). The fill of the basin is approximately 4000m thick and constitutes an overall regressive unit (Thurmond et al., 2008). The lower part of the basin contains slope deposits (San Vicente Formation). This formation is mud-dominated but includes several clastic turbidite systems (e.g. Gerbe-Banaston, Ainsa, Morillo, Figure 4.5). In this study, we focus on one of the three channel- complexes in the Ainsa turbidite system (Figure 4.5), the Ainsa II system. The facies distribution and large-scale geometry of the Ainsa II turbidite system may resemble depositional elements observed in complex turbidite systems offshore Angola.

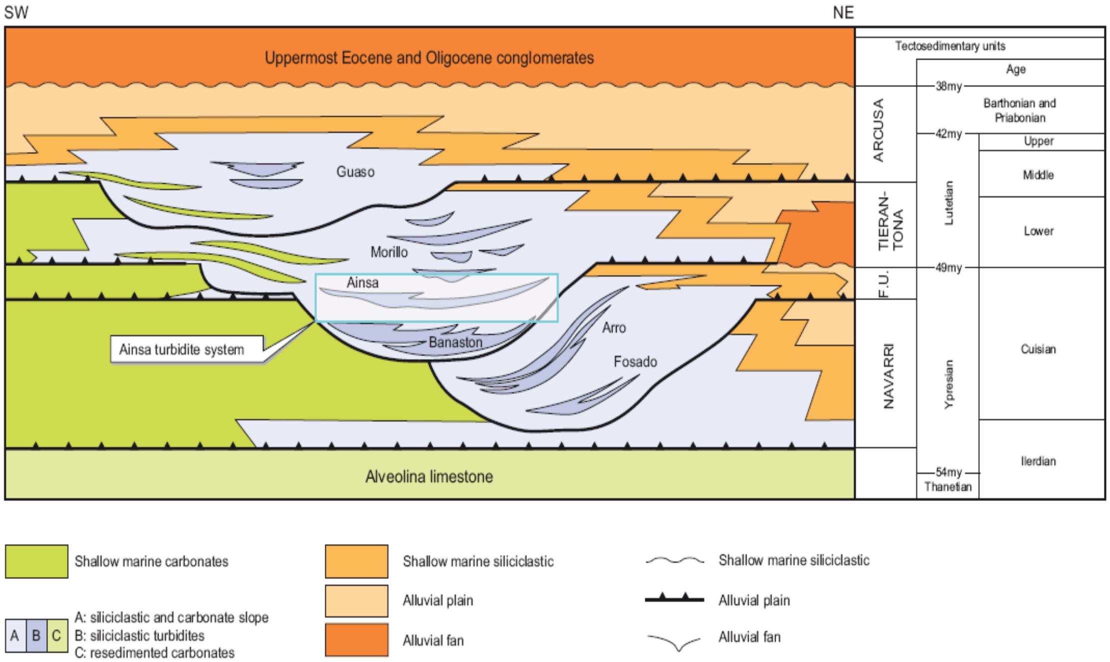

Figure 4.5: Stratigraphic cross-section of the Ainsa basin deposit (after Bakke et al., 2007)

4.4.2 The Ainsa II outcrop model

The Ainsa II outcrop model was provided by the Genetic Units Project (GUP). The original 2D model was derived from an outcrop photo-panel with a special care to include all the fine scale heterogeneities characteristic of deep water turbidite systems. The model was extended to the third dimension in order to perform fluid flow and seismic studies. The resulting 3D model consisted of 2,600,000 cells and is considered to be very fine scale as the cells are 5 meter long horizontally, in both the X and Y direction and 0.5 meter vertically. The model consisted of 5 channels, stacked both on the lateral and vertical directions and enclosed into a shale background (Figure 4.6). Three types of facies were defined: sand, shale, and debris flow (Figure 4.7). The shale background (displayed in grey in Figure 4.6) properties were modified to define an extra facies with moderate porosity and permeability to be used as an aquifer in fluids flow simulations.

Figure 4.6: A cross section view of the fine scale Ainsa II channels

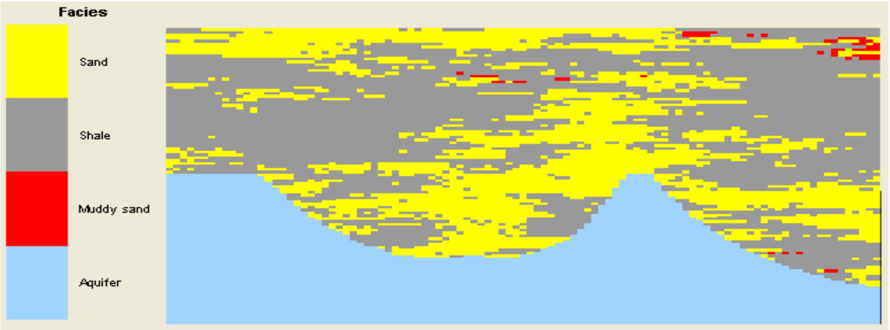

Figure 4.7: Facies of the Ainsa II Model

Facies	**NTG (frac)**	**Porosity (frac)**	**PermX (mD)**	**PermY (mD)**	**PermZ (mD)**	**Saturation table number**
Sand	**1**	**0.3**	**1500**	**1500**	**1500**	**1**
Debris Flow	**0.4**	**0.15**	**200**	**200**	**200**	**3**
Shale	**0**	**0.01**	**0.1**	**0.1**	**0.1**	**2**
Aquifer	**0.35**	**0.2**	**600**	**600**	**50**	**4**

Table 4.2: Rock properties for the Ainsa II Model

The five channels were populated with rock properties representative of the Girassol field offshore Angola (Table 4.2). Figure 4.8 shows a cross section of the model with the Net to Gross displayed.

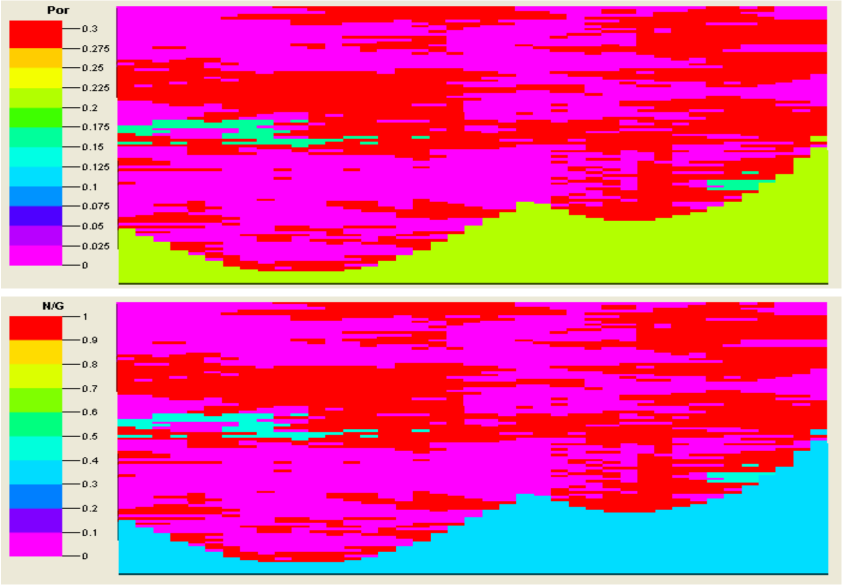

Figure 4.8: Porosity and Net to Gross cross section from the AINSAII geological model

4.4.3 The Ainsa II simulation model

For the purpose of this study, the original geological 3D model was up-scaled in the horizontal directions by a factor of 2.5, the thickness of the cells remained unchanged (0.5 meter) reducing the number of cells to 420,000 cells 12.5 meter long each. The reservoir model is 1262.5 meter long, 512.5 meter wide and 51 meter thick. The top reservoir was set at a depth of 2240 meter. The original OWC was set at 2270 meter.

Two vertical water injectors were put on one side of the model and three producers on the opposite side. The five wells were completed across the whole reservoir's thickness. (Figure 4.9)

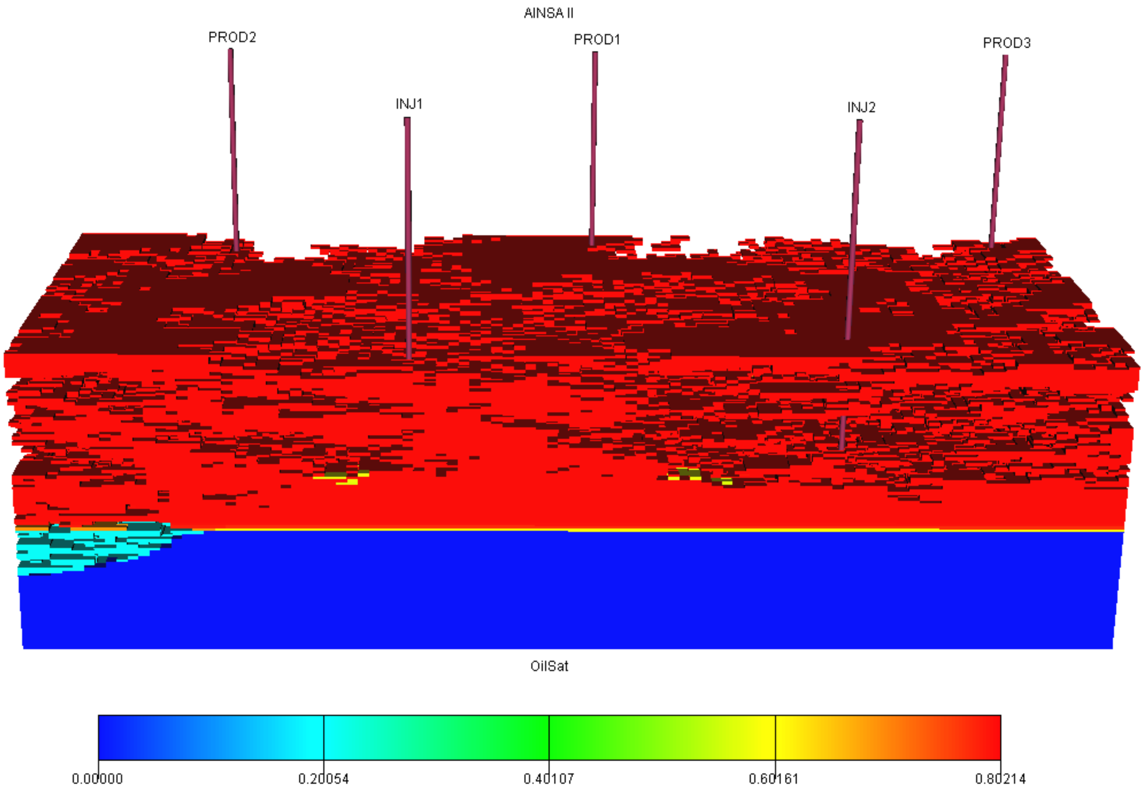

Figure 4.9: The Ainsa II simulation model. Initial oil saturation is displayed.

A set of relative permeability and capillary pressure curves was defined for every facies (Figure 4.10) and used for the simulation. Light oil (33º API) with an average viscosity of 1.5 cpoise was used. The Waterflooding was run under favourable conditions (mobility ratio =0.3 in sand). The simulation was run for 800 days with reports written every 40 days. The control mode was set to Bottom Hole Pressure (BHP) for both injectors and producers allowing a maximum pressure change of 20 bars during production. At the start of Waterflooding, the water displaces the oil in a piston like manner, forming a sharp waterfront, due mainly to the Waterflooding being applied under favourable conditions; i.e. a mobility ratio <1. But as the water injection continues, the water slumps down and follow some preferential pathways. The fact the water was not injected with much higher pressure than the original reservoir pressure led to the gravity effects to take over hence the water slumping into the lower part of the reservoir.

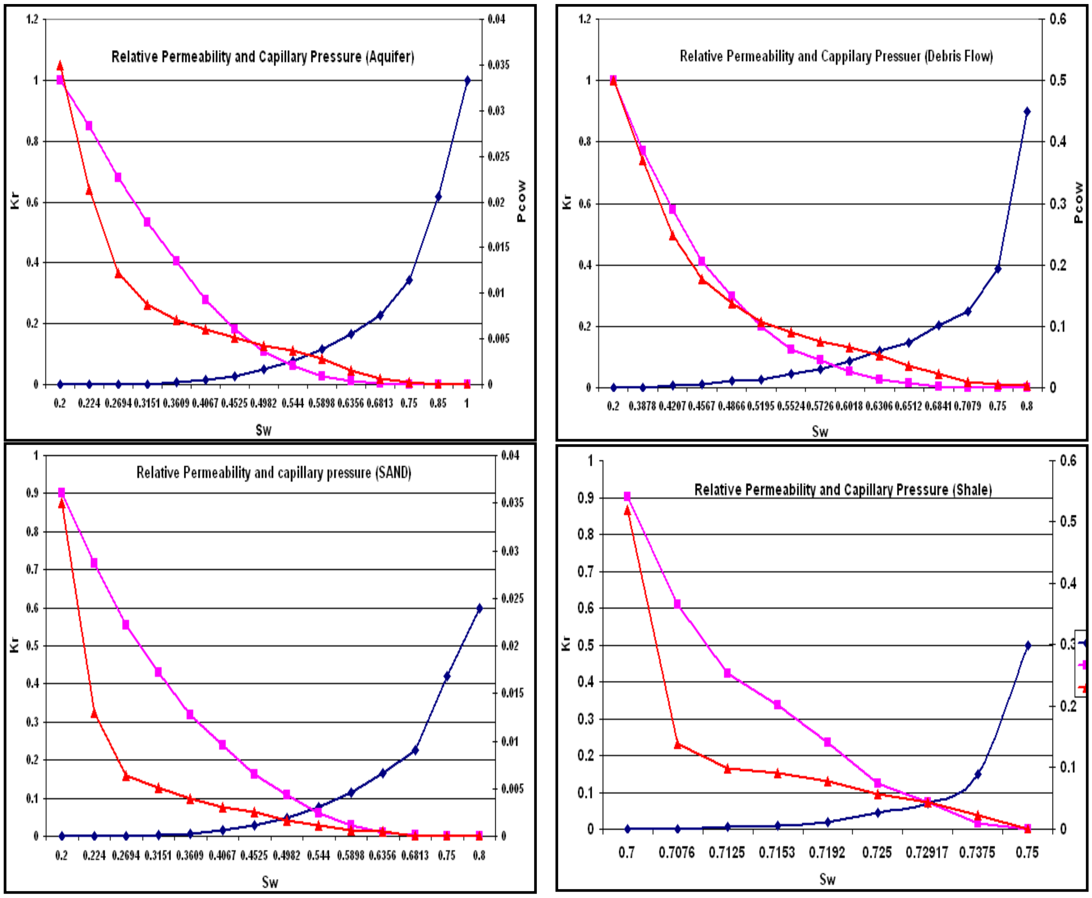

Figure 4.10: Relative permeability and capillary pressure curves used in the simulation

Figure 4.11 shows the oil saturation in a cross-section of the reservoir model, where the water injector INJ1 was placed, at different time steps of the Waterflooding. Figure 4.11-a shows the original oil saturation (before production), 4.11-b after 40 days, 4.11-c after 200 days and 4.11-d after 800 days.

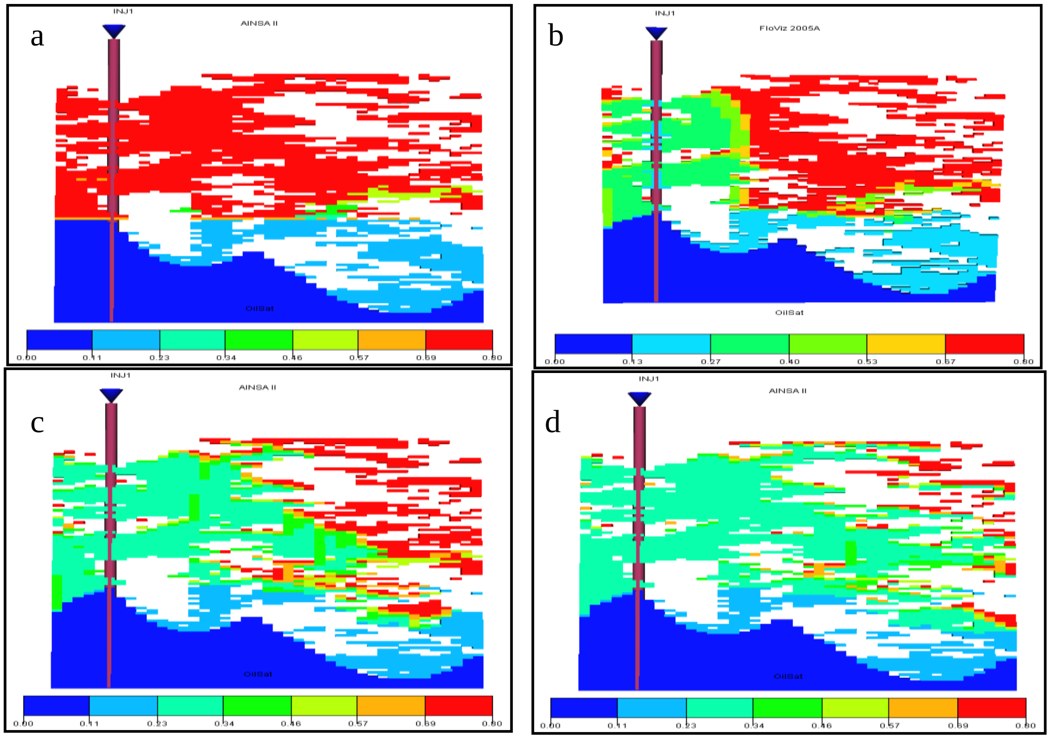

Figure 4.11: Oil Saturation before the start of production, after 40 days, 200 days and 800 days of Waterflooding

The shale cells were defined as inactive cells in the simulation model meaning that there is no fluids flow in the shale. The water flow is affected by those intra-reservoir shales and develops a complex waterfront directly linked to the facies distribution in the model Figure 4.12 shows the facies at the two water injectors INJ1 and INJ2 locations. It is clear that the injector INJ1 is more efficient in displacing oil toward the producers as it is completed across several high pay layers, while the well INJ2 will be injecting mainly in the aquifer. Lateral connectivity also has a major impact as of the radius of influence of the two wells.

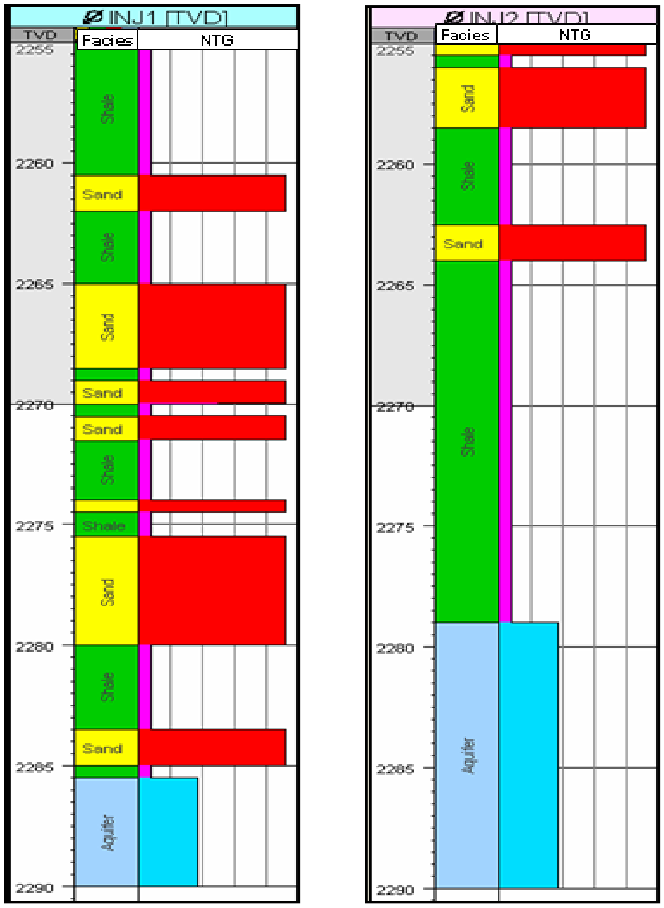

Figure 4.12: Facies and Net to Gross distribution at water injector wells INJ1 and INJ2 locations.

Figure 4.13 shows facies distribution at different layers of the reservoir model. The yellow colour represents the sand and the channelized nature of the reservoir is clearly shown. The lateral connectivity between the different wells in the model is highly variable with depth, resulting in a highly heterogeneous waterfront both in the vertical and lateral direction. Our study aims at understanding the 4D signatures of such complex waterfront.

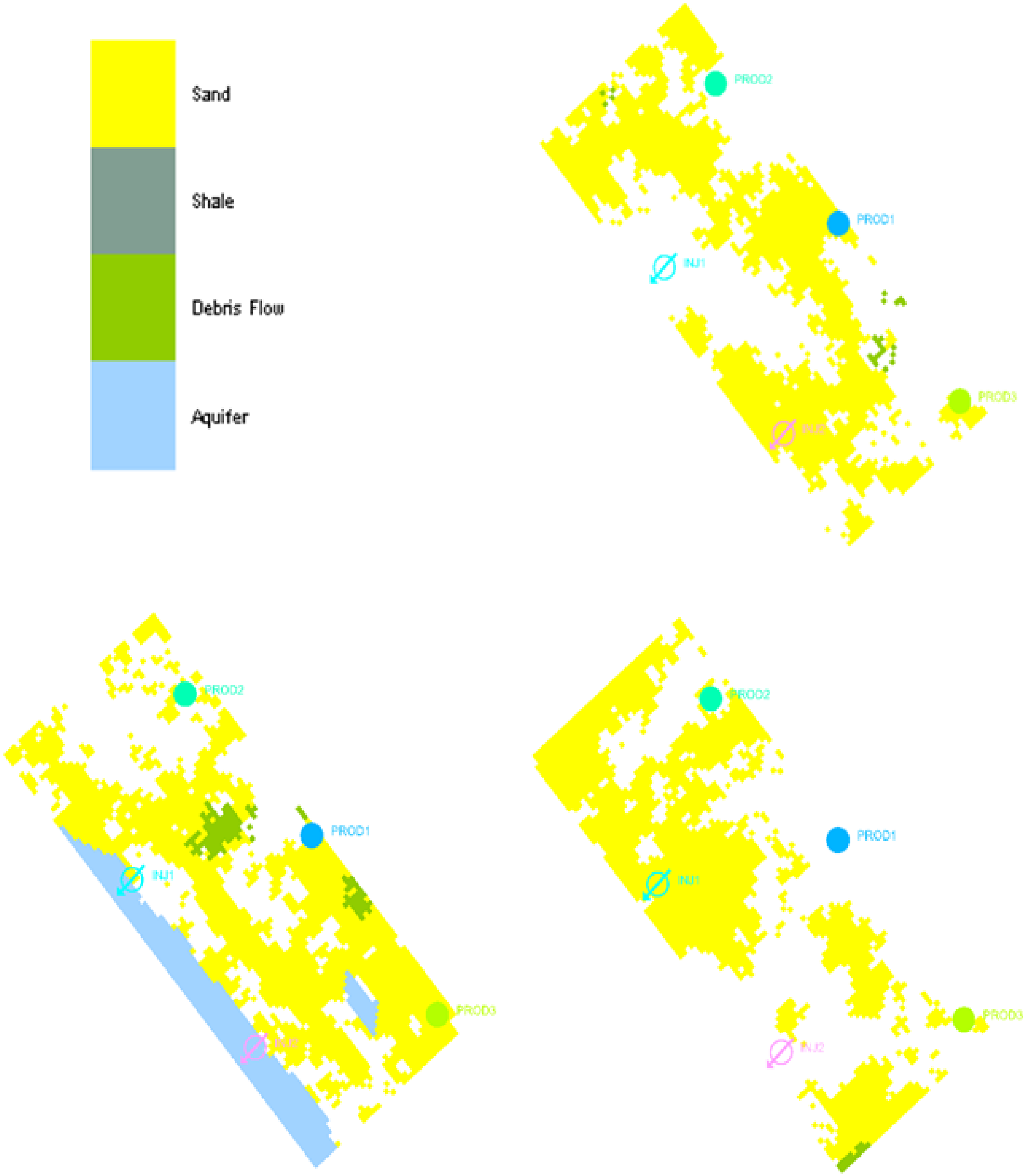

Figure 4.13: Facies distribution: a) top reservoir, b) layer 26 and c) layer 60

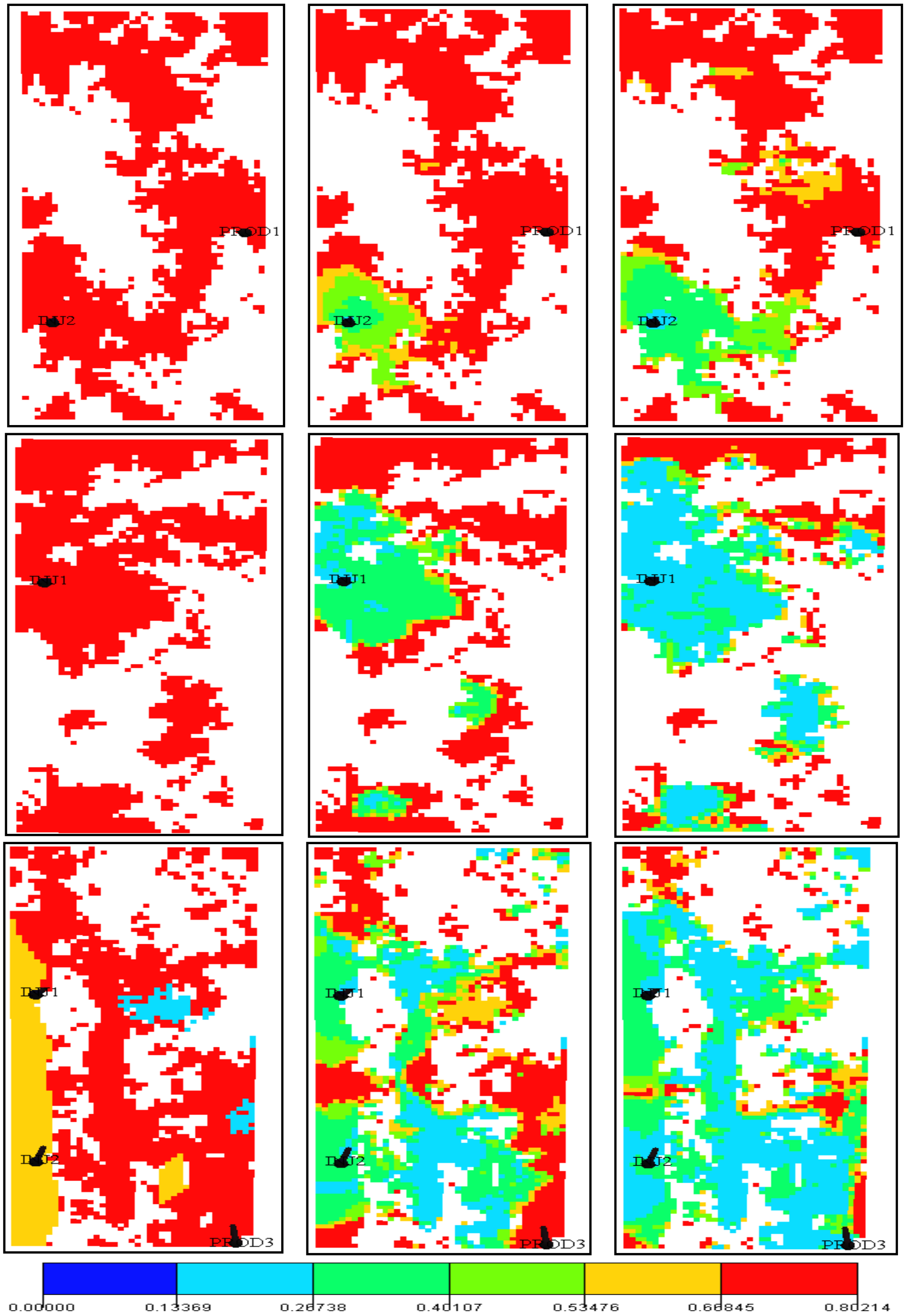

Figure 4.14: Oil saturation across three different layers of the reservoir model, from top to bottom: layer 1, layer 26 and layer 60. From left to right: pre-production, after 200 days and after 800 days of Waterflooding

Figure 4.14 shows the oil saturation at three different stages of Waterflooding, at different layers of the reservoir model. The injected water will flow into the sand bodies, following some preferential pathways and forms a heterogeneous waterfront highly affected by shales as flow barriers. At the end of Waterflooding, several bypassed oil pockets are left in the flooded areas; our study will also investigate the detectability of these zones with time-lapse seismic. Four time steps were selected to be studied: before the start of production (time step 1), after 200 days of Waterflooding (time step 2), after 400 days of Waterflooding (time step 3), and after 800 days of Waterflooding (time step 4).

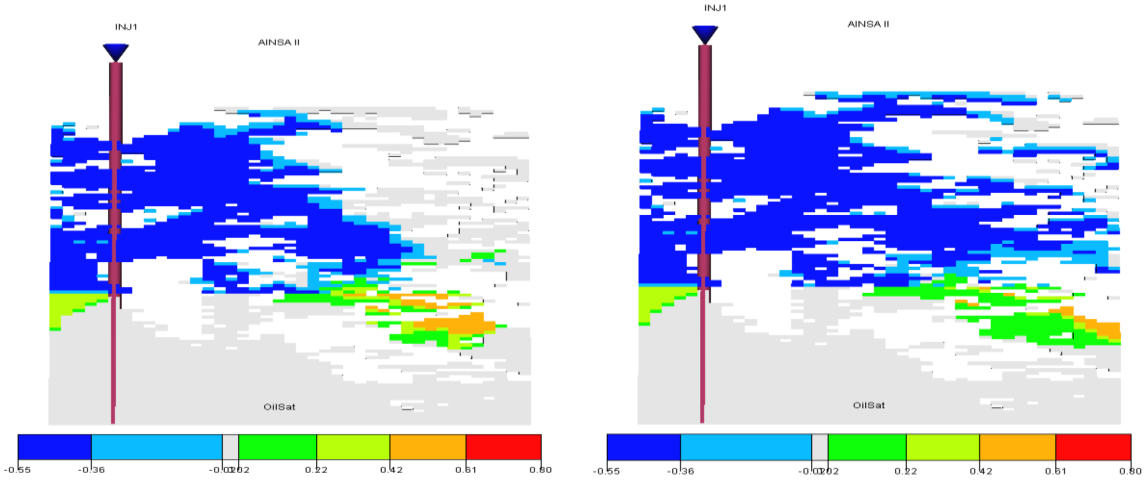

Figure 4.15: Oil saturation difference between time step 2 and 1 and time step 3 and 1.

Figure 4.15 shows the progression of the waterfront with continuing water injection. The OWC movement is rather steady and homogeneous, but as the cells are very thin (0.5 meters) the waterfront presents finger-like heterogeneities below seismic resolution. The positive oil saturation changes occur mainly below the OOWC at the very early stages of Waterflooding as oil slumps down and is trapped there even at the end of Waterflooding. The well displayed in Figure 4.15 (INJ1) is also injecting into the aquifer (below OWC). Figure 4.16 shows the pressure change around well INJ1. The pressure gradient smoothly decreases as we travel away from the injectors toward the producers. Due to our initial setting for the simulation, the pressure changes remain low (maximum 16 Bars).

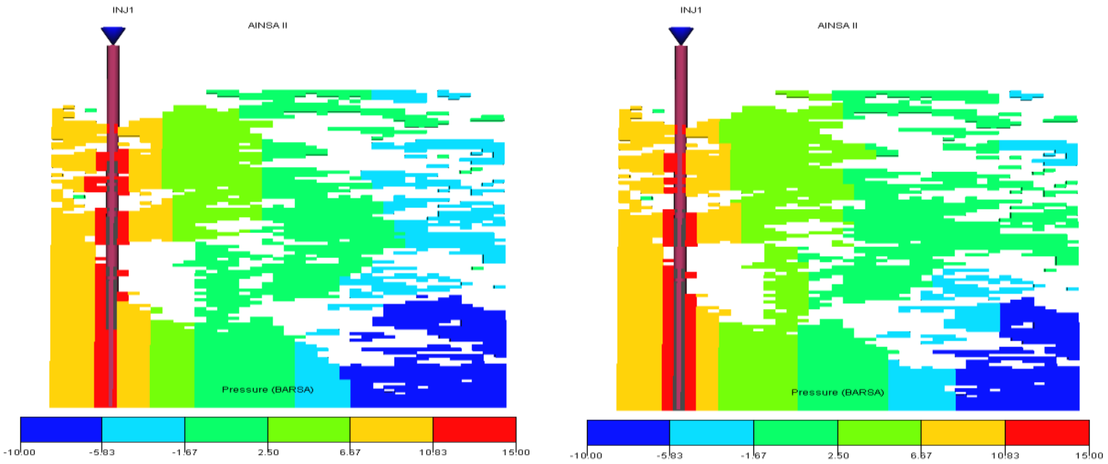

Figure 4.16: Pressure difference between time steps 2 and 1 and time steps 3 and 1. The smooth gradient of pressure change across the reservoir indicates that the reservoir is not compartmentalised. The different channels within the model are dynamically communicating.

4.5 Conclusion

Turbidite systems are major reservoirs in many sedimentary basins in the world. Exploration and production in deepwater and ultra deepwater is growing rapidly even though it remains an immature frontier, with many deepwater sedimentary basins being explored only lightly.

Turbidite reservoirs are quite variable and some of this variability can be predicted from seismic data, whereas other variations can only be detected with well data or during production. Technical and economic success will be based on the accurate prediction of the occurrence and identification of the characteristics of turbidite reservoirs.

Reservoir simulation has become an important tool in predicting the performance of turbidite reservoirs and to plan for reservoir development. Simulation models help provide timely reservoir development answers for fast-track projects (Smith, 1998).

Reliable simulation models are critical for Waterflooding projects and require good geologic model that captures the heterogeneity of the reservoir (Weimer and Slatt, 1999b).

Quantifying the heterogeneity of turbidite reservoirs for simulation is difficult and accounts for the use of geostatistical models. Continuity of gross turbidite intervals can be obtained from 3-D seismic horizon slices, as well as from interference and pressure tests. Quantification of bed thickness, connectivity, and reservoir quality can be accomplished from well information, but accurate prediction of these features away from the well is not wholly reliable using conventional wireline logs. Subtle features on dipmeter logs or borehole imaging tools may provide information on lateral attributes.

Outcrops, where sufficiently continuous, can provide the necessary quantitative lateral attributes of turbidite strata and can bridge the gap between wireline log and seismic scales.

An outcrop based reservoir model was built to simulate Waterflooding in turbidite reservoirs. The fluid flow simulation showed that the water will flow in some preferential pathways controlled by the reservoir internal geology. Permeability values and NTG distribution play a major role in the advance of the waterfront inside the reservoir and control its shape and location. Indeed, reservoir heterogeneities create a fractal-like waterfront surface that can vary greatly across the reservoir, both horizontally and vertically. Waterflooding simulation in a highly heterogeneous turbidite clearly showed the critical impact reservoir's heterogeneities (heterogeneous permeability and net-to-gross distribution) on sweep efficiency and recovery factors. By the end of the Waterflooding simulation, 80% of the oil in place is recovered, but the injection of several pore volumes of water was necessary to achieve this recovery factor, mainly due to the reservoir internal heterogeneities.

Chapter 5

Numerical modelling of Waterflooding in turbidite reservoirs and simulator to seismic study

In this chapter, petrophysical simulation results performed on the AINSAII simulation model output are discussed. Synthetic seismic was created for a set of three different dominant frequencies. Interpretation of 3D and 4D seismic signatures of Waterflooding is carried out on each seismic set. Resolution issues were addressed.

5.1 Introduction

Geoscientists share a common interest in investigating and characterizing the geological subsurface as accurately as possible. Hydrocarbon reservoirs are generally composed of irregular geological units with distinguishing characteristics. The boundaries between units create discontinuities that are further complicated by faulting, erosion and deposition. Within this heterogeneous complexity, geoscientists aim to develop a good understanding of the geological setting of the reservoir of interest.

Due to the limitation on the amount of information available to geoscientists in order to develop such an understanding, computer modelling is used to build geological models integrating all the available data and being as representative as possible of the real conditions in the subsurface. The accuracy of the geological model is crucial in the sense that these models are up-scaled in a later stage in order to simulate fluids flow within the reservoir as a tool to forecast future performance of the reservoir, a valuable tool in the assessing of the efficiency of the production scenarios proposed and gives a good estimate of the possible cost of such scenarios.

The development of a geologically constrained reservoir model and subsequent up-scaling of the model for reservoir simulation depends on critical input parameters defining both the geometrical attributes and distribution of the targeted facies. Integration of geologically based elements is a fundamental step in the characterisation of the probable vertical and lateral distribution of reservoir facies in the subsurface. Such a geologically based model will increase our understanding of reservoir heterogeneities and provides the foundation to build accurate simulation models.

In this study, an outcrop model was used to address uncertainty in recovery and sweep efficiency of Waterflooding in deep-water channelized reservoirs. Three dimensional heterogeneities were added to the outcrop model as they are of high importance for flow simulation and seismic studies. The results from the flow simulation were used in the petrophysical modelling to compute values of V_p, V_s and Rho at different time steps and in every grid cell. 3D Synthetic seismic cubes were created for 4 time steps corresponding to 4 different stages of Waterflooding. 3 different dominating seismic frequencies were modelled in order to investigate the effects of seismic resolution on the interpretation of the time lapse signature of Waterflooding in geologically complex turbidite reservoirs.

5.2 Petro-elastic modelling results

Gassmann (1958), Batzle and Wang (1992) and MacBeth (2005) equations were used in the transformation from the engineering domain (pressure and saturations distributions across the reservoir) to the petro-elastic domain (Vp, Vs and Rho).

Figure 5.1 shows the relative changes in density, P-wave and S-wave velocities and impedances after 200 and 800 days of Waterflooding. The displayed cross-section is extracted at one water injection well location. The magnitude of changes was the same after 200 days and 800 days of Waterflooding; i.e. the maximum P-wave velocity (for example) was 4% at the two time steps. The percentage of change is directly linked to the water saturation change in the reservoir. As the water is injected into the reservoir, it pushes away the oil and occupies the vacant pore volume left when the oil has moved. The changes from a fully oil saturated rock to a fully water saturated rock (irreducible saturations) happens gradually and not all the saturation changes are visible after the petro-elastic transformation.

The changes in P-wave velocity and density follow the same patterns; positive changes in the areas where water saturation increased and negative change where water saturation decreased. These changes are mainly controlled by the changes in fluids saturations rather than pressure; this is particularly visible on the density cubes. This could be explained by the fact that the pressure change, in the absence of any compartmentalisation within the reservoir, is not localised on a particular location inside the reservoir, but it is fairly smooth. Its effect is rather global and would result in a “dimming” or decrease in the magnitude of changes observed in P-wave and density cubes.

The changes in S-wave velocity due to Waterflooding are controlled by both changes in the bulk density of the reservoir rocks after fluids substitution and changes in pore pressure.

It is worth noticing that the shale cells were defined as inactive cells in the fluids flow simulation model, and therefore were assigned the same, constant petrophysical properties (V_p, V_s, and Rho). Changes observed on cross-sections of the modelled V_p, V_s and Rho are those occurring in the sand bodies within the reservoir. As the waterfront progresses, it illuminates new sections of the reservoir giving valuable information about the location of sand bodies within the reservoir, their extent and the degree of their hydraulic communication.

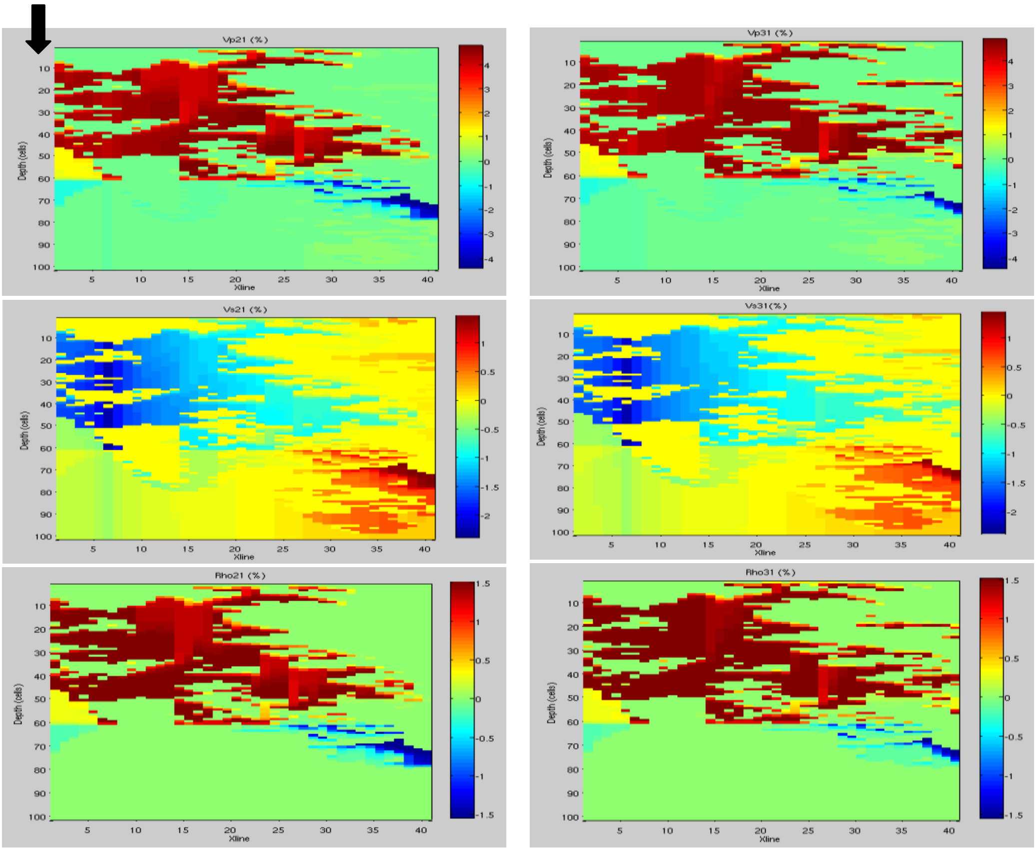

Figure 5.1: Results from the petrophysical modelling after 200 days (left) and 800 days (right) of Waterflooding: (a) Changes in V_p, (b) Changes in V_s, and (c) Changes in Rho. Notice the location of the water injector (Black arrow).

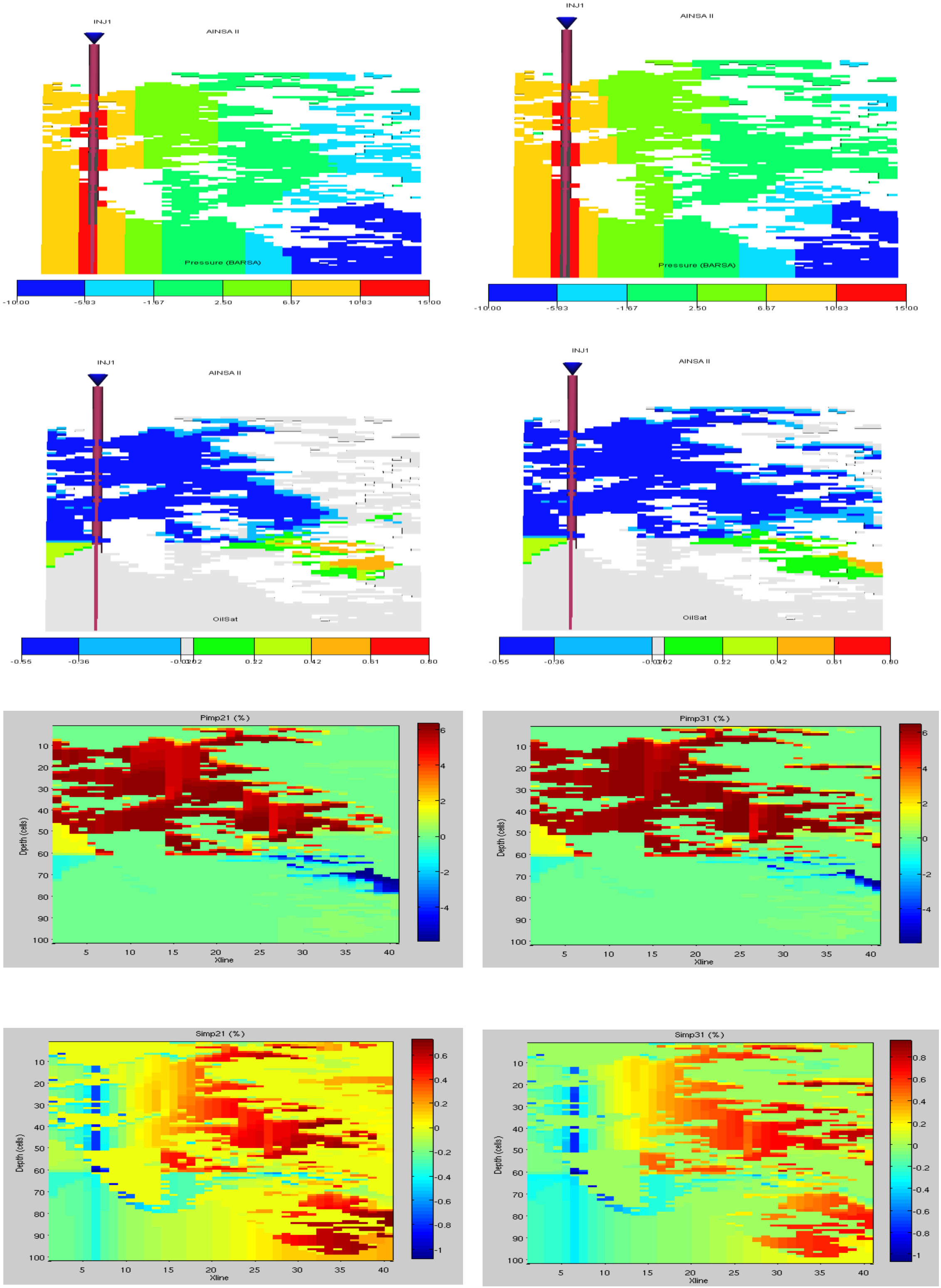

Figure 5.2: Pressure and saturation change after 200 and 800 days of Waterflooding. The corresponding changes in P-impedance and S-impedance.

Figure 5.2 shows the changes in pore pressure and water saturation after 200 and 800 days of Waterflooding and the corresponding changes in P-wave and S-wave impedance. It shows that there is a linear relationship between the changes in fluids saturation and the changes in P-wave impedance. Positive P-impedance change was observed where water replaced oil and negative P-impedance change where the oil replaced the water. The pressure signal seems to be overshadowed by the saturation signal. For the S-wave impedance, the saturation signal is as weak as the pressure signal and S-impedance cross-sections exhibit the effect of both pore pressure and fluids saturation effects.

5.3 Synthetic seismic modelling

The output from the petro-elastic transformation (P-wave velocity, S-wave velocity and density for each time step) is used as the input for the synthetic seismic creation. First, the Zoeppritz equation was used to compute the reflectivity coefficients at each interface. Then, the synthetic seismic is generated as the product of convolution between the reflectivity matrix and a Ricker wavelet.

Vertical seismic resolution is the ability to distinguish separate features. In order for two nearby reflective interfaces to be distinguished well, they have to be about ¼ wavelength in thickness (Rayleigh Criterion) (Figure 5.3).

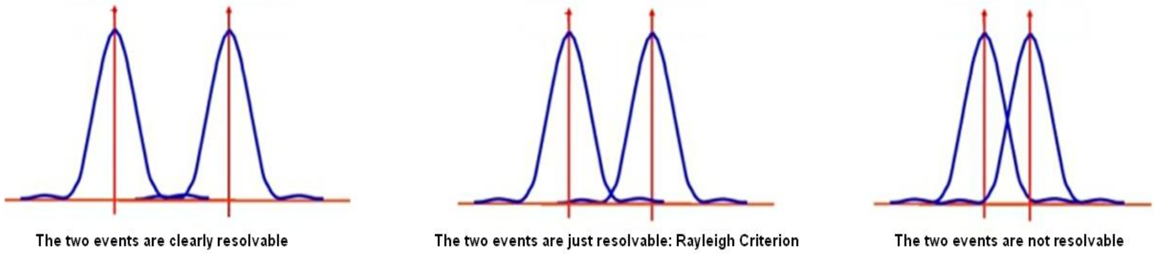

Figure 5.3: Rayleigh Criterion

The wavelength (λ) is defined by equation 4.1

$$V = f \times \lambda; \qquad 4.1$$

Where V is the velocity of the rock, f is dominant frequency of the seismic waves.

The reservoir top was set at 2240 m depth. There is a practical limitation in generating high frequencies that can penetrate large depths as the earth would act as a natural filter removing higher frequencies more readily than the lower frequencies. Three different wavelets were used with three different dominant frequencies, 35 Hz, 62Hz and 125 Hz (Figure 5.4). Figure 5.5 display the velocity distribution in our model. Nearly 90% of our model cells have a velocity comprised between 2200 m/s and 2400 m/s. Table 5.1 lists the different wavelengths for the three different frequencies.

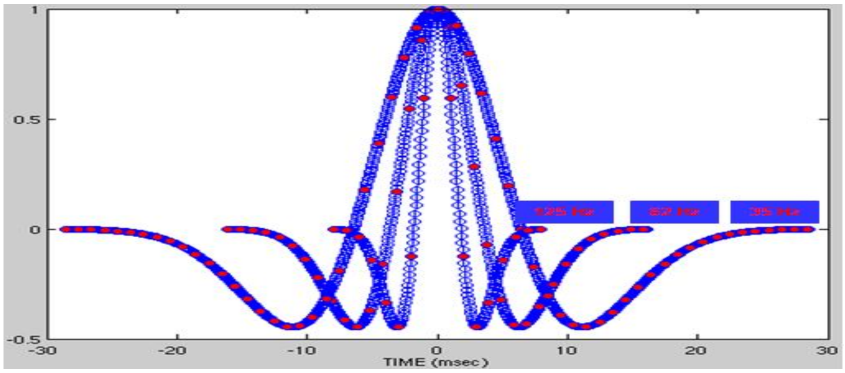

Figure 5.4: Ricker wavelets used in the synthetic seismic creation

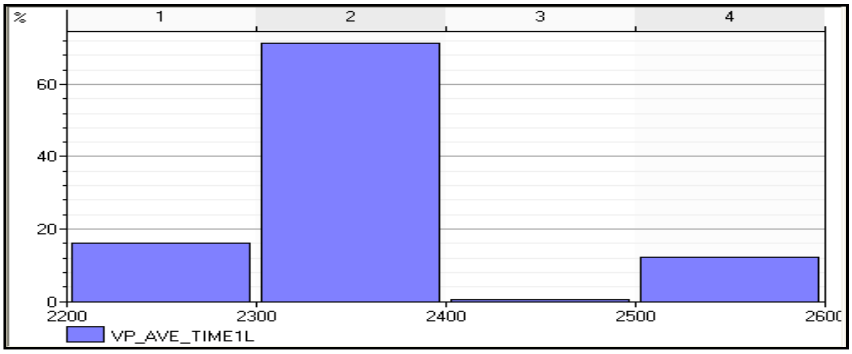

Figure 5.5: Compression waves velocities in the AINSAII model

V **f**	**35 Hz**	**62 Hz**	**125 Hz**
Min: 2200 m/s	62.857 m	35.483 m	17.6 m
Max: 2400 m/s	68.571 m	38.709 m	19.2 m
Average Tuning thickness	16.3 m	9.25 m	4.5 m

Table 5.1: Dominant Wavelengths (λ) used in the creation of the synthetic seismic. The average tuning thickness for every seismic frequency is also listed.

The seismic vertical resolution can be defined as ¼ of the dominant wavelength. The vertical resolutions associated with the three different dominant frequencies are listed in Table 5.2. One can expect a vertical resolution around 15 m with the 35 Hz wavelet, 10 m with the 62 Hz wavelet and 5 m with the 125 Hz wavelet.

f **Vertical Resolution**	**35 Hz**	**62 Hz**	**125 Hz**
High	15.7 m	8.9 m	4.4 m
Low	17.1 m	9.6 m	4.8 m

Table 5.2: Seismic vertical resolutions

5.4 3D seismic interpretation

Synthetic seismic volumes are calculated using a 35 Hz zero-phase Ricker wavelet, and also for 62 Hz and 150 Hz to compare resolution issues. Another set of seismic cubes is generated using a wavelet extracted from the post-stack Girassol seismic data to simulate the observed peak frequency in the Girassol field. As the frequency of the seismic data increases, the vertical resolution increases and different producing sands are resolved separately.

The 35 Hz peak frequency seismic shows a strong positive reflection (peak) at the top of the reservoir and a strong negative (trough) reflection at the base of the reservoir (Figure 5.6). The reflections inside the reservoir are rather continuous and the vertical resolution associated with a 35 Hz peak frequency (15 to 17 meters in our model) fails to pick the channelized nature of the reservoir. The reservoir's rocks were fully oil-saturated above the OOWC while only water exists in the rocks' pore space below the OOWC. The event at the OOWC is a flat-spot reflection but its interpretation remains highly uncertain due to reflections from other geological discontinuities and may require well log data for calibration. The original OWC displayed in cyan in Figure 5.6 was extracted from the reservoir simulation model and added to the seismic section for guidance purposes.

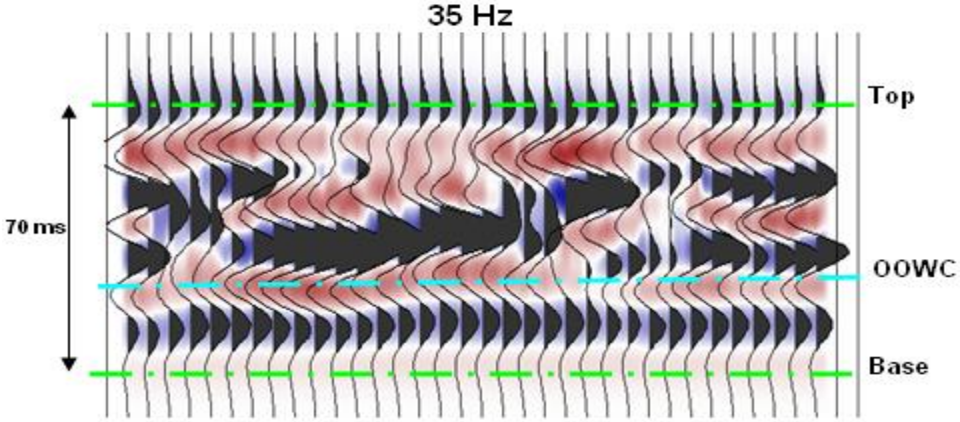

Figure 5.6: Cross-section from modelled seismic with a zero-phase 35 Hz Ricker wavelet. The structural complexity of the reservoir is poorly captured.

With a 62 Hz Ricker wavelet, the modelled seismic has a higher vertical resolution (around 9 meters in our model). Figure 5.7 shows the same cross-section as Figure 5.6 but for the 62 Hz peak frequency seismic. Besides the top and base of the reservoir that are associated with strong continuous reflections, the different channels are visible and different sand bodies can be interpreted directly from the 3D seismic. The increase of the seismic dominant frequency, and the resulting higher vertical seismic resolution, has made stratigraphic interpretation from seismic sections possible. Stratigraphic unconformities are easier to spot and interpret as angularity (onlap, downlap, etc) is more evident. However, the interpretation of the OWC is still challenging.

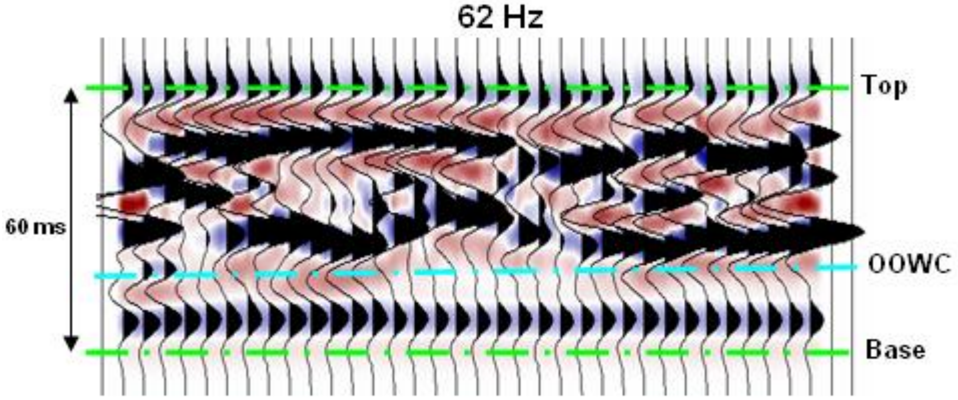

Figure 5.7: Cross-section from modelled seismic with a zero-phase 62 Hz Ricker wavelet. The structural complexity of the reservoir is fairly captured and some channels can be interpreted separately.

The 125 Hz seismic captures the heterogeneous nature of the reservoir. Individual sand bodies are resolved and the stacked channels are clear. Reflections from the OWC can be resolved separately from reflections from other geological interfaces. The aquifer exhibits a fairly strong trough over a peak reflection and can be separately interpreted from the OOWC (Figure 5.8).

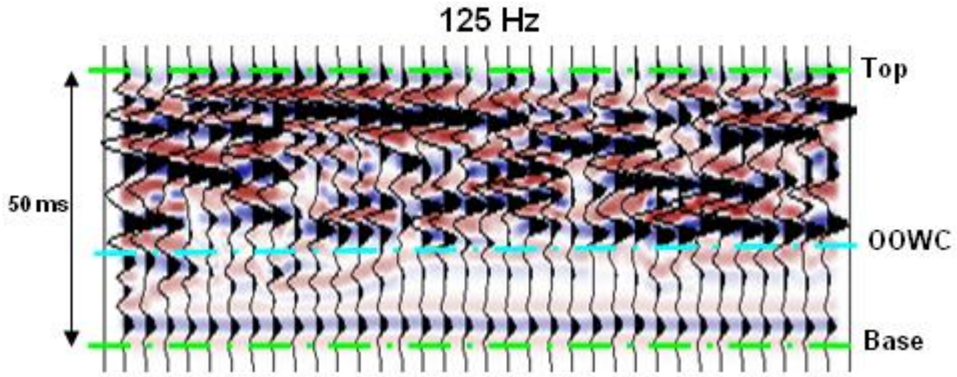

Figure 5.8: Cross-section from modelled seismic with a zero-phase 125 Hz Ricker wavelet. The structural complexity of the reservoir is well captured and different channels can be interpreted separately. Reflections from OOWC and the aquifer can be separately resolved.

The top and the base of the reservoir were picked on the base survey and the two monitor surveys for every frequency set. The Top horizon was picked as a peak on the seismic section whiles the Base horizon as a trough (Figure 5.9).

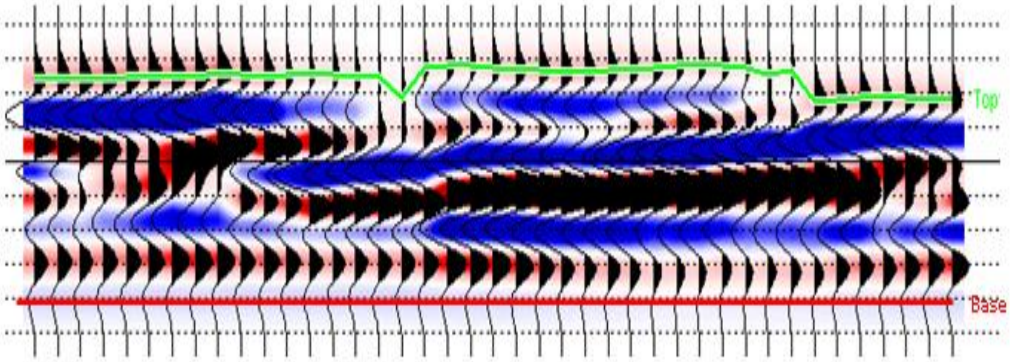

Figure 5.9: Top and Base reservoir picked on the 35 Hz base survey. Peak amplitude was selected to pick both horizons

Isochrones between Top horizon and Base horizon were computed. The velocity of the rock is modelled to be higher in the water-saturated areas. Seismic waves travel faster through water saturated rocks and the thickness-time of the reservoir would be lower in these areas. On an isochron map, the water saturated part of the reservoir would be the “slow” part, represented in blue in Figure 5.10, while the oil saturated part corresponds to the red areas. The isochrone maps computed for the three frequencies follow similar patterns but as the seismic frequency increases, the waterfront is resolved with increasing heterogeneity and it appears less smooth on the 125 Hz seismic than on the 35 Hz seismic. The high frequency seismic also captured the patchy nature of the water distribution inside the reservoir as opposed to the continuous distribution that could be interpreted from the lower frequency seismic. Some of the differences between the isochrones computed for the three different frequencies can be related to differences in the picking patterns of the top and base horizons, performed independently on each data set for every modelled frequency.

The amplitude RMS was also computed between the top and the base of the reservoir for the 3 frequency sets. Figure 5.11 shows the maps corresponding to the pre-production conditions. The three frequencies used during the seismic modelling yield three different RMS amplitude maps for the same reservoir and under the same conditions mainly due to different interferences patterns associated with the different simulated frequencies. The three modelled frequencies have three different tuning thicknesses and tuning effects will be different on each data set.

Interpretation could be challenging in terms of locating water saturated areas and oil saturated areas.

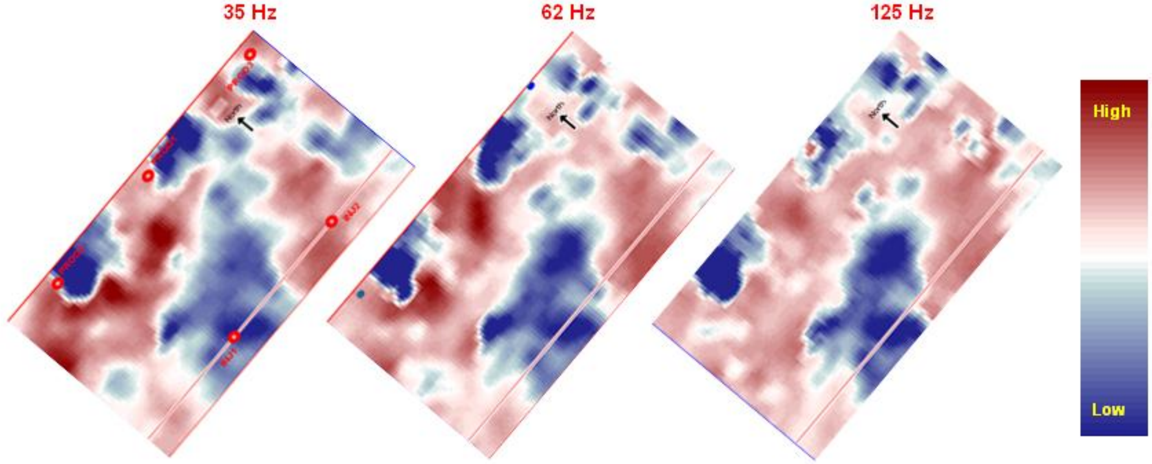

Figure 5.10: Isochrones between picked Top reservoir and Base reservoir for the three seismic frequencies (Base survey)

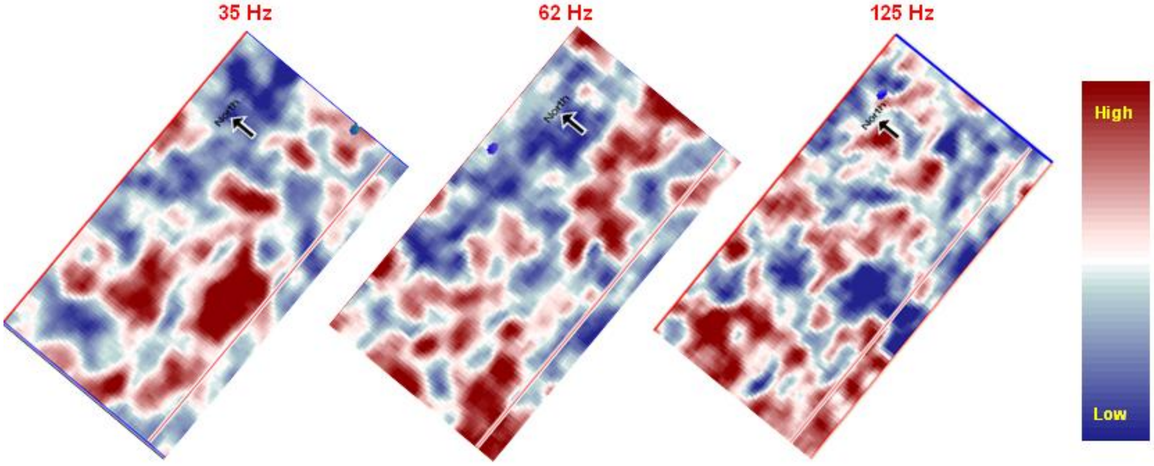

Figure 5.11: RMS amplitude between the top and the base of the reservoir for the 3 different frequencies (Base survey)

The visual correlation between isochrones, RMS amplitude maps and average saturation maps is not straightforward. Rock physical properties, such as velocity and density, were assigned different constant values for every geological facies in the reservoir model; therefore, these properties follow the same spatial distribution within the reservoir.

Figure 5.12 shows an average map for NTG, density, P-wave velocity, and the computed P-wave impedance across the reservoir thickness. It is clear that both the velocity values and the density values follow the same trend, also visible in the resulting impedance map. Areas of high P-wave velocity correspond to areas with low density and low P-wave impedance. The contrast between the density of shale and the density of sand, the two dominant facies in our model, is much higher than the contrast between the P-wave velocity of those two rocks and would control the magnitude of the P-wave impedance.

The channelized nature of the reservoir is clearly visible on the NTG map, but it is harder to imply on the velocity, density or impedance maps. This is mainly because velocity and density values at a specific location are affected by both the geology and the fluid saturations and pressure within the rock pores. Figure 5.13 shows average maps of pressure and water saturation across the reservoir thickness. The pressure variations are smooth, and one can assume that the pressure is constant across all the modelled geological facies. The water saturation is patchy with some localised high or low values. The P-wave impedance is then controlled in a large scale by the geology, as it follows the trend of the high NTG channels and in a more localised scale by the water saturation.

The seismic amplitude polarity and magnitude at a specific reflector are controlled by the contrast between the P-wave impedance values at each side of this reflector. This contrast is controlled by both the stratigraphic variations and the fluids content in the reservoir; therefore, amplitude variations are controlled by those two factors. Travel time of a seismic wave is controlled by the velocity of the rock the wave is travelling through which in turn is geology and fluids dependant.

Both attributes carry information about the stratigraphic variations of the reservoir and the fluids within its rocks' pores, and both attribute respond to these two factors in a different way. By working on 4D seismic data, one hope for the geology effects to be cancelled out and only changes related to the dynamic conditions of the reservoir would remain.

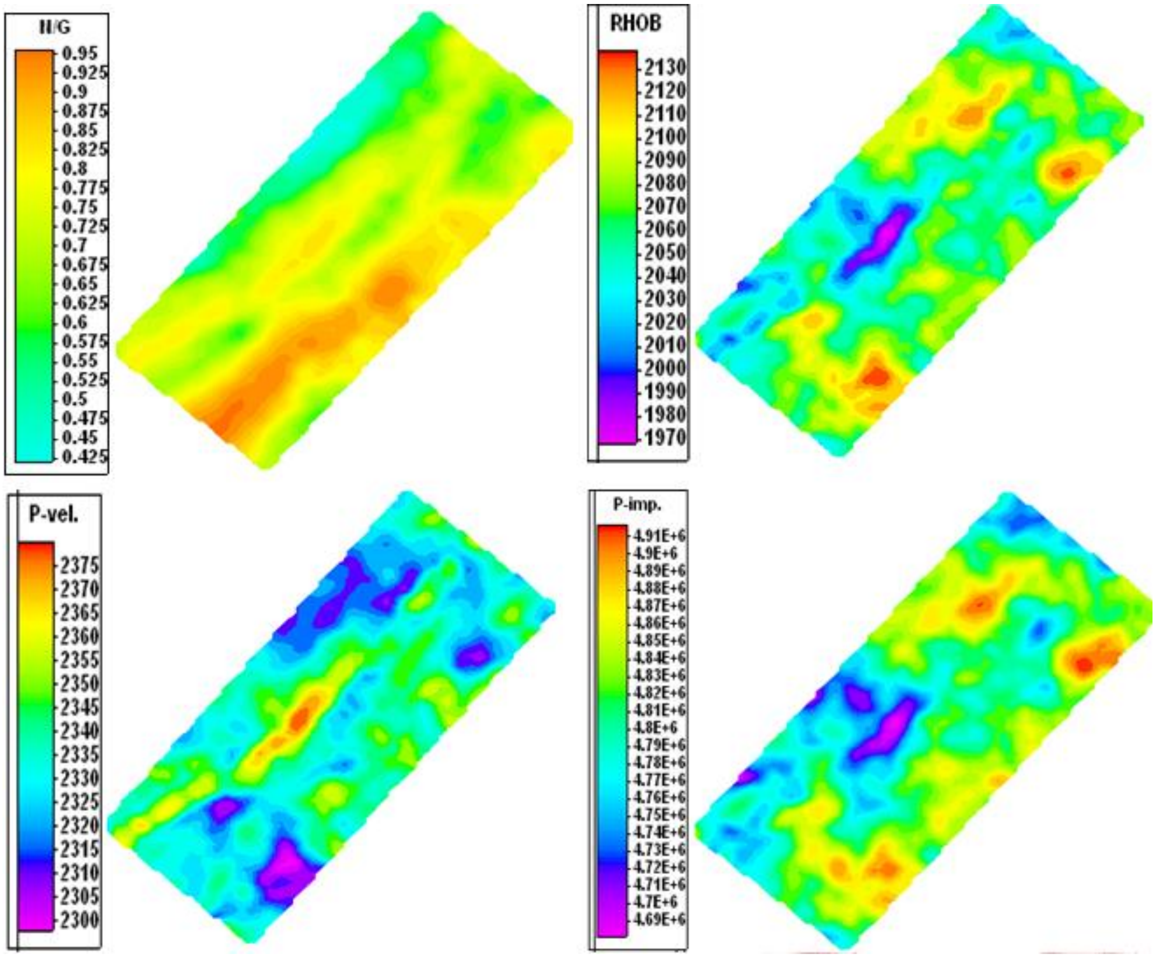

Figure 5.12: Average maps for NTG (top left), density (top right), P-wave velocity (bottom left), and P-impedance (bottom right) before Waterflooding

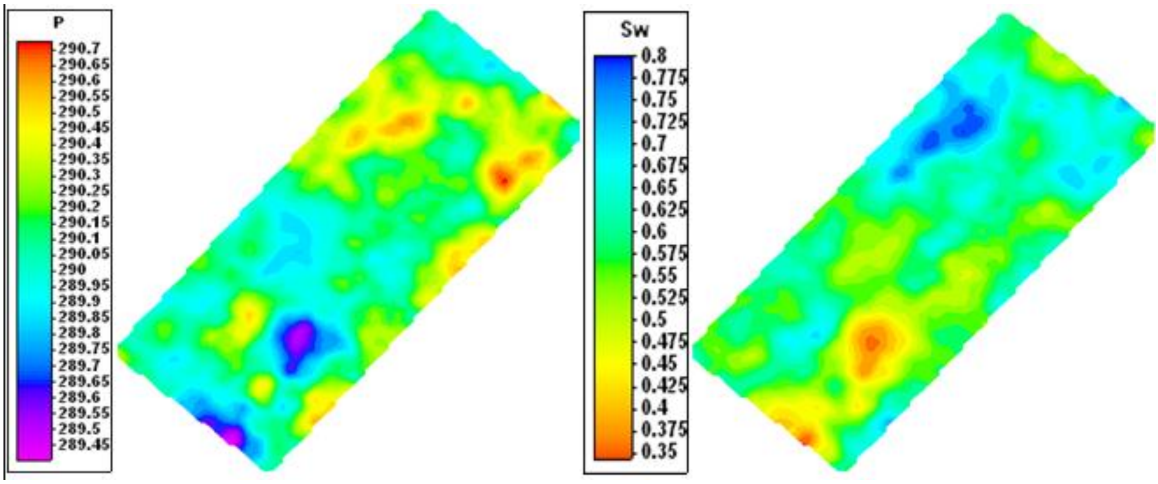

Figure 5.13: Average maps for pressure (left), and water saturation (right) across the reservoir thickness.

5.5 Time-lapse seismic analysis

Time-lapse seismic was computed as the difference between the monitor survey and the base survey. We had 3 different 4D seismic cubes corresponding to three different calendar times for every modelled frequency. Figure 14 shows three cross-sections from the three modelled time-lapse seismic. The 4D seismic cubes from which those sections were extracted were computed as the difference between the first monitor survey (shot after 200 days of Waterflooding) and the base survey.

The presence of intra-reservoir shales acting as flow barriers cannot be inferred on the 35 Hz seismic which displays smooth and even reflections at the OWC (peak over a trough). As the seismic dominant frequency increases, the 4D signature becomes more complex as more reservoir heterogeneities are revealed. The waterfront becomes increasingly uneven and different flooded areas are resolved separately. This is particularly visible around water injector INJ2, where due to the presence of shale at the vicinity of this well, the water spreads into two thin layers 4 to 5 meters thick each, leaving the low NTG areas unchanged. The 62 Hz and 125 Hz manage to highlight this behaviour and give different 4D signature from the 35 Hz seismic.

The 35 Hz time-lapse seismic exhibits two distinctive reflections: at the top of the swept zone (trough over a peak) and at the bottom of the swept zone (peak over a trough) highlighting areas where the movable oil, or a part of it, was displaced by the advancing water. However, seismic sections fail to reveal the highly uneven waterfront. Comparing those sections to water saturation sections, computed at the specific calendar time when the monitor was shot, shows that time-lapse seismic gives, even at low seismic resolution, a fairly good indication about the location of the fluid contacts and the shape of the waterfront but fails to capture the heterogeneous nature of the water distribution within the reservoir (Figure 5.14).

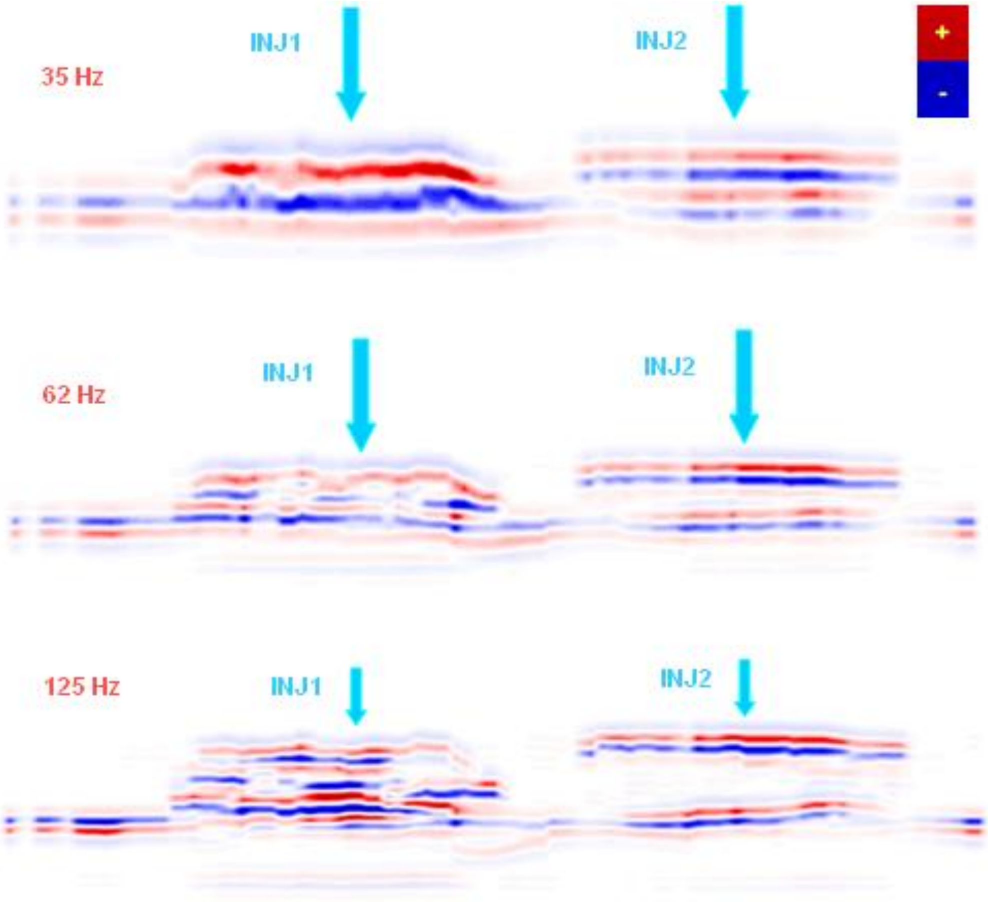

Figure 5.14: Cross-sections for the three modelled frequencies. From top to bottom: 35 Hz seismic, 62 Hz seismic and 125 Hz seismic. More details are exhibited as the frequency increases, highlighting the complex geology of the reservoir and an uneven waterfront. Notice that the lower frequency seismic did not capture the heterogeneous vertical distribution of the water, but still gave similar indication about the shape and location of the waterfront as the one inferred by the higher frequency seismic.

Figure 5.15 shows the water saturation around water injectors INJ1 and INJ2 and their corresponding 4D signatures. It is clear that the reservoir internal heterogeneity and rock properties are controlling the speed and direction of water progression inside the reservoir (mainly NTG and permeability in our model). Well INJ1 and INJ2 display two very different saturation profiles at the time of the first monitor (after 200 days of Waterflooding) and as a consequence, two different 4D signatures. The water spreads in a rather homogeneous fashion around well INJ1 developing a bell shaped waterfront. But due to the low NTG values around well INJ2, the water progressed into two thin layers, at the top of the reservoir and right above the OWC, leaving the areas with low

NTG and low permeability unswept. This is not visible on the time-lapse seismic sections. During the Waterflooding process, a part of the oil slumped down below the OWC and into the oil leg. This is illustrated by the negative change in water saturation in Figure 5.13. On a seismic section, it looks like a trough over a peak (P-wave impedance decreases as the water is replaced by oil within the rock pores). Time-lapse seismic computed with a 35 Hz wavelet fails to capture the signature of this process though. The oil slumping down into the aquifer has a weak pull-up effect which is hard to interpret on 4D seismic sections (red ellipses in Figure 5.15).

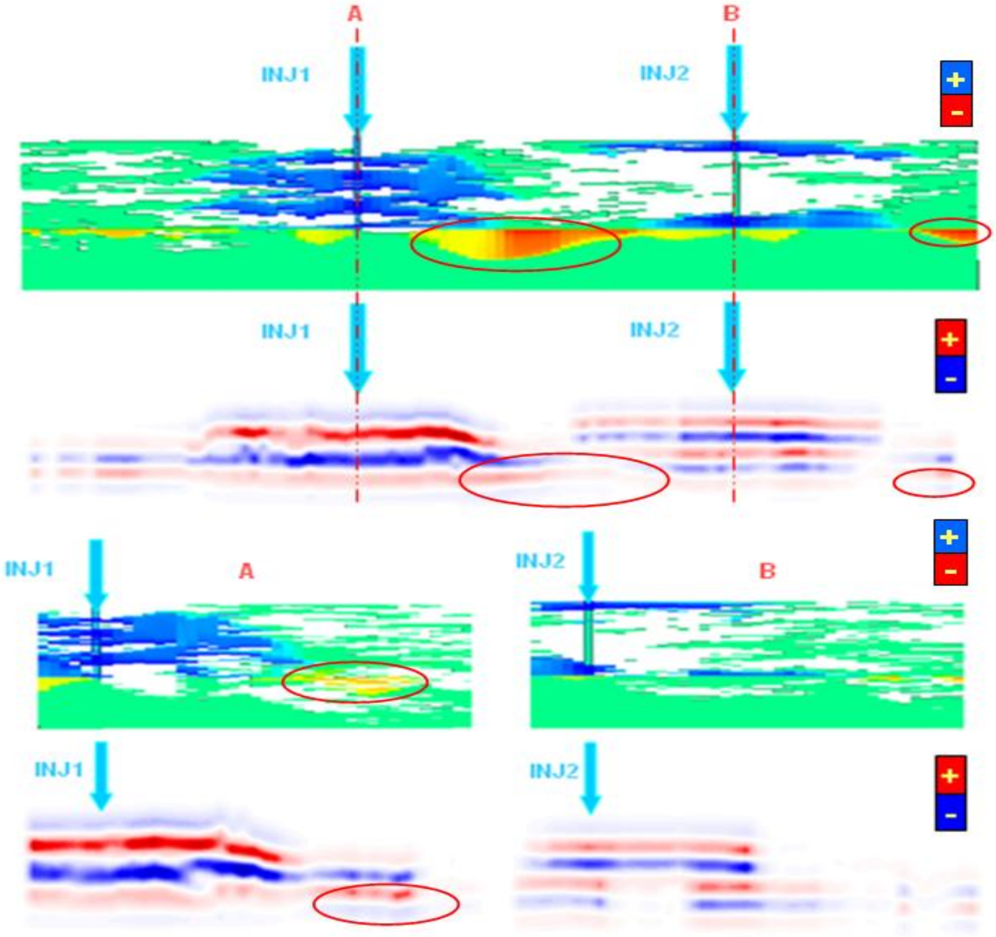

Figure 5.15: Comparison between water saturation change and time-lapse seismic amplitude changes around water injection wells for the 35 Hz seismic. Notice the very different water distribution around wells INJ1 and INJ2, mainly controlled by the NTG and permeability values. These two different behaviours have two very characteristic 4D seismic signatures.

Figure 5.16 shows the water saturation changes around water injectors INJ1 and INJ2 and their corresponding time-lapse signatures for the 62 Hz frequency. Time lapse seismic captures the highly heterogeneous waterfront but it is still challenging to infer the sub-seismic geological complexities as with a wavelength of approximately 35 meters, not all the producing sands are resolved individually in the vertical direction. However, 4D signatures around water injectors INJ1 and INJ2 carry more details about the flooding patterns within the reservoir hence providing a better interpretation for fluids contacts and allowing an accurate interpretation of separate flow units.

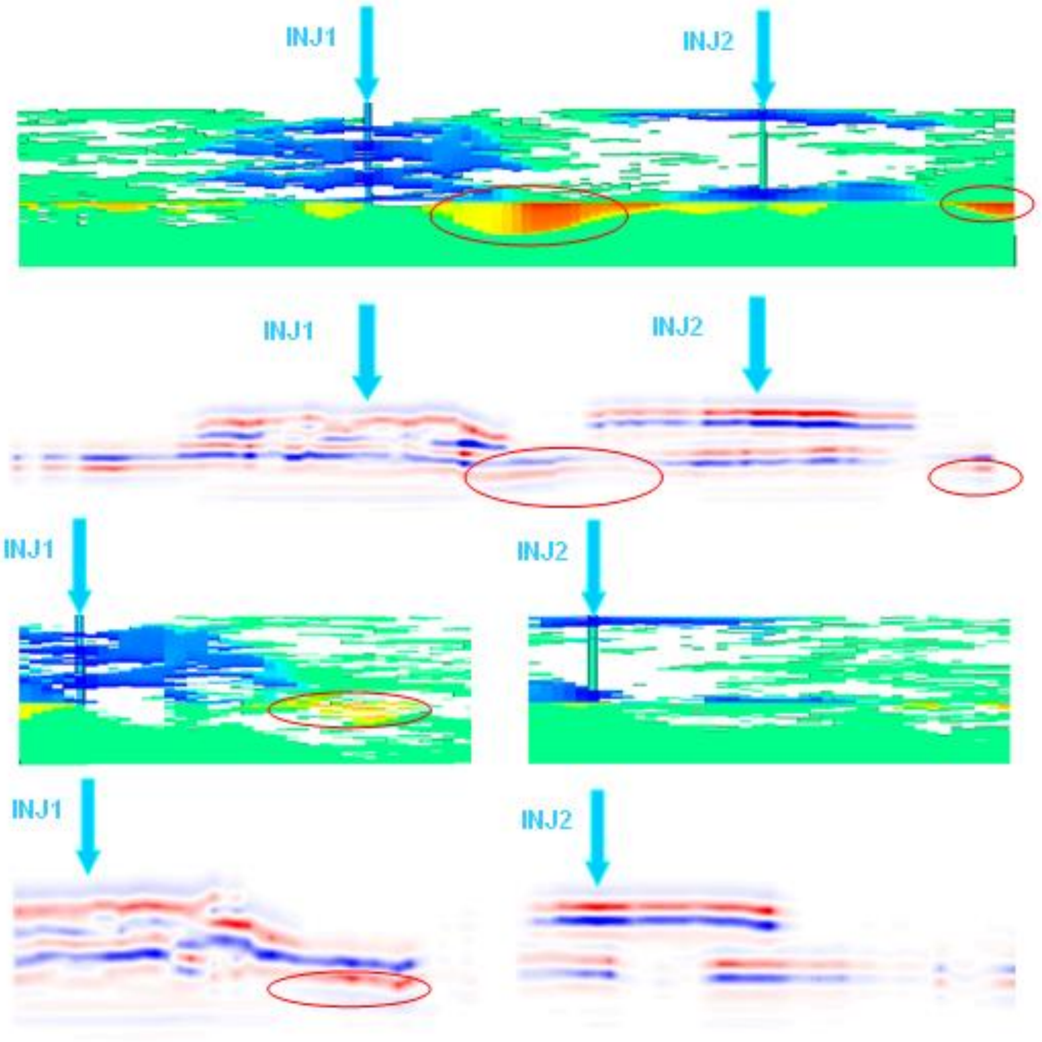

Figure 5.16: Comparison between water saturation change and time-lapse seismic amplitude changes around water injection wells for the 62 Hz seismic. The red ellipses highlight the areas where a decrease in water saturation occurred and the corresponding 4D signatures.

Figure 5.17 shows the water saturation changes and their corresponding 4D signature around water injectors INJ1 and INJ2 for the 125 Hz seismic. The heterogeneous waterfront, controlled by the NTG distribution, is well captured by the 4D seismic. The time-lapse signature around well INJ1 reflects the presence of thin layers of intra-reservoir shales while the one around well INJ2 is easily interpretable as two separated flooded areas with no hydraulic communication between the two. The signature of the oil slumping down into the aquifer, represented by the trough over a peak (red ellipses in Figure 5.17), is visible on the 4D seismic sections and it separately resolved from the OOWC.

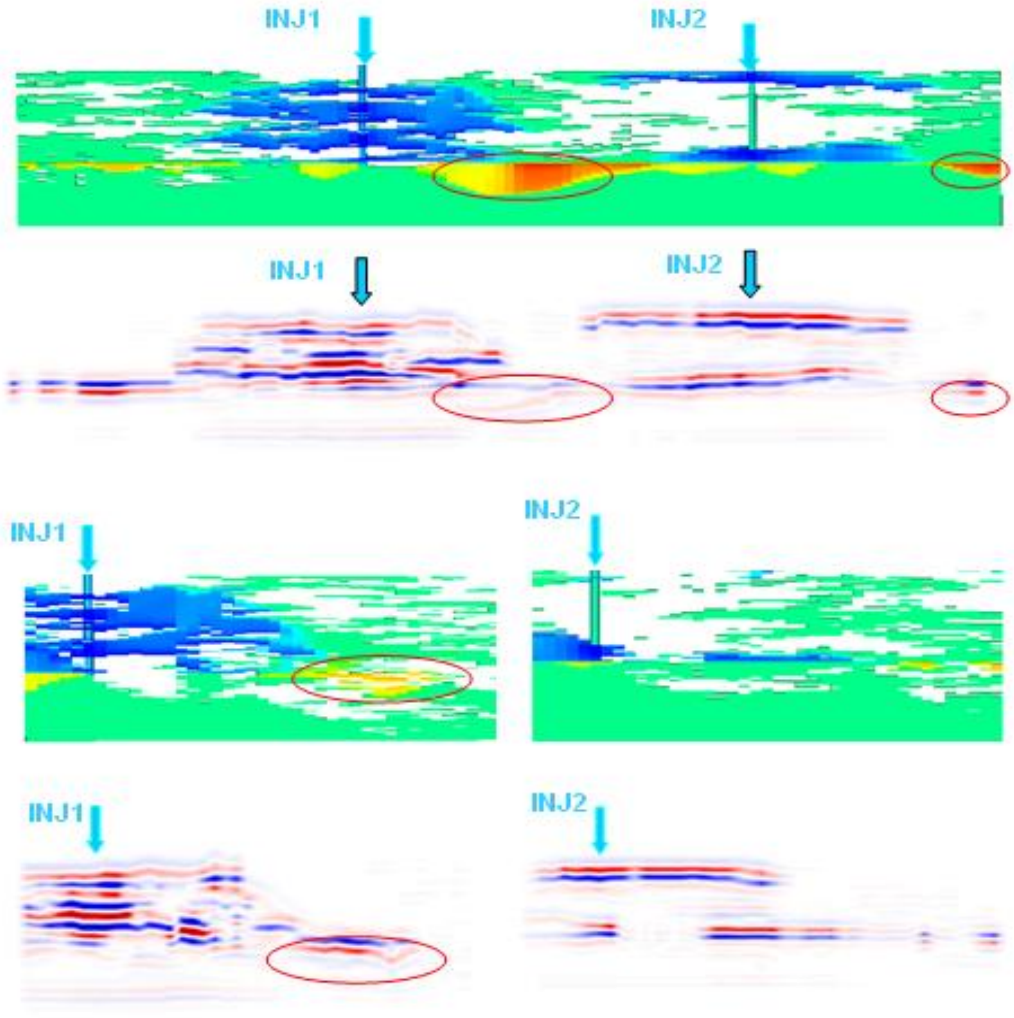

Figure 5.17: Comparison between water saturation change and time-lapse seismic amplitude changes around water injection wells for the 125 Hz seismic.

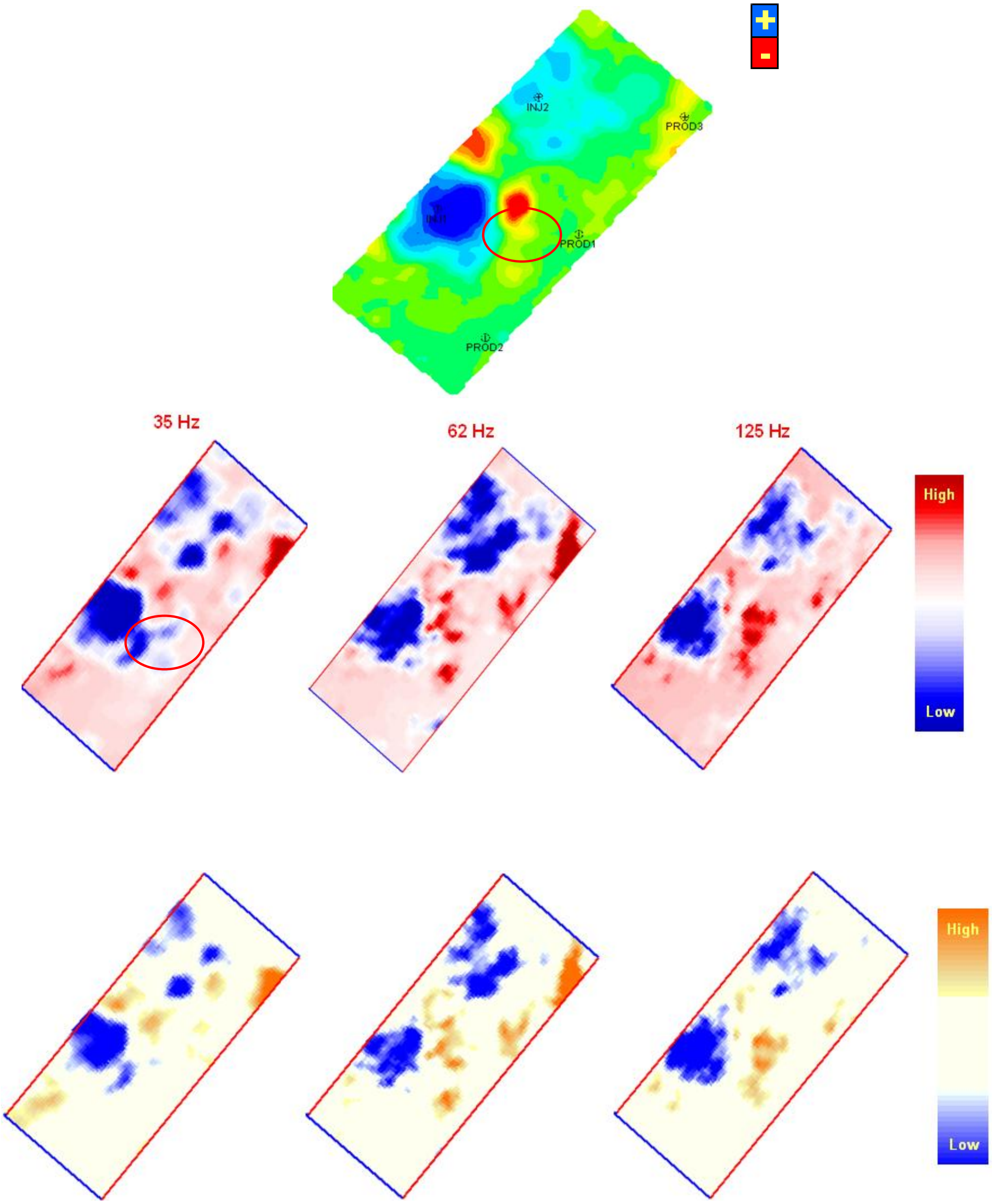

Figure 5.18: Water saturation change (top) and the resulting time lapse RMS amplitude maps computed across the whole reservoir thickness for the three modelled frequencies. Maps at the bottom show the time-lapse amplitude envelope. Amplitude envelope is similar to RMS amplitude due to the zero-phase nature of the seismic data.

Figure 5.18 shows maps of the average water saturation change inside the reservoir after 200 days of Waterflooding along with the resulting time-lapse RMS amplitude and amplitude envelope maps for the three modelled frequencies. At this early stage of Waterflooding, the water had not reached the producing wells yet. The saturation difference map (top) shows strong water saturation increase around injection well INJ1, and to a lesser extend around injection well INJ2. This is understood to be a direct result of the averaging process. In fact, even though the saturation changes around the two wells are of similar magnitude in the active cells (sand) around the two injectors; the low NTG cells, set to be inactive in our simulation model and are present in a greater number around well INJ2, had their properties unchanged by the injection of water yielding an average change of a weaker magnitude around INJ2. Had we opted to compute the average saturation change only across the sand cells, we would have had an average map exhibiting the same magnitude in water saturation change around both wells. We chose to compute the average maps across the whole reservoir in order for them to be comparable to the average 4D amplitude RMS maps computed from 4D seismic cubes.

The 4D amplitude RMS maps exhibit amplitude dimming resulting from impedance increases caused by water encroachment. Sustained high amplitudes and low impedances are areas that have remaining hydrocarbons present (bypassed oil) while areas with no amplitude change are areas unswept by the advancing water. The maps computed from the three different seismic sets, corresponding to the three different dominant frequencies, all exhibit areas with a decrease in amplitude around water injectors, an increase in amplitude where the oil replaced water in the aquifer, and very weak to nil signal elsewhere. It is on the level of details and the accurate mapping of fluids contacts that they differ.

The 35 Hz seismic gave a fairly good indication of the swept areas inside the reservoir. However, it was less accurate in areas with low NTG values due to the averaging properties of seismic waves propagation. Interpretation of the 4D signature of Waterflooding around both injection wells without a prior knowledge of the reservoir internal geology could lead to an erroneous assessment of the reservoir heterogeneities and compartmentalisation. The signature around well INJ1 displays features that could be easily interpreted as flooded areas where no saturation change has occurred in the simulation model (red ellipse in Figure 5.18). It also shows a dimming in 4D seismic amplitude where we had a negative change in water saturation (red ellipse in Figure 5.18), contrarily to what is expected. The 4D seismic signature around INJ2 could be interpreted as the result of flow barriers within the reservoir at the vicinity of this well as it is divided into two separate features inferring that there is no hydraulic communication between the corresponding areas within the reservoir, which is not correct. This is further highlighted in the amplitude envelope map. As the dominant seismic frequency increases, the seismic resolution increases as a consequence and more subtle details about the swept areas are shown in the 4D RMS amplitude maps. Most importantly, the 62 Hz seismic and the 125 Hz seismic successfully produced continuous drainage maps similar to those computed from the fluids flow simulation. Interpretation of 4D RMS amplitude and 4D RMS amplitude envelope maps yield an accurate mapping of fluids contacts and the highly uneven fluid front. The 125 Hz seismic resolved flooded areas as small as a few meter large. It also shows a less smooth and continuous waterfront, highlighting the strong variations of rock properties inside the reservoir.

As the Waterflooding process continued, water spread further into the reservoir producing an increasingly complex 4D signature. Figure 5.19 shows cross-sections of the 4D seismic created for the three studied frequencies along with the corresponding water saturation change profile. More reservoir internal heterogeneities are revealed showing that repeated 4D seismic acquisitions can be of a great value in managing Waterflooding in complex reservoirs and also in building a solid understanding of the reservoir geological settings. The accurate interpretation of the 4D signature requires such an understanding. Figure 5.20 shows an average map of water saturation changes across the reservoir and the corresponding RMS amplitude and RMS amplitude envelope for the three studied frequencies.

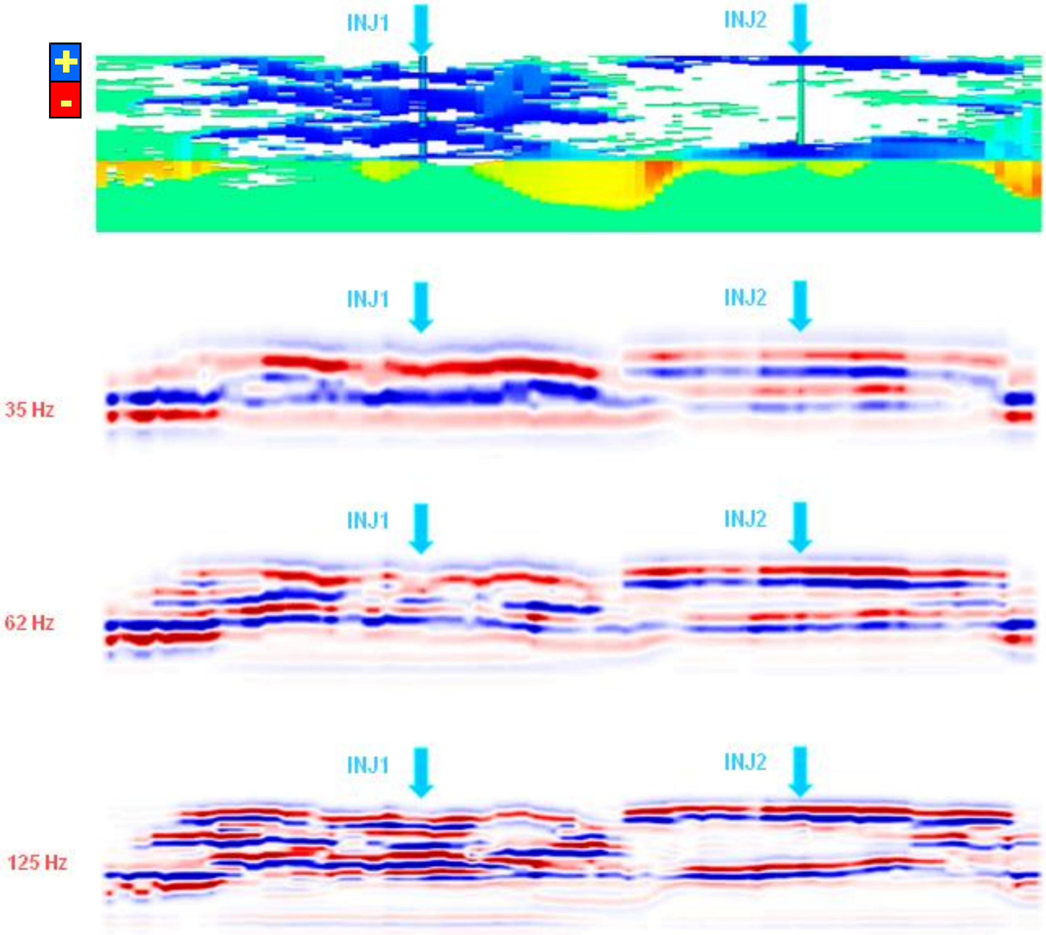

Figure 5.19: Water saturation change and resulting time-lapse signatures around water injection wells after 400 days of Waterflooding (2nd Monitor)

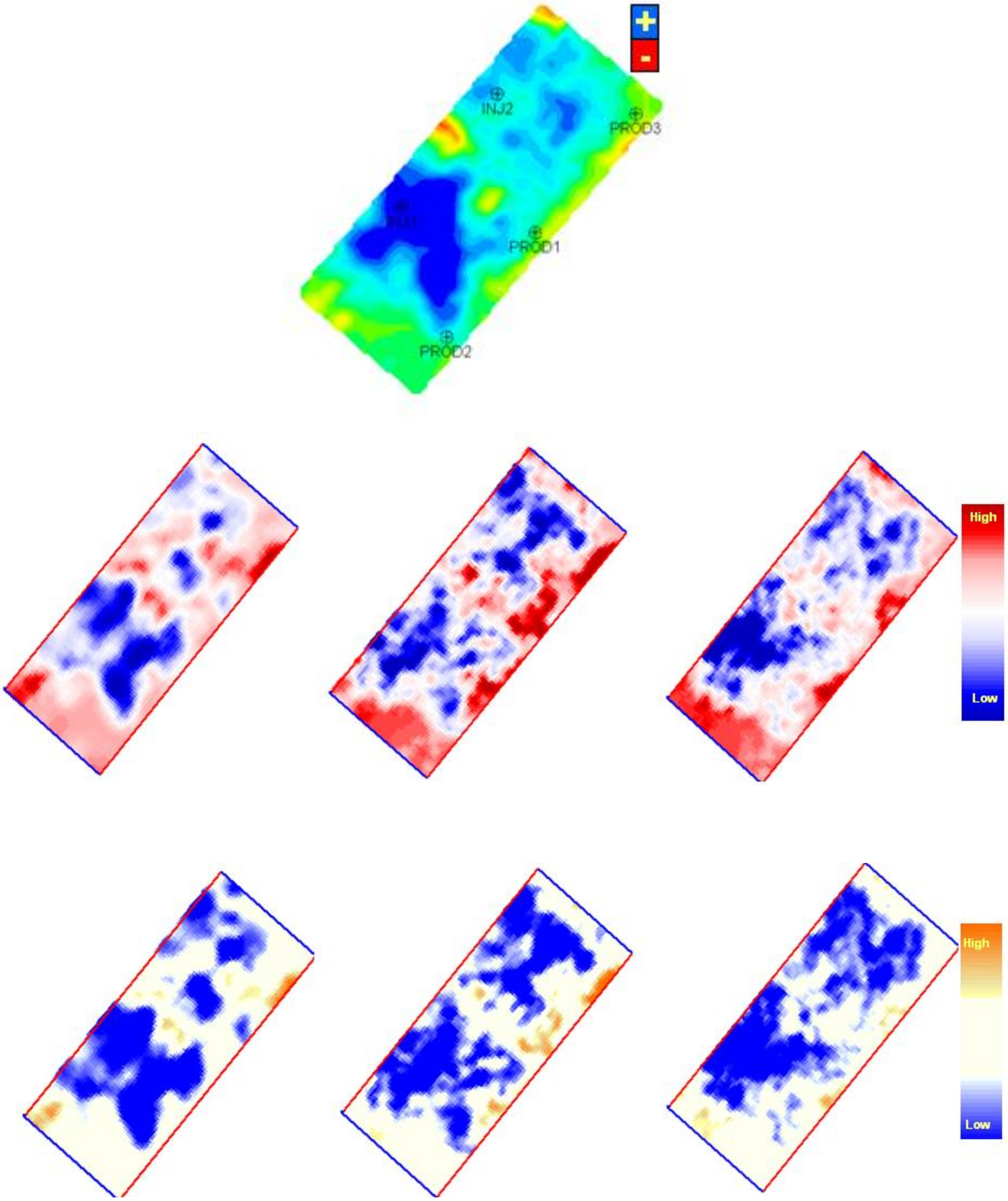

Figure 5.20: Water saturation change (top) and the resulting time lapse RMS amplitude maps for the three modelled frequencies after 400 days of Waterflooding. Maps at the bottom show the corresponding time-lapse amplitude envelope.

5.6 Conclusion

The results of the Waterflooding simulation, performed on the Ainsa II reservoir model, were inserted into a petro-physical model to compute the reservoir rock seismic properties at different calendar times. P-wave velocity, S-wave velocity, and density cubes corresponding to different stages of Waterflooding were generated. An increase in P-wave impedance of up to 7% could be expected as a direct result of water substituting oil within the rocks' pores. Saturation changes have a dominant effect on the time-lapse signature of Waterflooding, while the pressure had a global dimming effect on the magnitude of changes observed on time-lapse seismic attributes, due mainly to the absence of any internal compartmentalisation within the reservoir. The pressure drop caused similar changes in the rocks' seismic properties at either side of the waterfront.

Synthetic seismic created using three different frequencies imaged the reservoir's interior in different ways. As the seismic dominant frequency increased from 35 Hz to 125 Hz, the seismic vertical resolution increased and different interferences patterns occurs. On 3D seismic sections, different channels within the reservoir were resolved separately on the high resolution seismic. Tuning phenomenon is observed for the three modelled frequencies due to the presence of very thin beds (1-2 meter thick). The interpretation of the OOWC or the MOWC on those sections is challenging because the reflections at the fluids front are obscured by reflections from geological interfaces. The complex geology of the reservoir resulted in 3 different RMS seismic amplitude maps showing an increasing degree of heterogeneities as the seismic dominant frequency increased. The fluids-front is hard to interpret on both RMS seismic amplitude maps and isochrones maps as those two attributes carry information about the reservoir geology and fluids but are affected by them in different ways.

The analysis of time-lapse seismic sections and attributes maps showed that once the "geology effect" is removed, the three modelled seismic sets, with increasing dominant frequency, had similar signatures of the Waterflooding process. The shape and location of the waterfront can be interpreted on both low and high frequency seismic, with increasing level of details as the seismic frequency increases.

Chapter 6

Time-lapse seismic attributes analysis in a deepwater stacked turbidite reservoir

Time lapse seismic attributes analysis is performed on a high resolution seismic created from the simulation outputs of Waterflooding in the synthetic turbidite reservoir. Both time shift attributes and 4D amplitude RMS attributes are studied. The combined response from these two attributes is used to better assess the efficiency of the Waterflooding process by identifying swept areas and fluids contact more accurately.

6.1 Introduction

The success of time lapse monitoring of Waterflooding in geologically complex environments depends on several factors. The quality of seismic data plays a major factor toward a successful time lapse interpretation of the fluid front and the drainage patterns inside the reservoir. Careful planning for acquisition and processing of time lapse seismic data is of paramount importance as it increases the repeatability and decreases seismic noise. There were several major advances in time lapse seismic processing leading to excellent data quality with high repeatability and excellent signal to noise ratio. These advances, coupled with increasingly high seismic resolution, led to a better imaging of complex turbidite reservoirs and a more detailed understanding of their internal geology and production mechanisms.

The improvement of 4D seismic data quality led to more ambitious application of the technique; which evolved from qualitative observations to becoming more quantitative. Dynamic reservoir changes, such as pressure and fluids saturation, were directly estimated from 4D seismic data and used to update flow simulation models. Time-lapse seismic data was used successfully in the assessing of reservoir connectivity and in computing permeability trends and faults transmissibility. Time-lapse seismic data proved to be a very valuable part of Waterflooding monitoring programs. It allows the accurate mapping of fluids contacts movement and the identification of unswept areas thus bringing more confidence into any proposed infill drilling location and providing the possibility of pro-active actions to be taken in order to optimise reservoir performance.

We performed an in-depth analysis of the 4D seismic signature of Waterflooding in The Ainsa II reservoir model. The study is carried out on the synthetic seismic data created with a Ricker wavelet with a 62 Hz peak frequency. Seismic data with a peak frequency of 62 Hz is considered to be high resolution seismic data in the oil industry. Figure 6.1 shows a comparison between the synthetic seismic created using a 62 Hz Ricker wavelet and the synthetic seismic created using a wavelet extracted from the high resolution post-stack seismic data of the Girassol field. Both seismic were generated from the same petrophysical model.

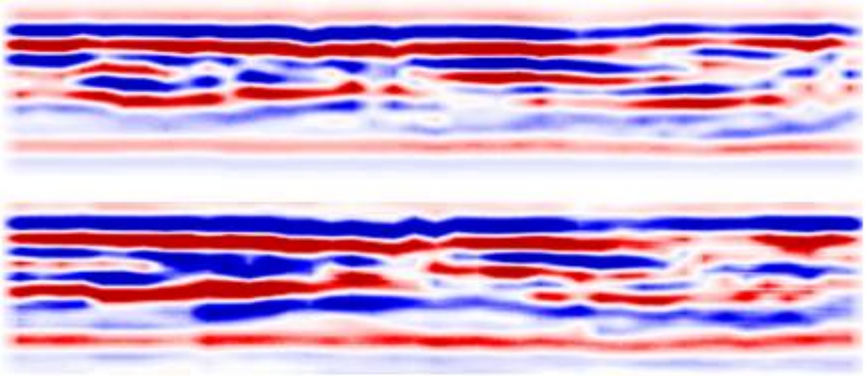

Figure 6.1: Cross-sections from synthetic seismic created using a 62 Hz Ricker wavelet (top) and a Girassol field wavelet (bottom). Both seismic exhibit the same level of details. Differences may be caused by the fact that only the Ricker wavelet is truly zero-phase.

6.2 Reservoir simulation, petrophysical modelling and seismic simulation

For the purpose of this study, the simulation model described in the previous chapter is used. Four time steps are investigated: before the start of Waterflooding (time step 1), after 200 days of Waterflooding (time step 2), after 400 days of Waterflooding (time step 3), and after 800 days of Waterflooding (time step 4 which corresponds to the end of the simulation) (Figure 6.2). The average water saturation across the reservoir increased from 59% prior to start of water injection, to 62% after (200) 120 days, 69% after 400 days, and 74% after 800 days of Waterflooding meaning that at the end of Waterflooding, most of the movable oil inside the reservoir has been produced. The average reservoir pressure remained fairly constant, around 290 bars. The same petro-elastic model used in the previous studies is used in this study.

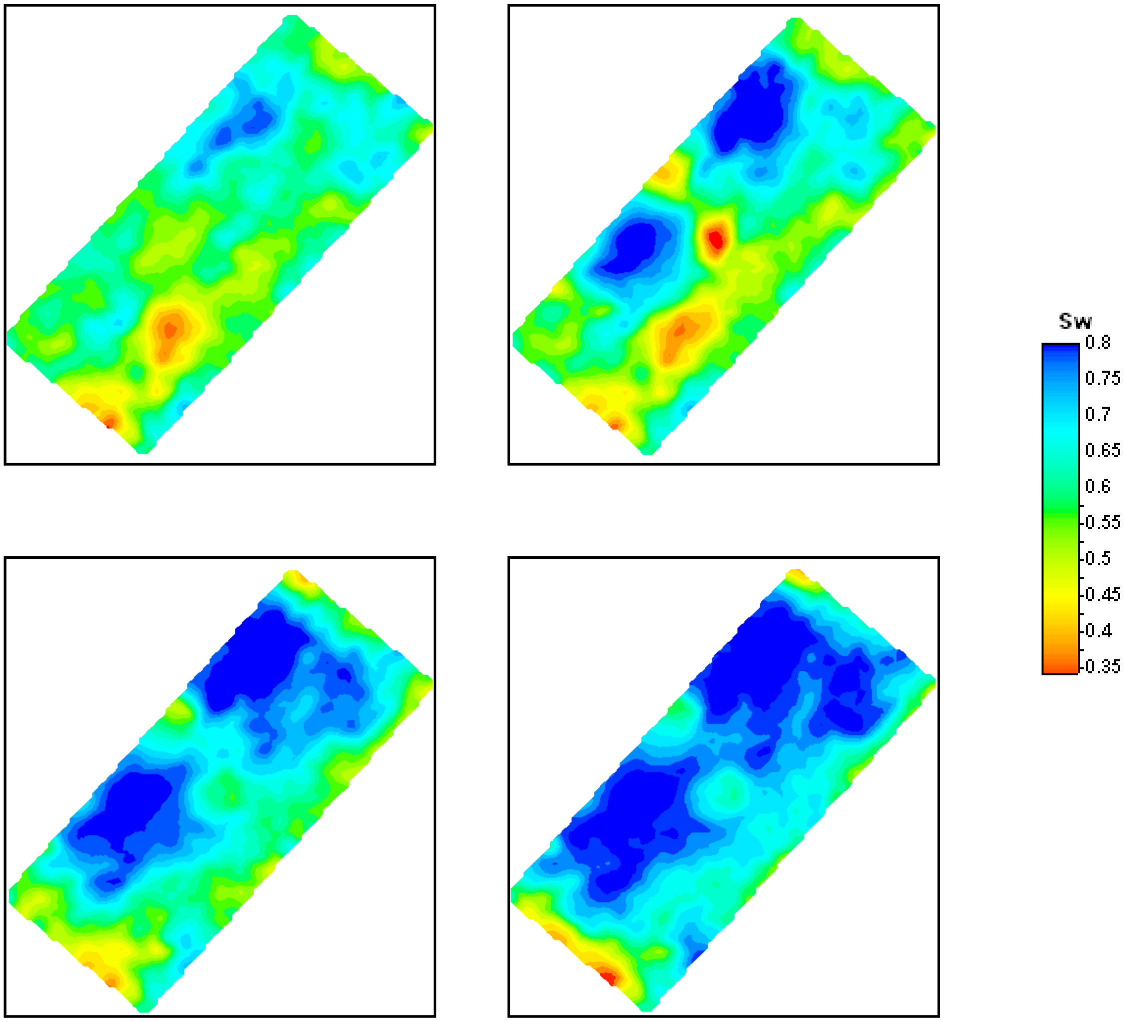

Figure 6.2: Average water saturation maps, from top left clockwise: pre-production, after 200 days of Waterflooding, after 400 days of Waterflooding, and after 800 days of waterfloofing. The map view can not capture the heterogeneous vertical water distribution inside the reservoir but gives a good indication as to the movement of the oil/water contact.

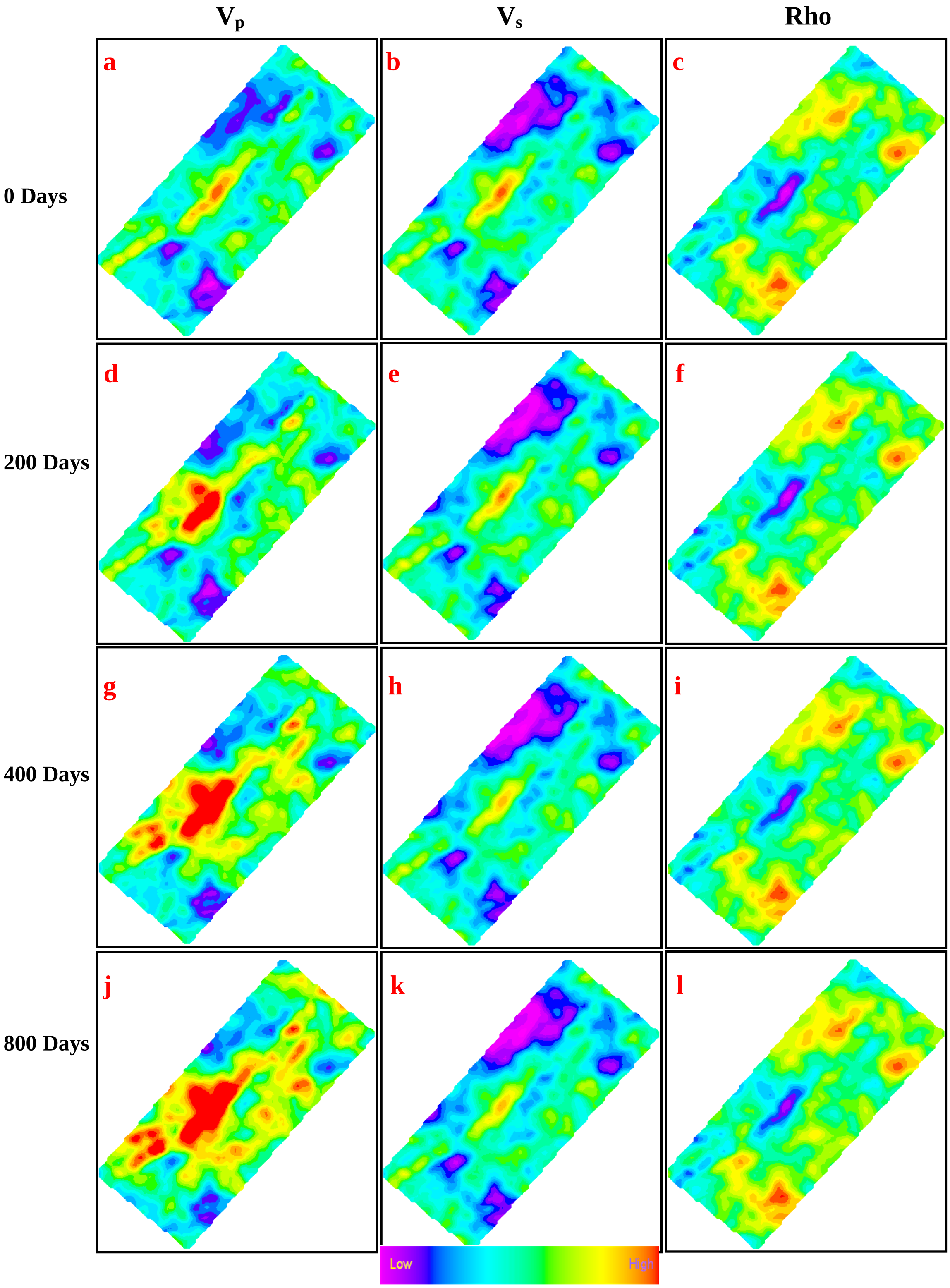

Figure 6.3: Average seismic properties after petrophysical modelling: From left to right: V_p, V_s, and Rho. From top to bottom: pre-production, after 200 days of Waterflooding, after 400 days of Waterflooding, and after 800 days of Waterflooding. Vp maps exhibit the most changes due to Waterflooding.

Figure 6.3 shows the converted P-wave velocity (V_p), S-wave velocity (V_s) and density (Rho) for time steps 1, 2, 3 and 4. Water flooded areas exhibit an increase in P-wave velocity allowing for the fluid front and the two-phase area (including both water and oil) to be interpreted from V_p maps. V_s is not sensitive to fluid changes and its changes are primarily caused by density changes. As with water saturation maps, the heterogeneous geology of the reservoir is highlighted by the patchy changes in V_p which occur mainly in the high NTG areas of the reservoir.

Figure 6.4 shows the average changes in reservoir pressure and water saturation at monitor 1 and monitor 2.

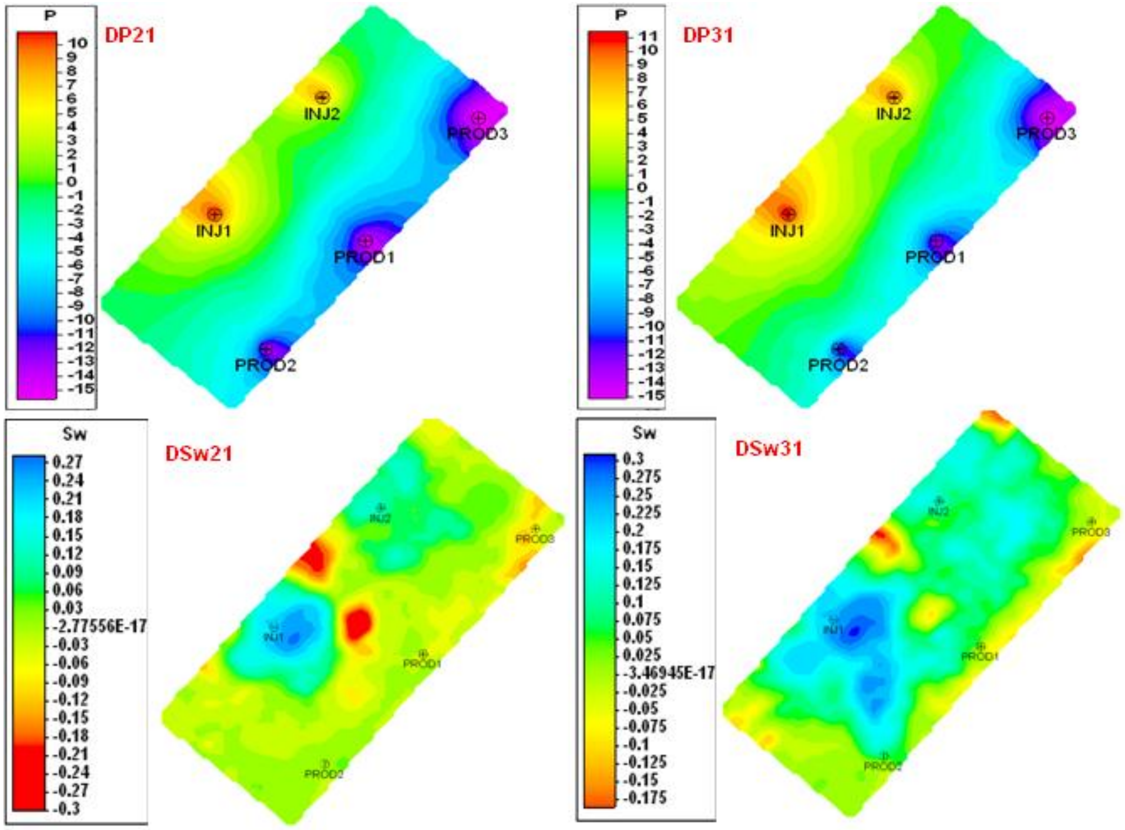

Figure 6.4: Changes in reservoir pressure and water saturation after 200 days and 400 days of Waterflooding.

Prior to Waterflooding, the reservoir pressure was constant across the reservoir. At the start of the Waterflooding process, pressure changes were localised at the well locations. A pressure increase of up to 11 bar (160 psi) is observed at the water injection wells while a pressure decrease of up to 15 bar (218 psi) is observed at the producing wells. As the Waterflooding proceeds, a smooth pressure front progresses from the injection flank (over-pressurised area) to the producing flank of the reservoir (under-pressurised area) unconditional of the underlying reservoir geology. The water injection/production scenario was set so the pressure gradient created at the start of the Waterflooding process remains constant until the end of the Waterflooding.

The water saturation changes were patchy and heterogeneous and are highly correlated to the high permeability/high NTG zones of the reservoir. Both negative and positive changes in water saturation were observed. At the start of the Waterflooding, the waterfront advanced from the injectors displacing the oil in an almost piston like manner toward the producers. A part of the injected water slumped down below the OOWC and got trapped there. As the Waterflooding continued, a part of this trapped water is recovered, but some of it remained trapped there until the end of the Waterflooding process.

Figure 6.5 shows average changes in P-wave velocity, S-wave velocity and density at the two monitors. Warm colours represent an increase in the displayed property after Waterflooding, while cool colours represent a decrease. The similarity in the patterns between the P-wave velocity difference map and the water saturation difference map infers that the mechanisms responsible for velocity changes at the two monitors are highly conditioned by the water saturation changes. The substitution of oil with water within the rocks' pores resulted in an increase of the P-wave velocity by up to 35 ms^{-1}, while a maximum of 23 ms^{-1} decrease is observed where water substituted oil. Changes in S-wave velocity are smoother and present similar patterns than changes in pressure. But since S-wave velocity is affected by changes in density, which in turn is affected by both changes in pressure and fluids saturation, some visual correlations between V_s changes and water saturation changes are obvious.

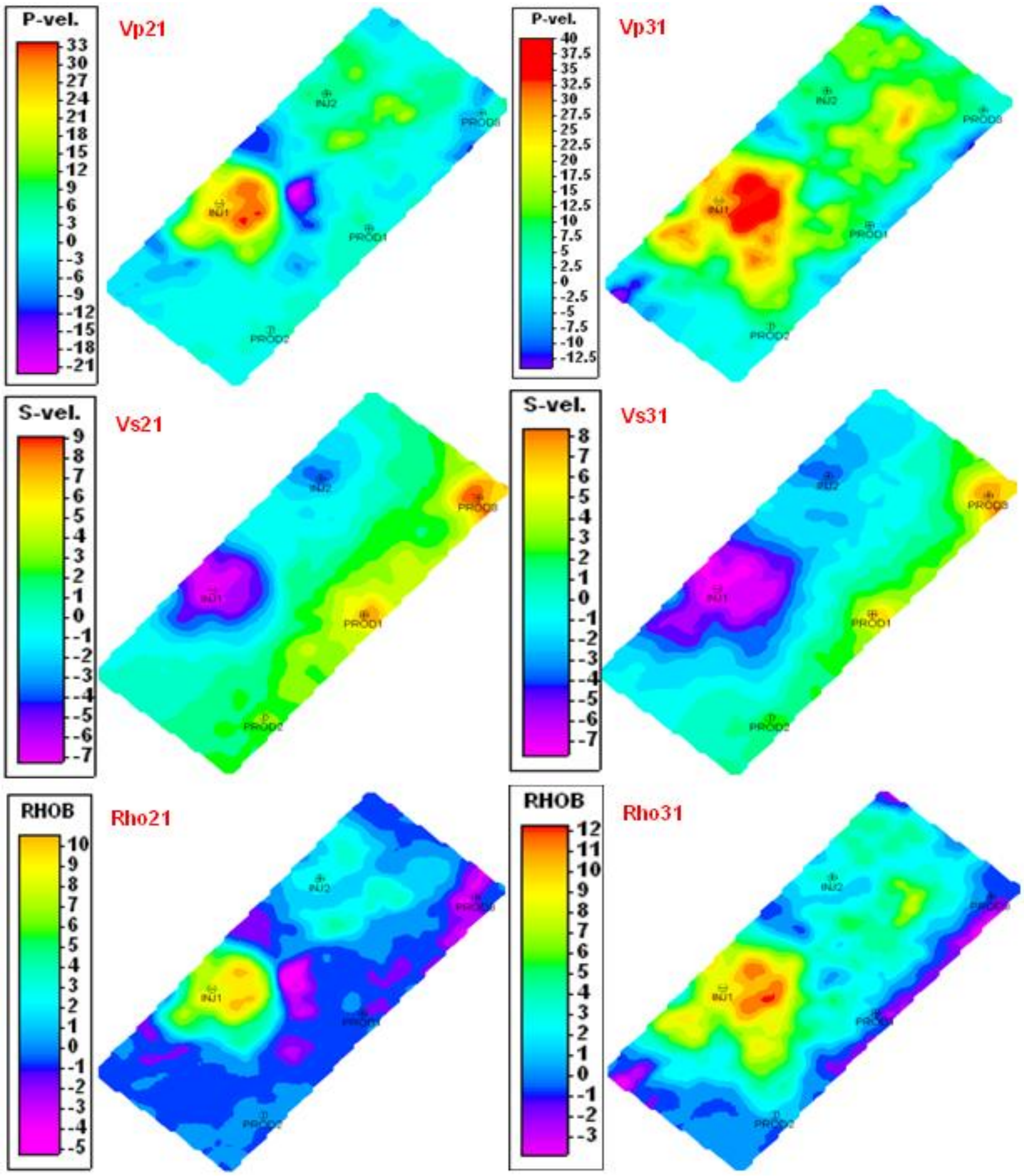

Figure 6.5: Changes in P-wave velocity, S-wave velocity, and density at Monitor 1 and Monitor 2.For the three displayed properties, most of the changes occurred at the water injector and behind the OWC. A strong signal is observed, however, on V_s *map around the producers.* V_p*,* V_s *and Rho exhibit different responses to Waterflooding processes.*

Figure 6.6 shows cross-plots of P-wave velocity changes against average water saturation changes, at the time of the first and the second monitor. A linear relationship links changes in V_p and changes in S_w. At the time of the first monitor, water saturation increased by only 3%, as the water didn't reach far into the reservoir. Only few cells were water flooded, and water saturation changes were significant only at the vicinity of the injection wells. This can be seen in the cross-plot graphs, where (Figure 6.6.a) most of the data was grouped in a cluster extending across water saturation changes ranging from -0.1 to 0.1. As the Waterflooding proceeded, a larger part of the reservoir was water flooded and the range of water saturation changes widened resulting in the cluster of data being less dense. The pressure has little impact on the P-wave velocity changes but it can be seen on the cross-plot graphs that areas where the pressure decreased would see a bigger change in V_p than areas where the pressure remained constant or increased.

Figure 6.7 shows a cross-plot of changes in V_p as a function of pressure changes. It is clear that changes in V_p are not related to pressure changes.

Figure 6.8 shows cross-plots of changes in S-wave velocity as a function of changes in pressure at Monitor 1 and Monitor 2. Changes in V_s are controlled by changes in reservoir pressure in a linear fashion. The cross-plots for Monitor 1 and Monitor 2 data look similar, suggesting that even though changes in V_s are mainly controlled by the pressure evolution inside the reservoir, these changes happened early in the Waterflooding process and stabilised after that. Examination of the evolution of S-wave velocity as a function of reservoir pressure changes over time, in a Waterflooding process, can give valuable information as to reservoir compartmentalisation and hydraulic communication.

Indeed, areas where significant changes in S-wave velocity, in a Waterflooding process, can be interpreted as a hydraulically isolated compartment inside the reservoir. If these changes are observed near a fault, they could give indication as to the sealing nature of that fault.

Figure 6.9 shows cross-plots of changes in V_s versus changes in water saturation at Monitor 1 and Monitor 2. The absence of clusters in the graph suggests that the water saturation have a random effect on changes in V_s.

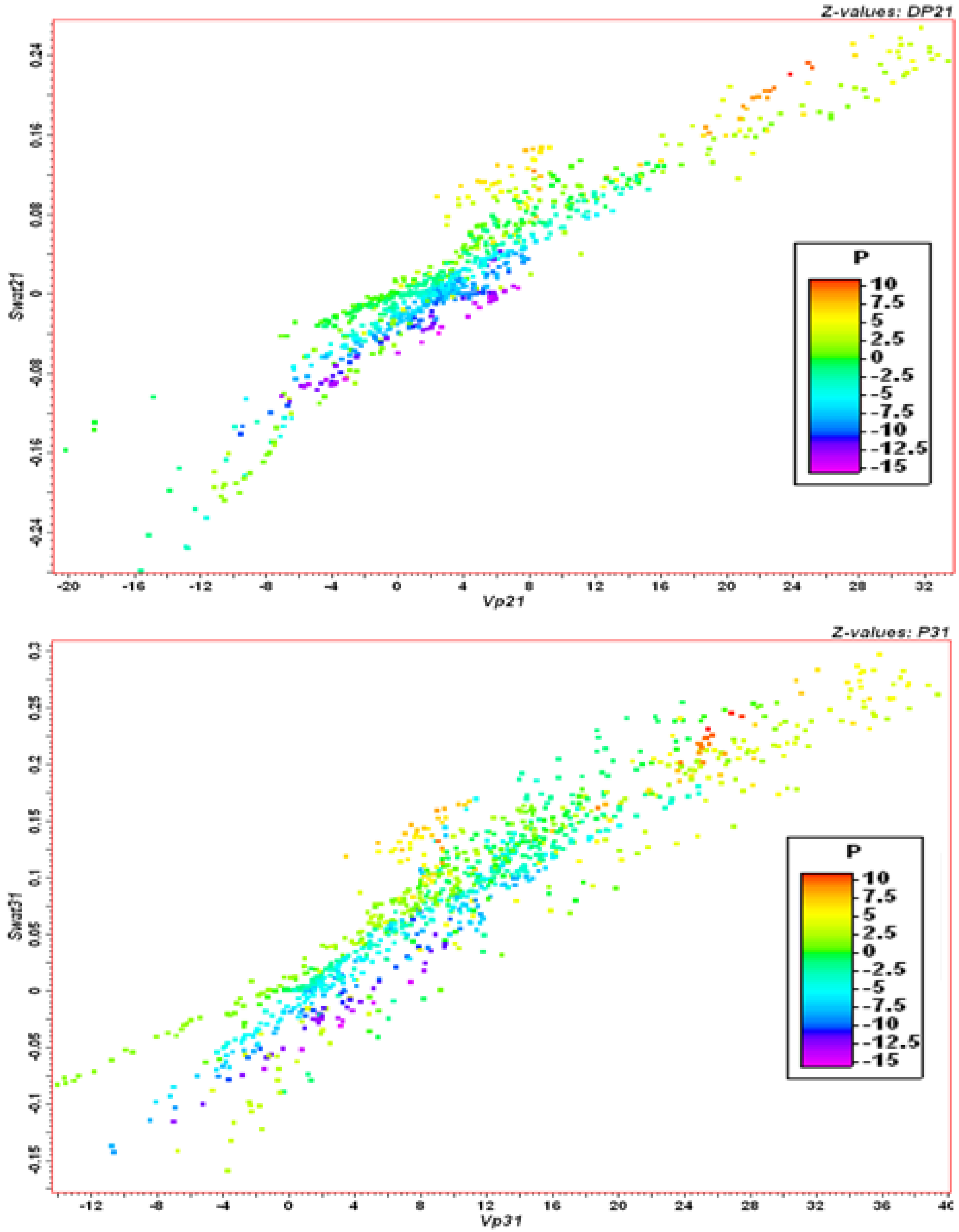

Figure 6.6: Changes in P-wave velocity versus changes in average water saturation. The pressure changes are also plotted. A linear relationship bound changes in V_p and S_w. The pressure effect is negligible.

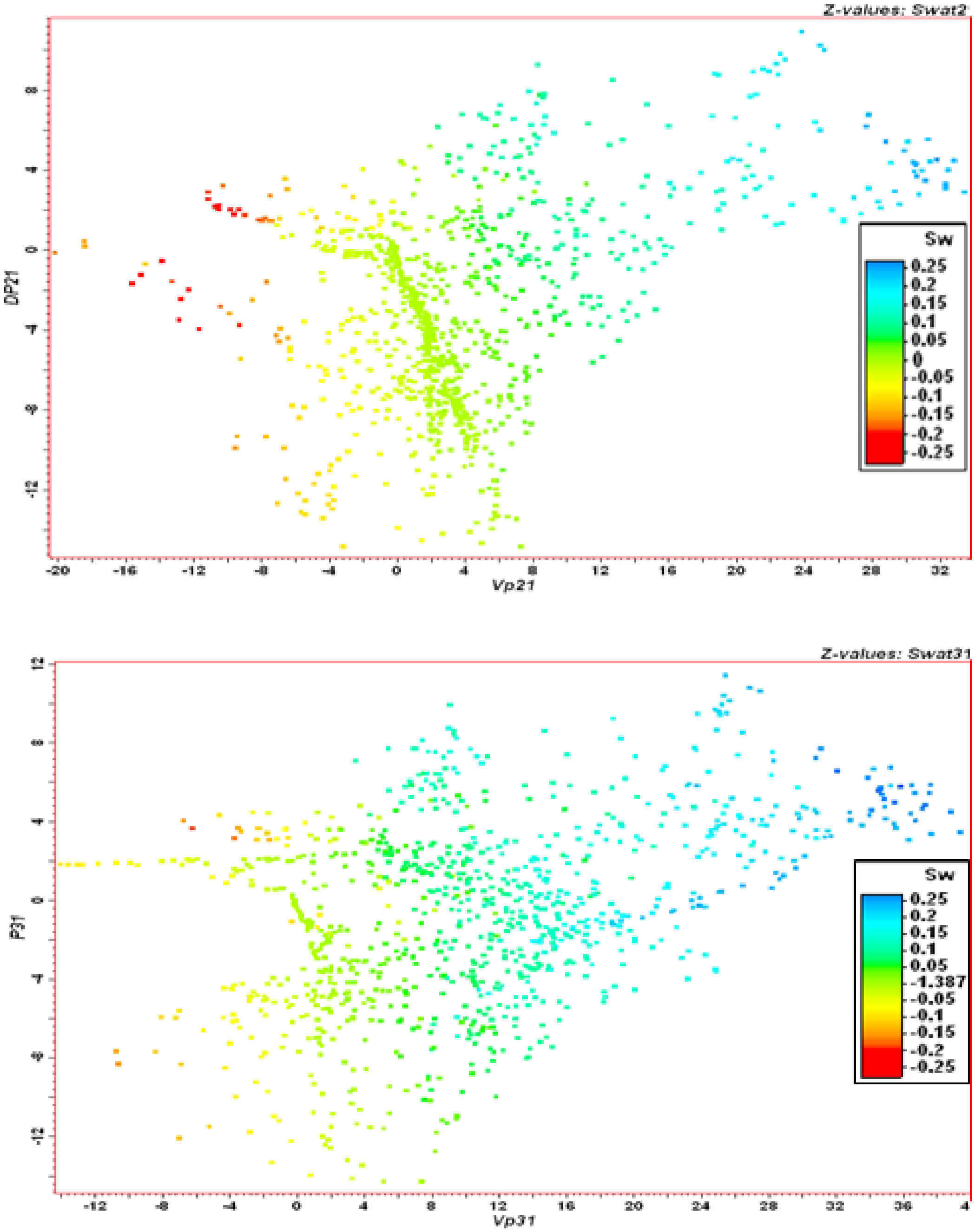

Figure 6.7: Cross-plots of V_p changes at monitor 1 and monitor 2 as a function of pressure change. No linear relationships between changes in V_p and pressure can be inferred but the saturation effect is visible. An increase in water saturation would result in an increase in V_p and vice versa.

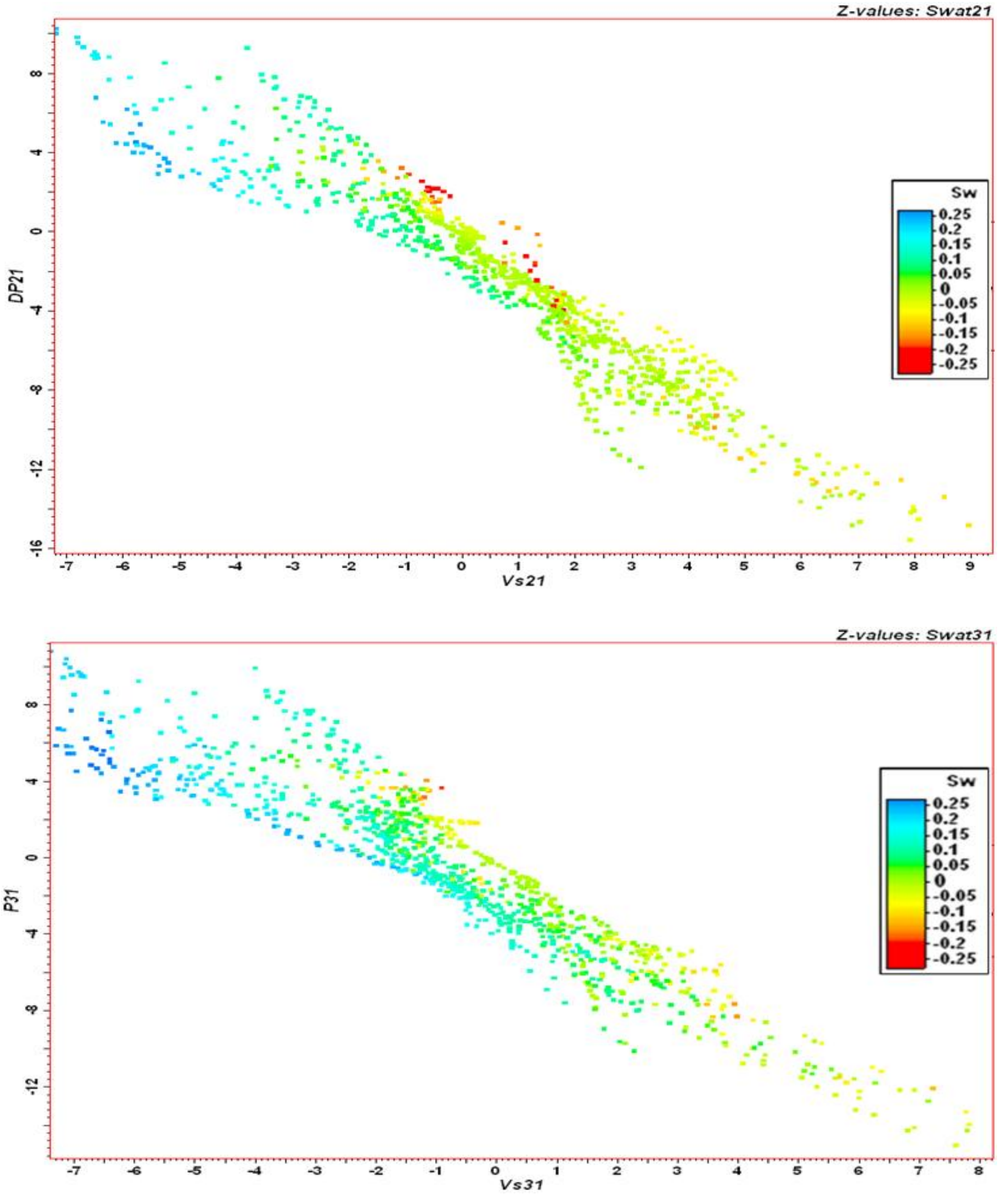

Figure 6.8: Changes in S-wave velocity versus changes in pressure. A linear relationship links changes in V_s to changes in pressure while the saturation effect seems to be random.

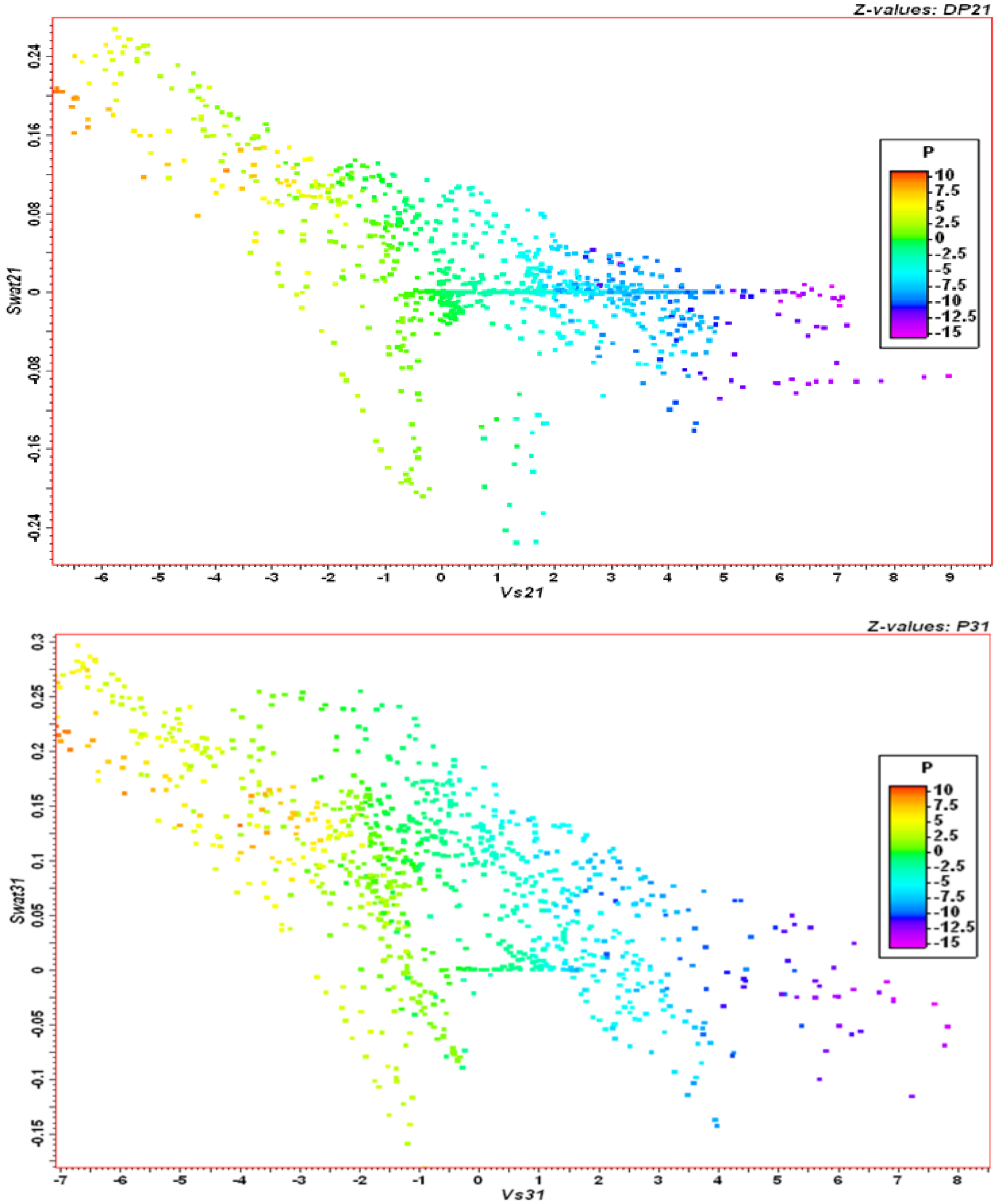

Figure 6.9: Changes in S-wave velocity versus changes in average water saturation. The pressure changes are also plotted. No particular trend or linear relationship can be inferred.

Figure 6.10 shows cross-plots of V_p/V_s at the time of the 1st monitor versus V_p/V_s at the time of the second monitor. Both the pressure change and water saturation changes are colour coded and plotted as the 3rd dimension. V_p/V_s ratio is commonly used as a fluid identification tool as it is more sensitive to fluids than V_p or V_s alone (Hamada, 2004).

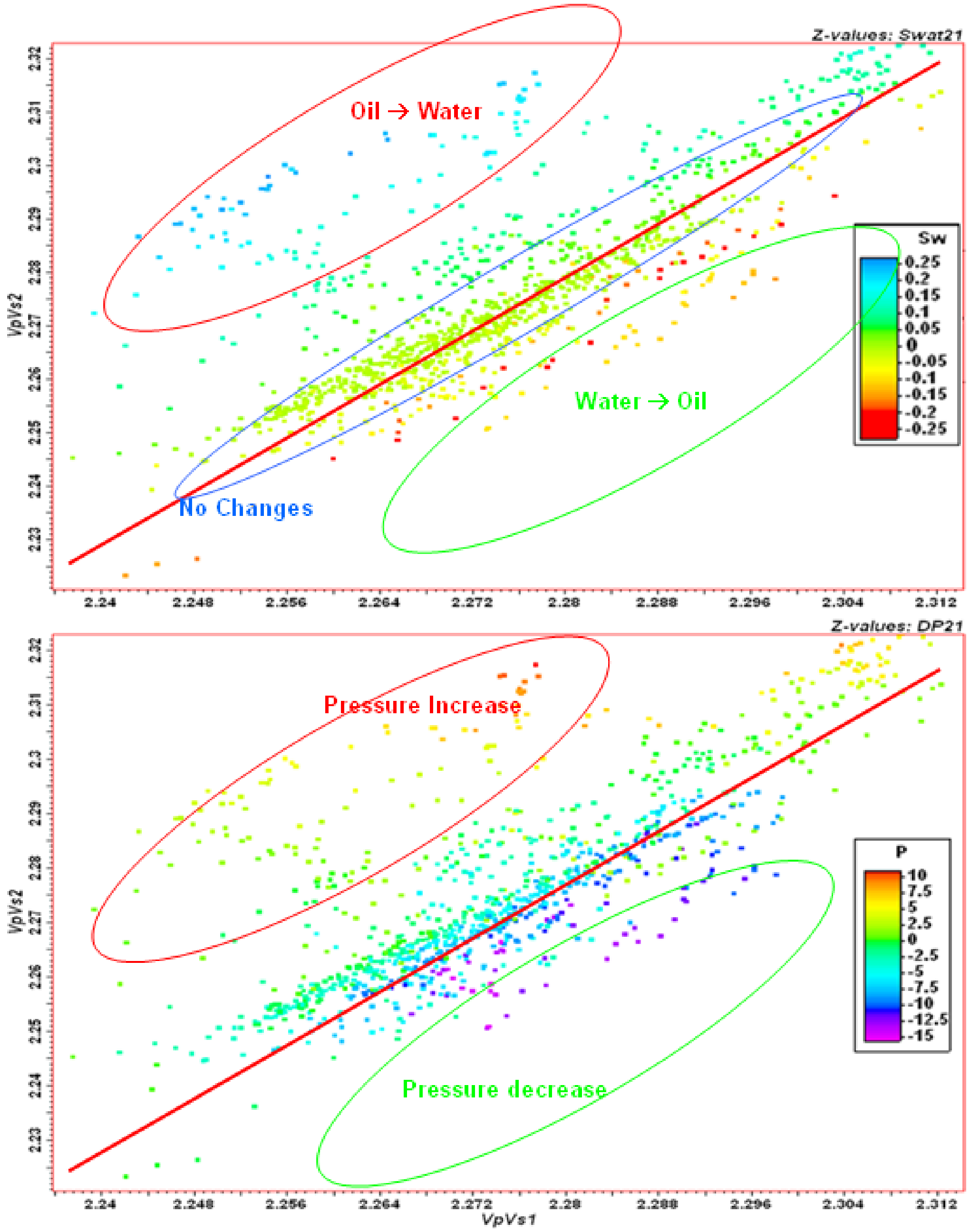

Figure 6.10: Changes in Vp/Vs ratio at Monitor 1. Pressure change and water saturation changes are plotted. V_p/V_s is a useful tool in fluids identification. Three clusters of data can be identified in Figure 10.a. Data grouped along the diagonal correspond to areas where water saturation remained constant at the time of the first monitor. The red eclipse corresponds to areas where V_p/V_s increased (water substituting oil, S_w increasing), while the green ellipse corresponds to areas where V_p/V_s decreased (oil substituting water, S_w decreased). The plot in Figure 10.b is useful in the identification of any pressure anomalies inside the reservoir, but can not help with the tracking of the waterfront.

Time-lapse seismic was computed as the difference between the monitor surveys and the base survey. The difference between the monitor survey and the base survey is a seismic cube (4D seismic cube) where geology effects (assumed to be constant during the fluids flow simulation and the seismic modelling) are cancelled, leaving only the effects of pressure change and fluids saturation changes. The pressure has a global dimming effect on seismic attributes which would not be investigated in this study as the pressure fluctuations were kept to a minimum during simulation. Four synthetic seismic cubes, corresponding to four different stages of the Waterflooding process, were created and used in this study. The first 4D seismic cube would highlight the changes in fluids distribution inside the reservoir after 200 days of water injection (1^{st} Monitor – Base), the second after 400 days (2^{nd} Monitor – Base), and the third at the end of Waterflooding (3^{rd} Monitor – Base).

6.3 Time-lapse seismic analyses

The turbidite reservoir model used for the purpose of this study is highly heterogeneous in the geological sense. The reservoir heterogeneity is captured in our model through stratigraphic variations in net-to-gross and the occurrence of intra-reservoir shales. This heterogeneity, present on a variety of scales within the reservoir, will strongly influence both vertical and lateral connectivity and hence fluid flow behaviour during production or injection (MacBeth et al., 2005). It could compromise our quantitative understanding of the time-lapse seismic signature. Figure 6.11 presents one-dimensional schematics illustrating the influence of the OWC movement in a clean sandstone reservoir and in a heterogeneous turbidite reservoir. The impedance values for the turbidite case were derived from impedance logs extracted from the petrophysical model at production well Prod2. The light blue colour represents the impedance change due to water replacing oil within the reservoir rocks. The water sand is modelled to be completely water saturated (aquifer, in blue in Figure 6.11), while the oil sand contains connate water saturation, S_{wc}.

In the clean sandstone model, the direct signature of Waterflooding is a characteristic trough-peak doublet, formed by the interference of reflected events from the original OWC and the moved OWC, which can be used to interpret and quantify oil-water contact movement (MacBeth et al., 2005). In the turbidite model however, a whole sequence of trough-peak doublet is present and interfere with the main signature of the OWC movement. This is caused by the presence of shale layers within the swept area. Indeed, interfaces between oil saturated sand and shale have a stronger reflection coefficient that the ones between water saturated sand and shale, meaning that reflections at sand-shale interfaces within the swept areas won’t be completely cancelled out in the difference data.

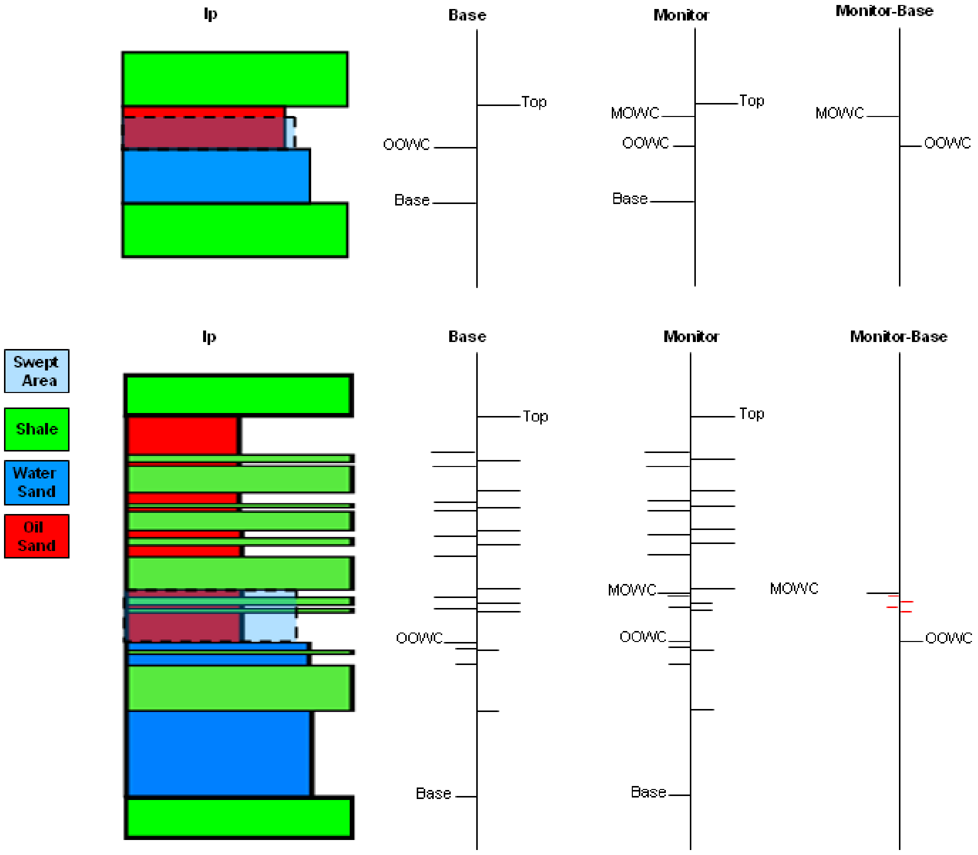

Figure 6.11: Schematics illustrating the effect of reservoir heterogeneity on the time-lapse signature due to oil-water contact movement. (top) Clean sandstone reservoir (high net-to-gross). (bottom) Stacked turbidite reservoir (low net-to-gross).

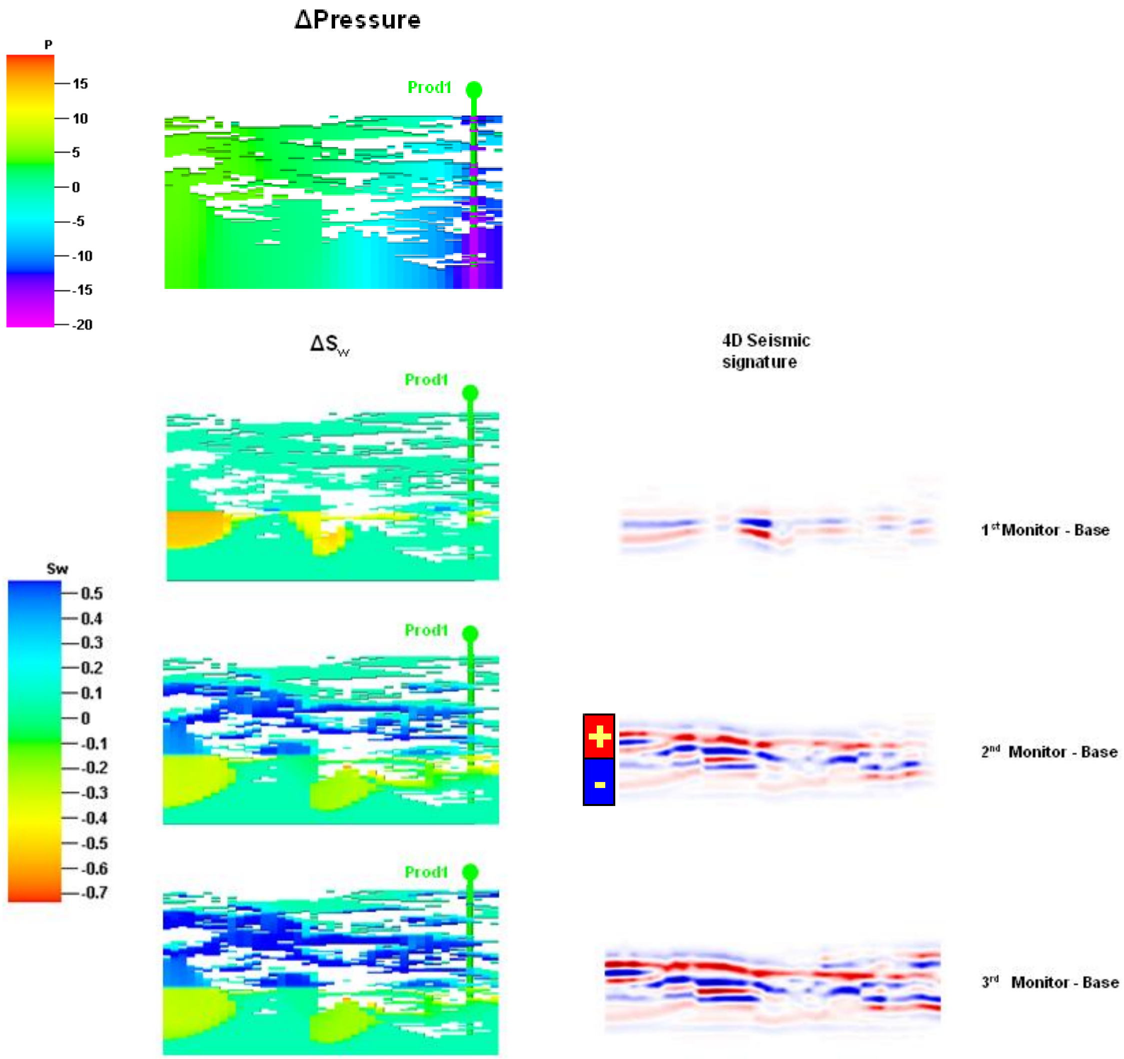

Figure 6.12: Time-lapse seismic and the corresponding water saturation and pressure changes at the three monitors. Only the pressure change at the 1st monitor is displayed as this change remained constant throughout the simulation.

Figure 6.12 shows the pressure and water saturation changes at the monitor survey, together with the resultant time-lapse signature of the Waterflooding. The 4D signature is more complicated than the ideal trough-peak signature suggested by 1D modelling. Instead, it displays a series of patchy and irregular trough-peak doublets where the main water saturation changes occurred. The patches of no signal correspond to zones where no discernable changes occurred. Areas with low net-to-gross values have a significantly reduced visibility. The 4D signature is closely related to saturation changes while there is little effect of the pressure change.

Figure 6.13 shows a cross-section of the time-lapse seismic amplitude (Monitor 1 – Base) and the corresponding Relative Acoustic Impedance, Amplitude Envelope, and Reflection Intensity attributes. Relative acoustic impedance is a running sum of regularly sampled amplitude values calculated by integrating the seismic trace and passing the result through a high-pass Butterworth filter. It shows apparent acoustic contrast, indicating sequence boundaries, unconformity surfaces and discontinuities. It may also indicate porosity or fluid content in the reservoir. The Envelope attribute is the total instantaneous energy of the analytic signal (the complex trace), independent of phase, also known as 'Instantaneous Amplitude', 'Magnitude' or 'Reflection strength'. Reflection intensity is the average amplitude over a specified window, multiplied with the sample interval. Reflection intensity integrates the instantaneous amplitude along the trace (using the trapezoidal rule). It useful for delineation of amplitude features while retaining the frequency appearance of the original seismic data.

The relative acoustic impedance cross-sections exhibit strong, continuous reflections at the fluid contacts, similar to those observed on the 4D seismic amplitude cross-section, but the highly heterogeneous nature of the reservoir is more accentuated. This can be seen around well Inj1, where the water distribution, conditioned by the inherent reservoir geology, is highly heterogeneous, resulting in a complex time-lapse seismic signature.

Due to the geological complexity of the reservoir, interpretation of different attributes cross-sections may be necessary and can bring new insights into the monitoring of Waterflooding processes. Different attributes would responds differently to changes in either fluids saturation or pressure and would be affected by the geology in a different way.

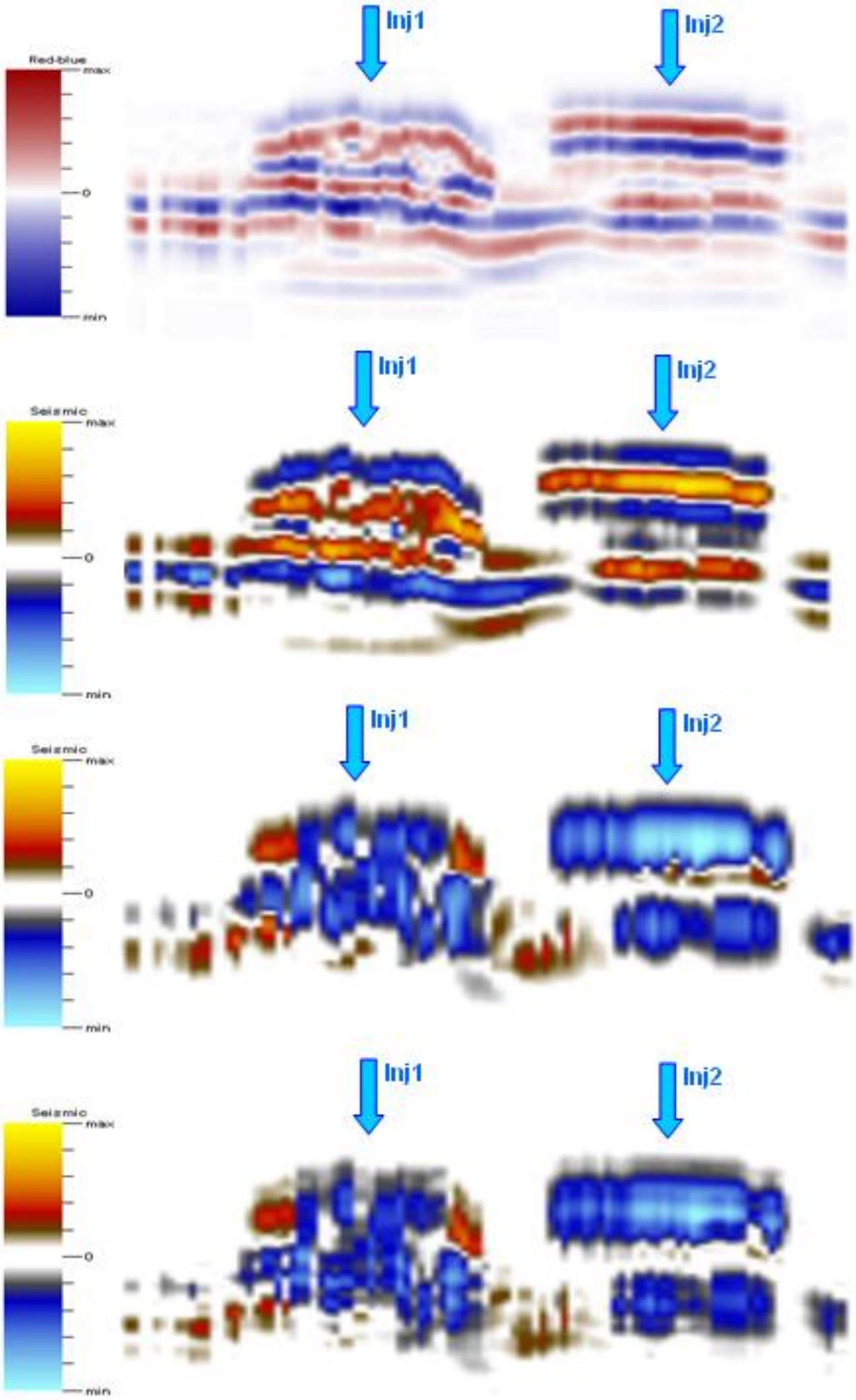

Figure 6.13: 4D seismic amplitude cross-section (top), relative acoustic impedance cross-section, envelope, and reflection intensity (bottom)

6.3.1 Time-shift analysis

Reservoir thickness-time was computed as the difference between the travel time at the top reservoir horizon and the travel time at the base reservoir horizon. The average reservoir thickness in time is 43 ms. As water is injected into the reservoir; the drained areas will see their rock velocities increasing allowing seismic waves to propagate faster through the reservoir thus decreasing travel time. Figure 6.14 shows the computed isochrones for the different studied time-steps.

The average reservoir thickness-time decreased through time from 43.7 ms before the start of Waterflooding, to 43.3 at the end of the process (after 800 days). As water is injected into the reservoir, computed isochrones exhibit more heterogeneity highlighting a patchy water distribution associated with complex drainage patterns guided by the reservoir inherent geology.

Interpretation of time-shifts observed on the simple sand block model (chapter 3) suggests that time shift computed across the whole reservoir thickness at a specific location is proportional to the height of the swept area at that location. While this statement holds true in a simple sand block model, it is not straightforward to extend it to geologically complex reservoirs. The heterogeneities of reservoir rock properties (i.e. NTG, permeability, porosity, etc) and the presence of intra-reservoir shales acting as flow barriers would condition the distribution of the injected water within the reservoir. To accurately correlate the observed time-shift with water saturation changes, one must account for the reservoir geology.

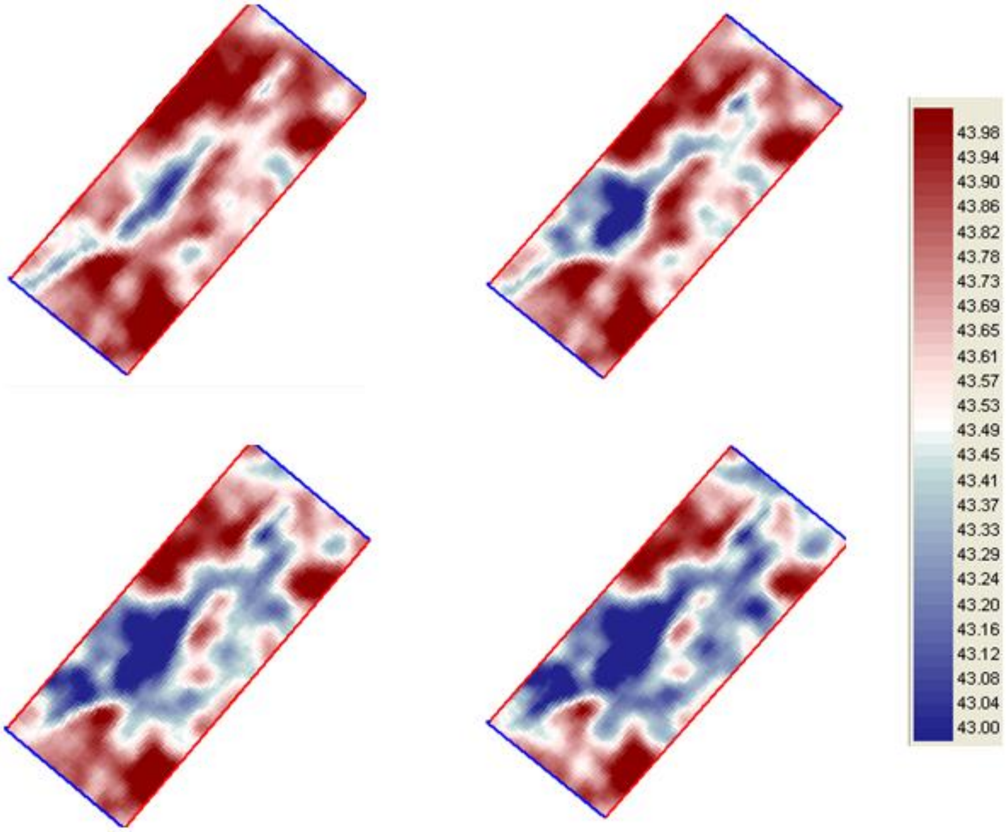

Figure 6.14: Reservoir thickness time at different stages of Waterflooding. Clockwise from top left: Base survey, 1st monitor, 2nd monitor, and 3rd monitor. Notice the heterogeneous variations of reservoir thickness time corresponding to a patchy water distribution within the reservoir.

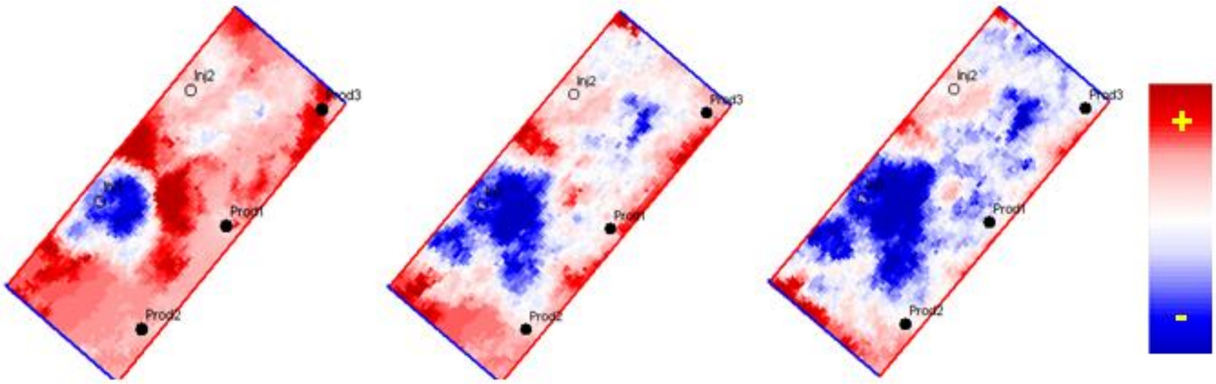

Figure 6.15: time shifts at the 1st monitor (left), the 2nd monitor (centre), and the 3rd monitor (right)

Figure 6.15 shows the computed time shift for the three monitors. A negative time-shift is observed in the water flooded areas of the reservoir. It is worth noting that an increase of water saturation does not automatically mean a negative time-shift (Figure 6.16).

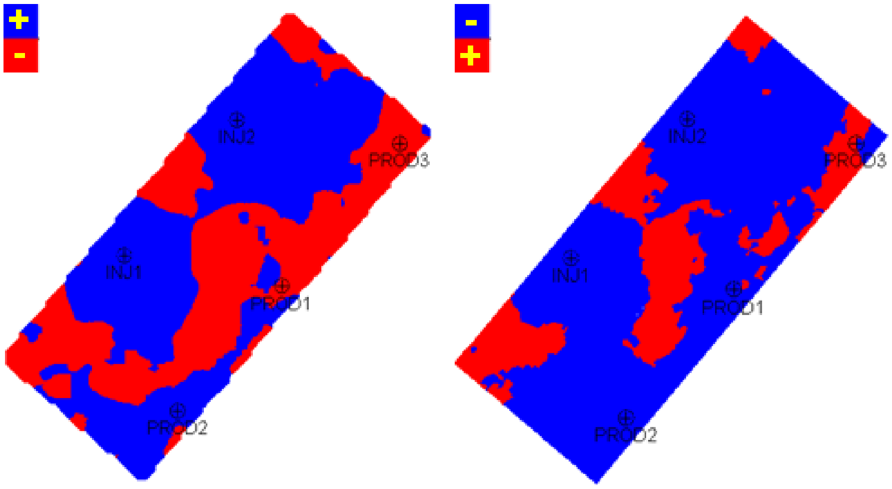

Figure 6.16: Water saturation change and the corresponding time shift at the 1st *monitor time. The colour bar was altered so that positive water saturation change and negative time-shift are represented in blue, while a decrease in water saturation and positive time-shift are represented in red. Visual comparison between the two maps shows good agreement; this agreement is less accurate in the producing side of the reservoir though. Notice that the time shift map captures subtle details of the waterfront.*

6.3.2 Time-lapse amplitude analysis

Time-lapse RMS amplitude maps were computed as the difference between RMS amplitude maps derived from the monitor survey and those derived from the base survey (Figure 6.17).

The water flooded areas are characterised by a dimming in the time-lapse amplitude, while the brightened areas are interpreted as zones where oil slumped down into the aquifer. At the first monitor, the injected water did not reach any of the producing wells yet, which is visible on the RMS map. The water front is clearly visible and as the waterfront proceeds, the wells became partially water flooded. Interpretation of the maps from the different monitors suggest that one should expect very low water cut values at the three wells at the time the 1st monitor was shot. This water cut is higher for wells Prod1 and Prod3 as a consequence of the water being pushed upwards above the original OWC when oil slumped down and replaced it. By the time the 2nd monitor was shot, production well Prod2 is water flooded along with the rest of the producers. Table 6.1 illustrates water cut values extracted from the simulation model. It is worth noticing that the water cut values for well Prod3 actually decreases at the 2nd monitor time, due mainly to the fact the high water cut values at this wells at the 1st monitor were mainly due to the production of aquifer water.

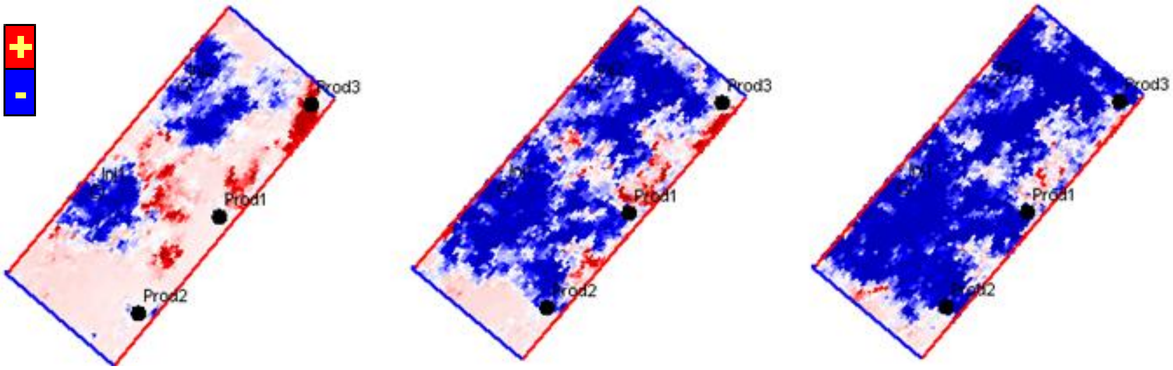

Figure 6.17: Time-lapse RMS amplitude maps at the three monitor surveys: from left to right, 1st monitor, 2nd monitor, and 3rd monitor.

Time Well	1st Monitor	2nd Monitor	3rd Monitor
Prod1	**0.1**	**0.15**	**0.4**
Prod2	**0.03**	**0.20**	**0.68**
Prod3	**0.17**	**0.13**	**0.72**

Table 6.1: Water cut at the three producing wells

6.3.3 Time-lapse RMS amplitude and time-shift attribute analysis

A new attribute was computed as the sum of the normalised time-shift attribute and 4D RMS amplitude attribute. The time-shift+4D RMS amplitude maps show a very good agreement with the water saturation changes (Figure 6.18).

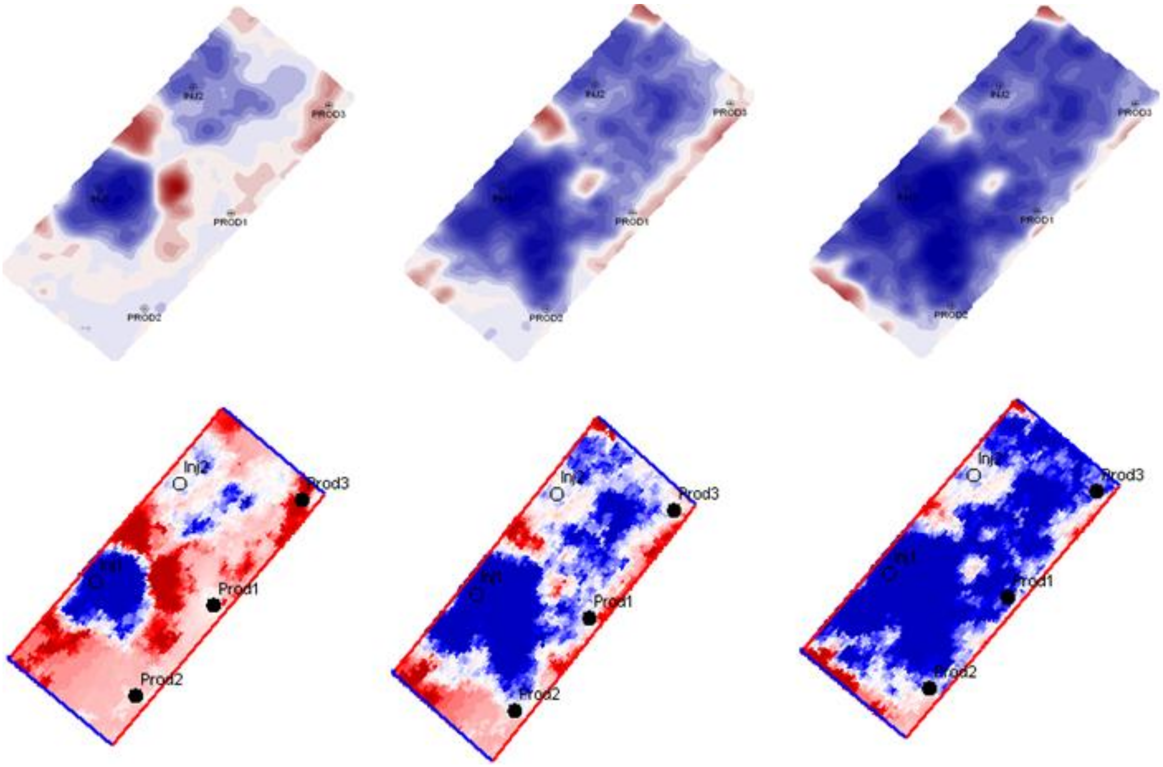

Figure 6.18: Water saturation changes and the time-shift+4D RMS amplitude attribute maps for the three monitors

6.4 Conclusion

Time-lapse signature of Waterflooding processes in turbidite reservoirs can be complex and difficult to interpret. The original and moved oil/water contact can be hard to interpret as it may be masked by reflections from geological interfaces.

Analysis of P-wave and S-wave velocity cubes showed that these two properties respond in different ways to Waterflooding. V_p is sensitive to water saturation changes while V_s is sensitive to pressure changes. V_p/V_s ratio can be used as a robust fluids indicator provided that both the base seismic survey and the monitor seismic survey have the correct velocity model. Petrophysical modelling suggests that P-wave velocity can be extremely sensitive to water saturation changes. Even the smallest changes (less than 10%) would have a noticeable effect on Vp values, which is of crucial importance when time-lapse seismic is to be used in a quantitative way.

Interpretation of time-lapse seismic cross-sections is challenging and the inclusion of different attributes in the interpretation workflow might be necessary in order to assess the complexity of the Waterflooding signature.

Interpretation of time-lapse attribute maps, computed of an RMS average across the reservoir thickness is useful in the global assessment Waterflooding efficiency as they provide a fair indication as to fluids fronts and bypassed oil. But the extrapolation to the vertical dimension may be very challenging in turbidite reservoirs.

Chapter 7

Conclusions and recommendations for future research

In this thesis, Waterflooding processes in geologically complex reservoirs were investigated. The investigation followed three different, yet inter-related directions: reservoir modelling and fluid flow simulation, petrophysical modelling, and seismic modelling and interpretation. This chapter presents a summary of the results from each chapter and the main concluding remarks of the thesis.

Recommendations for further improvement and application of this work are also addressed.

7.1 Conclusions

Several lessons have been learnt from the application of this approach to the different synthetic data cases:

1- Time-lapse seismic is used in a qualitative, semi-quantitative, and quantitative way to monitor Waterflooding processes. For the Time-lapse seismic data to be used in a quantitative way, calibration with other data (production data, etc) is needed.

2- Analytical and numerical engineering techniques were developed to assess the efficiency of Waterflooding processes. At present, numerical simulation models have assumed a considerable lead in Waterflooding efficiency calculations and become the standard tool for such studies. Numerical simulation of Waterflooding processes require the building of a numerical reservoir model, where the reservoir is subdivided into blocks or cells in each of which are reservoir rocks properties and quantities of fluids subject to the laws of fluid mechanics. Their essential advantage is to be able to represent the variations in characteristics of the reservoir, the fluids, the flow rates to the wells and the pressure within the reservoir. Analytical methods aim at generating a relationship between fractional flow and oil recovery. The reservoir is assumed to be zero dimensional and displays a tank like behaviour. The Buckley-Leverett equation is used to describe fluid flow inside the reservoir by determining an expression for the velocity of a plane of constant water saturation passing through the reservoir. A practical application of the equation is through the use of the Welge equation. To account for reservoirs heterogeneities, the reservoir is divided into several layers and recovery efficiency calculations are performed for each layer. The analytical methods tend to over simplify the reservoir geology by not including areal heterogeneities and lateral variations of layers thickness.

3- Permeability and its degree of variation across the reservoir is the most important parameter controlling the displacement efficiency in the case of water injection.

4- The 4D seismic signature of Waterflooding processes is a combination of pressure, saturation, and temperature changes within the reservoir at the monitor time, assuming the reservoir is not geomechanically active. The substitution of oil by water increases the P-wave velocity of the rock, while an increase in pore pressure decreases the P-wave velocity of the rock. During Waterflooding, saturation changes arrive after the pressure changes resulting in three distinct zones inside the reservoir that would exhibit different responses to Waterflooding (Figure 7.1):

- Behind the waterfront: The water saturation and the pore pressure increase ,so V_p can theoretically either increase or decrease. In all of our petrophysical modelling studies, V_p increased by up to 9%, regardless of the reservoir setting or production scenario. This is due to the fact that the saturation effect is stronger than the pressure effect.

- Between the Water Front and the Pressure Front: Water saturation unchanged, while the pore pressure increases so V_p is unchanged or decreases.

- Beyond the Pressure Front: The water saturation is unchanged, the pore pressure is unchanged or decreases, so Vp increase. This phenomenon was not observed in any of our petrophysical simulation studies, as the reservoir pressure equilibrated shortly (few days) after the start of water injection. In real case studies, this behaviour can be observed as a pressure build-up effect in the vicinity of sealing faults and at the boundaries of non-communication reservoir compartments.

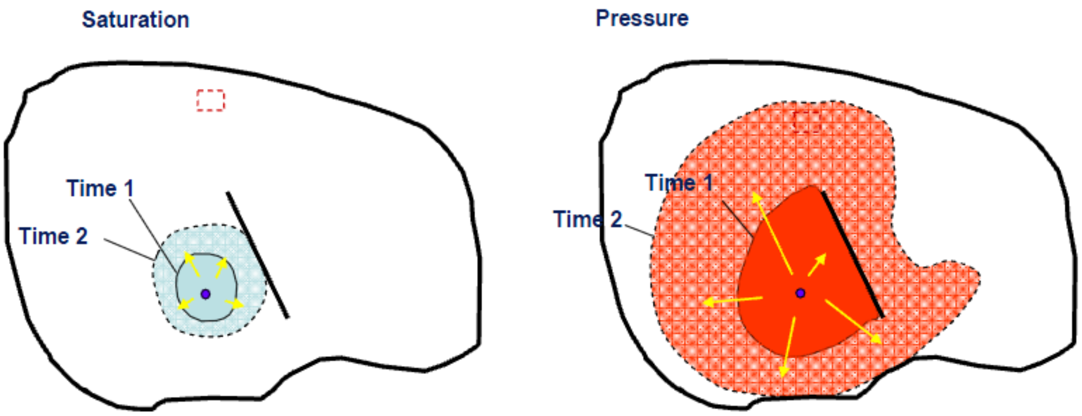

Figure 7.1: Saturation and pressure changes propagate within the reservoir in two different ways.

5- The pressure change has a global effect on the time-lapse seismic signature of Waterflooding. This is mainly due to the absence of compartmentalization inside the reservoir. In compartmentalized reservoirs, it would be useful to isolate the pressure signal from the saturation signal as it gives valuable information about the hydraulic communication between the different reservoir parts and the sealing nature of faults.

6- Time-lapse seismic gave very similar signatures of Waterflooding in idealised reservoirs whether the pressure dropped or remained constant, confirming that the 4D signature of Waterflooding is mainly controlled by the water saturation changes. It did manage to capture the different shapes of the waterfronts resulting from different geological settings.

7- Outcrop based reservoir models are highly recommended when studying heterogeneous reservoirs. They allow for the small heterogeneities, shown to have a significant effect on the efficiency of Waterflooding processes, to be correctly captured and included in the reservoir model. They are of a particular interest when studying turbidite reservoirs.

8- The same reservoir architecture picked up from the outcrop analogue can produce very different seismic response from one reservoir to another due to their different rock properties, misleading the interpretation of the reservoir when high density well control is not available. Accurate properties modelling will highly benefit the understanding of the seismic signature, especially in deep and ultra-deep reservoirs reducing the economic risks. When the seismic modelling is aimed at understanding the time-lapse seismic signature of Waterflooding in a given reservoir, one should construct an accurate database of rock parameters and fluids properties for that very same reservoir.

9- RMS seismic attributes maps are commonly used in time-lapse seismic interpretation. RMS averages are a good statistical measure of the magnitude of a seismic trace. Comparing RMS seismic attributes maps to average maps of reservoir properties (pressure, saturation, NTG, etc) should be performed with great care. Tuning phenomenon should also be considered.

7.2 Recommendations for future work

The investigation presented in this thesis have been developed and applied on synthetic data. Synthetic reservoir models, regardless of how realistic they can be, are merely a simplified representation of the characteristics of the subsurface. Based on lessons learned from this study, further research is needed to refine and make this approach more robust when applied to synthetic data and ultimately real data. This further research could be addressed under the following categories:

7.2.1 Building the simulation model

Virtually every turbidite reservoir contains significant amounts of shale. Shales either divide the reservoirs into separate hydraulic units, or, if they are discontinuous, set a tortuous environment in which fluids flow occurs. Although the sand/shale sequence in the well vicinity may be known, a reliable reservoir description must define quantitatively the lateral continuity of the shale, the shale distribution in un-sampled areas, and the effects of the shales on fluids flow.

Particular care should be paid to populate the reservoir model with the correct permeability values and distribution. Faults and fractures are common in turbidite reservoirs and should be included in the model. Particular care should be paid as to the sealing nature of faults/fractures.

Shales are defined as inactive cells in all our models. They are 100% water saturated and no fluid flow is allowed. As a result, shale characteristics remained constant during the petrophysical modelling workflow. In reality, shales would respond to Waterflooding and their physical properties would change, impacting the time-lapse seismic signal. A correct modelling of shale intervals within the reservoir is necessary if one is to use the time-lapse seismic data in a quantitative way. While it is common to assume that the shale beds are completely impermeable and therefore act as non-conducting barriers to fluid flow in the reservoir when performing reservoir simulation studies, it is crucial to consider the shales as fully active geomechanic, dynamic and elastically stress sensitive elements of the reservoir and to understand how they affect the reservoir stress sensitivity and hence the 4D seismic response (MacBeth et al., 2010). MacBeth et al. (2010) suggest that a precise quantitative prediction of the in situ variation in the elastic properties of the reservoir’s rock-mass with production-induced changes is an essential element of the petro-elastic model that links saturation and pressure changes to the corresponding 4D seismic signatures.

Figure 7.2 shows the stress sensitivity curves for reservoir sand and shale after pressure equilibration has occurred. Whilst the sands always compact as a result of the pressure drop, the shales will experience extension at first. However as time progresses the shales reverse their geomechanical behaviour and start to compact as the effective stress applied to the shales becomes increasingly more compressive.

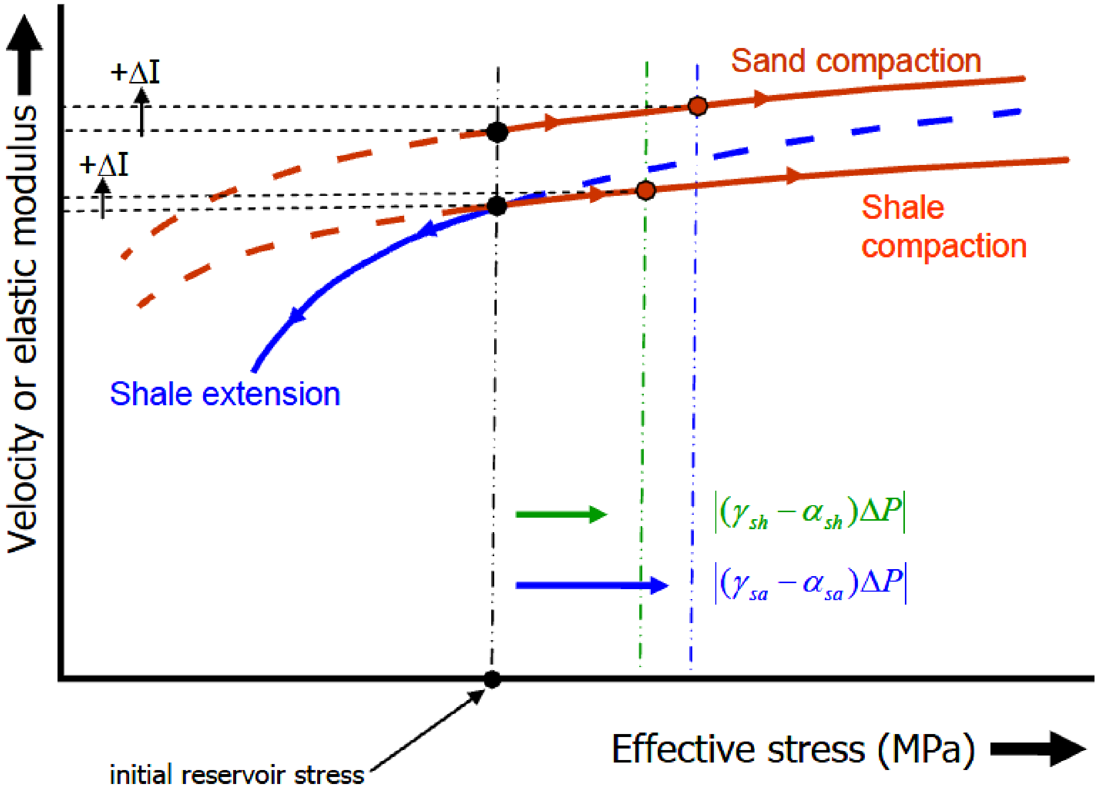

Figure 7.2: sand and shale stress sensitivity curves. (after MacBeth et al., 2010)

7.2.2 Petro-elastic modelling

An accurate Petro-Elastic model is of paramount importance when performing forward seismic modelling. To accurately replicate the observed time-lapse seismic signature of a given reservoir, one must account for the overburden heterogeneities. Domes et al. (2009) showed that errors originating from sand channels, faults or geomechanical changes above the reservoir are supposed to impact the time-lapse data.

In our modelling workflow, the overburden and underburden were defined as a homogeneous half-space, which is a flawed simplification of reality. In fact, the overburden is a part of the sedimentary basin enclosing the reservoir and it features all kind of heterogeneities common to sedimentary formations (Figure 7.3) (channels, faults, fractures, etc). The overburden also undergoes physical changes due to production from the reservoir which would influence the time-lapse seismic data.

Domes et al. (2009) suggest that the errors in the time-lapse amplitude attributes can be separated into errors originating from the acquisition non-repeatability and amplitude errors which are due to the overburden heterogeneities. Indeed, they showed that Channels in the overburden above the Nelson Field, North Sea, are found to cause errors in the time-lapse amplitudes. The magnitude of these amplitude errors decreases with increased repeatability of the monitor survey's source and receiver positions.

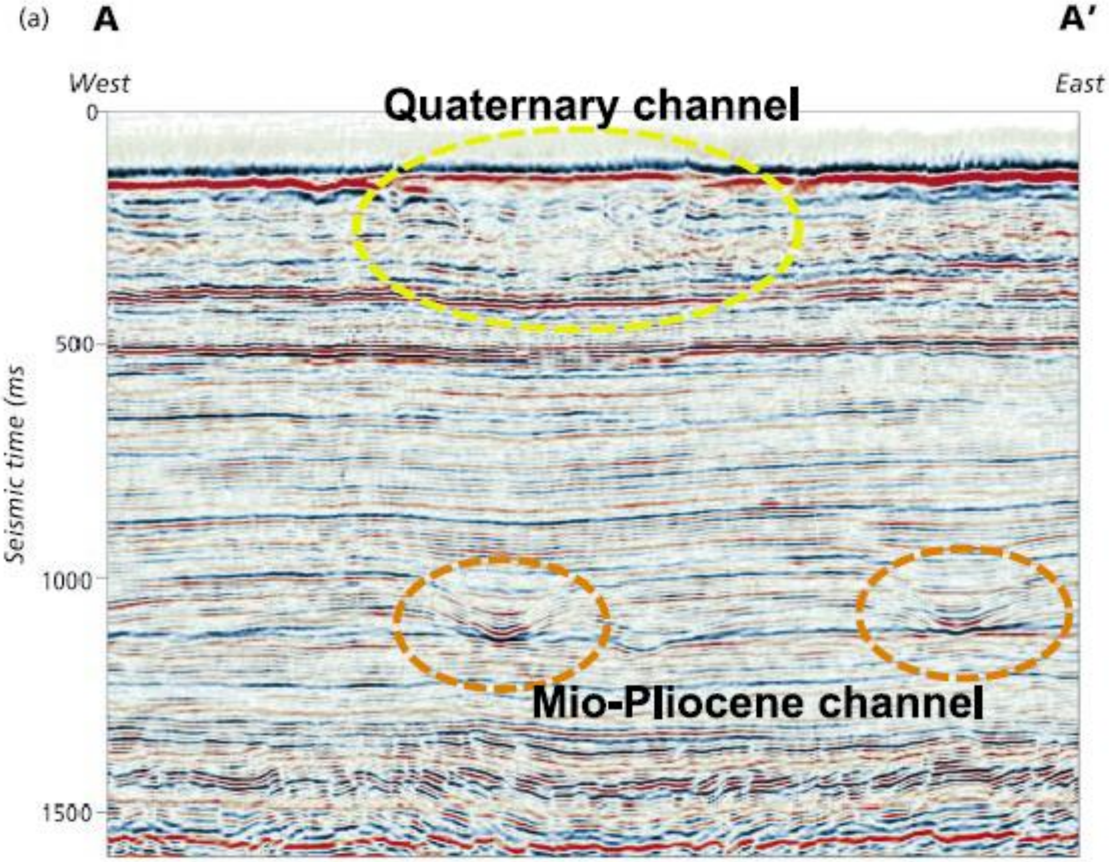

Figure 7.3: Typical Central North Sea seismic cross section. One Quaternary channel (yellow dashed line) and two Mio-Pliocene channels (brown dashed line)are marked (after Domes et al., 2009).

Domes et al. (2009) modelled the impact of two different types of channels in the overburden on the 4D seismic amplitude for two cases with poor and good repeatability. They found that the overburden channels have an effect on the time-lapse seismic signal for both cases, but that this error reduced by more than 50% in the case of high repeatability (Figure 7.4).

Therefore, it is concluded that the Mio-Pliocene and Quaternary channels induce locally significant amplitude errors, equal or greater than production-induced amplitude changes, thus impeding the time-lapse interpretation and any further quantification of the 4D signal.

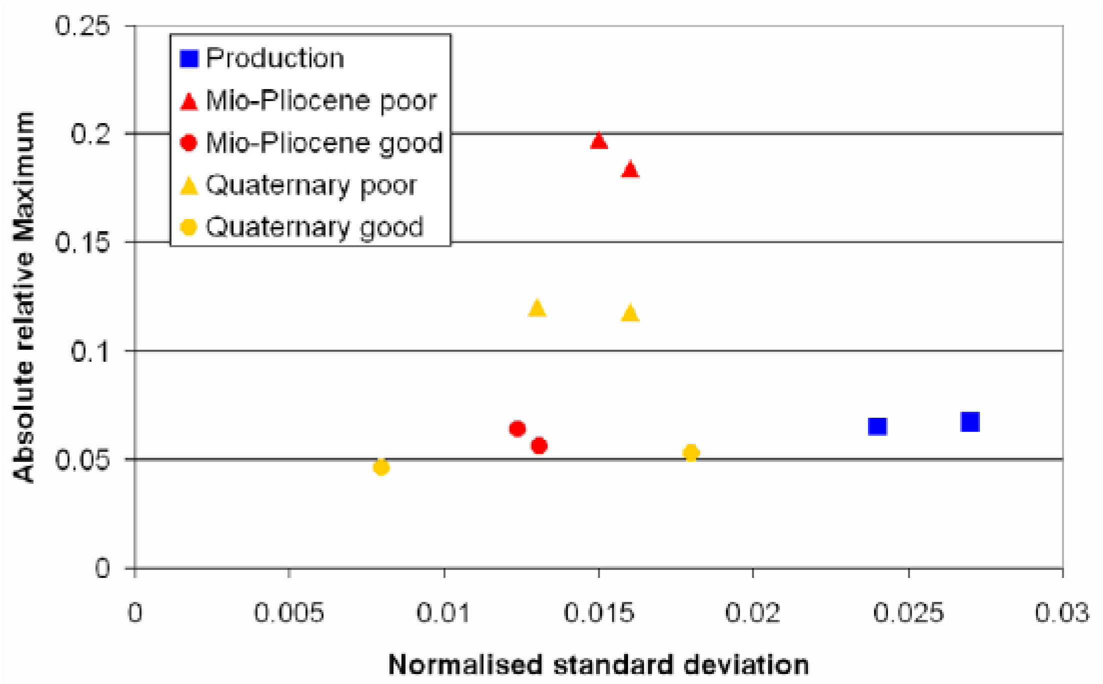

Figure 7.4: Amplitude errors caused by the Mio-Pliocene and Quaternary channel in case of the poor and good repeat survey.(after Domes et al., 2009). The red triangles represent the error caused by the Mio-Pliocene channel, with and without production, in the case of poor repeatability. The red circles represent the error caused by the Mio-Pliocene channel, with and without production, in the case of good repeatability. The yellow triangles represent the error caused by the Quaternary channel, with and without production, in the case of poor repeatability. The red circles represent the error caused by the Quaternary channel, with and without production, in the case of good repeatability. The blue squares represent the time-lapse seismic amplitude change due to production for the case of poor and goof repeatability.

7.2.3 Seismic modelling and interpretation

In reservoir characterization, the most commonly used seismic modelling technique is 1D convolution coupled with Zoeppritz equation. This approach was used in the creation of synthetic seismic all along this thesis. Several other techniques for seismic modelling were discussed in the geophysical literatures. Bourgeois et al. (2005) performed seismic modelling on a realistic turbidite reservoir model using two seismic modelling methods (1D convolution and 3D wave equation) and found that the resulting seismic data sets are in good agreement however they represented different degrees of complexity (Figure 7.5)

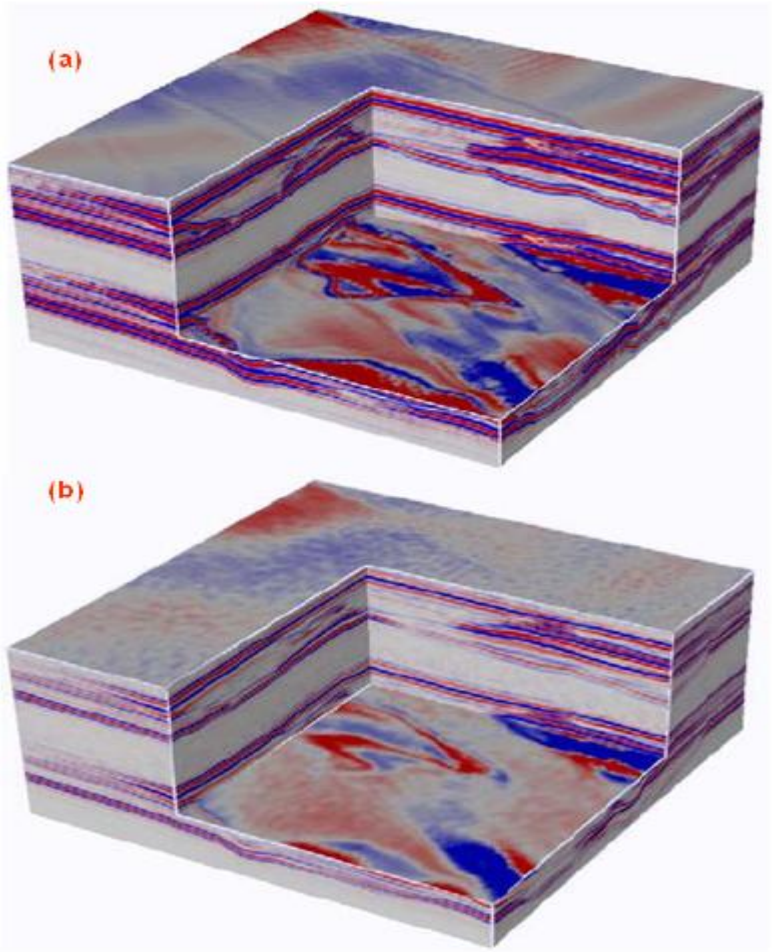

Figure 7.5 : synthetic seismic from a realistic turbidite reservoir model. (a) 1D convolution seismic, (b) 3D elastic modelling seismic. The 3D modelling have better agreement with the observed seismic data. (after Bourgeois et al., 2005)

Thore (2006) used both 1D convolution model and Finite Difference modelling to create synthetic seismic for a real West African deep offshore turbidite reservoir. He concluded that the two methods produced comparable synthetic seismic but also presented some differences (Figure 7.6). The origin of the differences is difficult to identify but can be assigned to the lateral heterogeneity of the reservoir model which is “smoothed” by the FD scheme and processing sequence and which is brutally reproduced by the multi 1D modelling with the Zoeppritz equation.

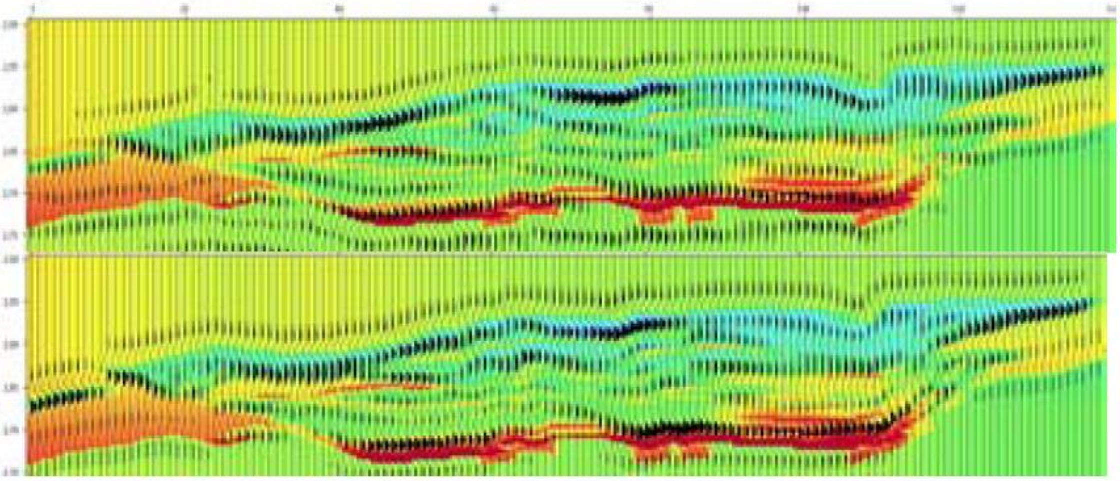

Figure 7.6: 0° section synthetic seismograms. Comparison of Zoeppritz (top) and FD (bottom) synthetic seismograms. (after Thore, 2006)

1D convolution techniques are simpler and faster to implement, therefore cheaper, than FD and 3D wave equation seismic modelling techniques and one should opt for the one method that would be suitable for the purpose of the study. For example if one is to estimate the expected change in seismic amplitude attributes due to production (through Gassmann fluid substitution equations, as a part of a 4D feasibility study), it is perfectly legitimate to use the convolution technique. However, if the synthetic seismic is to be inverted or used in reservoir characterisation workflows, then one must be careful as small differences in the seismic data would translate into large differences in the impedance after inversion that may lead to misinterpretation when compared with the observed data.

7.2.4 Application to real data

Simulator to Seismic study can be performed over a given reservoir, by combining petrophysical, engineering, and geophysical data into an integrated workflow. The calibration of the rock physics model (pressure sensitivity model and fluids model) is crucial to generate reliable time-lapse seismic attributes that can be used in conjunction with conventional seismic attributes to get more insight into the interpreted time-lapse seismic anomalies. Amini (2009) shows the importance of the calibration process by creating synthetic seismic for the Shiehallion field. Figure 7.7 shows synthetic V_p, V_s and Rho computed with a calibrated and non-calibrated PEM at a well location. The two data set are compared to V_p, V_s, and Rho values extracted from logs at that well location.

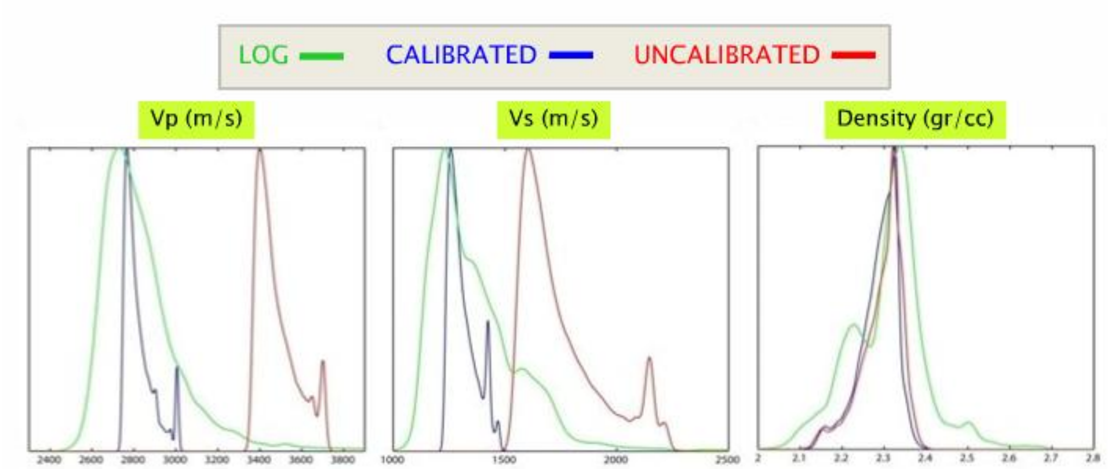

Figure 7.7: Calibration of the PEM reduces the error in the petrophysical modelling process. (after Amini, 2009)

Pressure sensitivity models for a particular reservoir would be facies dependant and ultrasonic laboratory measurements are generally used to generate relationships between velocities (or elastic modulus) and confining pressure for a specific reservoir.

Well data and ultra-sonic measurements are used to calibrate the equations used in the petrophysical modelling to determine the correct rock properties (matrix density, matrix bulk modulus, etc) and fluids properties. Shale cells and inactive cells have to be assigned realistic values and can be approximated from well logs and ultra-sonic measurements. During the 1D convolution process, a calibrated wavelet extracted from the observed seismic can be used instead of the generic Ricker wavelet.

Figure 7.8 shows a proposed workflow to apply the sim2seis technique on a real reservoir.

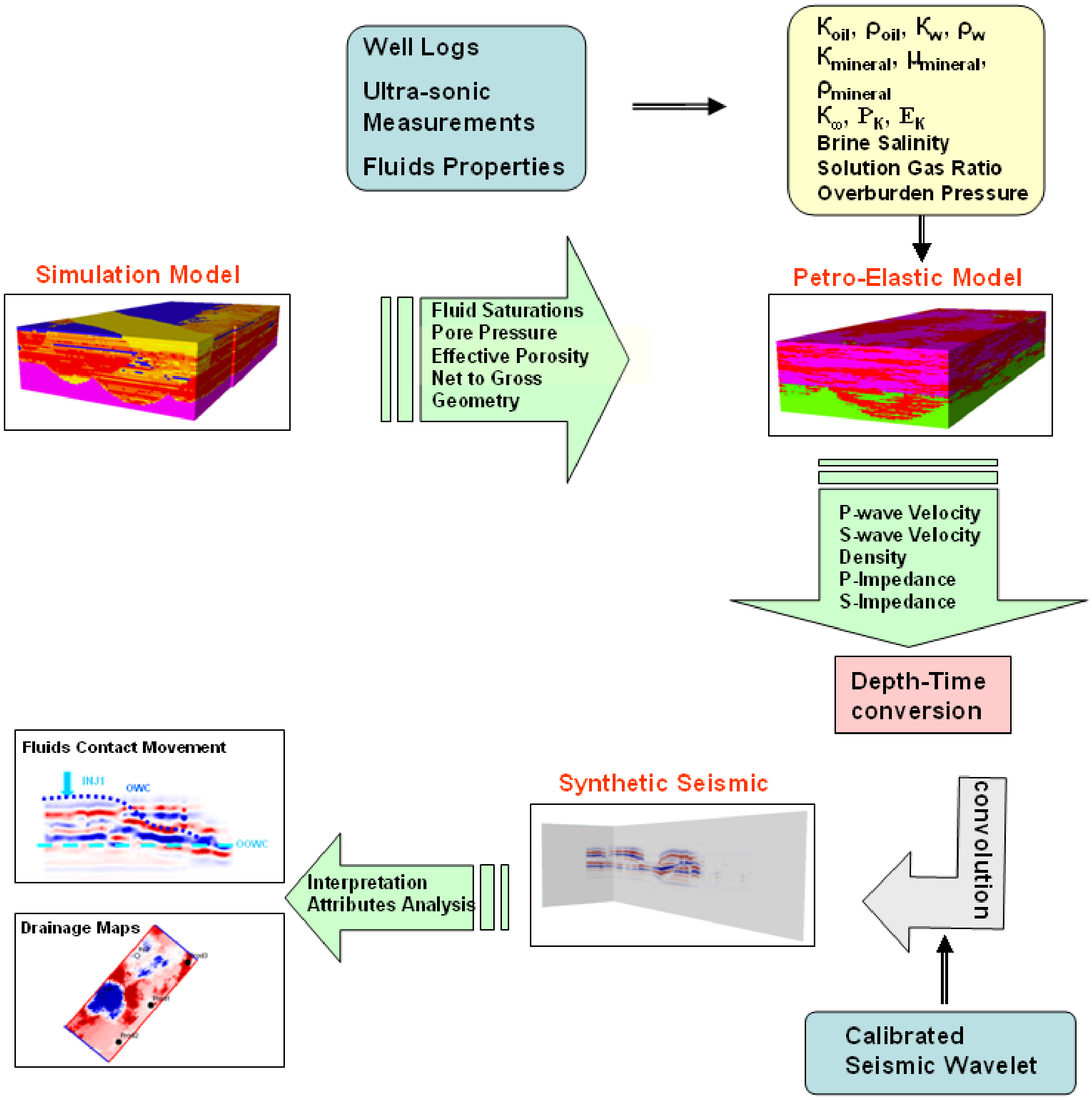

Figure 7.8: Proposed Sim2Seis workflow for application on real data.

Appendix A

Analytical methods for Waterflooding efficiency calculation

The impact of water injection on the production of oil was first appreciated in the Bradford field, USA, in the early 1900's, where the production rate with Waterflooding, was five times higher than the continuously declining rates under primary recovery (Willhite, 1986) (Figure A.1). Waterflooding process was poorly understood in the past and was practiced more as a rudimentary art. It is not until the late 1940's and 1950's, as naturally depleted reservoirs approached their economic limit in the United Sates, that operators sought to increase reserves and extensive research was carried out. This, combined with field experiences helped establish a scientific understanding for Waterflooding.

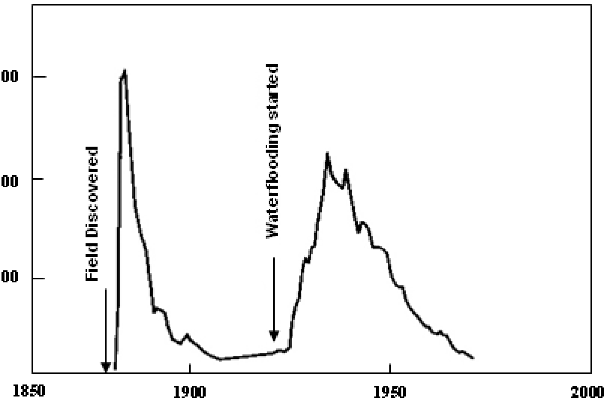

Figure A.1: Production history of the Bradford field. (after Willhite, 1986)

A tremendous effort has been made by the oil industry and others as early as the 1930's to develop an understanding of multiphase fluid flow through porous media. Much of this effort concerned displacement of a non-wetting phases such as gas or oil by water (Kimbler et al. 1962). A vast literature of concepts, field and laboratory data, experimental techniques and mathematical expressions has been developed. Many parameters believed to be important have been investigated. These include connate water saturation; relative permeability-saturation relations, sample wettability, and waterflood scaling (including the effect of such variables as pore size, flow rate, viscosities and interfacial tension of the fluids, sample size). Much of this work was aimed directly toward calculating reservoir performance.

A.1 Oil/water flow in porous rocks: theoretical background

The drainage of oil from a porous rock to producing wells occurs to a small extent because compressed rock, water and oil relax and expand when the high subsurface pressure is reduced through oil production (Clark, 1969). A large portion of the reservoir oil, however, must be replaced by some fluid; oil cannot be removed from its initial location in the rock pore space unless something takes its place. Therefore, the drainage of oil occurs naturally to a major extent because water or gas moves through the oil-filled pore spaces.

Oil recovery by Waterflooding can best be illustrated by observing what happens inside an individual pore channel during displacement. Figure A.2 shows two separate pore channels of different size. The large channel represents higher, and the small, lower permeability. Connate water is located adjacent to the sand grains, while oil occupies the middle of the pore channel. Reservoirs with this type of fluid distribution are termed water-wet reservoirs, a classification to which a large majority belong.

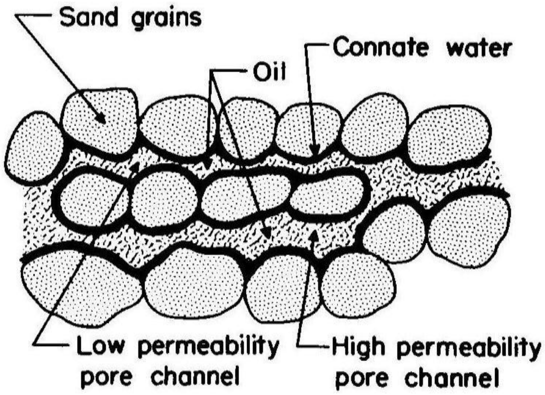

Figure A.2: Original oil and water saturations in pore space at equilibrium. (after Clark, 1969)

In a water-wet system, water forms a cup-like oil-water interface which tends to displace all the oil from a given point in the pore channel (Figure A.3).

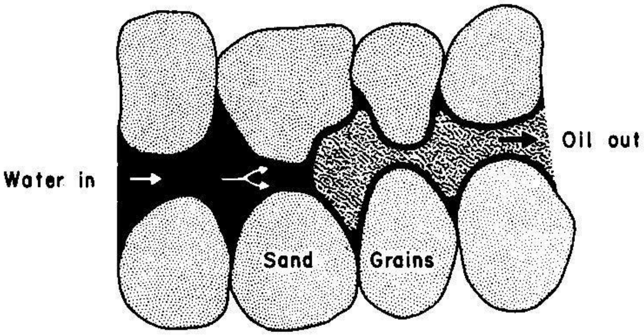

Figure A.3: Natural displacement of oil by water in a single pore channel. (after Clark, 1969)

Variations in the size and shape of the pore spaces in porous rocks control to some extent the degree of oil recovery from the rocks. Under waterdrive, the capillary forces cause water to move faster into the smaller, low permeability channels. As water saturation builds up in the large pore channel and oil saturation is reduced, the oil tends to take the shape of a smaller thread of oil. As this thread gets smaller, the interfacial tension increases until the surface snaps at points A and B along the pore channel, thus forming small droplets of oil which remain trapped within the pore spaces because their surface tension is greater than the forces acting to push them through the pore channel (Figure A.4). A large part of the residual oil in the reservoir will be trapped in the pore channels by the interfacial forces inherent between water and oil.

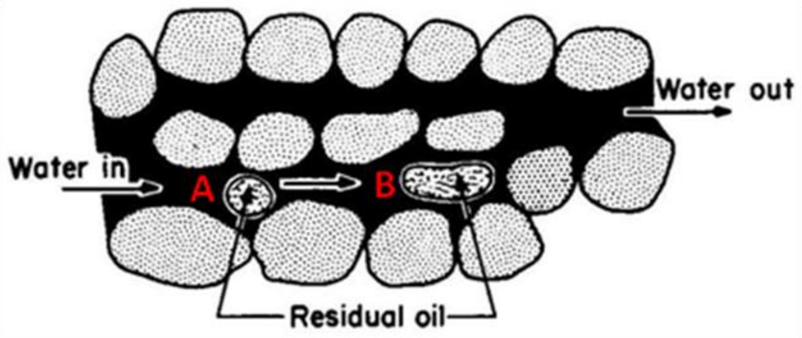

Figure A.4: Water drive leaves residual oil in sand pore channel as they trapped by interfacial forces. (After Clark, 1969)

The fluid displacement process requires contact between the displacing fluid and the displaced fluid. The movement of the interface between displacing and displaced fluids and the breakthrough time associated with the production of injected fluids at producing wells are indicators of sweep efficiency. One of the simplest and most widely used methods of estimating the advance of a fluid displacement process is The Buckley-Leverett displacement theory (Buckley and Leverett, 1942).

In their famous paper published in 1942, Buckley and Leverett described the mechanism of oil displacement by water (or gas). In fact, the water moves from a region of high water saturation into one of lower water saturation, removing the oil and converting the invaded region to one higher in water saturation. The amount of oil displaced by water during the process of Waterflooding depends upon the relative ease with which the fluids can move. The readiness with which a fluid flows through sand increases with its saturation in the sand. At the beginning of the water injection, the oil saturation in the sand may be high while the water saturation may be low; oil will flow easily and the water to a small extent only, if at all.

When two immiscible fluids, such as oil and water, are together in contact with a rock face, one fluid will preferentially adhere to the rock, this fluid is called the wetting fluid while the other fluid is called the non-wetting fluid. Depending on the wetting properties of the fluids there are essentially two different types of displacement in two-phase flow in porous media, drainage and imbibition. The drainage displacement occurs when a non-wetting invading fluid displaces a wetting fluid. The opposite case, imbibition, occurs when a wetting fluid displaces a non-wetting fluid. The mechanisms of the displacements in drainage and imbibition are quite different and the two cases should not be confused. The displacement of oil by water in a water wet reservoir is, therefore, an imbibition process, while the displacement of water by oil, in the same type of reservoir is a drainage process (Figure A.5). As imbibition proceeds, the permeability of the sand to oil will continuously decrease while the permeability to the water will continuously increase (Figure A.5), until the final part of the process where huge quantities of water are injected to displace only a slight amount of additional oil.

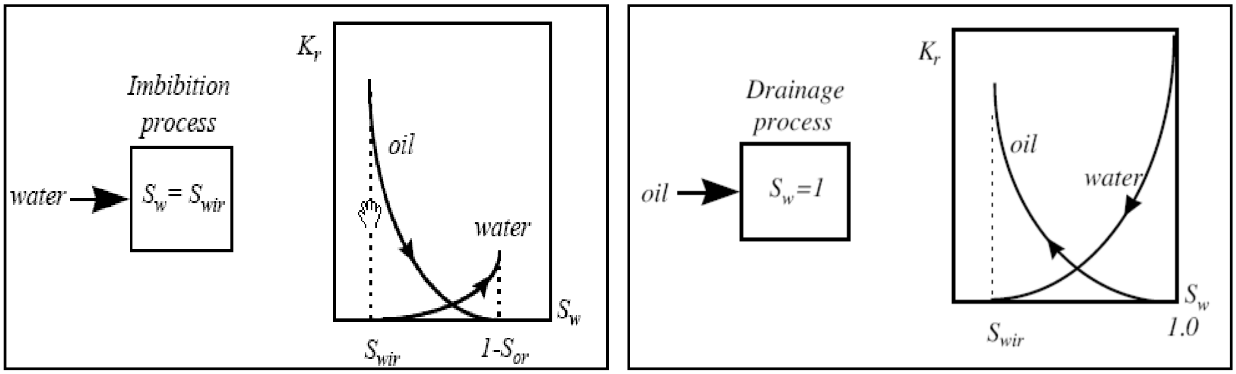

Figure A.5: Effect of saturation on relative permeabilities to water and oil in unconsolidated sands (after Kleppe, 2007)

Buckley and Leverett determined an expression for the velocity of a plane of constant water saturation passing through a core plug based on the results of experimental observations of the flow of mixtures of oil and water through sand. They derived their equation for a one dimensional displacement of immiscible fluids and with a constant pressure gradient throughout the Waterflooding. They applied the physical principle of mass conservation for displacement at constant pressure, as follows:

$$\left(\frac{\partial S_w}{\partial t}\right)_u = -\frac{q_T}{\phi A}\left(\frac{\partial f_w}{\partial u}\right)_t \tag{A.1}$$

where:

S_w = water saturation

t = time

u = distance along path of flow

q_T = total rate of flow through section

Φ = porosity

A = cross-sectional area

f_w = fractional flow of water

$f_w = \frac{q_w}{Q_T}$ $f_w = \frac{q_w}{q_T}$; where q_w = volumetric flow rate of water

This equation can be transformed to:

$$\left(\frac{\partial u}{\partial t}\right)_{S_w} = \frac{q_T}{\phi A}\left(\frac{\partial f_w}{\partial S_w}\right)_t \tag{A.2}$$

This states that the rate of advance of a plane that has a certain fixed saturation is proportional to the change in composition of the flowing stream caused by a small change in the saturation of water. By neglecting gravity and capillary pressure difference effects, f_w can be written as:

$$f_w = \frac{1}{1+\dfrac{K_{ro}\mu_w}{K_{rw}\mu_o}} \tag{A.3}$$

where K_{ro} and K_{rw} are the permeabilities of the sand to oil and water respectively, while μ_o and μ_w are the viscosities of the two fluids. The relation between the permeabilities ratio $\frac{K_{ro}}{K_{rw}}$ and the water saturation S_w is determined experimentally from the relative permeabilities curves for the specific sand being flooded. Then the relations between S_w and f_w and between $\frac{\partial f_w}{\partial S_w}$ and S_w are derived from equation (A.3). Assuming that $\frac{\partial f_w}{\partial S_w}$ is only related to S_w, being constant for a fixed S_w, from equation (A.2) it can be seen that each water saturation S_w moves through the porous rock at a constant velocity v

$$v = \frac{Q_w}{\phi A}\frac{df_w}{dS_w} \tag{A.4}$$

where Q_w is the total amount of water entering the system.

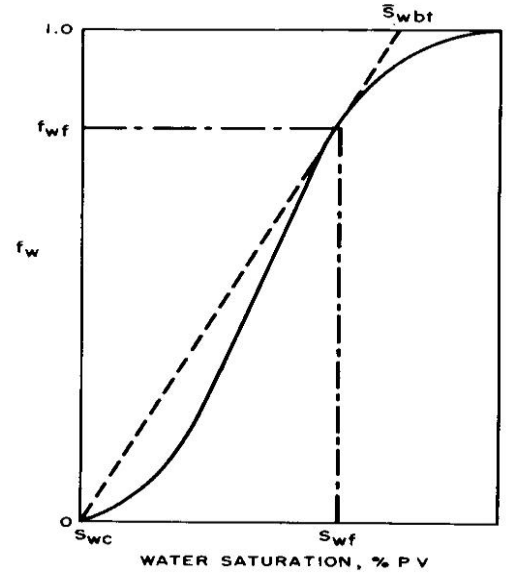

Figure A.6: Fractional flow for an unfavourable mobility ratio (after Willhite, 1986).

Equation (A.4) is the Buckley-Leverett equation, also known as the frontal advance equation. The solution of this equation, for specified boundary conditions, gives the saturation profile (Figure A.7).

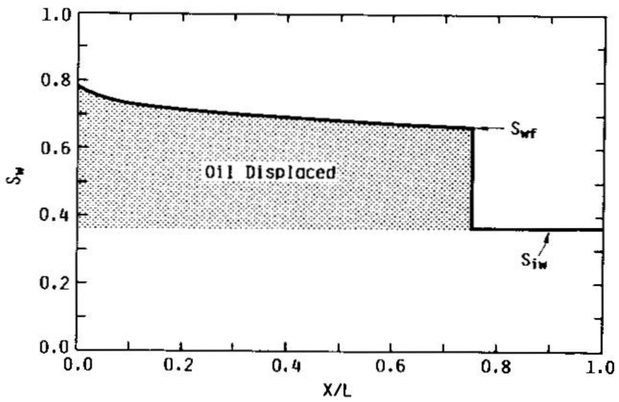

Figure A.7: saturation profile computed from the Buckley-Leverett solution (after Willhite, 1986). Notice the shock front at the flood front saturation.

The tangent point shown in Figure 2.6 defines the breakthrough or flood front saturation S_{wf} (Willhite, 1986). In the saturation profile (Figure A.7), S_{wf} corresponds to a discontinuity, called the saturation shock front. It is worth noting that the shape of the saturation profile between the initial water saturation, S_{wi} and the flood front saturation, S_{wf} cannot be predicted from the Buckley-Leverett solution, but it is rather approximated to be one step increase resulting in the shock front illustrated in Figure A.7.

The Buckley-Leverett theory was developed for a one-dimensional core flooding experiment. Dake (2001) states that since this theory is basically a statement of material balance, and material balance is zero dimensional, the Buckley-Leverett equation can be used to describe Waterflooding of a reservoir, quite irrespective of the system's size or shape.

A.2 Waterflooding performance calculation

A.2.1 Analytical methods for Waterflooding efficiency calculation

During the first half of the twentieth century, a great deal of research was carried on in idealized laboratory conditions, from which certain trends and theories have been indicated. The aim of this research work was to increase the engineers' knowledge of recovery processes and to develop techniques for the prediction and monitoring of their efficiency. Many techniques have been developed for the case of Waterflooding performance prediction but generally the methodology used for the calculation was universal and can be summarized in the graph shown in Figure A.8. These early hand-calculation methods are typified by the zero-dimensional, material balance calculation. In these analytical calculations, there was no need for detailed geological and production data as the reservoir was treated as a simple tank having average characteristics and properties.

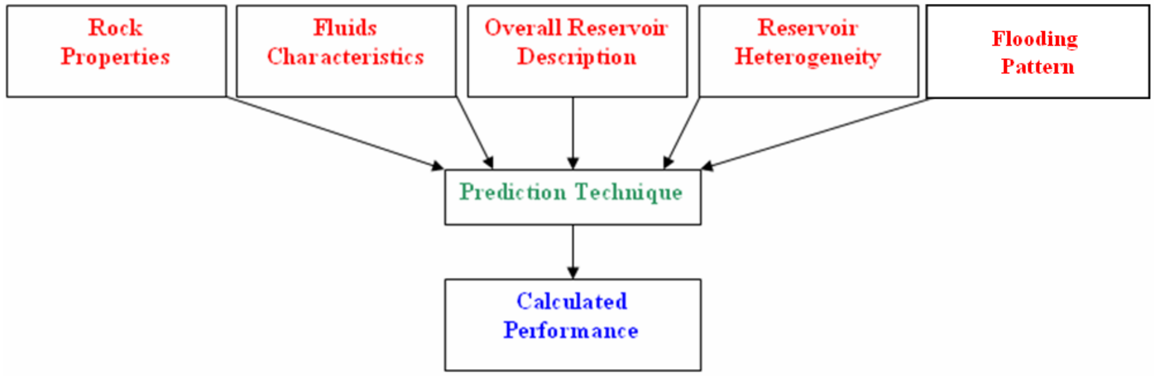

Figure A.8: Waterflooding performance prediction methodology (after Craig, 1973, modified)

A practical use of the Buckley-Leverett equation for computing oil recovery after a plug flooding was described by Welge (1952). Welge's paper presented an analytical method to calculate oil recovery as a function of the cumulative water injected. Welge determined the average water saturation, $\bar{S}_w$ in a core plug as the flood progressed and then applying equation (A.5) he accounted for the oil recovery:

$$N_{pd} = \bar{S}_w - S_{wc} \qquad \text{(PV)} \qquad \text{(A.5)}$$

where N_{pd} is the dimensionless cumulative oil recovery expressed in pore volume and S_{wc} is the connate water saturation.

To determine the average water saturation behind the flood front, Welge used a simple graphical technique. First, the fractional flow relationship is drawn (Equation A.3). Then, drawing the tangent from $S_w = S_{wc}$ to the fractional flow curve determines, at the point of tangency, the shock-front or breakthrough saturation, as the water first reaches the producing end of the plug. Extending the tangent to intersect the line $f_w = 1$ gives the average water saturation in the core plug at breakthrough, $\bar{S}_w$ (Figure A.9a).

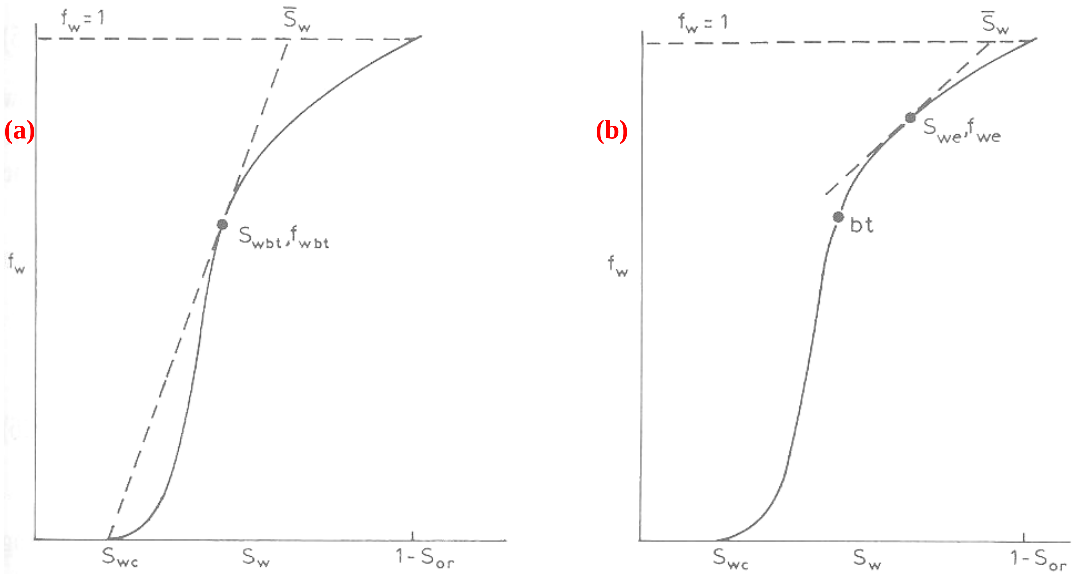

Figure A.9: Application of the Welge technique: (a) at breakthrough, (b) from breakthrough to flood-out (after Dake, 2001).

At this stage of the flooding, the oil recovery calculation is straightforward. As no water has been produced, all the injected water must have displaced an equal volume of oil, so at breakthrough:

$$N_{pd} = \bar{S}_w - S_{wc} = W_{id} \qquad \text{(PV)} \qquad \text{(A.6)}$$

where W_{id} is the dimensionless cumulative water injected in pore volumes.

After breakthrough, the procedure is to move around the fractional flow curve from $S_w = S_{wbt}$ to $S_w = 1 - S_{or}$ (Figure A.9b) choosing values of S_{we}, the increasing water saturation at the producing end of the plug as the flood progresses. Each time a new value of S_{we} is selected, extrapolation of the tangent at that point to the line $f_w = 1$ gives the increasing value of the average water saturation, $\bar{S}_w$, from which the recovery can be evaluated.

Waterflooding led to the development of one-dimensional techniques such as the Buckley-Leverett equation. Welge's graphical method of solution of the Buckley-

Leverett equation enabled the wide spread use of the method. These two works established the foundation for analytical design and evaluation of waterflood performance. More complications were later studied, such as layering which was simulated by methods such as the Dykstra-Parsons method (Dykstra et al., 1950) or the method presented by Stiles (Stiles, 1949) to calculate Waterflooding efficiency in layered reservoirs where there is no pressure equilibrium between the different layers.

A.2.2 Numerical methods for Waterflooding efficiency calculation: Fluids flow simulation

The advent of numerical simulation models revolutionised the techniques used in reservoir management. Computers took over as the main tool in the hands of reservoir engineers. The potential of simulation was recognized in the late 1940's and early 1950's by many companies in the oil industry. Their commitment of effort both to fundamental research on numerical analysis and to development of practical method for using available computers resulted in the development of simple yet useful, simulator by the mid 1950's. Nowadays, numerical reservoir simulators are widely used, primarily because they can solve problems that cannot be solved by analytical approaches. Reservoir simulation can project future performance of reservoirs. It can also be used to conduct sensitivity analysis on reservoir parameters. Simulation is the only way to describe quantitatively the flow of multiple phases in a heterogeneous reservoir having a production schedule determined not only by the properties of the reservoir, but also by market demand, investment strategies and government regulations (Figure A.10).

Figure A.10: Input and Output for a reservoir simulation model.

Reservoir simulation is the main tool for reservoir management. The first step in building the reservoir model consists of the integration of all the static (data acquired before the start of production) data available, i.e. the geology of the reservoir, well data and seismic data into a fine scale geological model. Seismic data permits the definition of the reservoir structure and the identification of its aerial and vertical extent by mainly identifying the top and bottom of the reservoir, and faults extent and positions, etc. In exploration and appraisal wells, logs and core samples are acquired. Log data and laboratory tests on cores reveal detailed information about the reservoir lithology and properties.

The resulting geological model is too fine-scaled; with cells in the order of tens of meters aerially and meters vertically. A typical geological model for an average seized reservoir comprises millions of cells. Running fluid flow simulation with such a detailed model is simply beyond the current computational capabilities. Generally, the geological model is up-scaled and the simulation is run on the up-scaled model (Figure A.11).

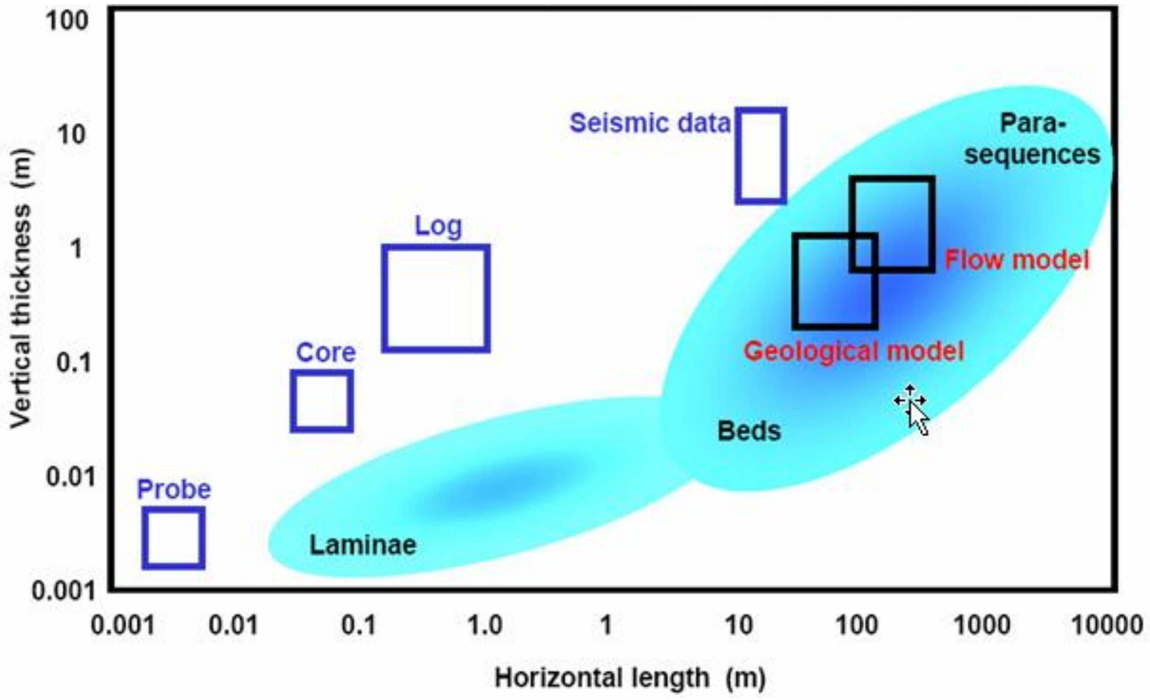

Figure A.11: Geological and simulation models scales (after Pickup and Hern, 2002, modified by Barkvo, 2004)

For the numerical simulation of Waterflooding, a reservoir simulation code solves the two-phase flow equations (Equations 2.7 and 2.8). These non-linear partial differential equations (PDEs) are derived from material balance equations and Darcy's law.

$$\nabla\left(\frac{kk_{ro}}{\mu_o B_o}\nabla P_o\right)-q_o=\frac{\partial}{\partial t}\left(\frac{\phi S_o}{B_o}\right) \tag{A.7}$$

$$\nabla\left(\frac{kk_{rw}}{\mu_w B_w}\nabla P_w\right)-q_w=\frac{\partial}{\partial t}\left(\frac{\phi S_w}{B_w}\right) \tag{A.8}$$

$$P_w = P_o - P_{cow}$$

$$S_o + S_w = 1$$

where:

k is the absolute permeability

k_{ro} and k_{rw} are the relative permeabilities to oil and water, respectively

μ_o and μ_w are the viscosities of oil and water, respectively

P_o and P_w are the oil and water pressure, respectively

S_o and S_w are the oil and water saturations, respectively

B_o and B_w are the formation volume factors for oil and water respectively

and P_{cow} is the capillary pressure between oil and water.

All the simulation studies described in this thesis were performed using the ECLIPSE™ black oil simulator. The ECLIPSE™ Black oil simulator uses a three-component model for reservoir situations in which oil reserves and oil recovery need to be known but the effects of fluid phase composition on flow behaviour do not need to be considered. Eclipse solves these coupled equations after discretisation with finite differences technique; it uses an iterative algorithm known as the IMPES approximation, which stands for Implicit in Pressure, Explicit in Saturation.

Simulation models offer engineers the possibility to run different scenarios, with different production strategies constrained with economical factors, to forecast production. In order to have reliable predictions, the simulation model has to be matched to the real field data in a process known as history matching (Figure A.12). To fit the observed behaviour or dynamic data, the reservoir simulation model parameters are perturbed. The reservoir simulation model is defined by a large set of parameters, some of which are specified for each grid block, others apply to the entire model. Perturbing all parameters involved is not feasible from a computational perspective. Moreover, the amount of data is insufficient to justify resolving all parameters. In other words, the problem is underdetermined; more than one combination of parameters fits the observed data. The parameter space has to be reduced by defining only a few parameters to be perturbed. This process, referred to as parameterisation, can be performed using different approaches and is based on experience or uncertainty and sensitivity analysis of the parameters. Parameterisation affects the type and quality of the solution that is obtained by history matching. Only when the model fits the historical behaviour of the actual reservoir, one may trust production forecasts and manage the reservoir accordingly.

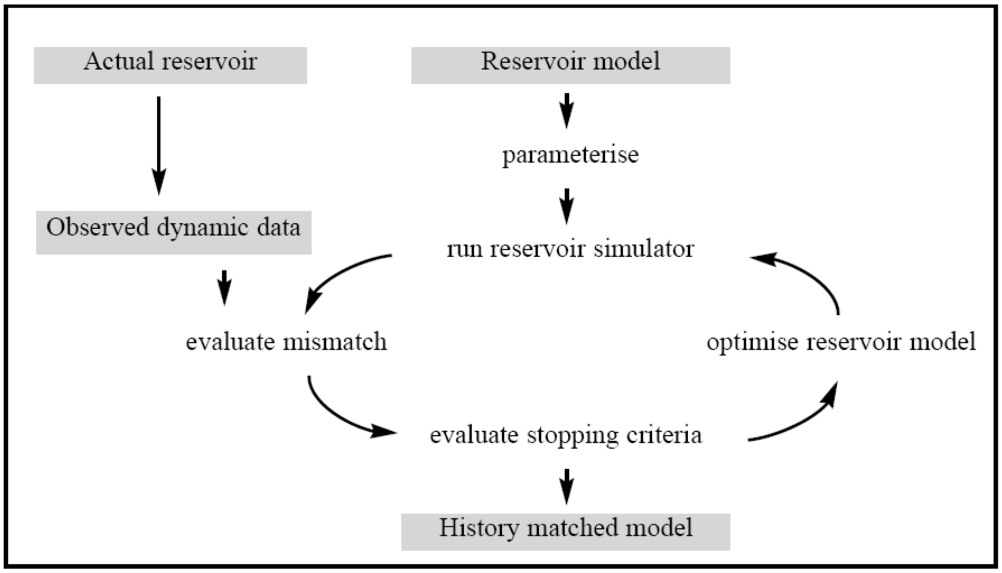

Figure A.12: History matching workflow (after Oldenziel, 2003)

Appendix B

Seismic characteristics of turbidite reservoirs

Advances in seismic reflection imaging have been a crucial element in the development of deepwater exploration. It significantly reduced the geological risk to acceptable levels (Rudolph, 2001). Advanced seismic imaging techniques, such as prestack depth migration (PSDM) have become critical tools for imaging deepwater traps during both discovery and appraisal allowing the imaging of the reservoir architecture and field extent in geologically complex settings (Weimer, 2004).

Different turbidite systems have different seismic stratigraphic responses. Gravel-rich turbidite systems occur near highland areas associated with fault-bounded basins. Deposition in proximal areas is by avalanching and debris flow whereas turbidite processes dominate toward the centre of the basin as flows become more fluidized. This results in poorly sorted deposits at the edges of the basins and well sorted channels basinward. They appear on 2D seismic as externally wedge shaped and show internally slightly diverging reflections toward the fault and converging reflections basinward. On 3D seismic, the complexity of sediments delivery systems is more accentuated and channels and chutes sometimes can be resolved. Figure B.1 shows a seismic section and the corresponding schematic of the Upper Jurassic Brae Field complex in the North Sea. The schematic cross-section shows abrupt lateral and vertical changes in stratigraphic units which are difficult to pick on seismic sections. Wireline logs are difficult to correlate making reservoir prediction and production hard and uncertain. This uncertainty can be reduced with 3D seismic interpretation.

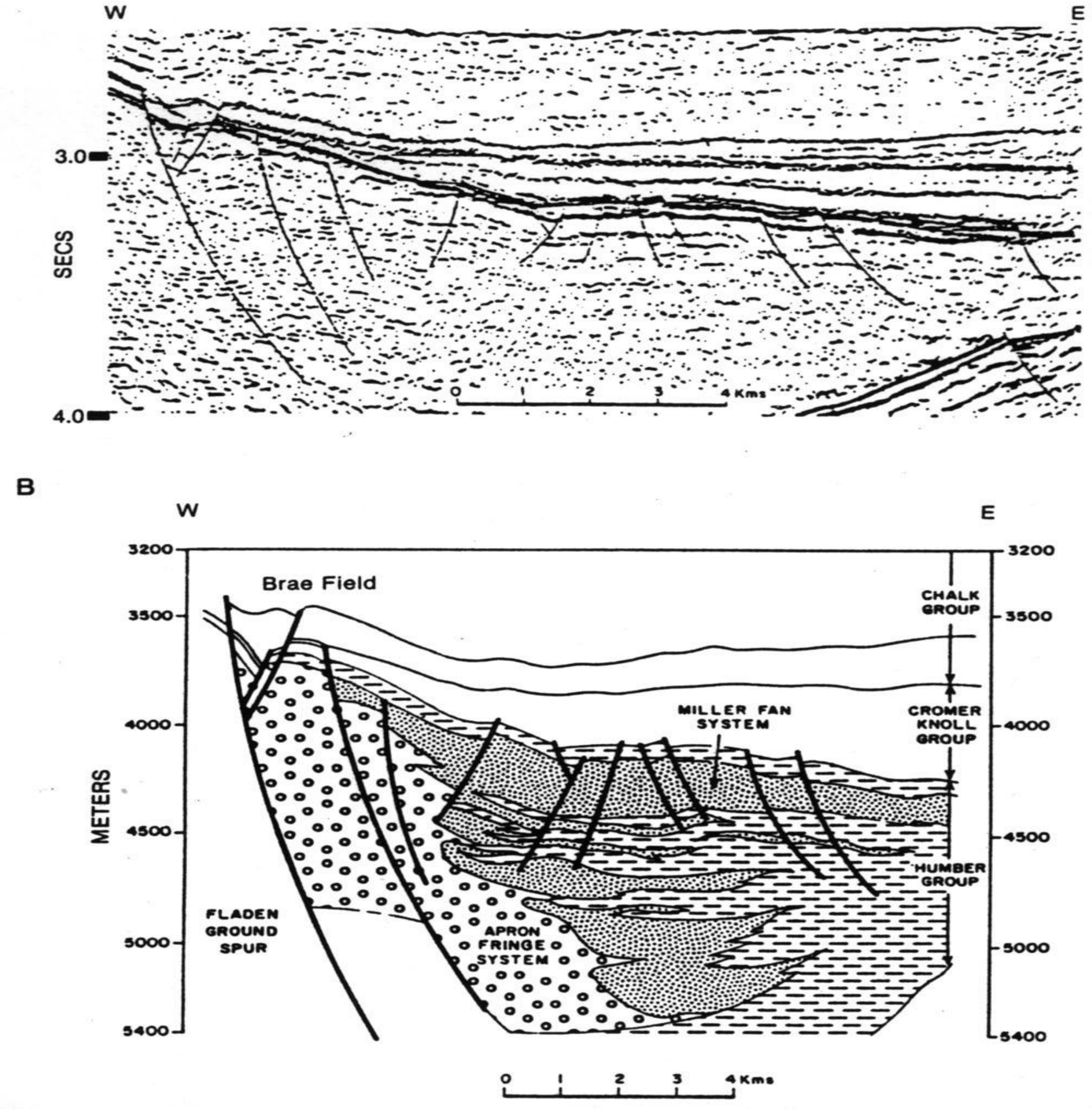

Figure B.1: Profiles across the Brae and Miller Fields, North Sea. (a) Seismic profile and (b) schematic cross-section. (After Weimer and Link.)

Sand-rich turbidite systems are characterized by channels with high net-to-gross sand (>70%) and usually do not have well developed levees. Amalgamated channels exhibit high production rates with good sweep efficiency. Lobes also exhibit high net-to-gross sand percentages (Figure B.2). Several Palaeogene reservoirs in the North Sea are sand-rich turbidite systems.

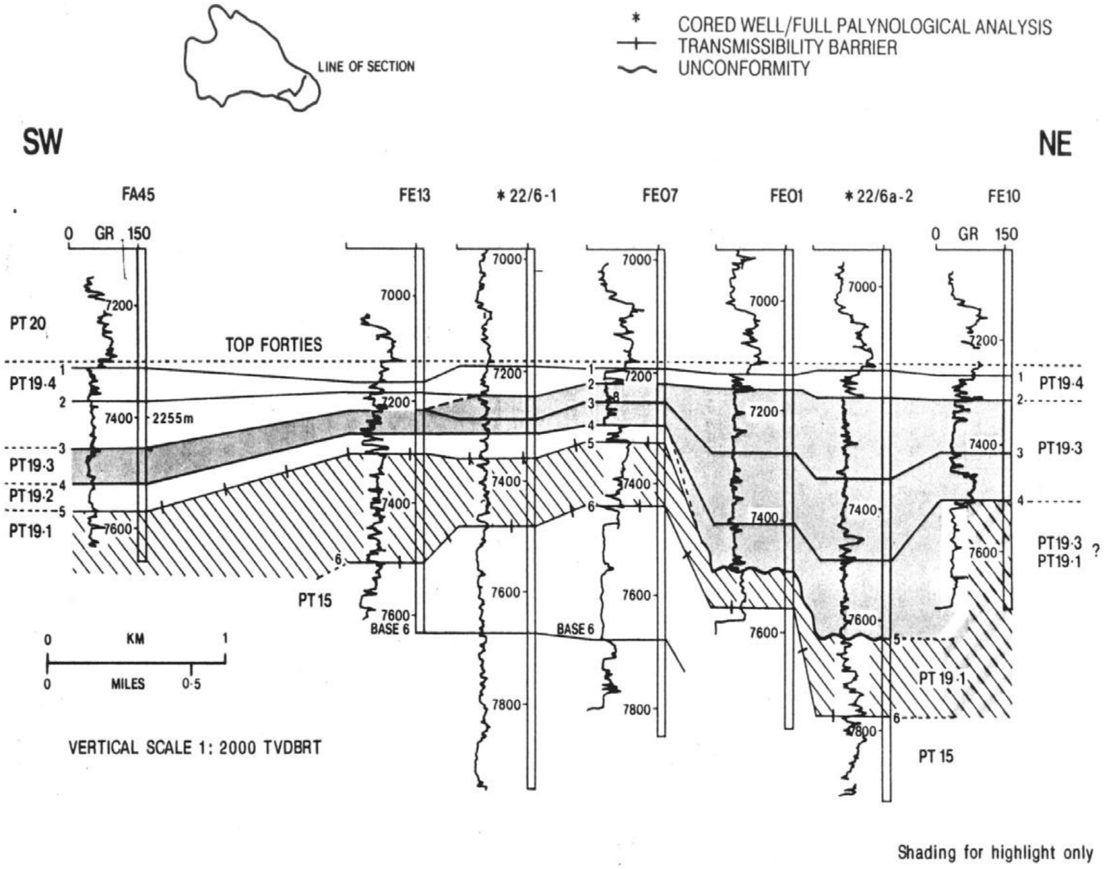

Figure B.2: Wireline log section across a sand-rich turbidite reservoir, Forties Field, North Sea. (After Kulpecz and Van Geuns)

On a 2D seismic section, channel fill is lens to mounded shape in strike-section, with erosional truncation at the base (Figure B.3). 3D seismic shows channels as linear to slightly sinuous while lobes tend to be stacked and laterally restricted.

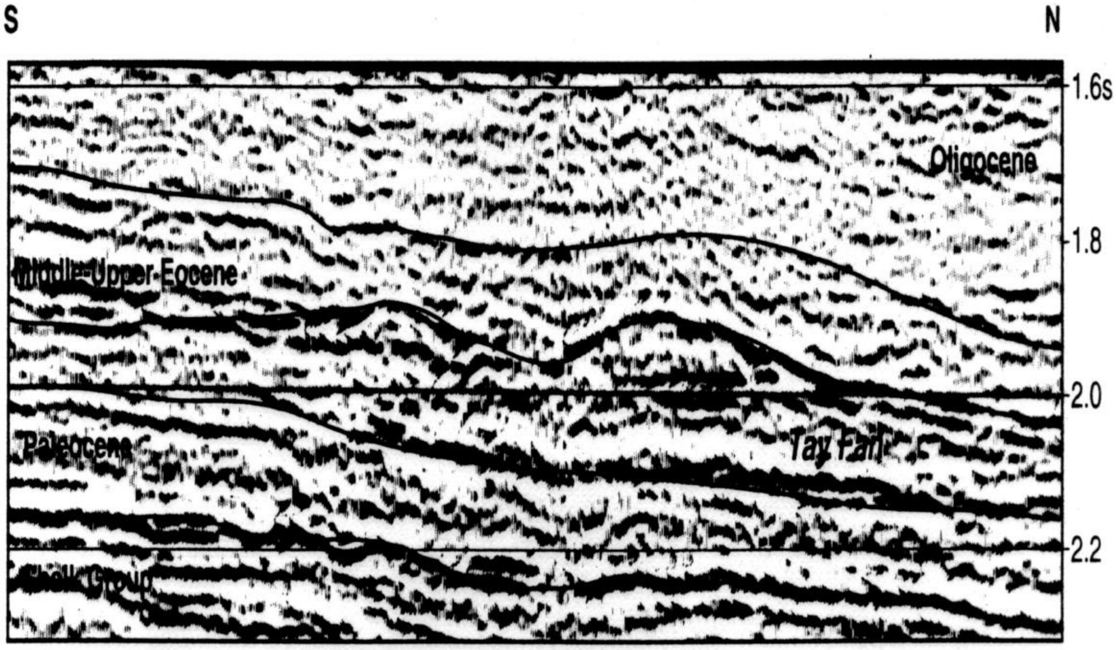

Figure B.3: Seismic profile across sand-rich turbidite system, North Sea. (After Jager et al.)

Mixed sand/mud turbidite systems represent a transition between sand-rich and mud-rich systems in terms of depositional elements and seismic facies, with generally moderate net-to-gross sand (50%). Examples of reservoirs from mixed mud-sand rich systems include the Eocene strata of the North Sea, Miocene strata of San Joaquin Basin in California, and portions of Cenozoic West Africa (Girassol and Dahlia fields). On 2D seismic, aggradational channels consist of discrete parallel reflections, with variable amplitude, flanked by levee-over-bank deposits (Figure B.4). On 3D seismic, channels are straight to sinuous, with amplitude generally different from the surrounding overbank deposits. The levee-overbank strata exhibit laterally continuous reflections of variable amplitude. Sheet sands exhibit parallel, laterally continuous reflections with discrete terminations (onlap, downlap).

Sheet sands show good lateral continuity where amalgamated. Channel fill exhibits blocky or upward-fining/thinning characteristics. Levees are generally thin (1-3 inches) planar to ripple laminated sandstones interbedded with shale (Figure B.5). Reservoir connectivity and communication is variable as channels and adjacent levees may not be in pressure or fluids communication.

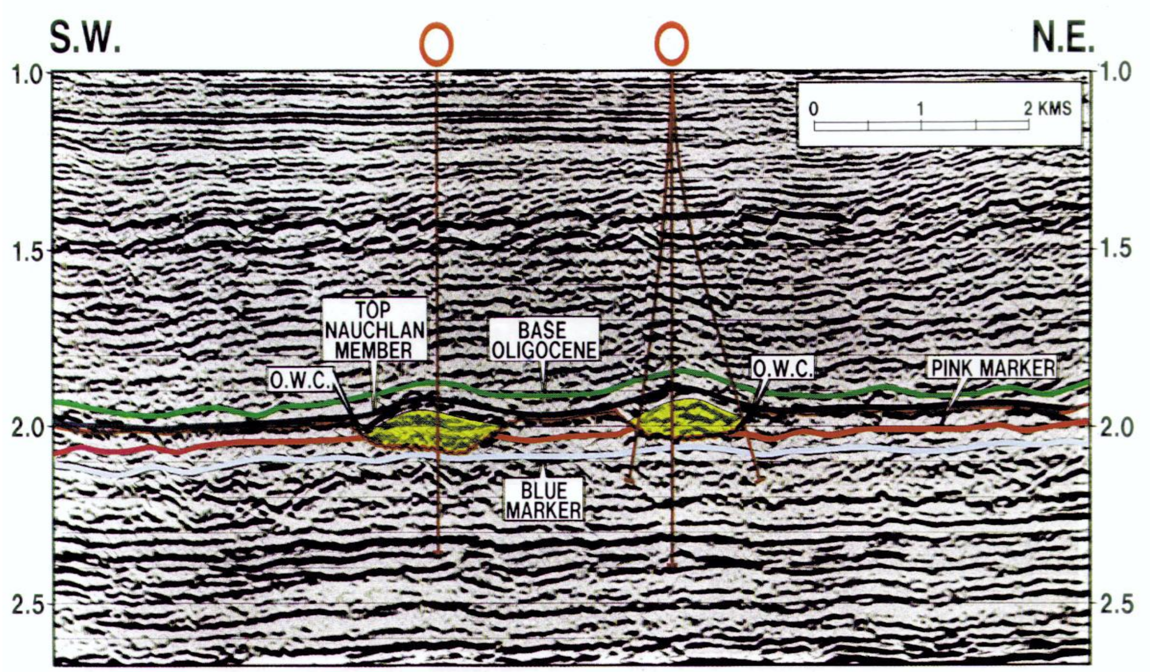

Figure B.4: Seismic profile across a mixed sand-mud rich turbidite system, Alba Field, North Sea. (After Newton and Flagran)

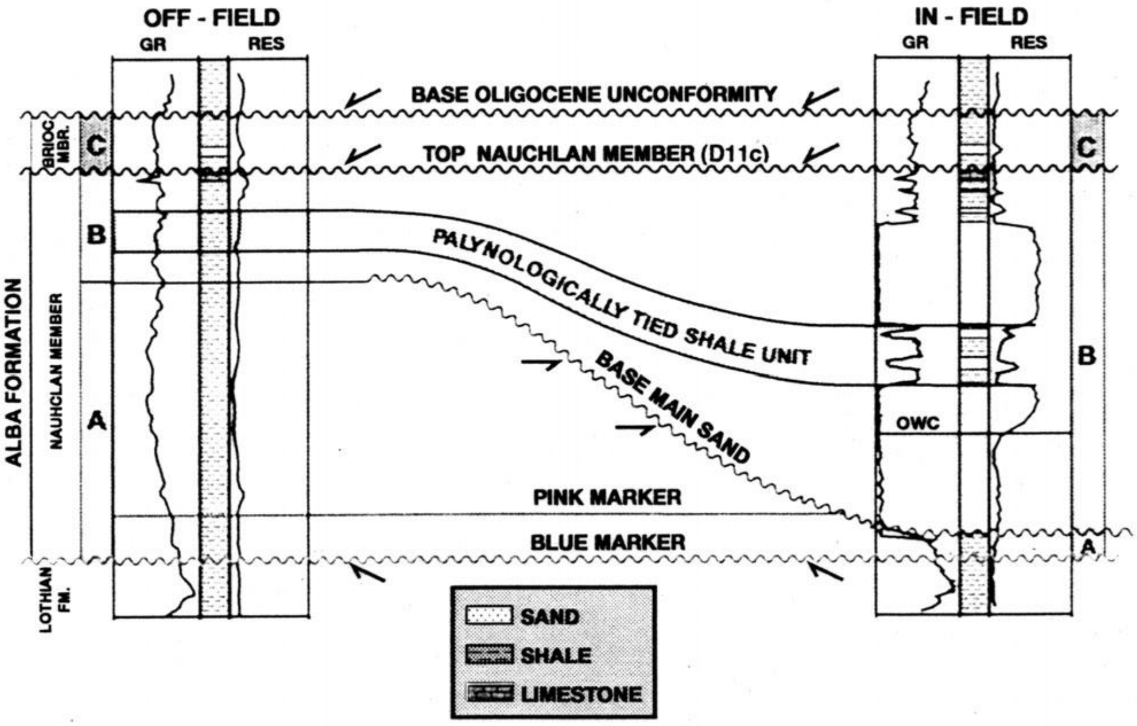

Figure B.5: Wireline log section across a mixed mud-sand turbidite reservoir, Alba Field, North Sea. (After Newton and Flanagan)

Mud-rich turbidite systems are characterized by low net-to-gross sand percentages within channel-levee systems, lobes (sheet sands), and slides (Figure B.6). Examples of mud-rich turbidite systems are the Neogene strata of the northern Gulf of Mexico and Upper Cretaceous strata of the Sacramento Valley (California). These systems are similar to mixed mud-sand systems but the net-to-gross sand is lower and levees volumetrically dominate over channels. 2D seismic cross-sections exhibit strong vertical changes from laterally continuous, sheets like reflections at the base of the reservoir to more discontinuous, channelized reflections toward the centre of the basin (Figure B.7).

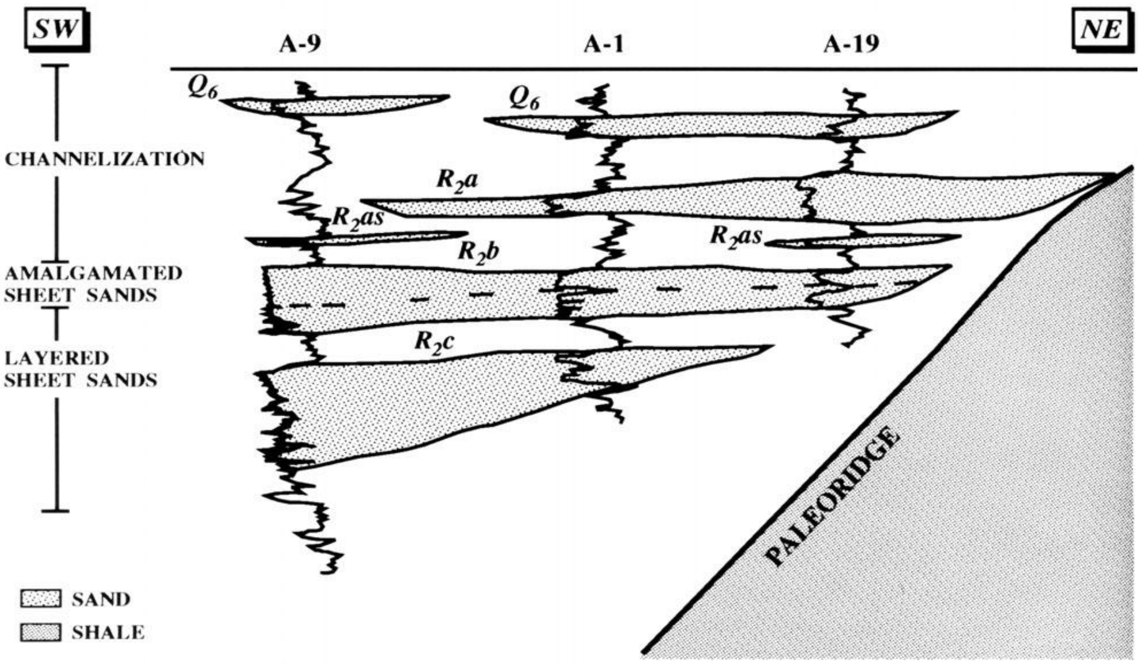

Figure B.6: wireline log section across a mud-rich turbidite systems, northern Gulf of Mexico. (After Weimer and Slatt, 1999).

The understanding of the key stratigraphic intervals and surfaces that bound turbidite systems and related elements is critical. These intervals and surfaces have been defined by integrating observations from modern and ancient turbidite systems, as derived from 2D and 3D seismic data, wireline logs, biostratigraphic data, reservoir pressure data, and outcrops.

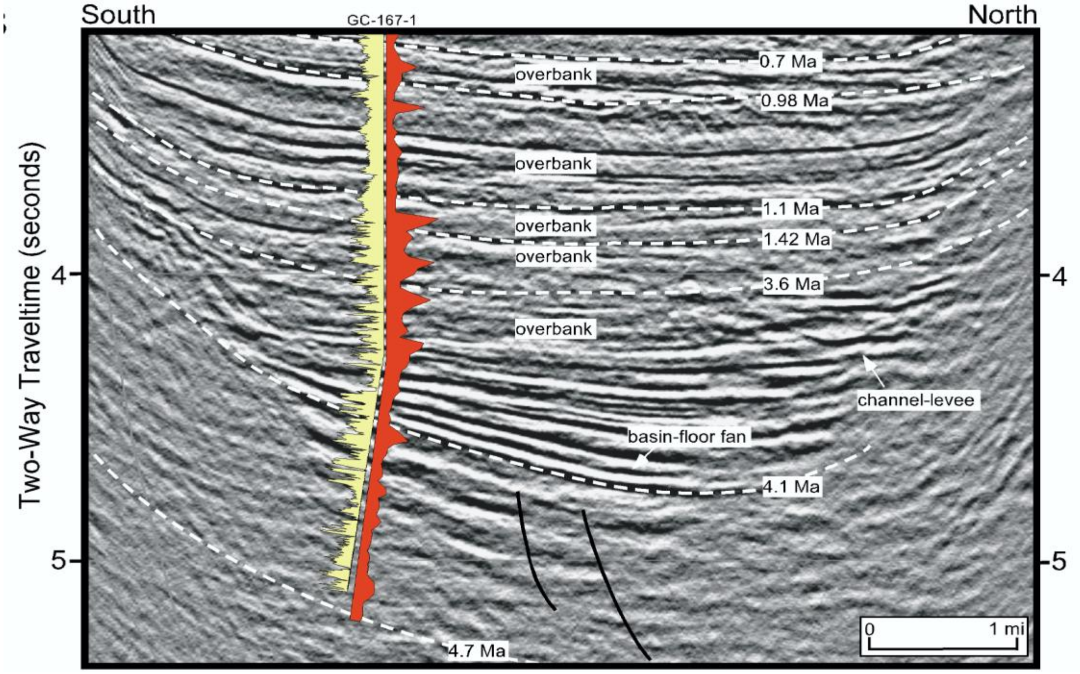

Figure B.7: Seismic profile from northern Gulf of Mexico. The yellow log is a time-based gamma log. (After Weimer and Slatt, 1999).

Two key intervals/surfaces are present in deepwater systems: condensed sections and sequence boundaries. Identifying these surfaces allows us to place turbidite systems within a sequence stratigraphic framework for the purpose of correlation, mapping, and reservoir characterisation.

Condensed sections are relatively thin layers of strata that reflect reduced sedimentation rates (Loutit et al. 1988). On seismic profiles, they exhibit laterally continuous reflections that drape the underlying sequence (Figure B.8). A sequence boundary is an erosional surface that separates cycles of deposition. Sequence boundaries have both erosional and conformable stratigraphic expressions in deep water (Figure B.8).

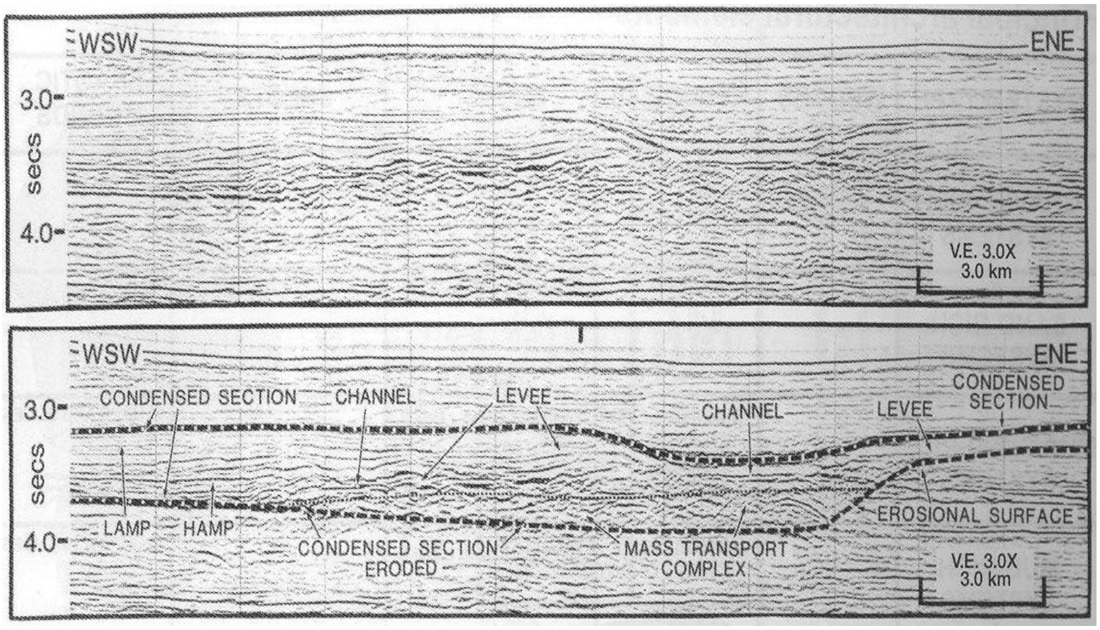

Figure B.8: Seismic profile across one deepwater depositional sequence (Upper Pleistocene) in the northern Gulf of Mexico. Key intervals/surfaces include a condensed section (laterally continuous doublet reflections) and erosional sequence boundary. Depositional elements include channel-fill, levee-overbank, and mass-transport complex. (after Weimer, 1990)

Appendix C

A brief history of petroleum use in human civilisation

Petroleum is not a new substance in human civilisation. Ancient people discovered many practical uses for petroleum substances (Forbes, 1964). Ancient civilizations from northern Iraq, south-west Iran and the Dead Sea area extensively used the abundant natural resources of petroleum, found in the form of natural bitumen deposits, oil seepage and liquid oil shows, until the Neolithic period (7,000 – 6,000 BC). Evidence of earlier use has been documented in the Syrian Desert (Boëda et al., 1996), where bitumen-coated flint implements, dated to 40,000 BC (Mousterian period), have been unearthed.

Bitumen was largely used in Mesopotamia and Elam as mortar in the construction of palaces (e.g. the Darius Palace in Susa), temples, ziggurats (e.g. the Tower of Babel in Babylon), terraces (e.g. the Hanging Gardens of Babylon) and exceptionally for roadway coating (e.g. the processional way of Babylon). Since the Neolithic, bitumen served to waterproof containers (baskets, jars, storage pits), wooden pots, palaces grounds, palm roofs, etc. Mats, sarcophagi, coffins and jars, used for funeral practices, were often covered and sealed with bitumen (Connan, 1999).

Bitumen was also considered as a powerful remedy in medical practice, especially as a disinfectant and insecticide, and was used by the ancient Egyptians to prepare mixtures to embalm the corpses of their dead during the mummification process. The use of petroleum substances in the ancient times was not limited to the Middle East area, ancient Far East civilisations, such as in China and in Japan, used oil for lighting and for medical purposes. Mediterranean civilisations used bitumen in many of their every day life tasks.

The modern history of the petroleum industry began when the process of refining kerosene from raw coal was discovered by Abraham Pinoe Gesner in the year 1846. Then there was literally no looking back for the growth of petroleum industry throughout the world. The first Russian refinery was built at Baku during the year 1861 and it accounted for around 90% of the world oil production.

During the 1800s the growth was gradual and quite slow. Before the 1850s, people often used whale oil for light. When whale oil became scarce, people began looking for other oil sources: kerosene. Colonel Edwin Drake drilled the first successful oil well in Titusville, Pennsylvania in 1859 looking for a source of kerosene to be used for lighting fuel. This primary market for oil had begun to disappear when Thomas Edison invented the light bulb and created the electrical generation industry.

For most of the 19th century, gasoline was simply a by product of the production of kerosene, with few commercial uses, but after the internal combustion engine was invented in 1896, there was a surge in the demand for petroleum products. The outbreak of World War I in 1914 changed the role of petroleum in the world forever. Motorized transport began to dramatically change the nature of war. The development of the airplane and of the tank, which was first used at the Battle of the Somme in 1918, provided both mobility and power that was unprecedented in the history of warfare; in some ways, oil was more critical to military success than ammunition.

The sale of oil became an important industry by the early 1900s. Oil fields were also discovered in places such as Canada, Iran, Mexico, Venezuela and Peru. At that same time, the automobile industry began to grow rapidly, opening up an enormous market for gasoline. New more efficient refining processes were invented and led to the production of more gasoline out of each barrel of crude oil. Farming productivity after the war was greatly improved by tractors and other oil-fuelled machinery. Similarly during World War II, the oil industry proved that it could boost production quickly and create specialized new products for military needs, such as high-octane fuel for airplanes and raw materials for synthetic rubber.

By the 1950s, oil had replaced coal as the world’s most important fuel, just as coal had replaced wood 150 years earlier. In addition to supplying the automotive market, oil had displaced coal as the major railroad fuel. Even more quickly, oil took coal's place as a shipping fuel. Oil also began to compete with coal in certain industrial applications and even, to some extent, in power generation.

References

Aki, A. and P.G. Richards, 1980, Quantitative seismology: Theory and methods: W.H. Freeman and Company.

Amini, H., 2009, ETLP Meeting, November 2009, personnel communication

Backus, G. E. (1962). Long-wave elastic anisotropy produced by horizontal layering. 67:4427–4440.

Bakke, K., Gjelberg, J. and Petersen, S.A., 2007, Compound seismic modelling of the Ainsa II turbidite system, Spain: Application to deep-water channel systems offshore Angola. Marine and Petroleum Geology 25 (2008) 1058-1073

Batzle, M. and Wang, Z., 1992, Seismic properties of pore fluids. Geophysics, 57(11):1396–1408.

Bentham, P.A., Burbank, D.W., Puigdefabregas, C., 1992, Temporal and spatial controls on the alluvial architecture of an axial drainage system: late Eocene Escanilla Formation, southern Pyrenean forland basin, Spain. Basin Research 4, 335–352.

Berryman, J. (1999). Tutorial: Origin of Gassmann's equations. Geophysics, 64:1627–1629.

Berryman, J. and Milton, G. (1991). Exact results for generalized Gassmann's equations in composite porous media with two constituents. Geophysics, 56:1950–1960.

Biot, M. (1956). Theory of propagation of elastic waves in a fluid saturated porous solid, Parts I and II. The journal of the Acoustic Society of America, 28:168–191.

Boëda, E., Connan, J., Dessort, D., Muhesen, S., Mercier, N., Valadas, H. & Tisnerat, N., 1996, Bitumen as a hafting material on Middle Palaeolithic artefacts. Nature 380, 336-338.

Bourgeois, A., Labat, K., Euzen, T., Le Bras,C., 2005, How to build a geological and geophysical realistic synthetic seismic data set for benchmarking reservoirs studies? SEG 2005 Annual Meeting, Houston, Texas, USA.

Brawis, J.H., McPherson, J.G. and Studlick, J.R., 1990, Sandstone petroleum reservoirs, Springer-Verlag New York Inc.

Buckley, S.E. and Leverett, M.C., 1942, Mechanism of Fluid Displacement in Sands, Transactions, AIME, 1942, Vol.146:107.

Byerley, G., Pederson, J., Roervik, K.O., Ranaweera, K. and Janssen, A., 2006, Reducing risk and monitoring water injection using time-lapse (4D) seismic at the Ekofisk field. SEG International Exposition and Annual Meeting, New Orleans

Chapin, M.A, P. Davis, J.L. Gibson, and H.S. Pettingill, 1994, Reservoir architecture of turbidite sheet sandstones in laterally extensive outcrops, Ross Formation, western Ireland, in P. Weimer, A.H. Bouma, and B.F. Perkins, eds., Submarine fans and turbidite systems: Gulf Coast Section-SEPM Foundation 15th Annual Research Conference, 53-68.

Connan, J., 1999, Use and trade of bitumen in antiquity and prehistory: molecular archaeology reveals secrets of past civilizations, Philosophical Transactions of the Royal Society B: Biological Sciences, 1999 January 29; volume 354, pp.: 33–50

Connan, J. & Deschesne, O., 1995, Archaeological bitumen: identification, origins and uses of an ancient near eastern material. Mat. Res. Soc. Symp. Proc. 267, 683-720.

Craig Jr., F.F., 1973, Engineering Waterfloods for Improved Oil Recovery
SPE Distinguished Lecture, SPE 4425-MS

Dake L.P., 2001, The Practice of Reservoir Engineering (revised edition), Elsevier.

Domes, F., MacBeth, C., and Brain, J., 2009, The Influence of Overburden on Time-Lapse Saturation Interpretation. *71th EAGE Meeting*, page Y002, Amsterdam, Netherlands.

Dreyer, T., Corregidor, J., Arbues, P., Puigdefabregas, C., 1999, Architecture of the tectonically influenced Sobrarbe deltaic complex in the Ainsa Basin, northern Spain. Sedimentary Geology 127, 127–169.

Dykstra, H. and Parsons, R.L, 1950, The Prediction of Oil Recovery by Waterflood, Secondary Recovery of Oil in the U.S., API, 160

Falcone, G., Gosselin, O., Maire, F., Marrauld, J., and Zhakupov, M. (2004). Petroelastic modelling as key element of 4D History Matching: A Field Example (SPE 90466). In SPE Annual Technical Conference and Exhibition, Houston, Texas

Floricich, M., 2006, An engineering-consistent approach for pressure and saturation estimation from time-lapse seismic data. PhD thesis, Heriot Watt University.

Fontana, D., Zuffa, G.G., Garzanti, E., 1989, The interaction of eustacy and tectonism from provenance studies of the Eocene Heocho Group

Forbes, R. J., 1964, Bitumen and petroleum in Antiquity. In Studies in Ancient Technology, 2nd edition. vol. 1, pp. 11-23.

Freund, D., 1992, Ultrasonic compressional and shear velocities in dry clastic rocks as a function of porosity, clay content and confining pressure. Geophysical Journal International, 108:125–135.

Garfield, T.R., D.C. Jennette, F.J. Goulding, and D.K. Sickafoose, 1998, An integrated approach to deepwater reservoir prediction. AAPG International Conference and Exhibition, Expanded Abstracts volume, 278-279.

Gassmann, F., 1951, Uber die Elastizitt Poroser Medien: Vierteljahrsschrift der Naturforschenden Gesellschaft in Zurich, 96, 1–23.

Hamada, G.M., 2004, Reservoir Fluids Identification Using Vp/Vs Ratio, Oil & Gas Science and Technology – Rev. IFP, Vol. 59 (2004), No. 6, pp. 649-654

Han, D., Nur, A., and Morgan, D., 1986, Effects of porosity and clay content on wave velocities in sandstones. Geophysics, 51(11):2093–2107.

Jager et al., 1993, Evolution of Palaeogene submarine fans of the North Sea in space and time, Petroleum Geology of Northwest Europe: Proceedings of the Fourth Conference, The Geological Society, London.

Kahar, Y., and Anno, P. D., 2006, Fluid flow phenomena from 4D interpretation, Heidrun Field, Norwegian North Sea. SEG Annual Meeting, New Orleans 2006.

Kimbler, O.K., Caudle, B.H. and Hutchinson Jr., C.A., 1962, A Fresh Look at Waterflood Theory and Practice, SPE 365-MS 1962

Kleppe, J., Review of relative permeabilities and capillary pressure, Reservoir Recovery Techniques, Handout note 3, Norwegian University of Science and Technology, Department of Petroleum Engineering and Applied Geophysics.

Koster, K., Gabriels, P., Hartung, M., Verbeek, J., Deinum, G. and Staples, R., 2000, Time-lapse seismic surveys in the North Sea and their business impact.

Kulpecz and van Geuns, 1990, Geological modelling of a turbidite reservoir, Forties Fields, North Sea, Sandstone Petroleum Reservoirs, Springer-Verlag

Landro, M., Solheim, O.A., Hilde, E., Ekren, B.O. and Stronem, LK., 1999, The Gullfaks 4D seismic study. Petroleum Geosciences, Volume 5, 1999, pp. 213-226

Loutit, T.S., J. Hardenbol, P.R. Vail, and G.R. Baum, 1988, Condensed sections: the key to age determination and correlation of continental margin sequences, in C.K. Wilgus, B.S. Hastings and C.G. St. C. Kendall, editions, sea-level changes: An integrated approach: SEPM Special Publication 42, 183-213.

Lumley, D., 2004, Business and technology challenges for 4D seismic reservoir monitoring. The Leading Edge, 23(11):1166–1168.

Lumley, D.E. and Behrens, R.A., 1998, Practical issues of 4D seismic reservoir monitoring: What an engineer needs to know, SPE Reservoir Evaluation and Engineering, 1998.

MacBeth, C., 2004, A classification for the pressure-sensitivity properties of a sandstone rock frame. Geophysics, Vol 69, No 2 (March-April 2004); P. 497-510.

MacBeth, C., Soldo, J., and Floricich, M., 2004, Going quantitative with 4D seismic. SEG International Exposition and Annual Meeting, Denver, Colorado.

MacBeth, C., Stephen, K. and McInally, A., 2005, The 4D seismic signature of oil-water contact movement due to natural production in a stacked turbidite reservoir. Geophysical prospecting, 2005, 53, 183-203.

MacBeth, C., HajNasser, Y., Stephen, K., and Gardiner, A., 2010, Exploring the effect of meso-scale shale beds on the reservoir's overall stress sensitivity to seismic waves. Geophysical prospecting, in press

Marsh, M., 2004, 4D in reservoir management - Successes and Challenges. IOR Views e-Newsletter, 8.

Marsh, J.M., Whitcombe, D.N., Raikes, S.A., Parr, R.S. and Nash, T., 2002, BP's increasing systematic use of time-lapse seismic technology. Petroleum Geoscience, Volume 9, pp. 7-13

Mutti, E. and W.R. Normark, 1987, Comparing examples of modern and ancient turbidite systems: Problems and concepts, in J.K. Leggett and G.G. Zuffa, eds., Marine clastic sedimentology: London, Graham and Trotman,1-38.

Mutti, E. and W.R. Normark, 1991, An integrated approach to the study of turbidite systems, in P. Weimer and M. H. Link, eds, Seismic facies and sedimentary processes of submarine fans and turbidite system: New York, Springer-Verlag, 75-106.

Newton and Flanagan, 1993, The Alba Field: evolution of the depositional model, Petroleum Geology of Northwest Europe: Proceedings of the Fourth Conference, The Geological Society, London.

Oldenziel, T., 2003, Time lapse seismic within reservoir engineering, PhD thesis, Delft University of technology, 2003.

Philip, J.R., 1991, Soil, natural science, and models. Soil Science Journal, Volume 151, January, pp 91-98.

Pickering, K.T., Corregidor, J., 2000, 3D Reservoir scale study of Eocene confined Submarine Fans, south Central Spanish Pyrenees. Deep Water Reservoirs of the World.

Gulf Coast Section, Society of Economic Palaeontologists and Mineralogists, Foundation 20th Annual Bob F. Perkins Research Conference, Houston, TX, pp. 776–781

Pickering, K.T., Corregidor, J., 2005, Mass-transport complexes (MTCs) and tectonic control on basin-floor submarine fans, middle Eocene, south Spanish Pyrenees. Journal of Sedimentary Research 75, 761–783.

Rauch, J., 2001, The new old economy: Oil, computers, and the reinvention of the earth, The Atlantic, January 2001

Reading, H.G. and M. Richards, 1994, Turbidite systems in deep-water basin margins classified by grain size and feeder system: AAPG Bulletin, 78, 792-822.

Rudolph, K. W., 2001, DHI/AVO analysis best practices: A worldwide analysis: AAPG Distinguished Lecturer abstract (www.aapg.org)

Schinelli, M., 2006, Using complex seismic attributes to improve 4D visibility of fluids contact movement, SEG Annual Meeting, New Orleans 2006.

Smith, P., 1998, Reservoir characterization, modelling, and fluid-flow simulation in Developing and Managing Turbidite Reservoirs: Case Histories and Experiences.

Staples, R., Cook, A., Braisby, J., Mabillard, A. and Rowbotham, P.S. 2006: Integration of 4D Seismic Data and the Dynamic Reservoir Model - Revealing New Targets in Gannet C, EAGE 68th Conference & Exhibition — Vienna, Austria, 2006

Staples, R., Stammeijer, J., Jones, S., Brain, J., Smit, F. and Hatchell, P., 2006, Time-Lapse (4D) Seismic Monitoring - Expanding Applications. 2006 CSPG – CSEG – CWLS Convention.

Stiles, W.E., 1949, Use of Permeability Distribution in Water Flood Calculations, Transactions, AIME, volume 186:9.

Tad M. Smith, Carl H. Sondergeldz, and Chandra S. Raiz, 2003, Gassmann fluid substitutions: A tutorial. Geophysics, Vol. 68, No. 2 (March-April 2003); P. 430–440.

Thore, P. 2006, Accuracy and limitations in seismic modeling of reservoir, SEG Annual Meeting, New Orleans 2006.

Thurmond, J.B., Løseth, T.M., Rivenæs, J.C., Martinsen, O.J., Aiken, C., Xu, X., 2008, Using Outcrop Data in the 21st Century – New methods and applications, with example from the Ainsa Turbidite System, Ainsa, Spain. AAPG Atlas of Deep Water Outcrops, in press.

Wang, Z., Hirsche, W. K. and Sedgwick, G., 1991, Seismic monitoring of water floods? A petrophysical study. SEG 60th Annual Meeting.

Wang, Z. and Nur, A., 1986, Effect of temperature on wave velocities in sands and sandstones with heavy hydrocarbons (SPE 15646), SPE Annual Technical Conference and Exhibition, New Orleans, Louisiana.

Wang, Z., Batzle, M., and Nur, A., 1990, Effect of different pore fluids on seismic velocities in rocks, Canadian Journal of Exploration Geophysics, 26(1 - 2):104–112.

Waggoner, J., 2000, Lessons learned from 4D projects (SPE 65369). SPE Reservoir Evaluation and Engineering, 3(4):310–318.

Weimer, P. and Slatt, R. M., 1999, Turbidite systems, Part 1: Sequence and seismic stratigraphy, The Leading Edge, April 1999

Weimer, P. and Slatt, R.M., 2004, Petroleum systems of deepwater settings: EAGE 2004 Distinguished Instructor Short Course.

Weimer, P. and Link, M.H., 1991, Global petroleum occurrences in submarine fans and turbidite systems: Seismic Facies and Sedimentary Processes of Submarine Fans and Turbidite Systems, Springer-Verlag.

Weimer, P., 1990, Sequence stratigraphy, seismic geometries, and depositional history of the Mississippi Fan, deep Gulf of Mexico, AAPG Bulletin, 74, 425-453.

Weimer, P. R.M. Slatt, P. Dromgoole, M. Bowman, and A. Leonard, 2000a, Developing and managing turbidite reservoirs: Case histories and experiences- Results from the AAPG/EAGE Research conference: AAPG Bulletin, 84, 453-464.

Weimer, P. and Slatt, R. M., 1999, Turbidite systems, Part 2: Sub-seismic scale reservoir characteristics, The Leading Edge, May 1999

Welge, H.J., 1952, A Simplified Method for Computing Oil Recovery by Gas or Water Drive, Petroleum Transactions, AIME, Volume 195, 1952, pages 91-98, SPE 124-G.

Willhite G.P., 1986, Waterflooding, SPE Textbook series Vol. 3

Wyllie, M., Gregory, A., and Gardner, G., 1958, An experimental investigation of factors affecting elastic wave velocities in porous media. Geophysics, 23(3):459–493.